Evolution of coalbed methane: Insights from stable and noble gas isotopes

Biying Chen

Submitted in fulfilment of the requirements for the degree of
Doctor of Philosophy

Scottish Universities Environmental Research Centre
College of Science and Engineering
University of Glasgow

September 2020

Abstract

Coalbed methane (CBM) is an important energy source in many countries. The origin and post-generation evolution of methane in coalbeds are rather poorly understood despite the importance of assessment of reserves and developing exploration strategies. Stable isotopes are the typical geochemical tools to analyse the gas origin and subsequent evolution. Noble gases are widely used for identifying the source of fluids in reservoirs and the impact of the tectonic and hydrologic activities on hydrocarbon generation and preservation. In this PhD, I have studied the composition of gases from the Southeast Qinshui Basin, the most CBM productive region in China, and the Liupanshui Coalfield, a CBM development target in southern China. Methane in these two regions was formed in the late Triassic during burial and heating driven by magmatic activity in Late Jurassic to Early Cretaceous. Cenozoic basin inversion brought the coals to a shallow depth. This study aims to establish how the gas formed, to estimate the contribution of magmatic heating on methane generation and the influence of basin exhumation on gas storage.

Nineteen gas samples were taken in April 2017 from methane-producing wellheads along an E-W transect perpendicular to the boundary fault in Southeast Qinshui Basin (SQB) in northern China. The stable isotope compositions ($\delta^{13}C$= -35.2 to -30.2‰, δD= -194 to -155‰) indicates a thermogenic origin with limited microbial input. They are, however, lighter than expected based on coal maturity, perhaps due to adsorption/desorption fractionation during commercial gas extraction. He-Ne-Ar isotopes are a mixture of crustal-radiogenic gas with air-derived noble gases from groundwater. ^{4}He concentrations (0.52 to 33.25 ppmv) and $^{4}He/^{40}Ar^{*}$ ratios (0.06–1.74) are unusually low. He-Ne-Ar concentrations are consistent with the open system Rayleigh fractionation of noble gases derived from air-saturated water (ASW) with $^{4}He/^{40}Ar^{*}$=1 during gas extraction. The low $^{4}He/^{40}Ar^{*}$ compared with average crust (5) or local production (13) values, implies that radiogenic ^{4}He produced in the coals was lost prior to equilibrium between gas and water phase in the reservoir. This likely occurred during rapid exhumation in Cenozoic. The event may have led to the loss of up to 44% of the methane from the coal seams. The

depletion of Xe and Kr without significant enrichment of Ne suggests the strong retention of Kr and Xe in SQB coals.

Ten CBM samples were collected in April 2018 from the four blocks containing different mature coals in Liupanshui Coalfield (LPC) in southern China. Two gas samples were collected from the same two wells in the Dahebian block in October 2018. This is the first gas geochemical work in LPC. Methane is mainly thermogenic in origin based on the $C_1/(C_2+C_3)$ ratio (16-971), $\delta^{13}C_{CH4}$ (-42.9 to -34.9‰) and δD_{CH4} (-206 to -140‰). The difference in major gas and stable isotope compositions between the four blocks of LPC is mainly due to the different extent of maturation of coals in each block. Noble gases in LPC are a mixture of air-derived gases from ASW with crustal gases in the reservoir. The lower proportion of nucleogenic Ne and $^4He/^{40}Ar^*$ ratios in gases from Qingshan block compared with other blocks implies an evident He and Ne loss. The gas loss is also inferred to be the result of basin inversion. $^{20}Ne/^{36}Ar$ ratios (0.23-0.70) are higher than local ASW (0.16), requiring a re-dissolution fractionation process similar to that proposed for CO_2 gas reservoirs (Gilfillan et al., 2008). $^{84}Kr/^{36}Ar$ and $^{132}Xe/^{36}Ar$ ratios in LPC are mostly higher than the modelled fractionation lines. This is explained by desorption of initial trapped Xe and Kr in the coal matrix. The Qingshan block gases contain the same depleted Kr and Xe pattern as SQB, suggesting the stronger adsorption capacity of local coals to Kr and Xe.

Over 93% of He and 9% of Ar budget of the coal basins is estimated to have been lost during the gas loss process. It explains the absence of mantle volatiles in the SQB and LPC CBM. This demonstrates the importance of basin inversion on gas preservation in shallow CBM and shows that the light noble gases are essential for tracing such a process.

Table of Contents

List of Tables

List of Figures

Acknowledgements

First of all, I present my sincerest gratitude to my supervisors, Prof. Finlay Stuart, Prof. Sheng Xu and Dr. Matthieu Clog.

Fin has shown incredible patience with me during the whole PhD study. He has always been willing to devote time on study discussion with me and correction of my poor English writing. Whenever I lost faith in the study, he reminded me to see the positive and boosted my confidence. His impact on me is not only in academic research but also in personal development. In such a special time, he has cared for my physical and mental health, which has released my stress from the lockdown and helped me to make progress of thesis writing.

I thank Sheng for the remarkable contribution to my PhD study, instructive suggestions in the future development of my academic work and his caring of daily life. A big thanks to him for the organisation of the field trip.

The great help from Matthieu in the thesis writing at the final stage is appreciated a lot.

I would like to thank Dr. Domokos Györe who has played a role in every corner of my PhD study. He has selflessly shared the experience of field sampling and the understanding of ultra-high vacuum and noble gas mass spectrometry. I have learned all the sample analysis and data calculation procedures from him and received generous help in data interpretation.

Thanks also to Dr. Marta Zurakowska who has given boundless assistance in my lab work. I am also grateful for all her comfort and encouragement whenever I met an obstacle, it supported me even in the toughest time.

I thank Terry Donnelly for the thorough guidance and assistance in the analysis of gas composition and stable isotopes, in particular his contribution to my training in gas chromatography and the vacuum line for methane combustion.

I would like to thank Tracey Mark for the organisation in the transport of the sampling device between China and Britain. To Dr. Luigia Di Nicola, Ross Dymock, Nicole Doran,

Allan Davison, Andrew Tait and Terence Donnelly, who helped me in various ways during the study.

I thank my fellow SUERC PhD students, David Currie, Dr. Emma Roberts, Felipe Sepulveda, Rasika Mahajan and Sophie McDonald, who reminded me that I am not alone in the struggle.

I thank the University of Glasgow and Scottish Universities Environmental Research Centre for the PhD funding. I am grateful to Lan Yan Coalbed Methane Company and Liupanshui Energy Investment Development Company for the permission to sample, provision of field information and permission to use the data. A special thank to Yanlong Li for the help in the organisation of sampling in Liupanshui coalfield.

I have been fortunate to gain support from Shiqi Hu, Hairong Xu, Kaixuan Ji and Dr. Anran Cheng, the best friends I have during the PhD study. A thank to Yan Ma, Liyan Wu, Yu Liu, Xian Chen, Ying Wang, Weiwei Xue and Jialong Wang, whose appearance has coloured my life in East Kilbride.

Finally, I want to show my gratitude to my parents and little brother. They have always been there as my biggest supporters.

Declaration

I declare that this thesis, except where the reference is made to the contribution of others, represents my independent research work from October 2016 to September 2020. The presented material has not been submitted for any other degree.

Biying Chen

22/09/2020

Chapter 1 Introduction

1.1 The history and importance of coalbed methane

The natural gas captured from coal seams, called as coalbed methane (CBM), coal seam gas or coal seam methane, is one of the unconventional natural gas resources (American Association of Petroleum Geologists, 2015; McGlade et al., 2013; Moore, 2012). Although gas produced from coal seams is rarely pure methane, CBM is widely utilised as it includes the two principal and the most attractive contents: 'coal' and 'methane' (Moore, 2012). CBM is defined to be the production before coal mining, setting it apart from coal mine methane (CMM) which is mainly released during and after coal mining (Karacan et al., 2011). Moreover, CMM development is mainly driven by mining safety and reduction of greenhouse gas, while CBM is considered as an energy resource and primarily related to market need (American Association of Petroleum Geologists, 2015). It is also worthwhile to distinguish CBM from coal-derived methane which belongs to conventional natural gas and has migrated from source to porous reservoirs (American Association of Petroleum Geologists, 2015).

Coal was one of the most important fossil fuel resources since the Industrial Revolution (Dudley, 2019; Park and Liang, 2016). Early coal mining in the United Kingdom and Europe concentrated on shallow buried coals or outcrops where the stored gases could have been vented naturally (Flores, 1998). With the exhaustion of shallow coals and improvement of technology, attention shifted to deeper coal mines where high methane contents could be preserved (Flores, 1998). The poor gas drainage during the mining allowed the accumulation of methane, which could be easily ignited and induce an explosion. Underground coal mine accidents were first documented in the United States in 1810, and have been occurring worldwide since the early to middle 19th-century (Flores, 1998). Methane emissions during standard coal mining and after closure are a serious contribution to greenhouse gas, as the actual greenhouse effect of methane is 20 times that of carbon dioxide (Flores, 1998; Luo and Dai, 2009; Zazzeri et al., 2016). With the increasing emphasis on CBM as a potential energy source, research has been aimed at

establishing the relation between reservoir characterisation with recoverability and producibility of CBM (Flores, 1998). Mastalerz (2014) reported global CBM resources of 1.1-1.2 $\times 10^{14}$ m^3, of which 4.2 $\times 10^{13}$ m^3 is recoverable. It is close to another estimate for the global remaining technically recoverable CBM resources of 3.9 $\times 10^{13}$ m^3 proposed by McGlade et al. (2013). It accounts for about 14% of global unconventional natural gas resources (Figure 1.1; McGlade et al., 2013). The estimates of CBM potential are mainly based on reservoir property and laboratory core analysis (Al-Jubori et al., 2009). It likely has large uncertainties considering the limited reachable information and complex conditions of coal seams (Moore, 2012).

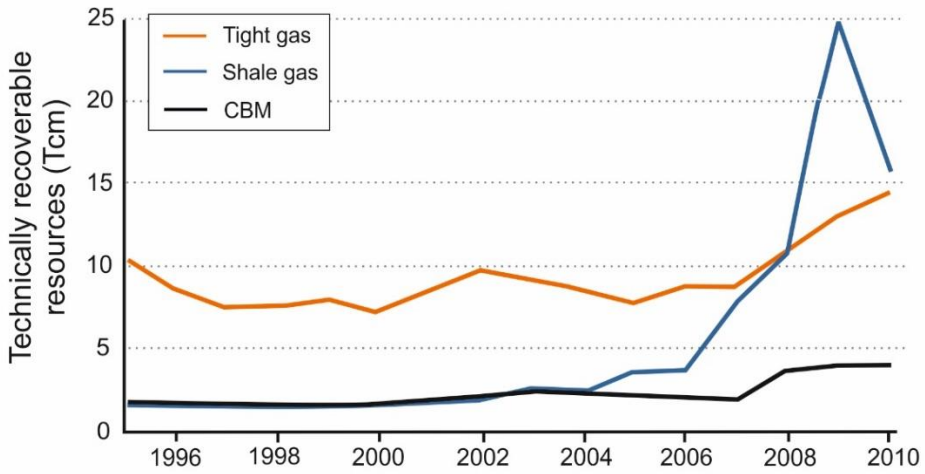

Figure 1.1. How estimates of remaining technically recoverable unconventional gas resources have changed with time. Tcm=trillion cubic meter. Taken from McGlade et al. (2013).

The United States currently leads the global production of CBM. The oil crisis in the 1970s stimulated the pioneering work to recover CBM in USA (Moore, 2012). The first successful product was from the test wells drilled in Black Warrior Basin (Flores, 1998). The application of vertical well technology in CBM drilling announced the possibility of commercial production of CBM in mid-1970s (Flores, 1998). The enactment of the 'Crude Oil Windfall Profit Tax of 1980' also promoted the development of CBM (Geny, 2010; Soot, 1988). The tax-credit provided CBM producers $0.75 per million Btu (British thermal unit) of gas sold in 1986, which was projected to $1.34 per million Btu of gas sold in 2001 (Geny, 2010; Soot, 1988). Although this tax-credit expired in 1992, the decline of

domestic natural gas production and corresponding high natural gas price in the early 2000s provoked the development of unconventional natural gas (Geny, 2010). The annual production of CBM in the USA from 1989 to 2017 is shown in Figure 1.2. The production reached a peak in 2008 with 5.6 $\times 10^{10}$ m^3 per year (American Association of Petroleum Geologists, 2015), occupying about 10% of domestic natural gas production (EIA, 2010). With the sharp growth of shale gas production since 2005, the natural gas price fell, which in turn cut the enthusiasm to exploit CBM (American Association of Petroleum Geologists, 2015; Rogers, 2011). The share of CBM in national natural gas production dropped to 5.5% in 2013, when it was still considered to be an important global energy resource (American Association of Petroleum Geologists, 2015). By 2017, CBM only accounted for 3% of national gas production (EIA, 2018), and onshore production was forecast to decline through 2050 due to unfavourable economic conditions (EIA, 2019). The proven reserve of CBM in the United States was 3.4 $\times 10^{11}$ m^3 in 2017, representing only 2.6% of the total proved natural gas reserves (EIA, 2018).

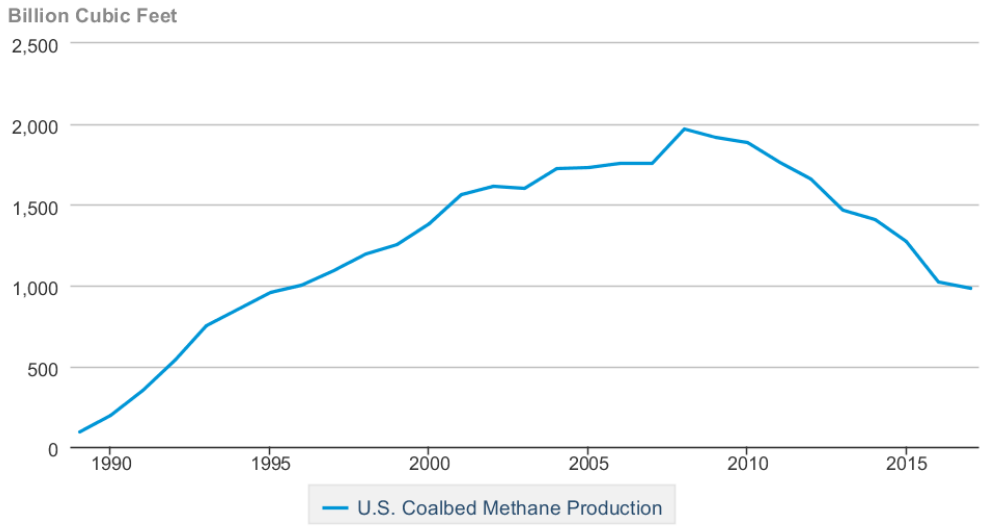

Figure 1.2. CBM production in the United States from 1989 to 2017. Source from: https://www.eia.gov/dnav/ng/hist/rngr52nus_1a.htm.

After the successful exploration of CBM in the United States in the 1990s, many other countries have paid attention to the development of CBM (Al-Jubori et al., 2009; Flores, 1998; Gunter et al., 1997; McGlade et al., 2013; Moore, 2012). So far, only Canada,

Australia, China and India have developed a major scale of production and sold CBM as pipeline gas (McGlade et al., 2013). Canada is the second to the USA in CBM production (Mastalerz, 2014). The CBM resource in Canada is estimated to be 2.8-15.5 $\times 10^{12}$ m^3 (Mastalerz, 2014), of which the technically recoverable resources are about 0.6-3.6$\times 10^{12}$ m^3 (McGlade et al., 2013 and reference therein). Alberta, British Columbia and Nova Scotia are the primary CBM resource areas (Coal Mine Methane Country Profiles, 2015). The production of CBM first occurred in the Horseshoe Canyon region, Alberta, in 2002 and has increased annually to reach about 9×10^9 m^3 in 2010 (Coal Mine Methane Country Profiles, 2015; Mastalerz, 2014). However, production has been declining since 2010. New drilling for the resource is considered to be uneconomic given the current low natural gas price assumptions (Board, 2018).

Australia has about 3.4 to 5.7$\times 10^{12}$ m^3 of the technically recoverable CBM resources (McGlade et al., 2013 and reference therein). Commercial production began in 1996 and grew sharply from 2001 (Moore, 2012). The national CBM production was about 7×10^9 m^3 in 2012, occupying about 13% of total natural gas production (American Association of Petroleum Geologists, 2015). Bowen and Surat basins, containing 90% of estimated resources, are the major production areas, while Sydney Basin has less production (Luke et al., 2018; Moore, 2012). Gunnedah, Gloucester, and Clarence-Moreton Basins are prospective regions (Luke et al., 2018; Mastalerz, 2014).

The desire for new CBM extraction has diminished due to the increasing production of other unconventional natural gases, like shale gas, and low gas price in the market. However, CBM is still a worldwide valuable energy resource, considering the increasing need for the secure and environment-friendly fuel resource (compared to coal burning), the relatively low cost of CBM exploitation and the efficient reduction of the release of greenhouse gas, especially in which natural gas resource is in shortage and coal is the dominant fuel resource.

1.2 The development of coalbed methane in China

Coal is the dominant source of /fossil fuel used for energy production and consumption owing to its abundant and relatively low cost of exploitation in China compared to other

fuels, such as natural gas and hydropower (Figure 1.3; Luo and Dai, 2009). Its share in national energy production has remained around 70% since 1978 (Ning, 2017). The reliance on coal has led to severe environmental problems, such as air pollution, acid rain, and an increase in respiratory system diseases (Luo and Dai, 2009). Conversion from coal to cleaner energy, like natural gas, is required, however natural gas only accounts for 5.3% of national power production in 2016 (Ning, 2017). The consumption of natural gas in China reached 2.8×10^{11} m^3 in 2018, while national production was only 1.6×10^{11} m^3 (Dudley, 2019). The shortage of gas production resulted in China being a net gas-importing country (Dudley, 2019). Hence, CBM is a critical fuel energy source in China.

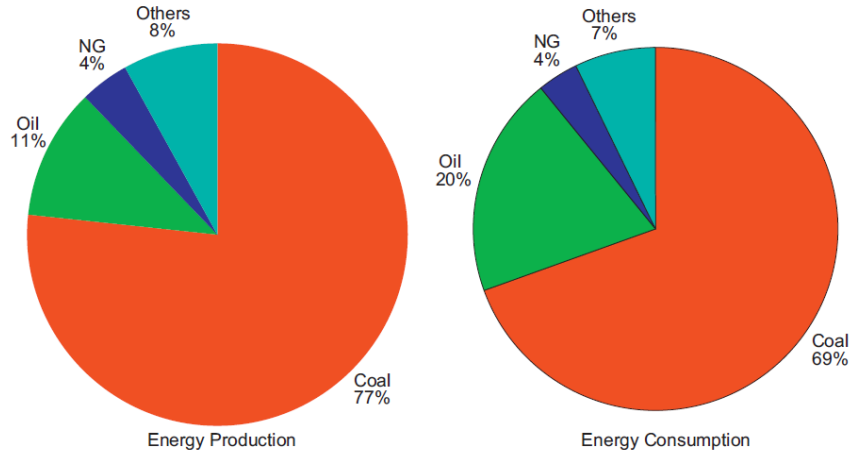

Figure 1.3. Energy production and consumption of China in 2017. Taken from Luo and Dai (2009). Data source: http://www.stats.gov.cn/tjsj/ndsj/2017/indexch.htm.

CBM resource in China is enormous, ranking the third in the world after Russia and the USA (Al-Jubori et al., 2009; Mastalerz, 2014). The original gas resource in place (OGIP) of CBM was estimated to be 3.7×10^{13} m^3, while recoverable resource was estimated about 1.1×10^{13} m^3 (Liu et al., 2009). The latter value is roughly equivalent to half of the recoverable conventional natural gas resource (Liu et al., 2009). Methane emission from coal mining in China was about 1.5×10^{10} m^3 per year (FYP, 2006). The replacement of the emitted methane to coal combustion could save about 2×10^7 t of coal per year and reduce the release of SO_2 by approximately 7.6×10^5 t (3% of total national emission) and soot by 1.9×10^6 t (FYP, 2006). For these reasons, CBM is actively developing in China.

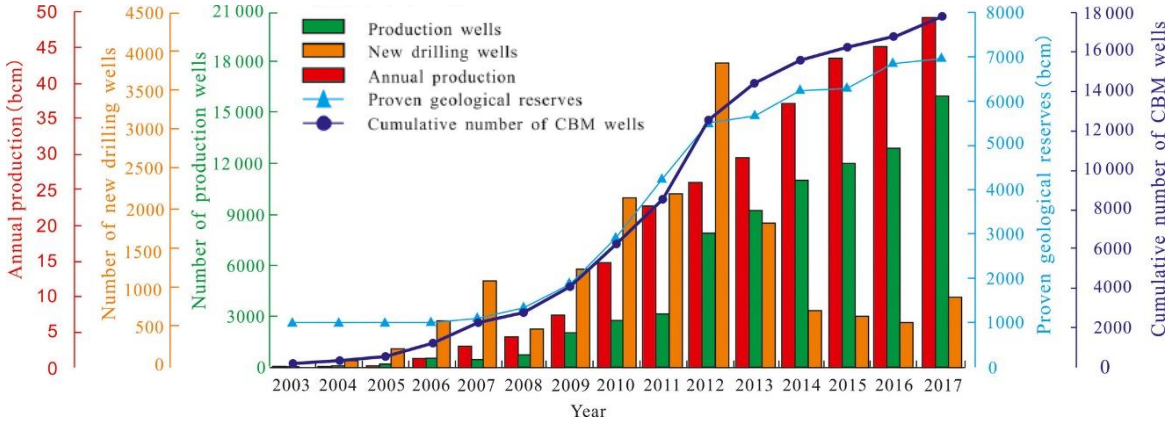

Figure 1.4. CBM development history in China from 2003 to 2017. Taken from Chen et al. (2019b).

The extraction of CBM in China started in the 1950s largely for mine safety, while geological exploration and drilling tests commenced in 1989 (Qin and Ye, 2015; Song et al., 2012). Commercial production of CBM started in 2003 in the Qinshui and Tiefa basins (Figure 1.4; Qin and Ye, 2015; Chen et al., 2019b). By 2005 there were 615 exploration wells in China, with annual CBM production of less than 1×10^9 m^3 (FYP, 2006). The development of CBM was first proposed in the 11th national five-year plan (FYP) in 2006 (FYP, 2006). It set up a goal of an annual CBM production of 5×10^9 m^3 and a utilisation rate of 100% by 2010 (FYP, 2006). The government provided a subsidy of 0.2 RMB/m^3 to CBM production and utilisation (FYP, 2006). During 2005-2010 CBM (plus CMM) usage reached 9.5×10^9 m^3, saving 1.2×10^7 t coal and reducing CO_2 emission by 1.4×10^8 t (FYP, 2011). In 2010 there were over 5000 surface drilling wells and an annual CBM production was 1.5×10^9 m^3 (FYP, 2011). However, the proven reserve was only 2.7×10^{11} m^3, far less than the estimated CBM resource (FYP, 2011). The 12th FYP aimed for CBM production of 1.6×10^{10} m^3 by 2015 (FYP, 2011). Local subsidies were also added, like an extra 0.1 RMB/m^3 in Shanxi Province and support of 0.8-1 million RMB for a new gas-electricity station in Hunan Province (FYP, 2016). However, although another 11,300 wells were drilled by 2015, national CBM production reached only 4.4×10^9 m^3 and the utilisation rate was 86% (FYP,2016). The failure to achieve the goals demonstrates the difficulty in exploring for CBM. However, the extraction of CBM has markedly improved the safety

of the coal mining industry. The mortality per million tons of coal in China decreased from 2.81 in 2005 to 0.293 in 2013 (Qin and Ye, 2015).

After more than two decades of exploration and development, by the end of 2017, China has drilled 17,800 CBM wells, of which over 90% are production wells with annual gas production of 5×10^9 m^3 (Chen et al., 2019b). Proven geological reserves are now 7×10^{12} m^3 (Chen et al., 2019b). The Ordos and Qinshui basins contain over 90% of the *discovered* CBM resources in China, the latter itself accounts for 70% of them (Lau et al., 2017). The two basins both have estimates of CBM resources over 5×10^{12} m^3 (Luo and Dai, 2009). So far, the Qinshui Basin and the eastern margin of the Ordos Basin are the most developed areas of CBM production in China (Chen et al., 2019b; Lau et al., 2017; Qin and Ye, 2015). The late Palaeozoic coal seams in these two areas have experienced several intensive tectonic periods, resulting in the high coal rank (high-volatile bituminous coal to anthracite) (Lau et al., 2017). These are distinct from the low rank and stable coal seams exploited for CBM in America, Canada and Australia (Song et al., 2012). The distinctive properties and history of the Chinese coals may result in different CBM formation and preservation, and could limit the applicability of the research and technological development done for the CBM exploitation elsewhere. Lau et al. (2017) reviewed the challenges of CBM development in China. They pointed out that the low permeability, sub-hydrostatic pressure gradients and especially the lack of understanding of coal connectivity are the dominant geological problems that need to overcome in order to enhance the national CBM production significantly.

1.3 Outlines of thesis

This study focuses on the analysis of C and H isotope composition of methane and the trace noble gas isotopes in the high mature coals to 1) distinguish the origin of the CBM, 2) evaluate the role of magmatic heating on methane generation and 3) determine the influence of current basin exhumation on gas storage in different mature coals. Two coal fields (Southeast Qinshui Basin and Liupanshui Coalfield) were chosen for the medium-

extremely high maturity and geological history of intensive tectonic activities. The thesis is organised into six chapters.

Chapter 1, present here, introduces the economic development of CBM in the world.

Chapter 2 briefly demonstrates the generation processes and storage mechanism of coalbed gases in the reservoir and comprises a review of tracing gas origin and evolution based on major gas and stable isotopic composition and noble gas isotopes.

Chapter 3 and 4 present the results of the geochemistry and isotope composition of CBM from the Southeast Qinshui Basin (north China) and the four main blocks in Liupanshui Coalfield (south China) and discuss the role of basin exhumation on gas migration in the coal seams with different maturities.

Chapter 5 reviews the available noble gas data in worldwide CBM fields. The linkage of He loss with basin exhumation and its implication is further discussed.

Chapter 6 summarises the dissertation and presents potential future work.

Chapter 2 Tracing the origin and evolution of coalbed methane by geochemistry

2.1 Overview

This chapter introduces the generation of coalbed gases (CBM) during the coalification process and reviews the storage mechanism of gases in coal seams. It is followed by a review of the previously published geochemical research, including how the major gas and the stable isotope composition of CBM have been used to determine the origin and evolution of CBM. The final section summarises how noble gases have been used to constrain the history of CBM.

2.2 The generation of coalbed gas

Coal is a sedimentary rock comprised of at least 50% by weight, and 70% by volume, carbonaceous material (Levine, 1993; Schopf, 1956). The organic matter in coals experiences a series of physical, chemical and biological transformations during burial history through the prograde alteration process that is termed 'coalification' (Levine, 1993). The coal rank reflects the degree of coalification from peat, lignite and sub-bituminous coals, bituminous coals (high-medium-low volatility), semi-anthracite and anthracite. It can be determined from several parameters, such as fixed carbon content, vitrinite reflectance and heating value (Levine, 1993). Vitrinite reflectance (R_o) is the most widely used index of the maturity of coal. Vitrinite is one of the macerals (microscopic constituents of coal), mainly produced from lignin and cellulose of plant cell walls that exist as huminite before the bituminous coal stage (Teichmüller, 1989). Most coals contain over 80% vitrinite among macerals that are classified as humic (Rice, 1993). The main kerogen type in coals is oxygen-rich type III based on H/C and O/C atomic ratios (Rice, 1993). Reflectance is defined as the percentage of vertically incident light (normally at 546 nm) reflected from a highly polished surface in an oil immersion medium (Levine, 1993; Strąpoć et al., 2011). Although the reflectance of huminite-vitrinite varies with the organic

matter type (i.e. categories of organic constituents) and grades (the relative proportion of organic vs inorganic constituents), it increases approximately monotonically with the process of coalification (Levine, 1993).

2.2.1 Methanogenesis in coals

Microbial degradation of organic matter is the main pathway for the production of methane (CH_4) in the early stage of coalification (Faiz and Hendry, 2006; Rice, 1993; Schoell, 1980; Strąpoć et al., 2011). The biodegradation mechanism is common for all type of organic matter (Figure 2.1). The methanogenic biodegradation process is widely studied (e.g., Conrad, 2005; Faiz and Hendry, 2006; Green et al., 2008; Jeris and McCarty, 1965; Lyu et al., 2018; Park and Liang, 2016; Strąpoć et al., 2011; Vinson et al., 2017; Whiticar et al., 1986; Winfrey and Zeikus, 1977; Zinder, 1993).

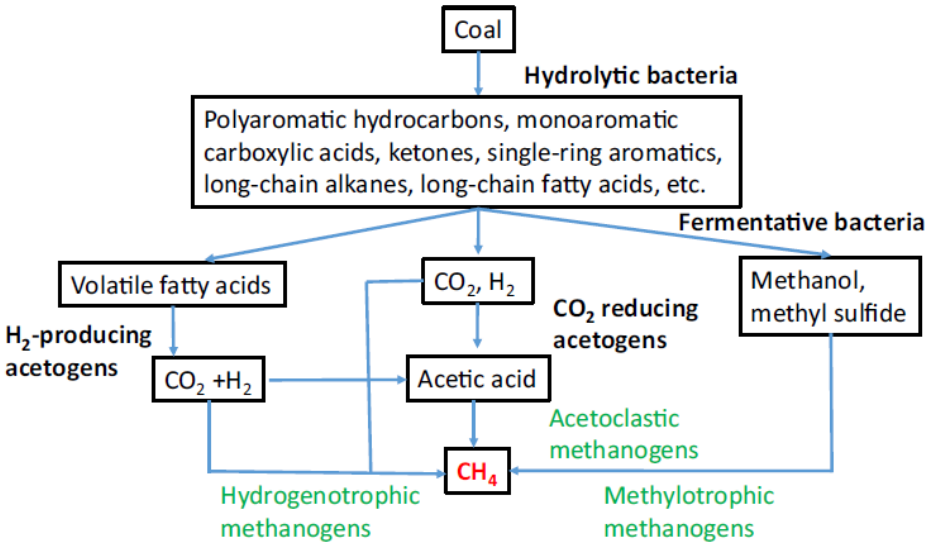

Figure 2.1. Simplified microbial methanogenesis pathway of coal. Taken from Park and Liang (2016).

As temperature increases during burial, organic compounds in plant material are decomposed through hydrolytic depolymerisations to simple molecules, like poly-aromatic hydrocarbons, long-chain fatty acids, monoaromatic carboxylic acids, ketones, and long-chain alkanes. These molecules are transformed into acetate, short-chain volatile

fatty acid, CO_2, H_2, NH_4^+ and HS^- by fermentative and syntrophic bacteria. More acetate, CO_2 and H_2 are generated by H_2-producing acetogens through the conversion of long-chain fatty acids. The molecules, like H_2, CO_2, acetate and formate, are eventually utilised to generate methane by obligate anaerobic Archaea, which produce methane under the oxygen-free condition by a process termed methanogens. The presence of inorganic electron acceptors (oxygen, nitrate, sulphate, etc.) hinders methanogenic activity. For example, the methanogens are readily out-competed by heterotrophic bacteria in the use of substrates as the latter could produce more unit free energy through non-methanogenic processes, like sulphate and nitrate reduction. Even with the absence of these electron acceptors, part of H_2 and CO_2 might be consumed by homo-acetogenic bacteria to yield acetate.

Under suitable conditions methane is generated by methanogens via three main pathways in natural environments (Figure 2.1; Blaut, 1994; Games et al., 1978; Jeris and McCarty, 1965; Lyu et al., 2018; Schoell, 1980; Vanwonterghem et al., 2016; Vinson et al., 2017; Whiticar, 1999; Whiticar et al., 1986):

1) Acetate fermentation/acetoclastic methanogenesis: reduction of a methyl group ($-CH_3$) from a substrate (typically acetate) to methane with the oxidation of the carboxyl group to CO_2:

$$^*CH_3COOH \rightarrow {}^*CH_4 + CO_2 \quad (2.1)$$

2) CO_2 reduction/hydrogenotrophic: reduction of CO_2 to methane with hydrogen as the electron source:

$$CO_2 + 8(H) \rightarrow CH_4 + 2H_2O \quad (2.2)$$

3) Methylotrophic methanogenesis: utilisation of carbon substrates, like methanol and methylamines, by methylotrophs. This process is restricted to marine, hypersaline and sulfate-rich conditions (Lyu et al., 2018; Vinson et al., 2017; Whiticar, 1999).

Methanogens are specialised in their use of substrates (Blaut, 1994). Most can use CO_2 and molecular hydrogen as substrates. Methanogens that are capable of using acetate as a substrate are limited. The free energy (ΔG_0') yielded to produce one-mole of methane by consumption of acetate (~ -31 kJ/mol) is lower than by CO_2 reduction (~ -131 kJ/mol)

(Blaut, 1994; Faiz and Hendry, 2006). Thus, CO_2 reduction methanogenesis is favoured and is done by almost all methanogenic orders (Vanwonterghem et al., 2016). The high sulphate content in rocks from marine conditions means that acetate is rapidly scavenged by sulphate reducing bacteria, leaving CO_2 reduction as the dominant methanogenesis process (Vinson et al., 2017). Approximately 70% of the microbial methane from freshwater sediments is generated by acetate fermentation due to the lack of initial sulphate (Vinson et al., 2017; Whiticar, 1999; Whiticar et al., 1986). Methanogens are active between 4 and 95°C, although the optimal temperature is 35-42 °C (Green et al., 2008; Jones et al., 1983; Zeikus and Winfrey, 1976).

Biogenic, *bacterial* and *microbial* are terms used to represent methane generated in this stage. Schoell (1988) suggested that *bacterial* and *microbial* are better terms, even though *biogenic* is more commonly used in literature. It was argued that *biogenic* methane defines all methane ultimately derived from organic matter, which includes *thermogenic* methane generated by thermal cracking of organic matter (Schoell, 1988). In this study, *microbial* is used to represent methane produced through methanogens.

2.2.2 Thermogenic coalbed methane

At temperatures higher than ~50°C, methanogenesis is inhibited. Due to the distinct H/C and O/C ratios, the generation sequence and relative quantity of the gas components in coals are different from that in type I and type II kerogen enriched organic matter (sapropelic source) (Figure 2.2; Clayton (1998)). Burial of coal-bearing strata leads to water and CO_2 released by decarboxylation and dehydration (Faiz and Hendry, 2006; Levine, 1993; Rice, 1993). At a temperature higher than 70-80 °C (Faiz and Hendry, 2006; Harris et al., 2008), i.e. coal rank of high volatile bituminous C (R_o = 0.5-0.6 %) (Rice, 1993), nitrogen, gaseous and liquid hydrocarbons are generated by thermocatalytic breakdown of residual organic matter (Moore, 2012). Small amounts of H_2S are sometimes generated (Figure 2.2). The existence of liptinite (maceral with high H/C ratio) and hydrogen-rich vitrinite is the additional source of oil, H_2S, liquid hydrogens and wet gas (ethane or higher hydrocarbons, C_{2+}) (Wilkins and George, 2002). The generation of wet gas and liquid hydrocarbons reaches its peak at high volatile bituminous coal rank (R_o =

0.6-1.35%) and sharply declines at R_o > 1.2% (Rice, 1993). At higher temperature, the long-chain hydrocarbons (including oil) are thermally cracked to methane. Ethane and propane can be cracked to methane by pyrolysis or the existence of redox couples at a temperature above 250°C (Burruss and Laughrey, 2010).

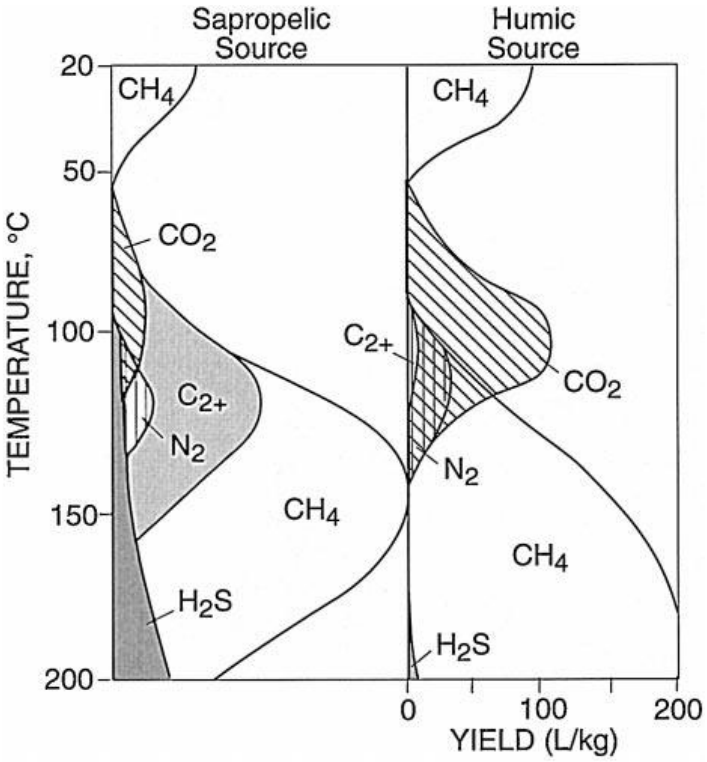

Figure 2.2. Gas generation in relation to temperature for humic-type and sapropelic-type organic matter. Taken from Clayton (1998).

Attempts to predict the amount of methane generated during coalification are based on numerical calculation and laboratory simulations (e.g., Clayton, 1998; Hunt, 1979; Jüntgen and Karweil, 1966; Jüntgen and Klein, 1975; Levine, 1993; Rice, 1993). Estimates of CH_4 yield are 100-300 cm^3/g of coals, and it is suggested that production increases with temperature/vitrinite reflectance (Figure 2.2). Rice (1993) proposed that the CH_4 yield in nature ranges from 150 to 200 cm^3/g coal. These estimates are based on several variables and assumptions. For example, the early model established by Jüntgen and Karweil (1966) neglected the amount of methane generated below the high-volatile bituminous rank and assumed a sole maturation pathway specifically for coals enriched in vitrinite and depleted

in hydrogen (Levine, 1993). In addition, it was pointed out that most experimental results of CH_4 yields are significantly lower than predicted values by modelling, and both of them are much higher than actual field data for coals in low-volatile bituminous rank or greater (Clayton, 1998 and reference therein). In general, the gas content of purely microbial CBM is lower than that of thermogenic CBM (Moore, 2012). For instance, the Illinois Basin (USA) contains high-volatile bituminous coals and hosts microbial methane concentrations of 2-3 m^3/t (Strąpoć et al., 2008), the medium volatile bituminous coals in Clackmannan coalfield (UK) has 8-10 m^3 methane per ton of coals (Bacon, 1995) and the methane content in anthracite of Qinshui Basin (China) could be up to 37 m^3/t (Song et al., 2018). Although this rule is not applicable for all CBM fields in the world (Clayton, 1998; Moore, 2012), it could be used to support estimates of gas reserves.

2.3 Gas storage in coals

CBM is stored in coals as 1) free gas within fractures and macropores; 2) adsorbed to the surface of coal matrix within micropores by physical adsorption; 3) chemically absorbed in the molecular structure of coals and 4) a solute in the water within the coals (Bustin and Clarkson, 1998; Ceglarska-Stefańska and Brzóska, 1998; Gray, 1987; Moore, 2012). Sorption (adsorption and absorption) is critical for gas storage, probably accounting for over 98% of the total gas budget of coals (Flores, 1998; Gray, 1987). Milewska-Duda et al. (2000) reported that adsorption is the primary storage mechanism for methane in coal seams. Consequently, pore surface area is more important than pore volume to gas storage (Moore, 2012).

Several factors can affect the sorption capacity of coals. The storage of methane is strongly related to hydrostatic pressure which ensures gas molecules are adsorbed on the pore surface of coal (Moore, 2012; Yee et al., 1993). Generally, the capacity increases with hydrostatic pressure (Yee et al., 1993). High temperatures decrease the sorption capacity of coals. The presence of inorganic minerals and moisture also reduces gas sorption because the former displaces the organic matter and has no contribution to sorption, and

the latter competes with methane at the sorption sites (Yee et al., 1993 and reference therein). The adsorption capacity in wetted coals increases with coal rank if all other variables (e.g. inorganic minerals) are equal (Al-Jubori et al., 2009; Bustin and Clarkson, 1998; Laxminarayana and Crosdale, 1999; Moore, 2012; Yee et al., 1993). However, heterogeneities within individual coal seams mean this relationship is not universally observed (Moore, 2012).

Aside from the intrinsic properties of coal seams, secondary processes, such as recharge of groundwater and basin inversion, can also impact gas storage. The recharge of freshwater can bring microbes into coal seams, which metabolise wet gases and other organic compounds in the coals to methane and carbon dioxide even after coalification has ceased (Aravena et al., 2003; Scott, 2002; Scott et al., 1994; Tao et al., 2007). This process also induces the migration of gases with water flow to the local barriers that have lower permeability (Flores et al., 2008; Scott, 2002; Scott et al., 1994). Basin inversion leads to depressurisation of the coal seams, resulting in the desorption and migration of CBM (Rice, 1993).

The determination of gas origin and its evolution is vital for estimation of resource potential, commercial gas extraction, understanding the organic matter decomposition and fluxes of carbon, stimulating the methanogenesis process to yield additional gas resources and assessing potential environmental impacts (e.g., Darrah et al., 2014; Moore, 2012; Strąpoć et al., 2011; Vinson et al., 2017; Wen et al., 2015; Zazzeri et al., 2016).

2.4 Tracing CBM by molecular and stable isotopic compositions

Approximately 20% of the natural gas resource is of microbial origin, whereas ~80% is thought to be thermogenic (Rice and Claypool, 1981; Schoell, 1988).

2.4.1 Molecular composition

As gas compositions in coal seams change during the coalification process (Figure 2.2), they can be an effective indicator of gas origin. Rice (1993) summarised the major gas and

stable isotopic compositions of CBM in global coal basins. The published data are compiled in Table 2.1. The data shows that in general methane is the major constituent of coalbed gases, although in several cases pure (99.8%) CO_2 or N_2-rich (up to 80%) gases are present (Table 2.1). Wet gas may be present up to 70%. Microbial methane generates low concentrations of C_{2+} (Davis and Squires, 1954). C_1/C_{2+} ratios (dryness index) are commonly higher than 1,000 (Bernard et al., 1976). The generation of wet gas during the thermogenic stage reduces C_1/C_{2+} ratios. C_{2+} concentrations in this stage are typically 2% or more, leading to C_1/C_{2+} lower than 50, which are a sensitive indicator of gas origin (Bernard et al., 1976; Faiz and Hendry, 2006; Rice and Claypool, 1981). Golding et al. (2013) argued that $C_1/C_{2+} < 50$ is characteristic of oil-associated systems and that coal and shale systems have values up to 100. In the late stage of coalification, cracking of long-chain hydrocarbons into methane, in reverse, increases C_1/C_{2+} ratio (Faiz and Hendry, 2006; Strąpoć et al., 2011; Whiticar, 1999).

The compiled data shows that C_1/C_{2+} ratio is not strictly related to the coal rank, and in some coal seams, the gas contains mainly CO_2 and/or N_2 rather than methane (Table 2.1). The type of sample collection is classified to identify its impact on major gas composition (Table 2.1). The proportion of wet gas in desorbed gas from coal cores recovered from the Illinois and Qinshui basins is higher than that from well production gas (Strąpoć et al., 2007; Zhang et al., 2018). It indicates the faster migration of methane compared to wet gas, albeit it is not significant enough to change the classification of gas origin. This eliminates the possibility that the gas collection method can significantly impact the major gas composition. The results reflect the complex origin and source of gas in the reservoir. Gas composition is fundamentally controlled by the components of source rock and the maturity of coals. However, as discussed above, secondary processes can have a significant influence. Secondary biodegradation (Prinzhofer and Pernaton, 1997; Scott et al., 1994; Tao et al., 2007) and dissolution of wet gas in fresh groundwater (Qin et al., 2006) can increase the proportion of methane. Adsorption/desorption of methane in coals (Rice, 1993; Smith et al., 1985; Xia and Tang, 2012) and diffusion (Prinzhofer and Pernaton, 1997; Prinzhofer and Huc, 1995) leave residual gases in the reservoir rocks that are more enriched in wet gas.

Table 2.1. Review of major gas and isotopic compositions of coalbed methane in different coal basins or coalfields.

Basin/ Coalfield	Coal rank	Major gas composition (wt %)				C_1/C_{2+}	Stable isotopes (‰)		Reference
		CH_4	C_2H_6 +	CO_2	N_2		$\delta^{13}C_{CH4}$	δD_{CH4}	
Well production gas									
San Juan (USA)	Subbituminous to low-volatile bituminous	81.4-96.0[a] 86.7[b]	0.1-12.3 2.5	0.1-18.0 10.3	0-1.2 0.2	8-738 212	-47.9 to -42.4 -44.1	-247 to -197 -211	Zhou et al. (2005)
Illinois (USA)	High-volatile bituminous	87.5-97.3 94.3	0.01-0.1 0.04	0.4-1.7 0.8	2-9.7 4.5	864- >10000 4221	-69.8 to -49.9 -58.4	-215 to -201 -207	Moore et al. (2018); Strąpoć et al. (2007)
Forest City (USA)	High-volatile bituminous	90.1-97.9 94.5	0.02-0.1 0.04	0.1-1.2 0.5	0.7-9.4 4.7	980-5761 3715	-69.9 to -57.6 -64.7	-224 to -218 -221	McIntosh et al. (2008)
Gulf of Mexico (USA)	Subbituminous	55.6-98.1 83.9	0-0.3 0.1	0.1-1.3 0.5	1.5-34.9 12.3	221-8270 2133	-65.6 to -58.6 -61.2	-221 to -179 -188	McIntosh et al. (2010)
Powder River (USA)	Lignite to Subbituminous	5.1-97.3 85.2	0.02-1.0 0.1	0.06-28.8 6.3	0-77.8 4.1	98-4240 1429	-83.4 to -51 -59.7	-328 to -283 -308	Flores et al. (2008)
Bowen (Australia)	Bituminous	95.0-99.2 97.1	0-0.1 0	0.5-1.6 0.8	0-4.2 2.1	>10000	-62.2 to -48 -57.1	-215 to -205 -211	Kinnon et al. (2010)
Surat (Australia)	Lignite to high-volatile bituminous						-57 to -44.5 -51.8	-234 to -209 -222	Baublys et al. (2015)

Table 2.1. continued

Basin/ Coalfield	Coal rank	Major gas composition (wt %)				C_1/C_{2+}	Stable isotopes (‰)		Reference
		CH_4	C_2H_6 +	CO_2	N_2		$\delta^{13}C_{CH4}$	δD_{CH4}	
Ishikari (Japan)		86.5-94.8 90.8		1.5-3.9 2.5	0.1-7.8 2.9	188-299 227	-45.1 to -42.5 -44.0	-234 to -228 -232	Shimizu et al. (2007)
Clackmannan (UK)	Mid-volatile bituminous					75-120 93	-41.8 to -40.2 -40.7	-200 to -188 -195	Györe et al. (2018)
Qinshui (China)	Semi-anthracite to anthracite	94.5-99.5 98.3	0-0.2 0.04	0.1-2.5 0.5	0.3-3.8 1.1	402- >10000 4600	-40.8 to -28.7 -30.9	-179 to -144 -163	Li et al. (2014); Xu et al. (2016); Zhang et al. (2018)
Ordos (China)	High-volatile bituminous to semi-anthracite	65.9-98.9 89.4	0-4.0 0.5	0.4-21.9 2.6	0.3-29.2 7.6	20-4137 1162	-59.0 to -28.8 -46.3		Chen et al. (2015)
Borehole gas									
Lower Silesia (Poland)	Mid-volatile bituminous to anthracite	0.1-97.2 44.0	0-16.1 1.9	0.1-99.8 33.5	0.1-80.2 20.8	1-5825 343	-66.1 to -24.6 -37.3	-266 to -117 -193	Kotarba and Rice (2001)
Upper Silesia (Poland)	Subbituminous to mid-volatile bituminous	14.4-99.0 91.2	0-0.8 0.1	0-16.7 1.6	0.8-76.2 7.0	115-9840 3124	-79.9 to -44.5 -64.3	-202 to -153 -178	(Kotarba, 2001)
Gas degassed from formation water									
Zonguldak (Turkey)	High to low - volatile bituminous	94-99.2 97.2	0.1-0.5 0.3	0.3-0.6 0.4	0.3-5.5 2.6	207-752 376	-51.1 to -49 -49.9	-190 to -183 -185	Hoşgörmez et al. (2002)

Table 2.1. continued

Basin/ Coalfield	Coal rank	Major gas composition (wt %)				C_1/C_{2+}	Stable isotopes (‰)		Reference
		CH_4	C_2H_6 +	CO_2	N_2		$\delta^{13}C_{CH4}$	δD_{CH4}	
Xinji (China)	High-volatile bituminous	0.2-95.8 78.4	0-0.4 0.1	0.5-7.2 1.4	2.9-91.4 19.5	144-2994 1113	-61.3 to -50.7 -56.6		Tao et al. (2007)
Gas desorbed from coal cores									
Illinois (USA)	High-volatile bituminous	87.7-98.6 94.0	0-11.1 4.0	1.0-2.9 1.9		5- >10000 2786	-66.5 to -47.1 -54.8	-225 to -187 -204	Strąpoć et al. (2007)
Qinshui (China)	Semi-anthracite to anthracite	46.5-99.0 92.1	0-2.2 0.4	0.1-2.7 1.0	0.3-49.1 6.7	21-9897 5138	-57.2-to 28.7 -34.8		Zhang et al. (2018)
Elk Valley (Canada)	Mid-volatile bituminous						-65.4 to -52.8 -57.5	-402 to -288 -336	Aravena et al. (2003)
Cook Inlet (USA)							-65.7 to -63.4 -64.8	-293 to -288 -290	Dawson et al. (2012)

[a]: the minimum value (left) to the maximum value (right); [b]: the average value.

2.4.2 Stable isotopic composition

Carbon and hydrogen isotopes have been used in conjunction with major gas compositions for decades to 1) distinguish microbial and thermogenic gases, 2) distinguish the pathways of microbial methane generation and 3) understand secondary processes that have affected gas after generation (e.g., Schoell, 1980; Scott et al., 1994; Vinson et al., 2017; Whiticar, 1999; Whiticar et al., 1986). The isotope data are expressed in delta (δ) values and calculated from:

$$\delta^{13}\mathrm{C} = \left(\frac{\frac{^{13}C}{^{12}C}_{sample}}{\frac{^{13}C}{^{12}C}_{standard}} - 1 \right) * 1000\ (‰) \tag{2.3}$$

$$\delta D = \left(\frac{\frac{^{2}H}{^{1}H}_{sample}}{\frac{^{2}H}{^{1}H}_{standard}} - 1 \right) * 1000\ (‰) \tag{2.4}$$

The bonds formed by the light isotopes are weaker than bonds between the light and heavy ones, which leads to the preferable breaking of the bonds involving light isotopes, i.e. 'kinetic isotope fractionation', and residual organic matter that is enriched in heavy isotopes during hydrocarbon generation (Clayton, 1991; Schoell, 1980; Whiticar, 1996).

The carbon isotope compositions of CBM is dominantly controlled by the composition of the precursor organic matter and the kinetic fractionation during the coalification process (Clayton, 1991; Whiticar et al., 1986). Bulk coal has a narrow range of $\delta^{13}C$ (-22 to -27 ‰) (Whiticar, 1996). In contrast, $\delta^{13}C_{CH4}$ from global CBM fields has a wide range, from -79.9 to -16.8‰ (Table 2.1; Rice, 1993). The insensitivity of carbon isotopes of coals to maturity might reflect that only a small proportion (<10%) of the bulk coal is readily biodegradable (Strąpoć et al., 2011; Vinson et al., 2017; Whiticar, 1996). The wide range of $\delta^{13}C_{CH4}$ suggests that it is mainly controlled by the methanogenetic process rather than the composition of the source matter. The compiled data suggest that thermogenic coalbed methane has $\delta^{13}C$ in the range of -50 to -20‰, while $\delta^{13}C$ of microbial methane varies from -110 to -50‰ (Schoell, 1980; Whiticar, 1999; Whiticar et al., 1986). For microbial methane, the two main methanogenesis pathways also lead to different $\delta^{13}C$ signatures.

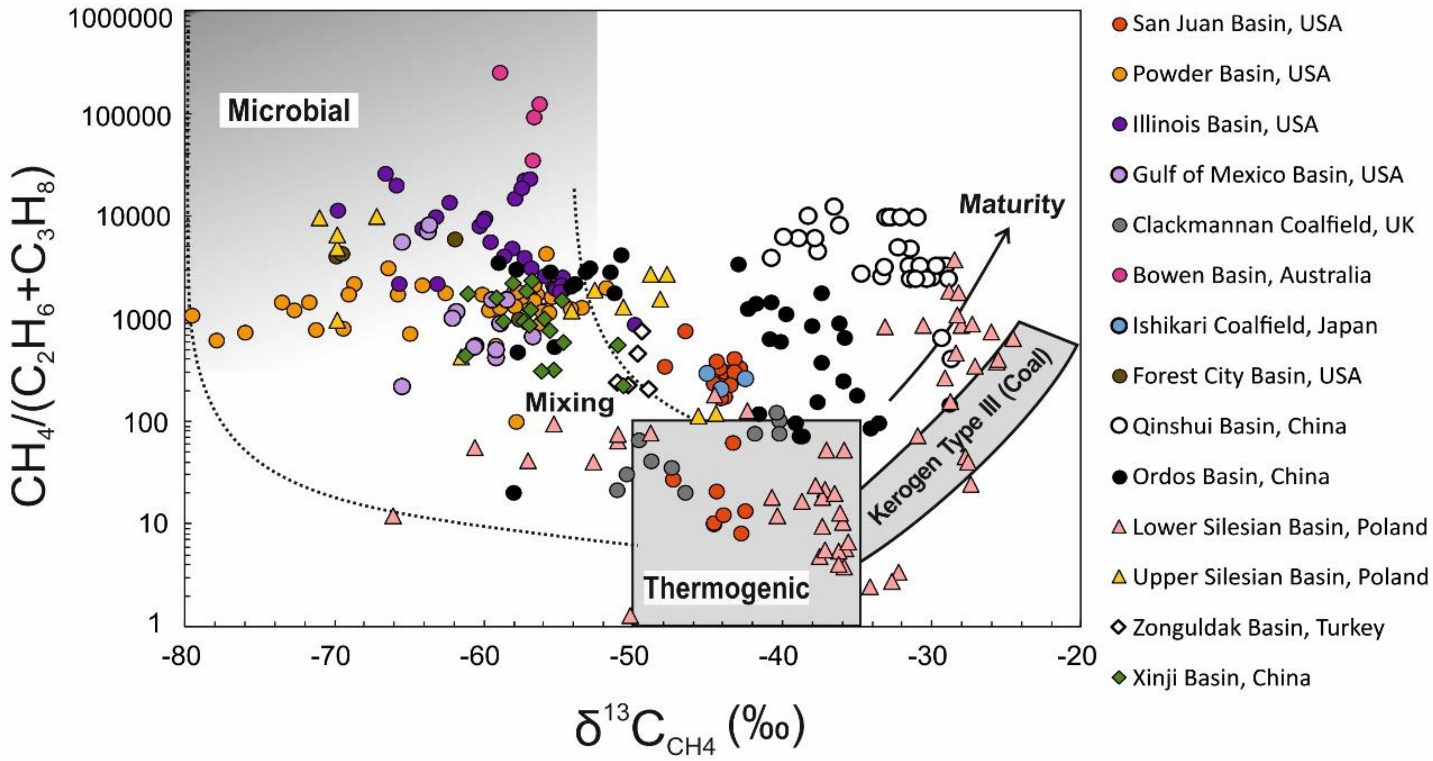

Figure 2.3. 'Bernard' diagram of C_1/C_{2+} ratio vs. $\delta^{13}C_{CH4}$. The dashed lines represent the mixing of microbial methane and thermogenic methane. Modified from Whiticar (1999). The circle, triangle and diamond symbols represent gases collected from production wells, boreholes and desorbed from coal cores, respectively. Data sources: San Juan Basin, (Zhou et al., 2005); Powder Basin, (Flores et al., 2008); Clackmannan coalfield, (Györe et al., 2018); Gulf of Mexico Basin, (McIntosh et al., 2010); Forest City Basin, (McIntosh et al., 2008); Bowen Basin, (Kinnon et al., 2010); Qinshui Basin, (Li et al., 2014; Zhang et al., 2018); Ordos Basin (Chen et al., 2015); Ishikari Coalfield, (Shimizu et al., 2007); Lower Silesian Basin, (Kotarba and Rice, 2001); Upper Silesian Basin, (Kotarba, 2001); Illinois Basin, (Moore et al., 2018; Strąpoć et al., 2008); Xinji Coalfield, (Tao et al., 2007).

Microbial methane from CO_2 reduction is less enriched in ^{13}C than that from methyl-type fermentation, with $\delta^{13}C_{CH4}$ = -60‰ widely applied as boundary (Whiticar, 1999; Whiticar et al., 1986). The process of acetogenesis by using CO_2/H_2 produces acetate with $\delta^{13}C$ that is more negative than the starting CO_2. The methane generated from this acetate would have more negative $\delta^{13}C$ and can overlap the values in CH_4 produced from CO_2 reduction (Vinson et al., 2017). As CO_2 is one of the sources to produce methane, the fractionation factor of carbon isotope between methane and co-existing CO_2 could also reflect the methanogenic pathways (Whiticar et al., 1986).

Figure 2.3 depicts the result of the combined utilisation of $\delta^{13}C_{CH4}$ and C_1/C_{2+} ratio in gas samples collected from global CBM basins. It illustrates that CBM exploration efforts cover methane from both microbial and thermogenic origins. The isotopic compositions of CBM have a roughly positive relationship with the maturity of coals (Table 2.1). The addition of secondary microbial methane is widely observed, e.g. Upper Silesia Basin (Kotarba and Rice, 2001) and Ordos Basin (Chen et al., 2015). Secondary microbial methane is generated by the addition of microbes from recharge groundwater after the main phase of coalification (e.g., Scott, 2002; Scott et al., 1994; Tao et al., 2007). It is compositionally similar to primary microbial methane, but is present in coals with R_o value exceeding the typical range for microbial methane (<0.5%).

Hydrogen can also be used to constrain the origin and evolution of methane. Hydrogen and deuterium (^2H, noted as D) have a large relative mass difference, which results in significantly different physical and chemical properties in the two isotopes and compounds with deuterium (Criss, 1999). Theoretically, the reaction rate of C-H bond is up to18 fold that of the equivalent C-D bond (Bigeleisen and Wolfsberg, 1957). Thus, δD in global bulk kerogen and coal has a large range of -175 to -75‰ (Vinson et al., 2017; Whiticar, 1996), while the δD of methane from coals ranges from -415 to -117‰ (Table 2.1). The isotopic mass balance calculations indicate that 45-79% of carbon-bound H in matured kerogen is derived from water (Schimmelmann et al., 1999). Therefore, the isotopic composition of the formation water (δD = -162 to -14‰, Figure 2.4) can strongly affect the hydrogen isotopic composition of methane. For microbial methane, previous studies have observed that one of four hydrogens of methane is sourced from water in the acetate fermentation

pathway, while all four hydrogens come from water during CO_2 reduction (Jeris and McCarty, 1965; Schoell, 1980; Whiticar et al., 1986). Empirical relationships between hydrogen isotope of formation water and microbial methane can be described by an equation as follows:

$$\delta D_{CH4} = A \times \delta D_{H2O} - B \quad (2.5)$$

where A=1 and B=160-180 for CO_2 reduction, A=0.25 and B=300-377 for acetate fermentation (Schoell, 1980; Whiticar, 1999; Whiticar et al., 1986). Methane formed from CO_2 reduction commonly has heavier hydrogen isotope compositions than methane formed via acetate fermentation (Figure 2.4). The compiled data indicate that CO_2 reduction is the main methanogenic pathway to generate microbial CBM (Figure 2.4).

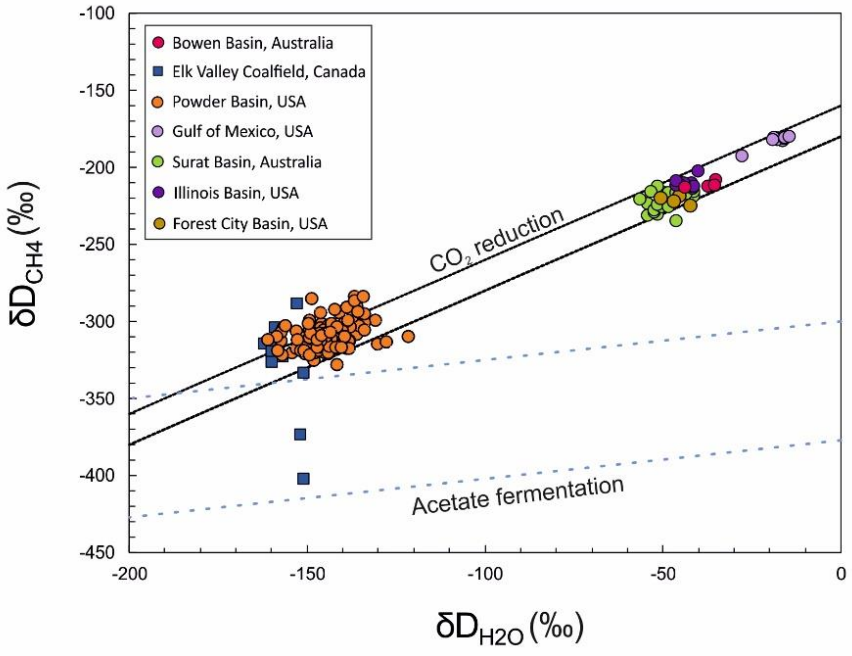

Figure 2.4. Hydrogen isotope composition of microbial methane and formation water from coal beds. Lines inferred for CO_2 reduction (black solid), and acetate fermentation (blue dash) pathways are based on Eq. 2.4. Data sources are the same as Figure 2.3, except: Elk Valley field, (Aravena et al., 2003); Surat Basin, (Baublys et al., 2015).

The possible further exchange of hydrogen isotopes between hydrocarbons and water may overprint the inherited information of methane from methanogenesis (Vinson et al., 2017).

Although it has been reported that, at low temperature (<50 °C) and short time (<10^4-10^8 years), this exchange can be totally neglected (Sessions et al., 2004; Vinson et al., 2017), clumped isotope studies suggest that in low H_2 content system (e.g. coals), hydrogen isotope equilibrium can be reached in long-lived methane and water systems (Wang et al., 2015b). With further maturation, the exchange of hydrogen between water and organic matter can be significantly enhanced (Schimmelmann et al., 2006), which would influence the hydrogen isotope of subsequently generated methane. An exchange between methane and water could also happen and control H isotope composition of methane, resulting in δD_{CH4} approaching -120‰ at 250-300 °C in coals (Schimmelmann et al., 2006).

Secondary processes after methane generation can change the stable isotopic compositions of CBM. For instance, the easier desorption and migration of $^{12}CH_4$ compared to $^{13}CH_4$ and/or $^{12}CH_3D$ leads to the lighter isotopic composition of produced methane (Qin et al., 2006; Xia and Tang, 2012; Zazzeri et al., 2016); the generation of secondary microbial methane depleted in ^{13}C lightens the isotopic composition of methane (Aravena et al., 2003; Scott, 2002; Scott et al., 1994; Tao et al., 2007); the preferential dissolution of ^{13}C and H to ^{12}C and D can/could result in the lighter C and heavier H isotopes of methane in the gas reservoir (Bacsik et al., 2002; Qin et al., 2006).

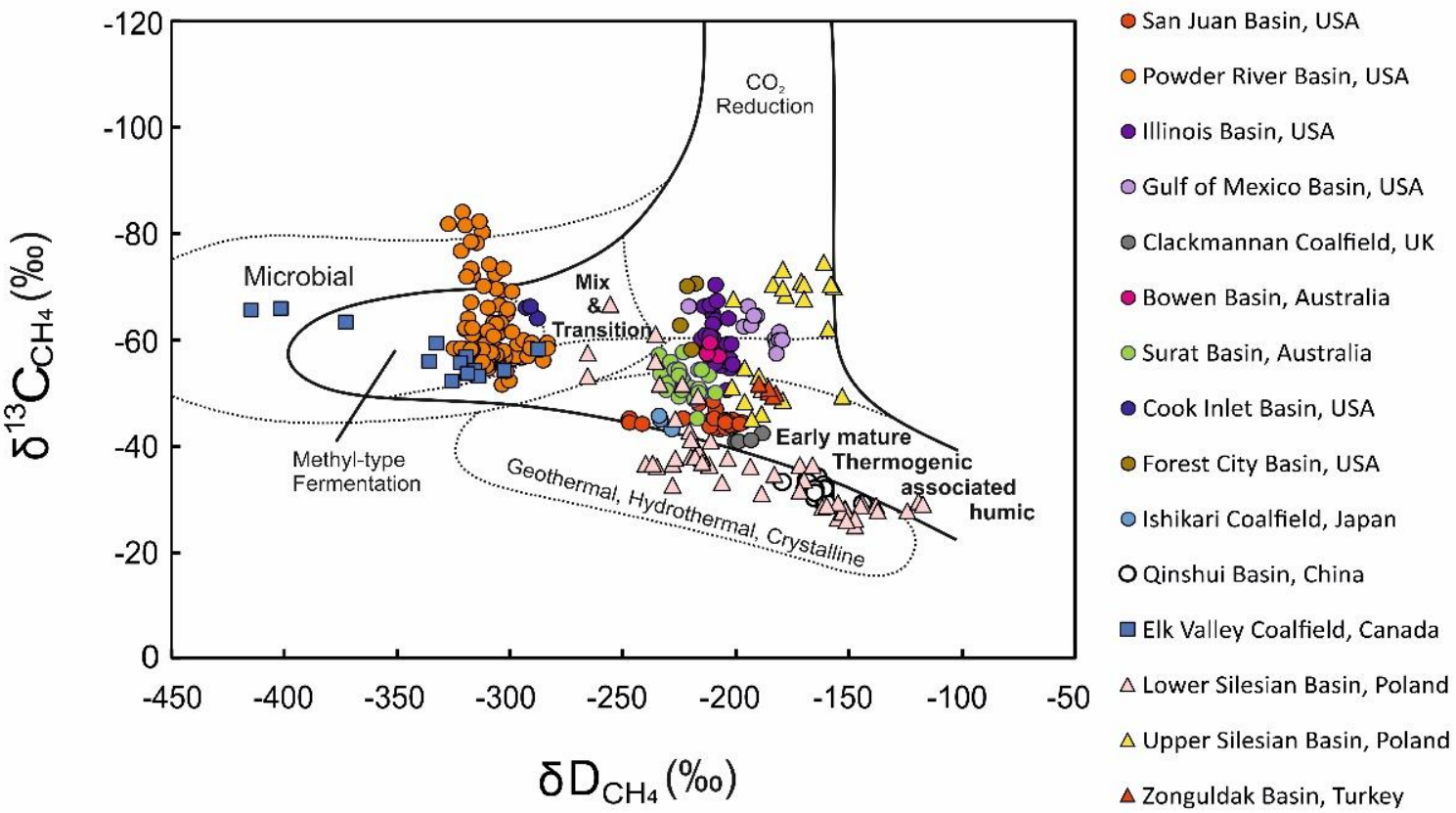

Figure 2.5. Compilation of CBM stable carbon and hydrogen isotopes. Field lines are from Whiticar (1999). Data sources are the same as Figure 2.3, and Figure 2.4, except: Zonguldak Basin, (Hosgörmez, 2007); Cook Inlet, (Dawson et al., 2012).

Combining carbon and hydrogen isotopes to identify the origin of methane is well established (Figure 2.5). The issue comes out when I compare the methanogenesis of microbial methane from $\delta^{13}C_{CH4}$-δD_{CH4} classification with $\delta^{13}C_{CH4}$-C_1/C_{2+} ratio classification (Figure 2.3) and δD_{CH4} - δD_{H2O} classification (Figure 2.4). The samples that show the mixing of microbial and thermogenic origin by $\delta^{13}C_{CH4}$ and δD_{CH4} classification locate in pure microbial origin though CO_2 reduction in $\delta^{13}C_{CH4}$ -C_1/C_{2+} and δD_{CH4} - δD_{H2O} classification, like Bowen Basin (Australia) (Golding et al., 2013). In addition, the origin of methane from Powder River (USA) and Elk Valley coalfield (Canada) is identified to be pure methyl-type fermentation based on $\delta^{13}C_{CH4}$ and δD_{CH4}, while the result becomes pure CO_2 reduction for Powder River and mixing of two pathways for Elk Valley coalfield based on δD_{H2O} and δD_{CH4} (Figure 2.3 and 2.4; Golding et al., 2013). Thus, Vinson et al. (2017) has argued that the application of δD_{CH4} to diagnose the methanogenic pathways of microbial methane is restricted. However, it is still indicative of the origin of methane, i.e., microbial or thermogenic (Figure 2.5).

2.5. Constrain of CBM evolution by noble gases

2.5.1. Noble gases in the Earth

The noble gases (He, Ne, Ar, Kr, Xe) are chemically inert and present in trace amounts in most rocks and fluids (Ozima and Podosek, 2002). There are two main sources of noble gases in the Earth; primordial isotopes trapped during Earth accretion, and radiogenic/nucleogenic/fissiogenic isotopes generated over Earth lifetime by nuclear processes (Ozima and Podosek, 2002). The abundance and isotopic compositions of noble gases in the major Earth reservoirs (crust, mantle, atmosphere) are distinct and well established (Ozima and Podosek, 2002), and have been used extensively to trace the origin and interaction history of fluids in petroleum and natural gas systems (Figure 2.6) (e.g., Zartman et al., 1961, Ballentine et al., 1991, Ballentine and O'Nions, 1992, Xu et al., 1995, Torgersen and Kennedy, 1999, Battani et al., 2000, Barry et al., 2016, Byrne et al., 2018, Sherwood Lollar et al., 1997).

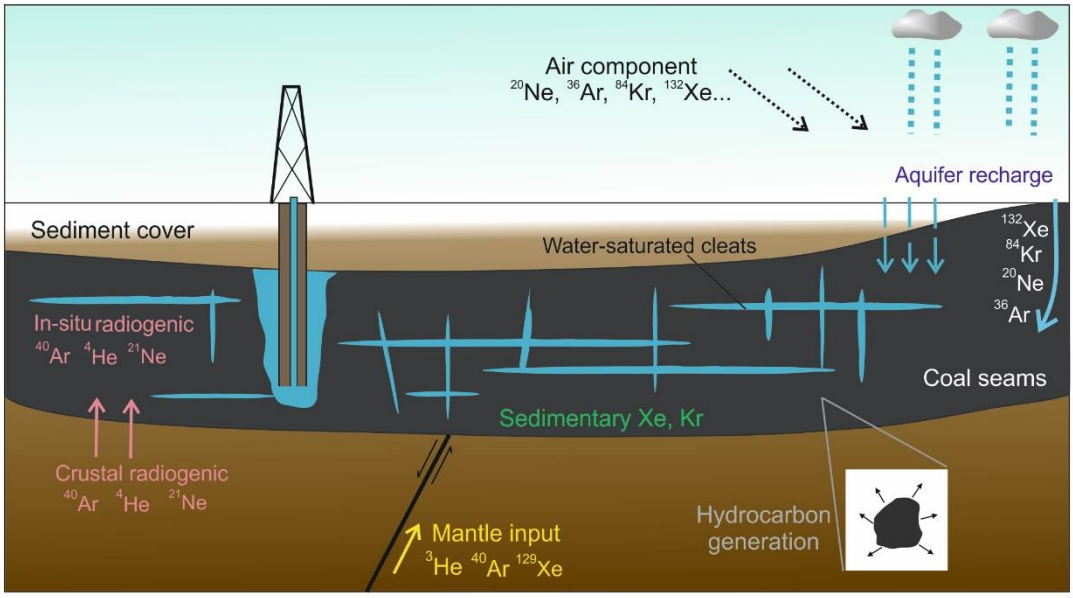

Figure 2.6. Diagram representing the noble gas components in different reservoirs. Redraw from Ballentine et al. (2002) and Byrne et al. (2017).

2.5.1.1. Atmosphere-derived noble gases

The concentration and isotope composition of noble gases in air are regarded as uniform (Table 2.2; Ozima and Podosek, 2002). They are mainly sourced from primitive volatiles trapped during the Earth accretion and radiogenic isotopes from the degassing of the solid earth (Brown, 1949, Ozima and Podosek, 2002, Porcelli and Ballentine, 2002). Atmosphere is assumed to be a conservative reservoir for all noble gases except for He (Ozima and Podosek, 2002). The escape of He into space is balanced by the terrestrial degassing flux from the solid earth (Ozima and Podosek, 2002, Torgersen, 1989). Atmospheric noble gas composition can reasonably be considered to be constant over most of Earth history.

Air-derived noble gases enter the subsurface dissolved in recharge groundwater. Water in contact with air rapidly reaches equilibrium, and air-saturated water (ASW) is widely considered to be the dominant source of atmospheric noble gases in the shallow crust. The abundance of noble gases in surface water is governed by their solubility (Henry's constants), environmental conditions, such as temperature, pressure (i.e. altitude) and

salinity of groundwater (Crovetto et al., 1982; Kipfer et al., 2002), and allows for tracking the subsequent partition of noble gases between different phases in the subsurface reservoirs.

Table 2.2. Elemental and isotopic composition of noble gas in dry air.

Gas	Volume Fraction	Isotope	Isotopic ratios
He	$(5.24 \pm 0.05)\times10^{-6}$	^{3}He	0.000001399 ± 13
		^{4}He	≡ 1
Ne	$(1.818 \pm 0.004)\times10^{-5}$	^{20}Ne	≡ 1
		^{21}Ne	0.00296±2
		^{22}Ne	0.1020±8
Ar	$(9.34 \pm 0.01)\times10^{-3}$	^{36}Ar	0.003378 ± 6
		^{38}Ar	0.000635 ± 1
		^{40}Ar	≡ 1
Kr	$(1.14 \pm 0.01)\times10^{-6}$	^{78}Kr	0.006087 ± 20
		^{80}Kr	0.03960 ± 2
		^{82}Kr	0.20217 ± 4
		^{83}Kr	0.20136 ± 21
		^{84}Kr	≡ 1
		^{86}Kr	0.30524 ± 25
Xe	$(8.7 \pm 0.1)\times10^{-8}$	^{124}Xe	0.003537 ± 11
		^{126}Xe	0.003300 ± 17
		^{128}Xe	0.07136 ± 9
		^{129}Xe	0.9832 ± 12
		^{130}Xe	0.15136 ± 12
		^{131}Xe	0.7890 ± 11
		^{132}Xe	≡ 1
		^{134}Xe	0.3879 ± 6
		^{136}Xe	0.3294 ± 4

Data from (Ozima and Podosek, 2002).

2.5.1.2 Crust-derived noble gases

The crust contains about 40% of the terrestrial radioactive elements associated with the production of noble gases (^{40}K, ^{230}Th and ^{238}U) (Rudnick and Fountain, 1995). ^{4}He, ^{21}Ne, ^{22}Ne and ^{40}Ar are the principal radiogenic or nucleogenic light noble gas isotopes. They are generated within the minerals and are released into surrounding fluid systems by recoil, diffusion or chemical breakdown of the host mineral (Ballentine and Burnard, 2002). The light noble gases are readily released from minerals at low temperature, and the

temperature control of loss processes tends to result in $^{4}He/^{21}Ne$ and $^{4}He/^{40}Ar$ ratios that are significantly different from production ratios (e.g., Elliot et al., 1993, Ballentine et al., 1994). The relatively low production rates of other noble gases, like ^{3}He and ^{20}Ne, result in the distinct isotopic composition in the crustal reservoir. For instance, the average crustal $^{3}He/^{4}He$ ratio is about 0.02 R_A (Ballentine and Burnard, 2002), where R_A is the atmospheric ratio.

2.5.1.3. Mantle-derived noble gases

The Earth's mantle contains a high proportion of primordial noble gases. The elemental and isotopic composition is heterogeneous in mantle due to the different extent of degassing. For instance, as ^{3}He is mainly primordial and preserved in mantle, $^{3}He/^{4}He$ ratio in ocean island basalt or mantle plume from the lower mantle is as high as about 50 R_A (Stuart et al., 2003). Gas from the mid-ocean ridge basalt (MORB) mantle, where partial melting occurs continually, has the $^{3}He/^{4}He$ =7 to 9 R_A (Allègre et al., 1995). The subcontinental lithospheric mantle has an even lower helium ratio ranging from 5 to 7 R_A (Gautheron and Moreira, 2002). The significant difference of $^{3}He/^{4}He$ in each terrestrial reservoir makes tracing the addition of mantle or air He into the subsurface crustal systems discernible. Neon isotopes in the mantle enriched in primordial ^{20}Ne relative to ^{21}Ne and ^{22}Ne in air and crust (Niedermann et al., 1997, Hiyagon et al., 1992, Ballentine et al., 2005, Staudacher, 1987). The enrichment of ^{40}Ar and ^{129}Xe is evident in mantle (Butler et al., 1963). The identification of mantle-derived noble gases in hydrocarbon systems typically trace the origin of non-hydrocarbon gases (CO_2 and N_2) and by identifying magmatic volatiles provides a novel constraint on the thermal history of the coal deposits that may have influenced the generation of hydrocarbons.

2.5.2. The application of noble gases in natural gas systems

Initial studies of noble gases in natural gases focused on the source and fate of radiogenic isotopes of noble gases (e.g., ^{4}He and ^{40}Ar) in sediments and revealed the emission of them from crust to atmosphere, and eventually to space (Zartman et al., 1961, Morrison and Pine, 1955). Transport and accumulation models of radiogenic noble gases have been widely

applied to groundwater dating and crust degassing rate (Torgersen, 1980, Torgersen and Clarke, 1985, Torgersen and Ivey, 1985, Castro et al., 1998, Zhou and Ballentine, 2006).

The presence of mantle-derived gases in natural gas reservoirs was another prosperous field in early studies. An excess of ^{129}Xe (primordial noble gas) was found in CO_2 wells from Harding County, USA (Butler et al., 1963). Subsequent studies discovered that the He, Ne, Ar isotopes and elemental ratio patterns of non-fissiogenic or non-radiogenic noble gases (e.g. ^{20}Ne, ^{36}Ar) are similar to those of gases from samples sourced from the upper mantle (Phinney et al., 1978, Staudacher, 1987). The $CO_2/^3He$ ratio in mid-ocean ridge basalts (MORB) has a narrow range ($1\text{-}7\times10^9$) (Trull et al., 1993), which allows quantification of the mantle CO_2 flux to be determined from He isotope measurements (Ballentine et al., 2001, Gilfillan et al., 2008, Sherwood Lollar et al., 1997). The combination of $CO_2/^3He$ ratio and $\delta^{13}C_{CO2}$ has been used to determine the fate of CO_2 (e.g. dissolution in water or precipitation to carbonate) (Gilfillan et al., 2009) and is widely utilised to estimate the potential of geological sequestration of anthropogenic CO_2 (Györe et al., 2015).

The partition of noble gases between ASW and oil/gas phases can be modelled based on the system conditions and fractionation mechanisms, such as batch fractionation, Rayleigh fractionation or diffusion fractionation in a closed or open system. They have proved adept at quantifying the volume of gas, water and oil that have participated in the interaction, identifying the role of formation water on gas production and estimating the amounts of gas that have migrated to adjacent reservoirs (e.g., Torgersen and Kennedy, 1999, Ballentine et al., 2002, Barry et al., 2016, Zhou et al., 2005, Györe et al., 2017, Byrne et al., 2020, Sathaye et al., 2016, Wen et al., 2015). These techniques can be extended to monitor environmental impacts based on noble gas data in water samples, e.g. the effect of hydraulic fracturing in shale gas exploitation on the quality of shallow aquifers (Darrah et al., 2015, Darrah et al., 2014, Wen et al., 2016).

Despite their obvious strengths, noble gases have, however, only been used sparingly in studies of CBM. Zhou et al. (2005) first used isotopic and elemental compositions of noble gases to identify the source of gases and revealed the degassing mechanism of coal seams during CBM extraction in San Juan Basin, USA. This research also quantified the volume

of water associated with gas production, identified no groundwater flow among wells and estimated the isolated radii of the water environment for each well based on the analysis of air-derived light noble gases (^{20}Ne, ^{36}Ar). The ^{4}He content in San Juan Basin CBM requires extra supply from the deep crust and has been used to determine the age of formation waters in reservoirs to constrain the timescale of hydrodynamic processes which have affected hydrocarbon preservation (Zhou and Ballentine, 2006). Györe et al. (2018) identified mantle volatiles in Airth field, central Scotland, and argued about the influence of external heating on gas generation. The high helium concentrations in CBM (100s-1000s ppmv) might be used to monitor gas leakage to shallow groundwater during CBM extraction activities. Noble gases in CBM samples from Illinois Basin, USA, were used to trace the origin of local hydrocarbons (Moore et al., 2018). The combined application of noble gases, major gas compositions and stable isotopes identified and quantified the exogenous thermogenic gas in the reservoir.

2.6 Conclusion

Coalification leads to the production of large amounts of methane. The main methanogenic pathways are by 1) low-temperature CO_2 reduction and acetate fermentation, and 2) thermal cracking of organic matter. The methane generated from the two stages is classified as *microbial* and *thermogenic*, respectively. The storage mechanism of methane in the coals is mainly by sorption. The methane sorption capacity of coals is controlled by several factors, e.g., coals rank, reservoir temperature and static pressure, moisture content and minerals.

Identification of methane origin and evolution is beneficial to evaluate the gas resource as thermogenic CBM usually has higher gas content than pure microbial gas. The common geochemical tools are major gas composition (e.g., C_1/C_{2+} ratio) and stable isotopes ($\delta^{13}C_{CH4}$, δD_{CH4} and δD_{H2O}). However, the post-generation processes, such as recharge of freshwater or basin inversion, could influence the preservation of gas and induce the alteration of these characteristics. This makes the methanogenic pathways ambiguous.

Noble gases are widely used to constrain the source and interaction of different fluids in natural gas systems. Although few studies of noble gases have been done in CBM

reservoirs, they show great potential for identifying the contribution of fluids from different continental inventories and the impact of the tectonic and hydrologic activities on gas generation and preservation.

Chapter 3 Evolution of coalbed methane in Southeast Qinshui Basin, China: Insights from stable and noble gas isotopes

3.1 Overview

This chapter presents the results of the study of the geochemistry and isotope compositions of coalbed methane (CBM) from the Southeast Qinshui Basin (SQB) in northern China. This basin is the most productive high-rank coal basin in China. The prototype of the basin was formed during the main Yanshanian Orogeny (Late Jurrasic to Early Cretaceous), and coal-bearing strata were largely deposited in the Late Carboniferous and Early Permian (Song et al., 2018). The basin experienced a rapid Cenozoic inversion, yet the extent to which this affected the preservation of in-place methane is poorly understood (Cai et al., 2011; Song et al., 2012). The geology and hydrology are well understood, and the extensive CBM extraction makes sampling gases relatively easy, making the SQB an ideal natural laboratory for determining the role of basin inversion on gas migration from the reservoir rocks.

This structure and content of this chapter are largely based on the paper published in Chemical Geology in 2019 (Chen et al., 2019a). This chapter differs slightly by including more information on the economic development of the Qinshui Basin, a fuller description of the methane generation history based on stable isotopes and a section interpreting the heavy noble gas (Kr and Xe) data at the end of the chapter.

3.2 Development history of coalbed methane in the Qinshui Basin

The Qinshui Basin (35-38°N, 111°30'-113°50'E, Figure 3.1) is located in the Chinese largest coal base, Shanxi Province in northeast China. The basin occupies an area of about 2.3×10^4 km^2 (Lv et al., 2012; Zhang et al., 2004) and has a proven methane reserve of about 4.35×10^{11} m^3, which makes up approximately 65% of national proven CBM reserves (Zhao et al., 2016).

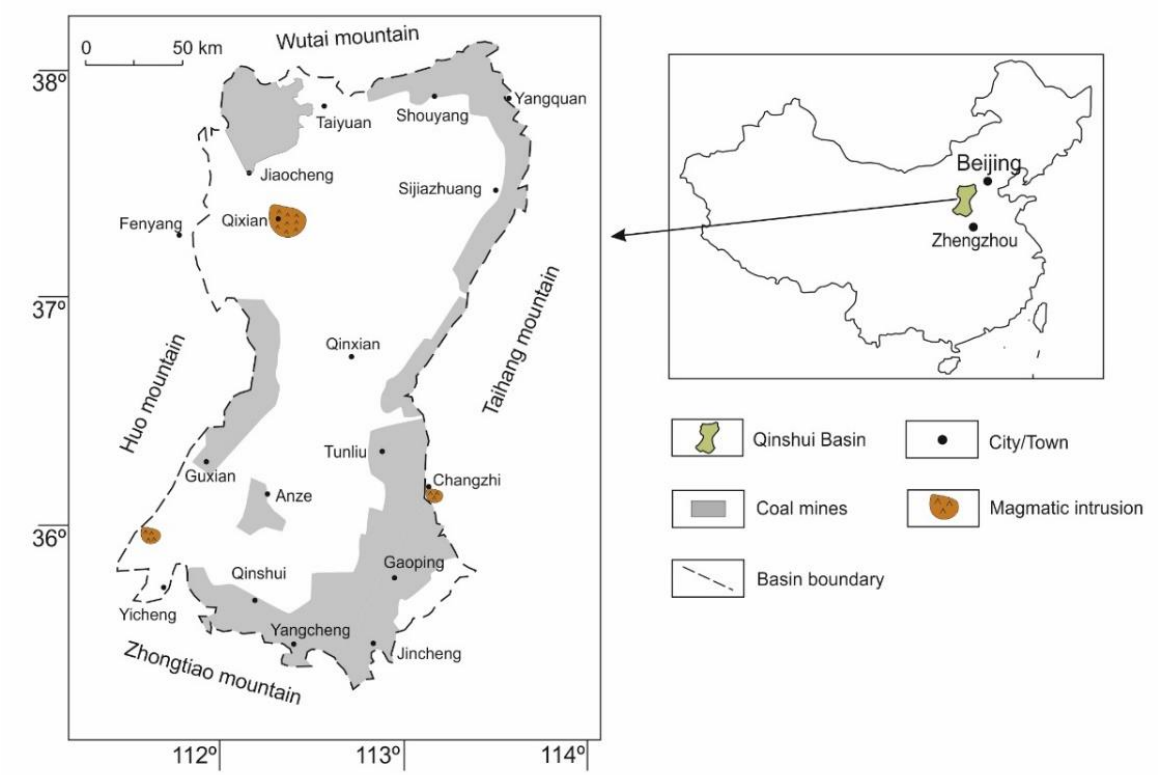

Figure 3.1. Location map of the Qinshui Basin and coal mining areas in the basin. Redrawn after Cai et al. (2011).

Gas exploration in the Qinshui Basin started in 1989, and the first well was drilled in Jincheng with funding from the United Nations Environment Program (Song et al., 2018). More test wells were drilled in the southern part of the basin in 1989-2002 with the support of PetroChina, Jincheng Mining Bureau and several smaller energy companies. These wells showed great commercial potential. The daily production from the test wells in the Zhengzhuang block was over 3,000 m^3 per well, and maximum daily production of over 4,000 m^3 occurred in a test well in the Fanzhuang block (Song et al., 2018). Commercial CBM supply commenced in 2003 (Qin and Ye, 2015). By 2005 there were approximately 300 wells in the basin, and the annual production reached 1.5×10^8 m^3 (Lv et al., 2012). The number of wells rose to about 5,000 by 2011 with an annual production of $15\text{-}20\times10^8$ m^3 (Lv et al., 2012). Currently, the basin has about 11,000 wells and by the end of 2017, 5×10^9 m^3 methane was produced, accounted for more than 70% of national CBM production (Song et al., 2018). The main commercial CBM extraction initially focused on the coal seams in the southern part of the basin. Exploration is extending into the central and

northern parts of the basin, e.g., Sijiazhuang mining area (Xu, 2017) and Anze block (Zhang et al., 2019a).

3.3 Geological setting

The Qinshui Basin is an intra-craton basin in northwest Shanxi province. It is a complex syncline with an NNE-SSW trending axis, surrounded by the Taihang Mountains in the east, Wutai Mountains in the north, Huo Mountains in the west and Zhongtiao Mountains in the south (Figure 3.1; Cai et al., 2011; Song et al., 2018; Su et al., 2005). The basement of it is composed of Archaean metamorphic rocks and Proterozoic mafic igneous rocks (Song et al., 2018; Xu, 2017; Zeng et al., 1999). The basin was part of the North China Craton in the Early Palaeozoic. The majority of the craton was exposed and eroded from Silurian to Mississippian due to the Caledonian Orogeny. Coal deposition started in the Pennsylvanian in response to marine transgression and ended in the Early Permian with fluvial-deltaic sedimentation (Ma et al., 2016; Su et al., 2005). Subsidence continued into the Late Triassic, the burial depth of the coal-bearing strata reached a maximum of more than 4 km depth (Su et al., 2005; Zeng et al., 1999). The Indonesian Orogeny resulted in uplift and erosion of the region in the Late Triassic (Song et al., 2018; Zeng et al., 1999). Basin inversion continued during the early Yanshanian movement (Jurassic) in response to the collision of the Pacific and Eurasia plates (Ren and Zhao, 1997; Xu, 2017). The basin was separated from adjacent Ordos Basin in the Late Jurassic to Early Cretaceous and developed into the prototype of a complex syncline, combined with NE, NNE and NW-direction short-axial folds and faults (Cai et al., 2011; Ren and Zhao, 1997; Song et al., 2018).

The basin underwent a major phase of exhumation during the Cenozoic that is ultimately related to the extensional tectonic regime induced by the subduction of the Indian Plate in the southwest, or rollback of the subducting Pacific Plate in the east (Cai et al., 2011; Cao et al., 2015). Fission-track thermochronology of detrital apatite and zircon from sediments overlying the SQB coal seams reveal that the basin cooled from over 200°C to ~100°C in the last 50 million years, then experienced a pulse of rapid cooling to less than 60°C in the

last 10 million years (Cao et al., 2015; Ren et al., 2005). Uplift and denudation continued until at least 5 million years ago (Cao et al., 2015).

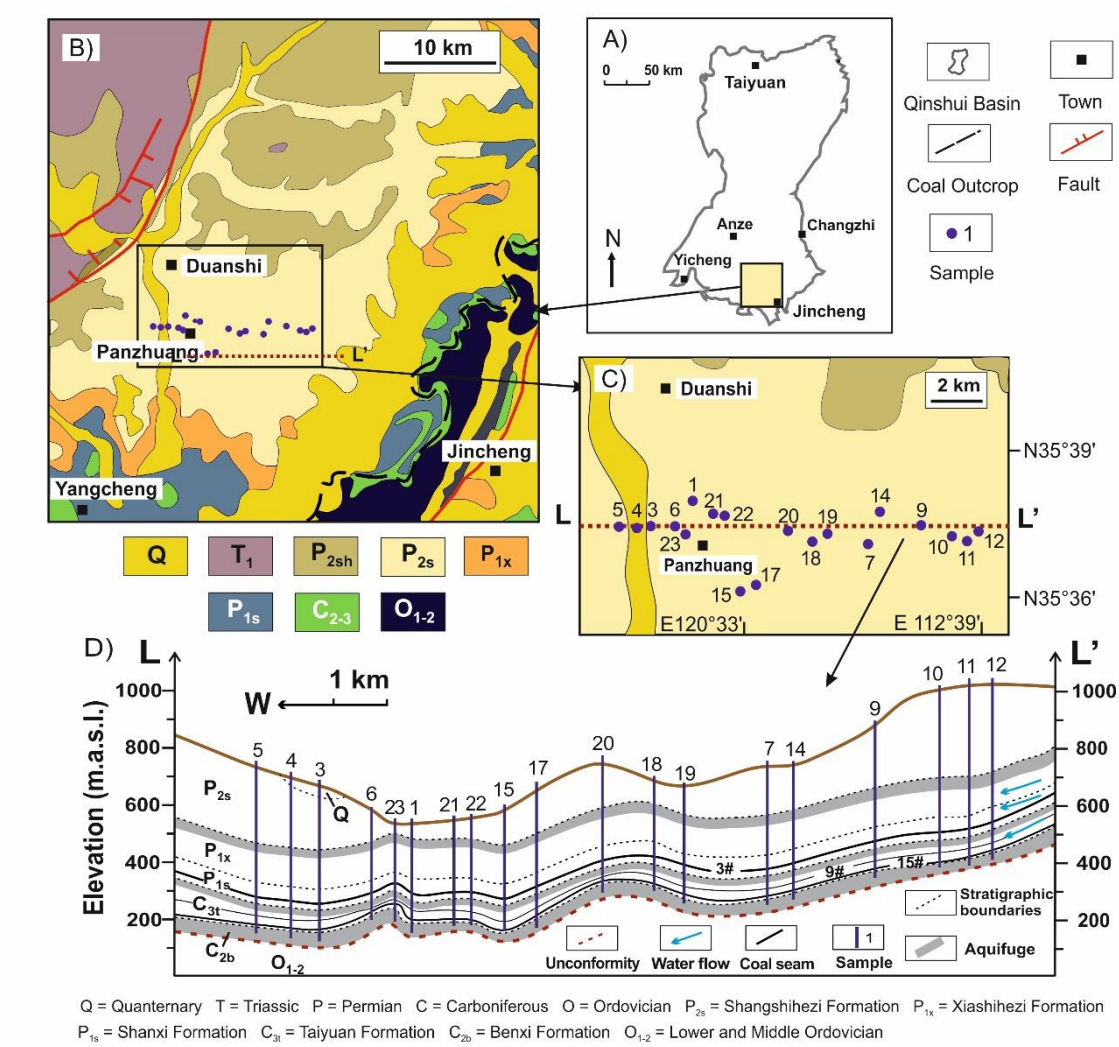

Figure 3.2. Location and geologic map of the Southeast Qinshui Basin (China). A) The location of the study area in Qinshui Basin; B) Simplified geological map of Southeast Qinshui Basin; C) Location of wells sampled in this study; D) Simplified hydrological cross-section of the basin along the line L-L' above. Figures are modified after Wang et al. (2014) and Zhang et al. (2015).

The main coal-bearing strata in SQB are the 76-127 m thick Pennsylvanian Taiyuan Formation and the 35-59 m thick Early Permian Shanxi Formation (Figure 3.3) (Su et al., 2005). It contains 21 distinct coal seams with a total average thickness of 146 m (Wang, 2013). The no. 3 coal seam (2-7 m thick) in the Shanxi Formation (R_o = 2.5-4.5%) and no.

15 coal seam (1-6 m thick) in the Taiyuan Formation (R_o = 2.7-4.5%) are present across the whole basin and are the most economically important coal seams (Song et al., 2018; Su et al., 2005). The Taiyuan Formation coal seams are mostly located at depths of less than 700 m, approximately 80 m deeper than the main Shanxi Formation coals. In the study region, the SQB, a third major coal seam (no. 9) in the Taiyuan Formation (40 m deeper than coal seam 3) is co-exploited with seams 3 and 15 (Wang et al., 2013).

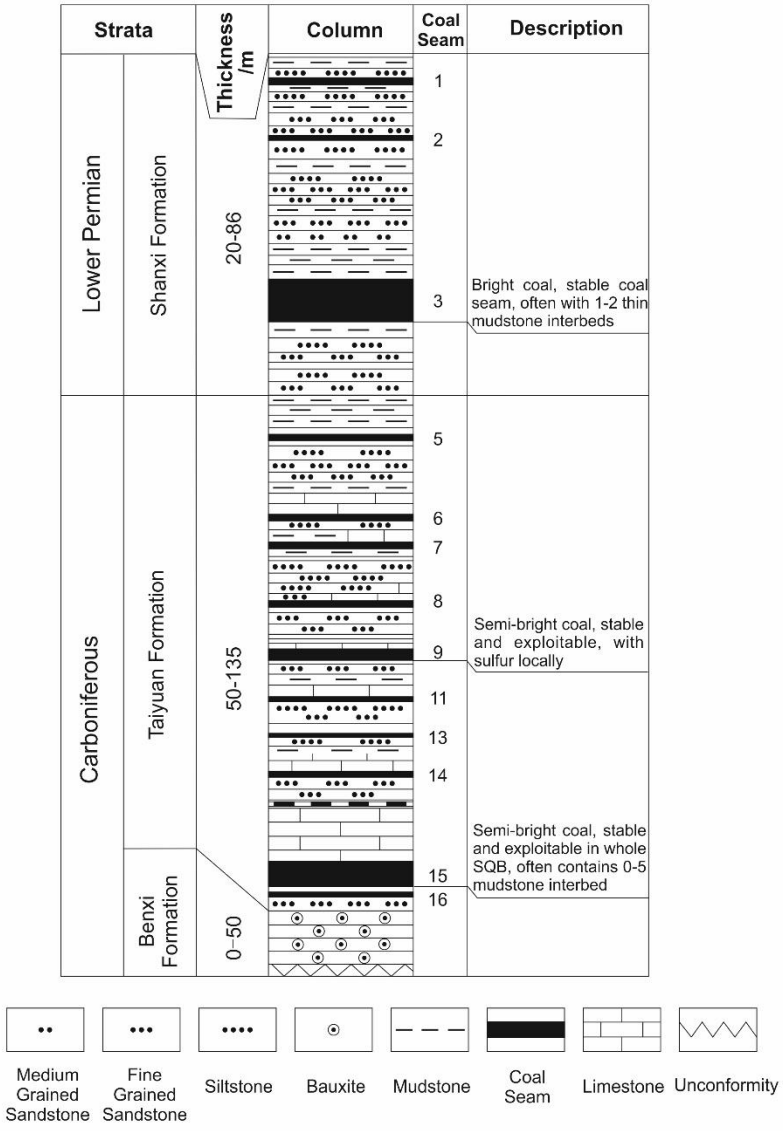

Figure 3.3. Stratigraphic column of the coal-bearing formations in Southeast Qinshui Basin. Modified after Su et al. (2005) and Cai et al. (2011).

The main hydrological influence on coal seams is sourced from the confined C_3t aquifer and P_1s-P_1x aquifer (Figure 3.2D) (Zhang et al., 2015). The no. 9 and 15 coal seams in the Taiyuan Formation are isolated from the underlying aquifer by bauxite and shale in the Benxi Formation (Figure 3.3) (Zhang et al., 2015). The roof of the no. 15 coal seam is a 2-30 km thick limestone, belonging to the C_3t aquifer. The no. 9 coal seam is sealed by underlying and overlying mudstones (Wang et al., 2013). The no. 3 coal seam belongs to P_1s-P_1x aquifer (Zhang et al., 2015). The roof and floor are fine sandstone and mudstone, respectively, which seal the layer as an individual aquifer (Su et al., 2005). The outcrops of the east and south coals in the SQB are the main source of recharging water (Su et al., 2005; Zhang et al., 2015). The groundwater recharges at the outcrop and flows northwest, and is prevented by a gas/water-sealed fault, Sitou Fault (Su et al., 2005).

3.4 Generation of coalbed methane in the Southeast Qinshui Basin

The organic matter in the Carboniferous sediments experienced coalification during the deep burial in the Late Palaeozoic and Mesozoic. The maturity of coal reached the first peak in the Late Triassic for the maximum burial depth by which time the temperature in coals reached ~135°C based on a normal geothermal gradient of 3°C/100 m, inducing the first period of methane generation and maturation of coal to medium volatile bituminous (vitrinite reflectance, $R_o \approx 1.2\%$) (Cai et al., 2011; Su et al., 2005; Zeng et al., 1999). Since that time the basin largely experienced inversion except for modest sedimentation in the Late Jurassic that did not induce further coalification (Ma et al., 2016; Zeng et al., 1999). However, Late Triassic burial temperature following the normal geothermal gradient cannot explain the high R_o values of the SQB coals. It is widely reported that magmatic activity during the Yanshanian Orogeny (Jurassic to Cretaceous) has caused the abnormally high temperature in the coals, over 200°C suggested by zircon fission-track data (Ren et al., 2005). This resulted in the conversion of the bituminous coals to semi-anthracite and anthracite with R_o values reaching 2.2-4.5% and a concomitant second period of gas generation (Su et al., 2005). Since then, the basin experienced exhumation, and no further coalification occurred.

3.5 Previous geochemical studies on coalbed gas from Qinshui Basin

The geochemical studies of CBM from the Qinshui Basin include well gas (Chen et al., 2007; Hu et al., 2007; Li et al., 2014; Xu et al., 2016; Zhang et al., 2018) and desorbed gas from coal cores (Chen et al., 2007; Zhang et al., 2018; Zhang and Tao, 2000). The Qinshui Basin gases are typically methane-rich (47-99%, mainly >95%) with minor nitrogen (0-49%, mainly <3%), carbon dioxide (<4%) and trace ethane (<0.3%), resulting in the $CH_4/(C_2H_6 + C_3H_8)$ ratio in the field widely higher than 1000. $\delta^{13}C$ of methane ranges from -61.7‰ to -26.4 ‰ (mainly > -40‰), while δD ranges from -179.3‰ to -168.3‰ (Chen et al., 2007; Li et al., 2014; Su et al., 2005; Zhang et al., 2018; Zhang and Tao, 2000; Zhang et al., 2019a). The carbon isotope of ethane and carbon dioxide ranges from -24.8‰ to -12.5‰ and -17.2‰ to 28.4‰, respectively (Chen et al., 2007). These gas and stable isotopic compositions imply a dominantly thermogenic origin. Minor contributions of secondary microbial methane were observed in gas desorbed from coal in the Zhengzhuang block, due to the proximity of minor faults where fresh meteoric water could recharge into the coal reservoir (Zhang et al., 2018). Su et al. (2005) also concluded that the proportion of secondary microbial methane increases towards the basin margin, as does the proportion of nitrogen and carbon dioxide.

3.6 Sampling and analytical procedures

The southern part of the Qinshui Basin is the focus of commercial CBM extraction, and thus sampling is relatively easy. Nineteen gas samples were taken in April 2017 from methane-producing wellheads along an E-W transect perpendicular to the boundary fault in the Panzhuang block (Figure 3.2). This transect is approximately along the groundwater recharge pathway. Seventeen gas samples are from vertical wells, all but one combine gas from the three main coal seams (coal seam nos. 3, 9 and 15). Well gas Qs 19 is from only coal seam 15. Two gas samples (Qs 15 and Qs 17) are from horizontal wells within coal seam 15. Well depths vary from 300 to 650 m (Table 3.1). The wells have been producing methane for between 3 months and 15 years (Table 3.1).

A detailed explanation of sampling processes and analysis methods are reported in Appendix I. Samples were collected and stored in Cu tubes at 1.5-2 bar using the method described in Györe et al. (2015).

Approximately 50% of the gas in each tube was used for the determination of the major gas composition and stable isotopes. Major gas composition was determined in nine samples using a Hewlett Packard 5890 gas chromatograph in SUERC. The uncertainty (1σ) of gas abundance is ± 0.3%. The methane carbon isotopic composition (δC_{CH4}) was determined using a VG SIRA II dual inlet isotope ratio mass spectrometer (Dunbar et al., 2016) using established procedures in Györe et al. (2018). $\delta^{13}C_{CH4}$ values were determined relative to PDB (Craig, 1957). The hydrogen isotope composition (δD_{CH4}) was analysed by a VG Optima dual inlet isotope ratio mass spectrometer (Donnelly et al., 2001). δD_{CH4} values were determined relative to V-SMOW (Gonfiantini, 1978). Experimental uncertainties (1σ) of $\delta^{13}C_{CH4}$ and δD_{CH4} values are ±0.3‰ and ±3‰, respectively (Appendix I).

The remaining gas was used for noble gas analysis using a MAP 215–50 mass spectrometer following procedures described in Györe et al. (2015) and Györe et al. (2017). Blank levels for all isotopes are negligible compared with the signal of samples. Mass spectrometer sensitivity and mass fractionation were determined using the HESJ standard for He (Matsuda et al., 2002), and air for Ne, Ar, Kr and Xe (Eberhardt et al., 1965; Lee et al., 2006; Mark et al., 2011; Ozima and Podosek, 2002). The reproducibility of the absolute concentrations is <4%, and isotopic ratios are less than 2%.

3.7 Results

Methane is the dominant gas (>95%) in all samples, with minor N_2 and trace CO_2. The wet gases (C_2H_6, C_3H_8) were below the detection limit (0.1%) of the gas chromatograph used in this study, which indicates the $CH_4/(C_2H_6 + C_3H_8)$ ratio is higher than 1000. The CH_4/CO_2 ratio varies from 152 to 806 (Table 3.1). The carbon and hydrogen isotopic

compositions of methane range from -30.2 to -35.2‰ and -155 to -194‰, respectively (Table 3.1).

Table 3.1. Gas compositions and stable isotopes of coalbed methane from Southeast Qinshui Basin.

Sample ID	Depth (m)	Distance to basin margin (km)	Gas extraction duration (month)	Total gas produced ($\times 10^5$) m^3 STP	CH_4/CO_2	$\delta^{13}C$ (‰)	δD (‰)
Qs1	406	20.2	132	125	na	-32.7	-178
Qs3	567	21.3	86	24.4	na	-32.4	-176
Qs4	585	21.8	25	41	na	na	na
Qs5	606	22.5	96	335	152	-31.6	-183
Qs6	390	20.4	96	377	na	-30.4	-162
Qs7	529	13.8	83	105	na	na	na
Qs9	552	12.0	69	39.1	349	-31.4	-180
Qs10	638	10.8	99	138	423	-33.5	-185
Qs11	673	10.2	125	217	na	-33.4	-173
Qs12	660	9.9	128	57.9	na	-32.0	-155
Qs14	487	13.6	71	6.51	806	-35.1	-194
Qs15	446	17.4	23	10.4	na	na	na
Qs17	519	16.8	15	0.85	329	-34.3	-185
Qs18	394	15.3	24	2.5	na	-35.2	-166
Qs19	420	14.9	3	0.29	na	na	na
Qs20	482	16.5	27	52.7	330	na	na
Qs21	375	19.3	25	36.7	237	-31.8	-194
Qs22	390	18.9	26	29.1	na	-33.0	-159
Qs23	361	20.0	96	40.5	235	-30.2	-171

1σ standard deviation for CH_4/CO_2, $\delta^{13}C$ and δD is 2%, 0.3‰ and 3‰, respectively.

$\delta^{13}C_{CH4}$ and δD_{CH4} are relative to PDB (Craig, 1957) and V-SMOW (Gonfiantini, 1978), respectively.

na: not analysed.

Table 3.2. Noble gas compositions of well gases from Southeast Qinshui Basin.

Sample ID	^{4}He ($\times10^{-6}$)	^{20}Ne ($\times10^{-8}$)	^{40}Ar ($\times10^{-5}$)	^{84}Kr ($\times10^{-9}$)	^{132}Xe ($\times10^{-11}$)	$^{3}He/^{4}He$ (R_A)	$^{20}Ne/^{22}Ne$	$^{21}Ne/^{22}Ne$	$^{40}Ar/^{36}Ar$	$^{38}Ar/^{36}Ar$	$^{40}Ar^{*}$ ($\times10^{-5}$)
Qs1	4.15(12)	0.75(3)	4.8(2)	2.5(1)	3.8(1)	0.031(8)	9.81(3)	0.0288(4)	431(2)	0.202(5)	1.46(5)
Qs3	29.23(86)	9.36(34)	13.8(5)	3.9(1)	4.7(2)	0.032(2)	9.94(3)	0.0290(3)	392(2)	0.188(3)	3.29(13)
Qs4	22.24(65)	3.25(12)	5.0(2)	3.9(1)	5.3(2)	0.026(2)	9.81(3)	0.0290(3)	401(2)	0.190(5)	1.28(5)
Qs5	8.27(23)	1.20(4)	5.2(2)	2.0(1)	4.5(2)	0.030(1)	9.73(3)	0.0292(4)	497(1)	0.193(5)	2.09(8)
Qs6	0.52(2)	0.115(4)	2.3(1)	1.4(1)	3.5(1)	0.017(4)	9.77(3)	0.0297(3)	493(2)	0.189(4)	0.92(3)
Qs7	8.47(25)	561(20)	229(8)	116(4)	323(13)	0.428(20)	10.06(4)	0.0293(3)	291(3)	0.187(4)	n/a
Qs9	3.10(9)	187(7)	72(3)	36(1)	85(3)	0.482(7)	10.07(3)	0.0296(3)	291(1)	0.187(6)	n/a
Qs10	1.58(5)	2.86(10)	11.3(4)	6.7(3)	9.6(4)	na	9.82(9)	0.0285(5)	341(1)	0.186(4)	1.39(6)
Qs11	0.96(3)	2.59(9)	9.2(3)	3.1(1)	2.3(1)	na	9.84(3)	0.0289(2)	343(2)	0.187(8)	1.20(6)
Qs12	1.27(4)	3.46(13)	10.1(4)	2.3(1)	3.3(1)	0.027(3)	9.84(6)	0.0294(7)	320(2)	0.188(5)	0.68(6)
Qs14	2.55(7)	84(3)	42(2)	20(1)	44(2)	0.307(10)	10.08(3)	0.0296(3)	298(1)	0.190(5)	n/a
Qs15	18.30(54)	195(7)	86(3)	40(2)	94(4)	0.115(4)	10.04(4)	0.0295(3)	302(2)	0.185(5)	0.91(43)
Qs17	33.25(96)	na	18.8(7)	5.0(2)	6.2(3)	0.026(1)	na	na	368(1)	0.188(10)	3.58(14)
Qs18	2.16(6)	0.51(2)	12.5(4)	6.2(2)	4.1(2)	0.013(1)	9.87(3)	0.0295(3)	358(2)	0.196(4)	2.06(9)
Qs19	3.50(10)	52(2)	31(1)	16(1)	47(2)	0.153(3)	10.18(3)	0.0293(2)	309(1)	0.186(4)	1.06(10)
Qs20	6.38(18)	3.83(14)	12.3(4)	4.9(2)	5.7(2)	0.022(1)	9.69(9)	0.0289(5)	365(1)	0.196(4)	2.23(8)

Table 3.2. Continued

Sample ID	^{4}He ($\times10^{-6}$)	^{20}Ne ($\times10^{-8}$)	^{40}Ar ($\times10^{-5}$)	^{84}Kr ($\times10^{-9}$)	^{132}Xe ($\times10^{-11}$)	$^{3}He/^{4}He$ (R_A)	$^{20}Ne/^{22}Ne$	$^{21}Ne/^{22}Ne$	$^{40}Ar/^{36}Ar$	$^{38}Ar/^{36}Ar$	$^{40}Ar^{*}$ ($\times10^{-5}$)
Qs21	0.93(3)	0.150(6)	2.8(1)	2.0(1)	2.9(2)	0.023(3)	9.81(3)	0.0301(7)	451(2)	0.187(1)	0.95(4)
Qs22	2.38(7)	0.37(1)	5.2(2)	5.0(2)	4.1(2)	0.009(2)	9.78(3)	0.0297(4)	428(3)	0.184(8)	1.56(6)
Qs23	14.14(42)	10.54(38)	19.1(7)	6.3(2)	6.2(2)	0.037(2)	9.91(3)	0.0289(3)	370(3)	0.193(10)	3.71(18)
Air	5.24(5)	1645(4)	934(1)	650(6)	2339(27)	1.000(9)	9.80(8)	0.0290(2)	298.6(3)	0.1885(3)	

1σ standard deviation is shown as the last significant figures in parentheses.

Noble gas concentrations are in unit of cm^3 STP/cm^3 with standard conditions after (Ozima and Podosek, 2002) (p =0.101 MPa, T = 0 °C).

Air composition is after Eberhardt et al. (1965); Györe et al. (2019); Lee et al. (2006); Mark et al. (2011); Ozima and Podosek (2002). R_A is the atmospheric $^{3}He/^{4}He$ ratio of 1.34×10^{-6} (Mishima et al., 2018). $^{40}Ar^{*}$ is calculated air-free ^{40}Ar.

na: not analysed; n/a: not applicable.

^{4}He concentrations range from 0.52 to 33.3 ppmv (Table 3.2). ^{3}He/^{4}He ratios vary from 0.009 ± 0.002 to 0.482 ± 0.007 R_A, where R_A is the atmospheric ratio of 1.34×10^{-6} (Mishima et al., 2018). ^{20}Ne concentrations range from 0.001 to 5.61 ppmv. Neon isotopes appear to be largely air-derived without clear evidence for significant mantle or crustal contributions; ^{20}Ne/^{22}Ne and ^{21}Ne/^{22}Ne ratios vary from 9.69 ± 0.09 to 10.18 ± 0.03 and from 0.0285 ± 0.0005 to 0.0301 ± 0.0007, respectively. Radiogenic ^{21}Ne is unequivocally present in only three samples relative to air-derived ^{21}Ne/^{22}Ne of 0.0290 ± 0.0003 (Eberhardt et al., 1965); Qs 6, Qs 21 and Qs 22. ^{40}Ar concentrations range from 23 to 2290 ppmv. ^{40}Ar/^{36}Ar ranges from 291 ± 1 to 497 ± 1. Samples Qs 7, Qs 9 and Qs 14 have ^{40}Ar/^{36}Ar ratios that are lower than the air value (298.6 ± 0.3; Lee et al. (2006); Mark et al. (2011)). In all cases, ^{38}Ar/^{36}Ar ratios are indistinguishable from air (0.1885 ± 0.0003; Lee et al. (2006); Mark et al. (2011)). The gas from coal seam 15 (Qs 15, Qs 17 and Qs 19) is not evidently distinct from the combined-seam gases in gas compositions, stable isotopes and noble gases.

3.8 Discussion

3.8.1 The post-generation fractionation of molecular and stable isotopic compositions

The C and H isotopic compositions ($\delta^{13}C_{CH4}$ = -30.2 to -35.2‰ and δD = -155 to -194‰) of the methane are indicative of a thermogenic origin. However, based on the coal maturity in SQB, the lowest $\delta^{13}C_{CH4}$ value is predicted to be -27‰ (Hu et al., 2001; Li et al., 2014). This is up to 8 ‰ higher than measured values and hints at modification by other process(es). The stable isotope composition of the SQB methane is apparently lighter than reported for methane from other CBM reservoirs of similar maturity, e.g. Kotarba and Rice (2001). Further, C_1/C_{2+} ratios are significantly higher than typical thermogenic gases (<50; Bernard et al. (1976)).

The unusual light stable isotopes and high C_1/C_{2+} in SQB have been commonly reported (Chen et al., 2007; Hu et al., 2001; Li et al., 2014; Qin et al., 2006; Zhang et al., 2018). These have previously been explained as due to the preferential dissolution of $^{13}CH_4$ and

heavy hydrocarbons in groundwater (Li et al., 2014; Qin et al., 2006). However, this is difficult to reconcile with experimental work that demonstrates that dissolution of methane should result in only small depletion of $\delta^{13}C$ (< -0.5‰) in the free methane phase, and a δD enrichment (<16‰) that is in the opposite sense to that recorded by the methane (Bacsik et al., 2002).

The addition of secondary microbial methane has been proposed in several studies to explain the high C_1/C_{2+} and light $\delta^{13}C$ of SQB methane (Chen et al., 2007; Li et al., 2014; Rice, 1993; Zhang et al., 2018). The light $\delta^{13}C_{CH4}$ (up to -61.7‰) of methane desorbed from SQB coal cores supports the addition of microbial methane. However, fewer than 10% of all SQB samples have $\delta^{13}C_{CH4}$ lighter than -40‰. Using an upper limit of $\delta^{13}C$ = -50‰ for microbial methane, and $\delta^{13}C$ = -27‰ for thermogenic methane (Li et al., 2014), the methane sampled in this study should be up to 35% microbial in origin. This would result in an increase of C_1/C_{2+} by less than the factor of two, which is not high enough to explain the high C_1/C_{2+} (> 1000) in the SQB gases. Thus, while there may be modest contributions of microbial methane, it is unlikely to be the key to the ubiquitous high C_1/C_{2+} and light $\delta^{13}C_{CH4}$.

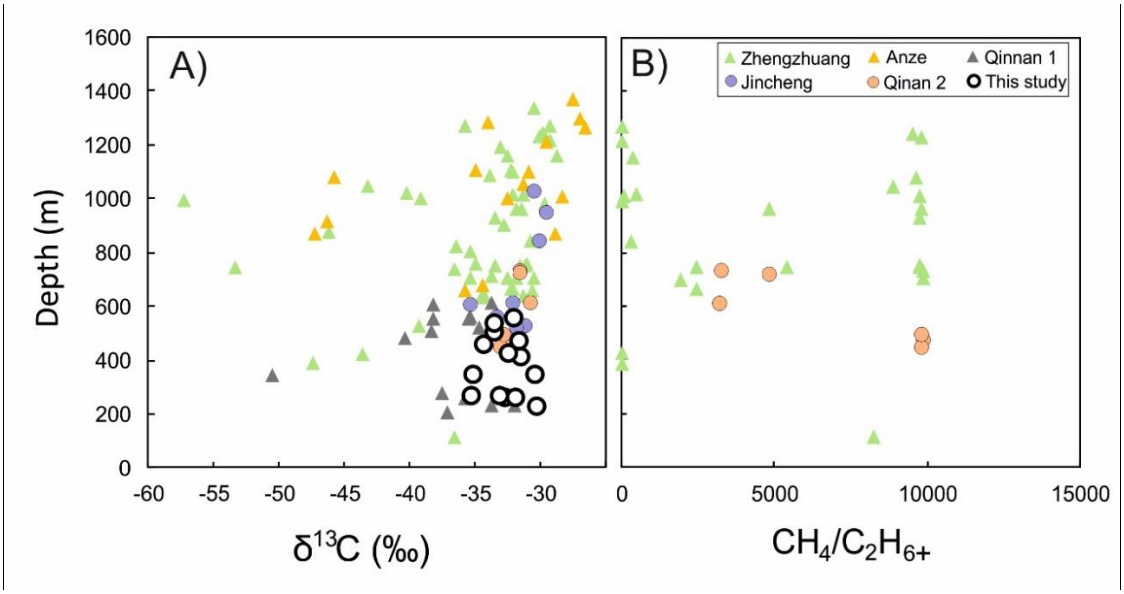

Figure 3.4. Burial depth vs. A) $\delta^{13}C_{CH4}$ and B) $CH_4/(C_2H_{6+})$. Triangles and circles represent the desorbed gas from coal cores and production wells. $\delta^{13}C_{CH4}$ and $CH_4/(C_2H_{6+})$ are not evidently correlated with the burial depth of coal seams. Data source: Zhengzhuang (Zhang et al., 2018), Anze (Zhang et al., 2019a); Qinnan 1 (Chen et al., 2007); Jincheng (Hu et al., 2001); Qinnan 2 (Li et al., 2014). 1 σ errors are smaller than the symbols.

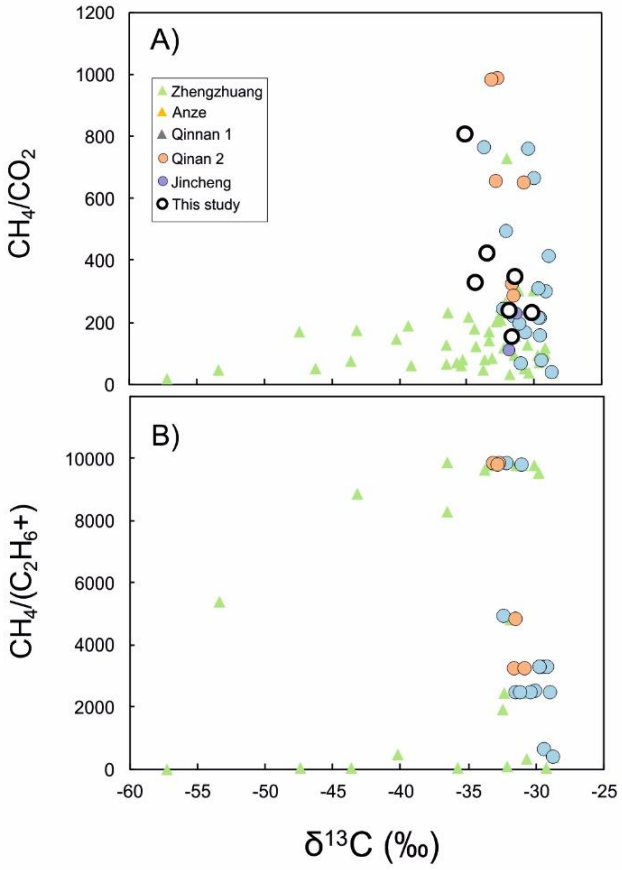

Figure 3.5. The relationship between $\delta^{13}C_{CH4}$ with molecular composition of gases. Triangles and circles represent the desorbed gas from coal cores and production wells. A negative trend between C_1/C_{2+}, C_1/CO_2 and $\delta^{13}C_{CH4}$ could be observed in gas from production wells but not desorbed gas from coal cores. Data source is the same as Figure 3.4.

Desorption and diffusion of deep methane to shallow depths during basin exhumation has also been proposed to explain the high C_1/C_{2+} and light $\delta^{13}C_{CH4}$ (Chen et al., 2007; Zhang et al., 2018; Zhang et al., 2019a). The $\delta^{13}C$ of methane gas desorbed for 4 hours from SQB anthracite is 8‰ lighter than the methane collected after 96 hours of desorption, supporting the hypothesis that light methane readily desorbs at early stages (Zhang and Tao, 2000). If isotopically light methane migrates up-seam, there should be a positive relationship between burial depth and $\delta^{13}C_{CH4}$. The C_1/C_{2+} and C_1/CO_2 ratios are also expected to increase with decreasing burial depth in theory as C_{2+} and CO_2 are harder to desorb and diffuse in coalbeds than CH_4 (Bae and Bhatia, 2006; Rice, 1993). Although a weak positive trend between $\delta^{13}C_{CH4}$ and burial depth of coal seams has been observed locally (Zhang et

al., 2019a), it is not evident when a more comprehensive compilation of data from SQB is present (Figure 3.4 A). C_1/C_{2+} in CBM gas is also unrelated to the burial depth (Figure 3.4 B). However, a negative trend between C_1/C_{2+}, C_1/CO_2 and $\delta^{13}C_{CH4}$ exists in gas collected from production wells but not in desorbed gas from coal cores (Figure 3.5). It reveals that molecular and isotopic fractionation is related to the gas extraction process. The change of $\delta^{13}C_{CH4}$ and C_1/CO_2 with increasing gas production supports this hypothesis (Figure 3.6). The most easily desorbed gases are produced druing the early stage of extraction, and as production continues and the rate of gas production rises, the isotopically heavier CH_4 and the more adsorbate gases (C_{2+}, CO_2) are released (Figure 3.5 and 3.6).

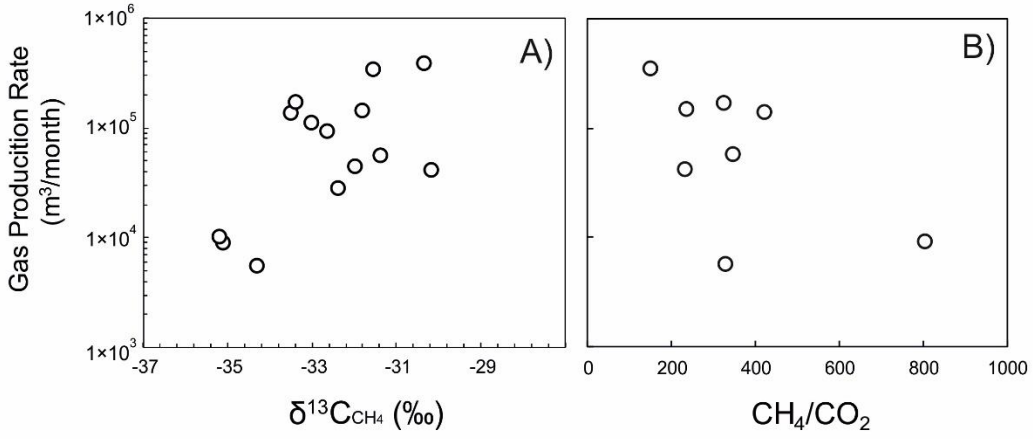

Figure 3.6. The relationship between gas production rate with A) $\delta^{13}C_{CH4}$ and B) CH_4/CO_2. The trends between $\delta^{13}C_{CH4}$ and CH_4/CO_2 with gas production rate indicate that molecular and isotopic compositions of produced gases have been affected by diffusive fractionation during gas extraction. Data source is the same as Figure 3.4. 1 σ errors are smaller than the symbols.

It is important to note that even when $\delta^{13}C_{CH4}$ approaches the predicted value (-27‰), the C_1/C_{2+} ratio (> 400) is higher than typical thermogenic values (< 50) (Figure 3.5B; Zhang et al., 2018). Even considering the addition of microbial methane, the maximum C_1/C_{2+} ratio can only be about two times higher. Ethane and propane are cracked to methane by pyrolysis or by reactions involving redox couples at temperatures in excess of 250°C (Burruss and Laughrey, 2010). The absence of heavy hydrocarbon gases in SQB is thus likely to be the result of cracking of wet gases into methane at high temperature. This is consistent with the detrital zircon fission-track thermochronology that indicates such

temperatures were attained during the early Cretaceous (Ren et al., 2005). This gives further credence to the idea that the methane generation occurred during the Yanshanian Orogeny.

3.8.2 Identifying the noble gas components

The He and Ne in the SQB gases appear to plot on mixing lines between a deep gas with high He/Ne (> 700)-low $^{3}He/^{4}He$ (< 0.03 R_A) and noble gases with a composition that can be derived from mass fractionated air (Figure 3.7A). The five gases with the lowest $^{4}He/^{20}Ne$ (grey circles in Figure 3.7A) have air-like $^{40}Ar/^{36}Ar$ ratios and high concentrations of ^{20}Ne and ^{36}Ar (Table 3.2) that are consistent with being dominated by air-derived noble gases. Both the high and low He/Ne samples have a similar range of ^{4}He concentrations, but the air-rich (low He/Ne) gases have higher ^{20}Ne concentrations (Figure 3.7B), suggesting that air-derived noble gases have been added to deep gas. As well as fractionated He/Ne (Figure 3.7A), the five air-rich samples have Ne isotopes that plot along the mass fractionation line in the $^{20}Ne/^{22}Ne$ vs $^{21}Ne/^{22}Ne$ space (Figure 3.8), and three samples have $^{40}Ar/^{36}Ar$ ratio that is lower than air value, also suggestive of fractionation (Table 3.2). The fractionated air-derived light noble gases may originate in liquids injected during hydraulic fracturing before pumping (Barry et al., 2018) or acquired during the sampling process. They dominate the noble gases of the five low He/Ne samples and these samples are not discussed further (in this and Chapter 5).

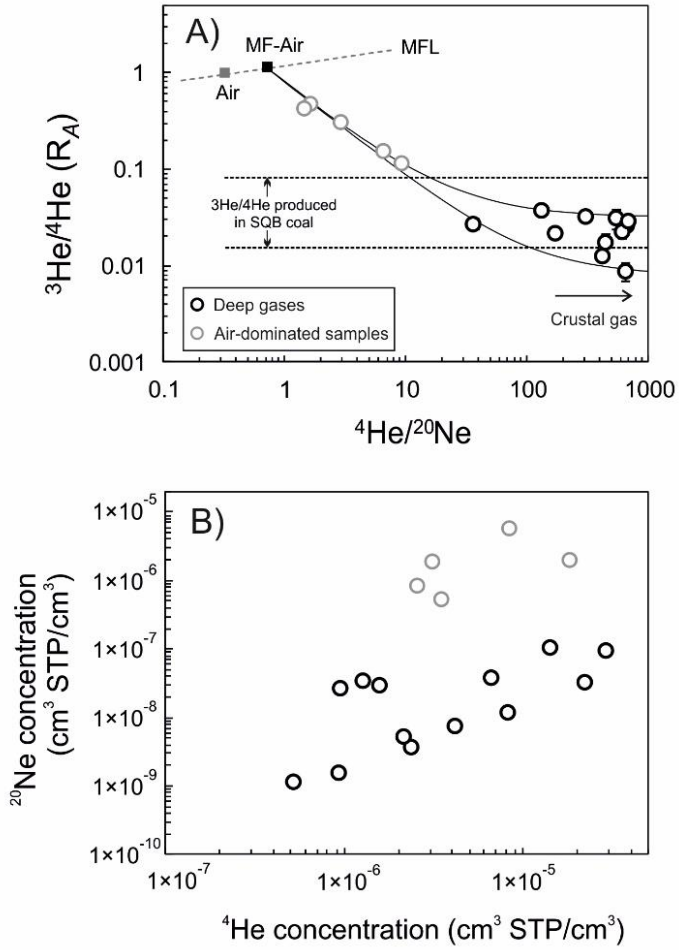

Figure 3.7. The He and Ne systematics of CBM gases from SQB. A) $^{3}He/^{4}He$ ratio plotted against $^{4}He/^{20}Ne$ of SQB methane. The solid black lines are mixing lines between deep gases, with high $^{4}He/^{20}Ne$, and mass fractionated air. The range of $^{3}He/^{4}He$ of radiogenic He produced within the coals (see text) is shown by the black dashed lines. MFL: Mass fractionation line after square root law (Kaneoka, 1980). The black circles represent deep gases; grey circles represent air-dominated samples. The black and grey squares represent the mass fractionated air and air, respectively. B) ^{20}Ne vs. ^{4}He concentrations. Air-dominated samples have relatively higher ^{20}Ne concentration but similar ^{4}He concentration range with deep gases. Uncertainties are 1 σ.

The high $^{4}He/^{20}Ne$ ratio (37-691) of the remaining samples rules out a significant contribution of air. The $^{3}He/^{4}He$ can be corrected for minor air-derived He on the basis of the atmospheric He/Ne (0.32) (Craig, 1978) where:

$$(^{3}He/^{4}He)_{co} = \frac{(^{3}He/^{4}He)_{s} \times (^{4}He/^{20}Ne)_{s} / (^{4}He/^{20}Ne)_{a} - (^{3}He/^{4}He)_{a}}{(^{4}He/^{20}Ne)_{s} / (^{4}He/^{20}Ne)_{a} - 1} \quad (3.1)$$

Subscripts co, s and a represent the corrected, measured and air-derived ratios, respectively. The gases yield $^{3}He/^{4}He$ of between 0.008 and 0.035 R_A after correction. This range is typical of crust-derived gases where radiogenic production of ^{4}He occurs by U and Th decay and nucleogenic production of ^{3}He by the reaction $^{6}Li(n,\alpha)^{3}H(\beta^{-})^{3}He$ (Morrison and Pine, 1955). Using the range of Li measured in coal seam 15 (12-78 ppmm, n=12), and the concentration of the large neutron cross-section elements (B, Be, Nd, Gd, etc.) in the Jincheng coals which is the closest coal mine to the study site (Zhang et al., 2004; Zhao, 1997; Zhao et al., 2018), I calculate a $^{3}He/^{4}He$ production ratio of 0.015 to 0.085 R_A (Figure 3.7A). This covers much of the range measured in the high He/Ne gases. The extremely low $^{3}He/^{4}He$ of samples Qs18 and Qs22 implies that, locally, Li concentrations may be lower, or the concentration of large neutron cross-section elements may be higher.

There is a possibility that the range of $^{3}He/^{4}He$ is due to the presence of a small contribution of mantle-derived He ($^{3}He/^{4}He_{magma}$ = 5-7 R_A; Gautheron and Moreira (2002)) from the early Cretaceous Yanshanian magmatism (Ren et al., 2005; Xu et al., 2004). Using the lowest measured $^{3}He/^{4}He$ (0.008 R_A) as representative of the crustal radiogenic He composition, and 6.1 R_A to represent the mean magmatic end-member of the subcontinental lithospheric mantle, the highest measured $^{3}He/^{4}He$ requires a maximum mantle He contribution of 0.5%. This is trivial and provides no support for the hypothesis that the main methane generation occurred in response to magmatic heating (e.g., Ren et al., 2005; Song et al., 2018; Su et al., 2005). In addition, mantle-derived Ne also has been observed in CBM deposits from sedimentary basins that have been intruded by magmatic bodies (e.g. Györe et al. (2018)). The absence of mantle-derived Ne in the SQB methane is consistent with the He isotope record.

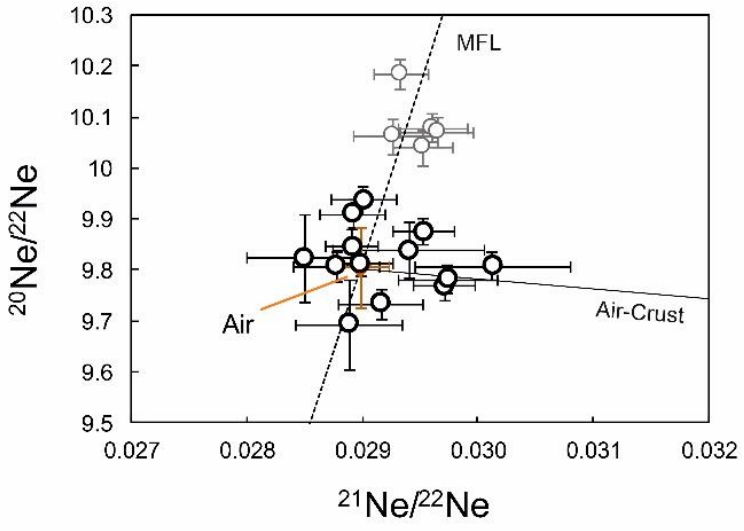

Figure 3.8. $^{20}Ne/^{22}Ne$ vs. $^{21}Ne/^{22}Ne$ for SQB methane-rich gases. Air is after Eberhardt et al. (1965) and Györe et al. (2019). The air-dominated samples (grey circles) are following the mass-controlled fractionation line (MFL) in consistent with He-Ne molecular trend. The deep gases (black circles) are mainly air-derived without evident crustal addition of ^{21}Ne. Uncertainties are 1 σ.

3.8.3 Helium loss during Cenozoic exhumation

The maximum 0.5% He mantle addition excludes the significant mantle contribution in the gas field. ^{40}Ar in gases are air-derived and radiogenic. The radiogenic ^{40}Ar (denoted as $^{40}Ar^{*}$) could be calculated by removing atmospheric ^{40}Ar:

$$[^{40}Ar]_c = [^{40}Ar]_t \times (1-(^{40}Ar/^{36}Ar)_a / (^{40}Ar/^{36}Ar)_s) \quad (3.2)$$

Subscripts c, t, a and s represent the radiogenic and total ^{40}Ar concentrations, air-derived and measured ^{40}Ar /^{36}Ar ratios, respectively. Compared with other CBM reservoirs of a similar age (e.g., Illinois coals, Moore et al. (2018); Central Scotland coals, Györe et al. (2018)), the ^{4}He concentrations in the high $^{4}He/^{20}Ne$ SQB gases are extremely low (Figure 3.9A). However, the concentration of $^{40}Ar^{*}$ in the SQB natural gases overlaps the range recorded by CBM from similar age coals above (Figure. 3.9B). Consequently, $^{4}He/^{40}Ar^{*}$ ratios (0.06 to 2) in the SQB gases are lower than the average production ratio of the upper continental crust (Ballentine and Burnard, 2002). $^{40}Ar^{*}$ is generated by the decay of ^{40}K. The locally low (U, Th)/K ratio in the coals might explain the low $^{4}He/^{40}Ar^{*}$ ratio in CBM gas. I could estimate the local in situ production rates using following equations (Craig and Lupton, 1976; Torgersen, 1980):

$$J(^4He) = 1.207\times10^{-13}[U] + 2.871\times10^{-14}[Th] \quad (3.3)$$

$$J(^{40}Ar) = 3.81\times10^{-14}[K] \quad (3.4)$$

where J(i) is the production rate of crustal noble gas i in cm^3 STP $^4He/(g_{rock}\ yr)$, U, Th are in ppmm, while K concentration is in wt%. The local $^4He/^{40}Ar^*$ ratio is predicted to higher than 13 based on the lowest U (0.5 ppmm) and Th (0.6 ppmm) (Zhang et al., 2004) and highest K concentration (0.16%, Zhao (1997)), far higher than measured ratios.

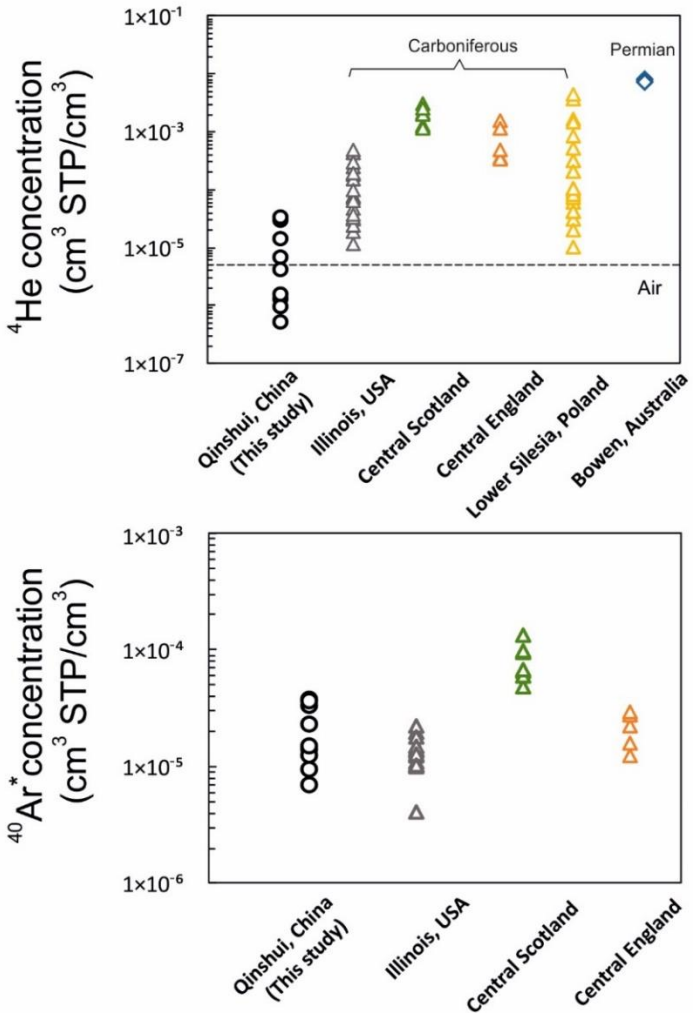

Figure 3.9. He and Ar contents of Carboniferous and Permian coals worldwide. The concentration of ^4He in the SQB is evidently lower than that in other basins with similar age (A). $^{40}Ar^*$ concentrations in gases from SQB overlaps with that in other basins (B). Data source: Illinois, USA (Moore et al., 2018); central Scotland (Györe et al., 2018); central England (Györe et al., 2018); Lower Silesia, Poland (Kotarba and Rice, 2001), Bowen, Australia (Kinnon et al., 2010). 1σ errors are smaller than symbols.

$^{4}He/^{40}Ar^{*}$ in natural gases are commonly higher than produced in the shallow crust (Ballentine et al., 1994), a function of the low-temperature mobility of He relative to Ar. Considering the evident fractionation of C isotope composition and the C_1/CO_2 ratio of the SQB gases during the gas production process, it is reasonable to assume that $^{4}He/^{40}Ar^{*}$ ratio also experienced fractionation during this process. I use the Rayleigh fractionation law (Eq. 3.5) to test it:

$$(\frac{A}{B})_w = (\frac{A}{B})_o f^{(\alpha-1)} \quad (3.5)$$

where $(\frac{A}{B})_w$ is the current elemental ratio in the water phase, $(\frac{A}{B})_o$ is the initial elemental ratio in the water phase, f is the proportion of residue B in the water, and α is the fractionation factor. Assuming the ratio of water to gas volume (V_w/V_g) at each degassing stage is close to zero, the partition of noble gases reaches equilibrium. The elemental ratios of noble gas in gas bubbles can be estimated by Eq. 3.6:

$$(\frac{A}{B})_g = (\frac{A}{B})_w \alpha \quad (3.6)$$

where $(\frac{A}{B})_g$ is the elemental ratio in the gas. Initial $^{20}Ne/^{36}Ar = 0.154$ in formation water is calculated from air-saturated water (ASW) equilibrated 10°C at a local average altitude of 740 m, with 10% excess air for Ne (Gilfillan et al., 2008; Kipfer et al., 2002; Peeters et al., 2003). The fractionation factors are calculated for Henry's constants of noble gases and corrected from liquid phase activity coefficients and gas phase fugacity coefficients (Ballentine et al., 2002; Crovetto et al., 1982; Smith and Kennedy, 1983) in groundwater at an average depth of 420 m, corresponding to a hydrostatic pressure of 4 MPa and a temperature of 27°C, and salinity of 0.04 mol/L (Wang et al., 2015a). The calculation details of initial ASW ratios and fractionation factor are shown in Appendix II. If the kinetic diffusion under non-equilibrium condition controls the noble gases partition, the Rayleigh equation is still applicable, only with the fractionation factor proportional to the inverse of the square root of the reduced mass which could be assumed to be equal to the mass of noble gas isotope (Ballentine et al., 2002; Zhou et al., 2005). However, the extent of $^{20}Ne/^{36}Ar$ change for mass-controlled kinetic fractionation cannot explain the range observed in the samples (Figure 3.10). The least air-contaminated SQB gases (i.e.

$^{4}He/^{20}Ne > 400$) plot on a trend in $^{4}He/^{40}Ar^{*}$-$^{20}Ne/^{36}Ar$ space that is consistent with open system Rayleigh fractionation of gas with $^{20}Ne/^{36}Ar$ of ASW based on local conditions (Figure 3.10). This indicates that the radiogenic ^{4}He and ^{40}Ar in the reservoir were dissolved in the formation water and degassed during CBM extraction. Formation water with an initial $^{4}He/^{40}Ar^{*}$ ratio of 13.0 (local production in coals) and ~5 (average continental crust) provide poor fits to the data. The best fit to the data is derived for an initial $^{4}He/^{40}Ar^{*}$ that approaches a value of 1.0. This implies that the formation water had an abnormally low $^{4}He/^{40}Ar^{*}$ prior to commercial extraction of methane.

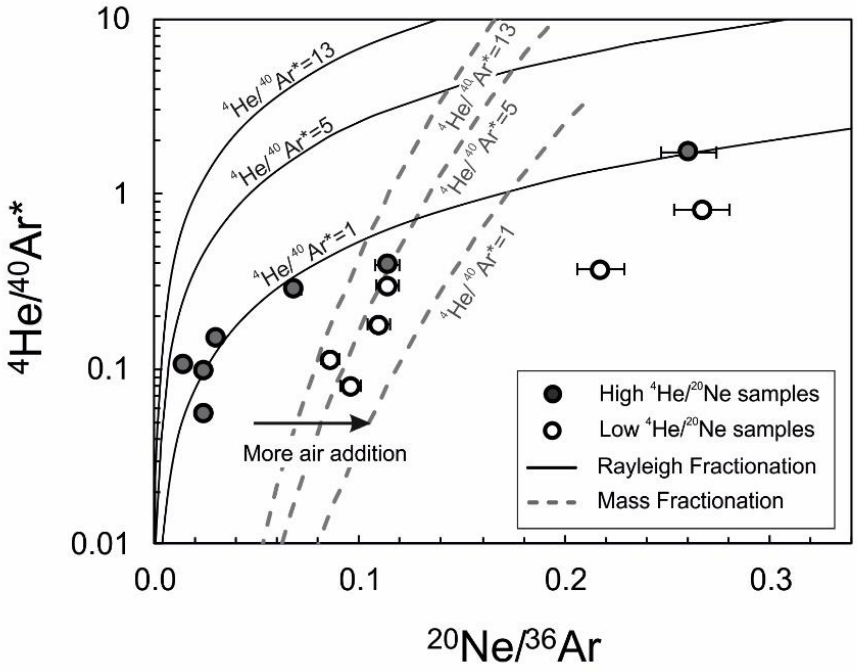

Figure 3.10. $^{4}He/^{40}Ar^{*}$ vs. $^{20}Ne/^{36}Ar$ for Southeast Qinshui Basin CBM. The black lines reflect solubility-controlled Rayleigh fractionation of open system with an initial ASW $^{20}Ne/^{36}Ar$ of 0.154. The grey dashed lines are mass-controlled kinetic fractionation (Ballentine et al., 2002; Zhou et al., 2005). Open system Rayleigh fractionation of gas from formation water with initial $^{4}He/^{40}Ar^{*} = 1$ provides the best fit to the least air-contaminated gas samples (black filled circles, $^{4}He/^{20}Ne$ >400). This implies that radiogenic ^{4}He and ^{40}Ar in the reservoir were dissolved in the formation water and degassed with air-derived ^{20}Ne and ^{36}Ar during the pumping process.

The main storage mechanism of gas in coal is by adsorption on the coal matrix or absorption in the micro-pores (Al-Jubori et al., 2009; Hildenbrand et al., 2012; Rice, 1993).

The rapid uplift of sedimentary basins induces a drop of reservoir pressure, weakening the sorption capacity of coal (Rice, 1993; Xia and Tang, 2012). Adsorbed and absorbed gases are desorbed and accumulated in coal microstructures, generating concentration and pressure gradient that results in gas escape by diffusion or viscous flow (Hildenbrand et al., 2012; Rice, 1993). Gas escape is mainly controlled by the effective permeability of the coals between the gas phase and wetting phase (Hildenbrand et al., 2012). The rapid Cenozoic inversion of the Qinshui Basin, from >3 km to <400 m is likely to have resulted in episodic gas expulsion from the coal seams. A series of detailed gas breakthrough experiments on high rank coals (R_o = 2.3%) from the Qinshui Basin mimicked the effect of over-pressure (Han et al., 2010a). It revealed that He and Ar escape from the wet-coal matrix by mainly diffusion and rarely capillary-viscous flow if macro fractures (e.g. cleats) existing in coalbeds (Han et al., 2010a). They also showed that the effective permeability of He for diffusion is significantly higher than for Ar (Han et al., 2010a). Consequently, during continuous and intensive basin inversion, Ar is likely to have remained trapped in the coalbeds while most of the He lost. The escape mechanism is discussed in more detail in Chapter 5. Further, the solubility of Ar in water is higher than He (Crovetto et al., 1982; Smith and Kennedy, 1983). Thus the preservation of old formation waters in the SQB (Wang et al., 2018) will tend to have further reduced the $^{4}He/^{40}Ar^{*}$. The loss of He after magmatic events explains the absence of mantle He in the SQB methane.

As no evident mantle Ne contributions are observed in the samples, ^{21}Ne excess (denoted as $^{21}Ne^{*}$) in samples is generated by nucleogenic reactions, $^{18}O(\alpha,n)^{21}Ne$ and $^{24}Mg(n,\alpha)^{21}Ne$, in the coals (Yatsevich and Honda, 1997). Nucleogenic ^{21}Ne can be calculated by:

$$[^{21}Ne]_c = [^{21}Ne]_t \times (1-(^{20}Ne/^{21}Ne)_a / (^{20}Ne/^{21}Ne)_s) \quad (3.7)$$

Subscripts c, t, a and s represent the nucleogenic and total ^{21}Ne concentrations, air-derived and measured $^{20}Ne/^{21}Ne$ ratios, respectively. Only samples Qs6, Qs21 and Qs22 have $^{21}Ne^{*}$ excess ($9.6 \pm 3.3\times10^{-14}$ to $3.1 \pm 1.6\times10^{-13}$ cm^3 STP/cm^3) beyond analytical uncertainty. It gives the $^{21}Ne^{*}/^{40}Ar^{*}$ ratio of $1.1 \pm 0.6 \times10^{-8}$ to $2.0 \pm 1.0 \times10^{-8}$ in these three samples. The *in situ* production rate of nucleogenic ^{21}Ne can be predicted from (Ballentine and Burnard, 2002):

$$J(^{21}Ne) = (1.48[U]+0.186\ [Th])\times[O]+(0.105[U]+0.179\ [Th])\times[Mg]\times10^{-22} \quad (3.8)$$

where J is the production rate of crustal ^{21}Ne in cm^3 STP $^4He/(g_{rock}\ yr)$, U, Th are in ppmm, while O and Mg concentrations are in wt%. The minimum theoretical local production of $^{21}Ne^*/^{40}Ar^*$ in SQB is estimated to be 7.8×10^{-8} based on O (5.5%), Mg (0.4%) (Yin et al., 2016; Zhao, 1997), lowest U, Th concentrations and highest K concentration in coals. It is far higher than the calculated value in the samples. The absence of crustal Ne in the samples demonstrates that most of the non-atmospheric Ne has been lost with He.

As the He in the SQB well gases has mainly degassed from the coal formation water, the accumulation time of ^4He can be estimated (Zhou and Ballentine, 2006) from Eq 3.9:

$$[He]_{in\ situ} = \frac{\rho\Lambda J(1-\varphi)}{\varphi}\ t \quad (3.9)$$

where $[He]_{in\ situ}$ is the *in situ* accumulation rate in formation water in cm^3 STP $^4He/(cm^3_{H_2O}\ yr)$, ρ is the density of the coal in g/cm^3, Λ is the fraction of He generated in the coal that enters the pore fluid and assumed to be 1 following Zhou and Ballentine (2006). φ is the porosity of the coal, and J is the production rate of ^4He calculated based on Eq 3.3. Assuming that the coals have a density of 1.6 g/cm^3, porosity of 5% (Cai et al., 2011), and all the ^4He has been generated in rock with average U and Th concentrations of 3.9 ppmm and 8.5 ppmm, respectively (Zhang et al., 2004), it gives the *in situ* production rate of 1.8×10^{-11} cm^3 STP $^4He/(cm^3_{H_2O}\ yr)$ in SQB coals. As He-Ne-Ar follows the open system Rayleigh fractionation, with the assumption that the original $^{20}Ne/^{36}Ar$ in formation water is ASW (0.154), the residual ^{36}Ar (*f*) in the formation water can be calculated based on Eqs 3.5 and 3.6, allowing the initial $^4He/^{36}Ar$ to be calculated. The initial ^{36}Ar in ASW under local conditions is about 1.2×10^{-6} cm^3 $STP/cm^3_{H_2O}$. The initial concentration of ^4He in formation water before fractionation is therefore easily estimated and gives the He accumulation age of between 0.5 and 11 million years, which is much younger than the age of coal (Late Carbonaceous to Early Permian). It supports the contention that the majority of He has been lost. This contrasts with the observed $^{40}Ar^*$ concentration. Using the maximum concentration of K and assuming the transfer rate of Ar from rock to fluid

of 1, it gives the maximum *in situ* production rate of 1.5×10^{-13} cm^3 STP $^{40}Ar^*/(cm^3_{H_2O}$ yr). As the solubility of $^{40}Ar^*$ and ^{36}Ar is indistinguishable at this scale, the calculated $^{40}Ar^*$ concentration in formation water requires ~200-1,600 million years, which exceeds the deposition age of coal, and requires the incorporation of the crustal flux of ^{40}Ar flux and/or ^{40}Ar exsolved from solidifying mantle melts (Castro et al., 1998; Györe et al., 2018; Torgersen et al., 1989). Both of these processes will result in the incorporation of ^4He in excess of *in situ* production.

Following the method of Zhou and Ballentine (2006), with a total thickness of three coal seams to be 8.6 m, I assume that the regional ^4He and $^{40}Ar^*$ fluxes are 4.9×10^{-8} cm^3 STP $^4He/(cm^3_{H_2O}$ yr) and 8.6×10^{-9} cm^3 STP $^{40}Ar^*/(cm^3_{H_2O}$ yr), respectively. With both *in situ* and external production, the accumulated age for ^4He is ~$200 – 4\times10^3$ yr and $3\times10^3 – 3\times10^4$ yr for $^{40}Ar^*$. The older age defined by $^{40}Ar^*$ again supports the contention that He has been most efficiently lost from SQB coals. The $^{40}Ar^*$ age overlaps the ^{14}C age of the production water from other regions in SQB ($5\times10^3 – 4\times10^4$ yr) (Wang et al., 2018).

Based on the local $^4He/^{40}Ar^*$ production rate of 13, the initial $^4He/^{40}Ar^*$ ratio of 1 before fractionation indicates that over 92% of He has been lost during basin inversion. The possible addition of external ^4He suggests the loss proportion is underestimated. However, the SQB coals have, obviously, retained economic quantities of methane. This reflects different physical behaviours between CH_4 and the light noble gases. Compared with He and Ar, methane is strongly adsorbed onto the coal and only moves by diffusion in SQB coalbeds (Han et al., 2010a; Han et al., 2010b; Hildenbrand et al., 2012). A model which considers both adsorption/desorption and diffusion during methane loss has been introduced by Xia and Tang (2012). For total organic carbon of 71% (Yin et al., 2016), assuming overpressure of 60 MPa and 250°C before basin inversion and final conditions of 4 MPa and 27°C after basin inversion, the free methane concentration decreases from 692 mol/m^3 to 81 mol/m^3, assuming the Peng-Robinson equation of state. The adsorbed gas amount drops from 786 mol/m^3 to 749 mol/m^3 following the Langmuir equation (Xia and Tang, 2012). Considering both the loss of free and adsorbed gas, approximately 44% of the methane has been lost from the SQB during basin inversion. Based on the model in

Xia and Tang (2012), the $\delta^{13}C$ of the residue methane would be less than 2‰ heavier than the initial composition. This contrasts with the observed lighter $\delta^{13}C_{CH4}$ values in SQB methane samples compared to the predicted value. Thus, although the carbon isotope of methane might have been influenced by gas loss, it has been obscured by later fractionation caused by desorption during gas extraction. This suggests that basin inversion and gas loss are not recorded by stable isotopes (or major gas composition). Although the noble gases experienced open system Rayleigh distillation during gas production as well, through modelling, the gas loss could be revealed by light noble gases (He-Ne-Ar). In particular, the radiogenic ^{4}He and $^{40}Ar^{*}$ provide a keen tracer of the timing of gas loss during basin inversion.

3.8.4 The storage of heavy noble gases in the Southeast Qinshui Basin coals

Natural gases are commonly enriched in the air-derived Kr and Xe relative to their proportions in the atmosphere-equilibrated reservoirs as a consequence of desorption of gases that were initially trapped in the source rocks (Torgersen and Kennedy, 1999; Zhou et al., 2005). For instance, $^{132}Xe/^{36}Ar$ can be hundreds of time higher than the ratio in ASW (Torgersen and Kennedy, 1999).

The $^{132}Xe/^{36}Ar$ (0.00009-0.00074) of the SQB gases is lower than ASW values by up to thirty times and $^{84}Kr/^{36}Ar$ (0.007-0.042) by up to five times (Figure 3.11A). I have already shown that the He-Ne-Ar data require open system Rayleigh fractionation during degassing from groundwater, likely induced by the gas extraction process (Figure 3.10). The relative abundances of Ar-Kr-Xe should reasonably be expected to follow this trend. However, they are significantly below the predicted trend, though are more enriched in Kr compared to Xe (Figure 3.11A). As heavy noble gases readily remain dissolved in the oil phase, this pattern is consistent with equilibrium with oil (Ballentine et al., 2002; Torgersen and Kennedy, 1999; Zhang et al., 2019b). The re-dissolution fractionation processes proposed in Gilfillan et al. (2008) could also cause low $^{132}Xe/^{36}Ar$ and $^{84}Kr/^{36}Ar$ ratios. However, no oil has ever been drilled from the SQB. Furthermore, both mechanisms would lead to an enrichment of ^{20}Ne compared to ^{36}Ar, leading to $^{20}Ne/^{36}Ar$ ratios that are significantly higher than ASW values. This is not the case for most SQB gases (Figure

3.11B). Thus, neither mechanism can explain the heavy noble gas depletions. These depletions cannot be explained by the mixing between air, characterised by low $^{132}Xe/^{36}Ar$ (0.00075) and $^{84}Kr/^{36}Ar$ (0.0021) ratios, and ASW-derived noble gases (Figure 3.11A). To our knowledge, this is the first observation of heavy noble gas depletion in natural gas systems.

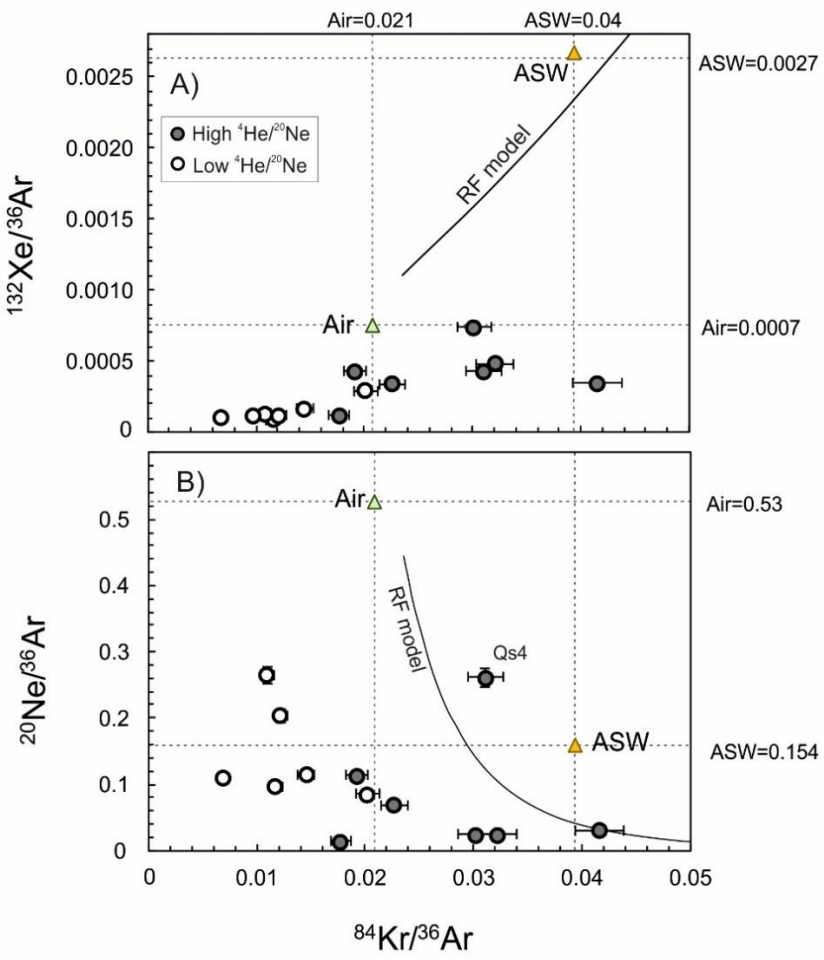

Figure 3.11. $^{84}Kr/^{36}Ar$ vs. $^{132}Xe/^{36}Ar$ (A), and $^{20}Ne/^{36}Ar$ (B) for SQB coal bed methane samples. All gases have a relative deficiency of noble gases in heavier mass than predicted for open system Rayleigh fractionation of ASW-derived noble gases (black line).

Adsorption/retardation and/or throat constrictions in sediments could inhibit diffusion of noble gases and be related to the atomic radius (Torgersen et al., 2004). The dominant distribution of micro-pores (<10 nm in diameter) and transition pores (10-100 nm in diameter) in SQB coals (Liu et al., 2015), hinders the movement of Kr and Xe compared to Ar. It might induce diffusive fractionation of noble gases in formation water during its

migration in coal seams. The enhanced adsorption of heavy noble gases in SQB coals could also cause more Kr and Xe to be retained in a trapped water phase than in normal case during degassing process, that is, enhancing the fractionation extent of Xe/Ar and Kr/Ar. The greater depletion of Xe than Kr is consistent with the larger radius of Xe than Kr. It supports the idea that the large-radius gases are more easily adsorbed to the surface of organic matter or trapped in the coal matrix. Thus, it seems likely that the physical characteristics of the extremely mature SQB coals, i.e. strong retentivity, low permeability, high proportion of micro-pores, have affected the behaviour of Kr and Xe in formation waters, leading to 1) low initial $^{132}Xe/^{36}Ar$ and $^{84}Kr/^{36}Ar$ in formation water after migration in coal seams; and 2) smaller fractionation factors of $^{132}Xe/^{36}Ar$ and $^{84}Kr/^{36}Ar$ during the degassing process. This will result in lower concentrations of ^{84}Kr and ^{132}Xe in the exsolved gas compared to open system Rayleigh fractionation.

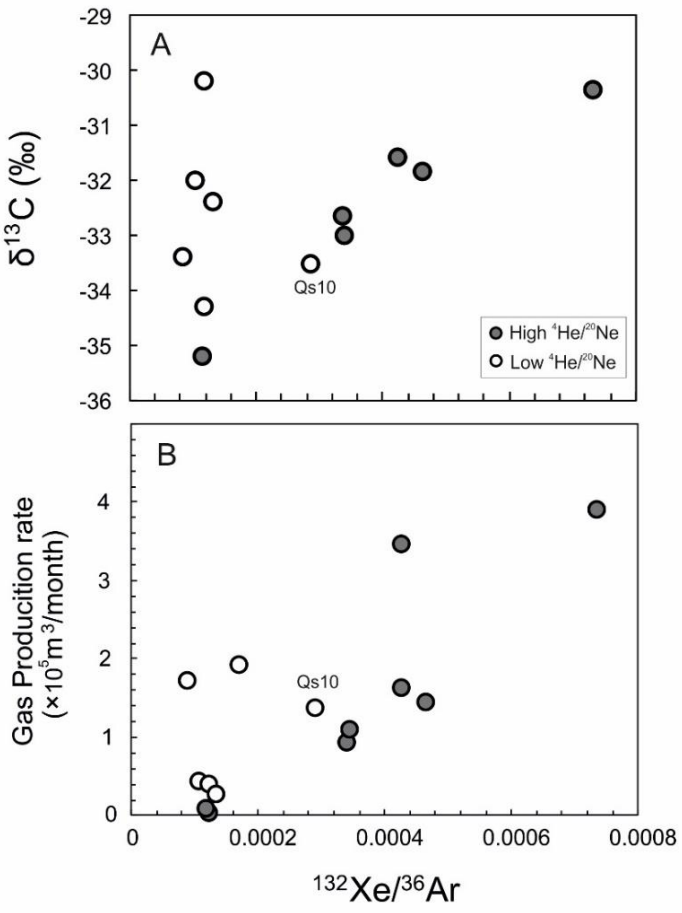

Figure 3.12. $^{132}Xe/^{36}Ar$ vs. $\delta^{13}C_{CH4}$ in SQB samples (A), and methane production rate of each well (B). Positive correlations exist between $^{132}Xe/^{36}Ar$, $\delta^{13}C_{CH4}$ and methane production rate in high

$^{4}He/^{20}Ne$ samples. $^{132}Xe/^{36}Ar$ ratios in low $^{4}He/^{20}Ne$ samples remain unchanged with varied $\delta^{13}C_{CH4}$ and methane production rate.

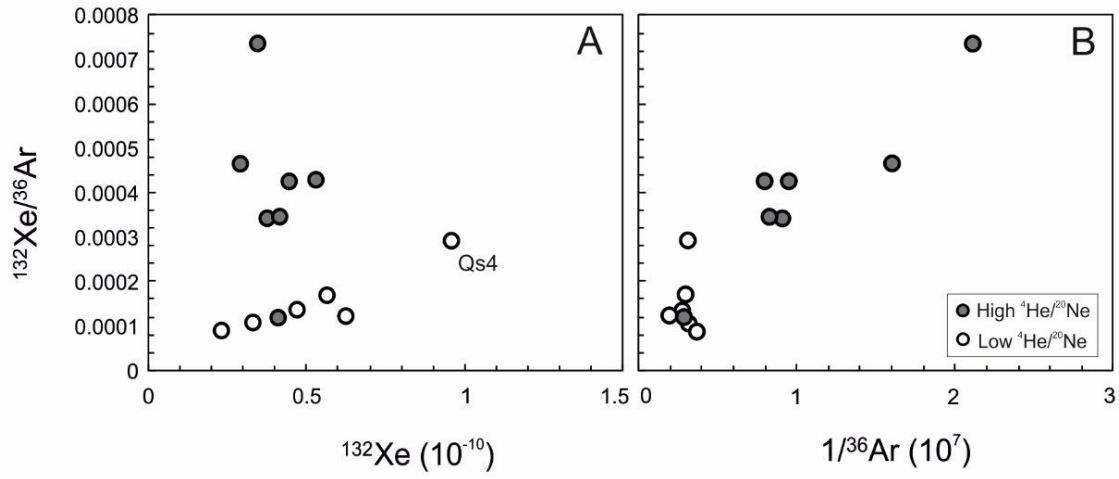

Figure 3.13. $^{132}Xe/^{36}Ar$ vs. ^{132}Xe (A) and $1/^{36}Ar$ (B) in SQB samples. The $^{132}Xe/^{36}Ar$ ratios in the high $^{4}He/^{20}Ne$ ratio gases are mainly controlled by ^{36}Ar concentrations, while those in the low $^{4}He/^{20}Ne$ gases are controlled by ^{132}Xe concentrations.

This assumption is supported by the coherent behaviour of Xe and methane in the gases (Figure 3.12). A strong positive relationship between $^{132}Xe/^{36}Ar$, $\delta^{13}C_{CH4}$ and methane production rate is present in high $^{4}He/^{20}Ne$ ratio samples (Figure 3.12). It indicates that Xe abundance was also controlled by the adsorption of methane from the coal during gas extraction. With continuous pumping, more Xe will be exsolved from water. In contrast, $^{132}Xe/^{36}Ar$ ratios in the low $^{4}He/^{20}Ne$ ratio samples are relatively consistent (except Qs10) in spite of variation in $\delta^{13}C_{CH4}$. I compare $^{132}Xe/^{36}Ar$ ratios with ^{132}Xe concentrations and $1/^{36}Ar$ in both groups (Figure 3.13). The high $^{4}He/^{20}Ne$ ratio group has relatively stable Xe concentrations but a wide range of ^{36}Ar concentrations. The decrease of ^{36}Ar concentration with the rise of $^{132}Xe/^{36}Ar$ ratios followed the solubility-controlled fractionation process. The decoupling of ^{132}Xe concentrations is more evidence of the coherent behaviour of Xe and methane. The low $^{4}He/^{20}Ne$ ratio group gases have consistently high ^{36}Ar concentrations, leading to the low $^{132}Xe/^{36}Ar$ ratios in the samples (Figure 3.13; Table 3.2). This group also has an enrichment of ^{20}Ne with higher air-derived $^{20}Ne/^{36}Ar$ than modelled values (Figure 3.10; Table 3.2). The high ^{20}Ne and ^{36}Ar abundance in gas samples could

be an indication of continuous groundwater recharge during gas extraction, which supplies air-derived ^{20}Ne and ^{36}Ar. It is important to note that the low $^{4}He/^{20}Ne$ ratio gases are more depleted in heavy noble gases than the high $^{4}He/^{20}Ne$ ratio group. It reflects that the $^{132}Xe/^{36}Ar$ ratio in recharge water has fractionated during the migration, consistent with the hypothesis.

If correct, this hypothesis implies the strong Kr and Xe adsorption capacities of extremely high-maturity SQB coals. This is consistent with the prosperous storage of methane in SQB even most of He has been lost. The similar behaviour of heavy noble gases and methane hints that Kr and Xe might be a better tracer of the migration of methane in the high-mature coal reservoir.

3.9 Conclusions

The stable isotope and major gas compositions of CBM from the Qinshui Basin indicates a thermogenic origin with limited microbial methane. The characteristics have been over-printed by fractionation during gas extraction. The noble gases reveal a mixture of air-derived gases from groundwater (ASW) with deep gases in the reservoir. The mixing of radiogenic ^{4}He and ^{40}Ar and ASW derived noble gases occurred in the water phase. Then, they degassed from water following open system Rayleigh fractionation during gas extraction. Gas loss before the commercial extraction can explain the significantly lower $^{4}He/^{40}Ar^{*}$ in all samples even considering the fractionation process. Meanwhile, it also explains the absence of mantle volatiles in the reservoir although the basin was thought to be heated during a magmatic activity in Yanshanian movement. The He loss is related to the exhumation of the basin mainly during the Cenozoic. Compared with He, Ar, with lower diffusive efficiency and higher solubility, was partly stored in the coal and dissolved in water, which caused the low $^{4}He/^{40}Ar^{*}$ ratio in formation waters. Although about half of the methane also lost during basin inversion, the diagnostic of stable isotopes is weak and easily overprinted by post fractionation processes. This study demonstrates the possibility of using He-Ne-Ar content in natural gases to track gas evolution caused by recent basin activities. This study is the first to report the depletion of Xe and Kr in natural gas systems

without significant enrichment of Ne. This pattern is the result of the strong retention of Kr and Xe in the high maturity SQB coals.

Chapter 4 Evolution of coalbed methane in Liupanshui Coalfield, Southern China: Insights from stable and noble gas isotopes

4.1 Overview

The breakthrough of commercial coalbed methane (CBM) development in the Qinshui Basin at the start of the 21st century drove the development of methane exploitation in many other Chinese coal districts. The Liupanshui Coalfield in Guizhou Province, southern China, was proposed as a critical area for CBM exploration in the 13th national five-year plan (FYP, 2016). Compared to the Qinshui Basin, the commercial development of CBM in the region is still in its infancy. Academic research is sparse, and consequently, the origin of the gas is poorly understood.

The CBM is present in Late Permian coals of the upper Yangtze sedimentary basin. The basin was separated into several blocks during the main stage of Yanshanian Orogeny in the Late Jurassic-Early Cretaceous. Since then these blocks have experienced different burial and exhumation histories such that the coals in each block have markedly different maturity (Dou, 2012). Currently CBM extraction is carried out in more than ten blocks. Consequently, the Liupanshui Coalfield is a good natural laboratory for studying the role of coal rank on the generation, preservation and transport of natural gas during and after inversion.

This chapter presents the results of the study of the geochemistry and isotope composition of CBM from the four main blocks in the Liupanshui Coalfield. I use the stable isotope and the major gas composition of gas from the coalfield to trace the origin of methane. The noble gases provide an understanding of gas transport and retention during basin inversion and allow me to evaluate the extent of gas loss in each block.

4.2 CBM development in the Liupanshui Coalfield

In comparison to other regions of China, Guizhou Province has poor gas and oil resources. However, it has the largest coal resource in southern China, with an estimated 400 billion tons of coal present in the upper 2,000 m (Di et al., 2009). The evaluation of the CBM resource and research on gas content and reservoir properties of the region started in the 1980s (Xu, 2012). A recent study estimates that 3.06×10^{12} m^3 of methane resource is stored in coals of Guizhou Province (Ren et al., 2018).

The Liupanshui Coalfield (LPC) covers an area of 1.5×10^4 km^2 in western Guizhou Province (Figure 4.1). The geological CBM resource of the field is estimated to be 1.4×10^{12} m^3, which represents 45% of the total Guizhou Province resource (Shan et al., 2018). CBM is mainly present in blocks within synclines, which cover around 5,000 km^2 (Gui, 1999). The initial phase of exploration saw five test wells drilled between 1998 and 2002 without effective gas production (Xu, 2012). The first commercial CBM project started in the Baotian-Qingshan block in 2006, when six wells were drilled for determining reservoir parameters. The vertical test well Yangmeican-1 drilled in 2016 in the Yangmeishu syncline block produced over 4,000 m^3 CH_4/day for over seven months, with the maximum daily production exceeding 5,000 m^3. This well marked a breakthrough in CBM exploration in southwest China. At the same time, vertical drill holes in the Dahebian block typically reached a stable production of 1,000 m^3/day, with the highest rate of 1,800 m^3/day. Six cluster wells drilled during 2017-2018 in this block supported the total production of 9,000 m^3/day in 2019 (Bao, 2019). So far over 170 wells have been drilled in the LPC. Of these, 88 wells are currently productive, leading to an annual production of ~1.7×10^7 m^3 methane.

4.3 Geology of Liupanshui Coalfield

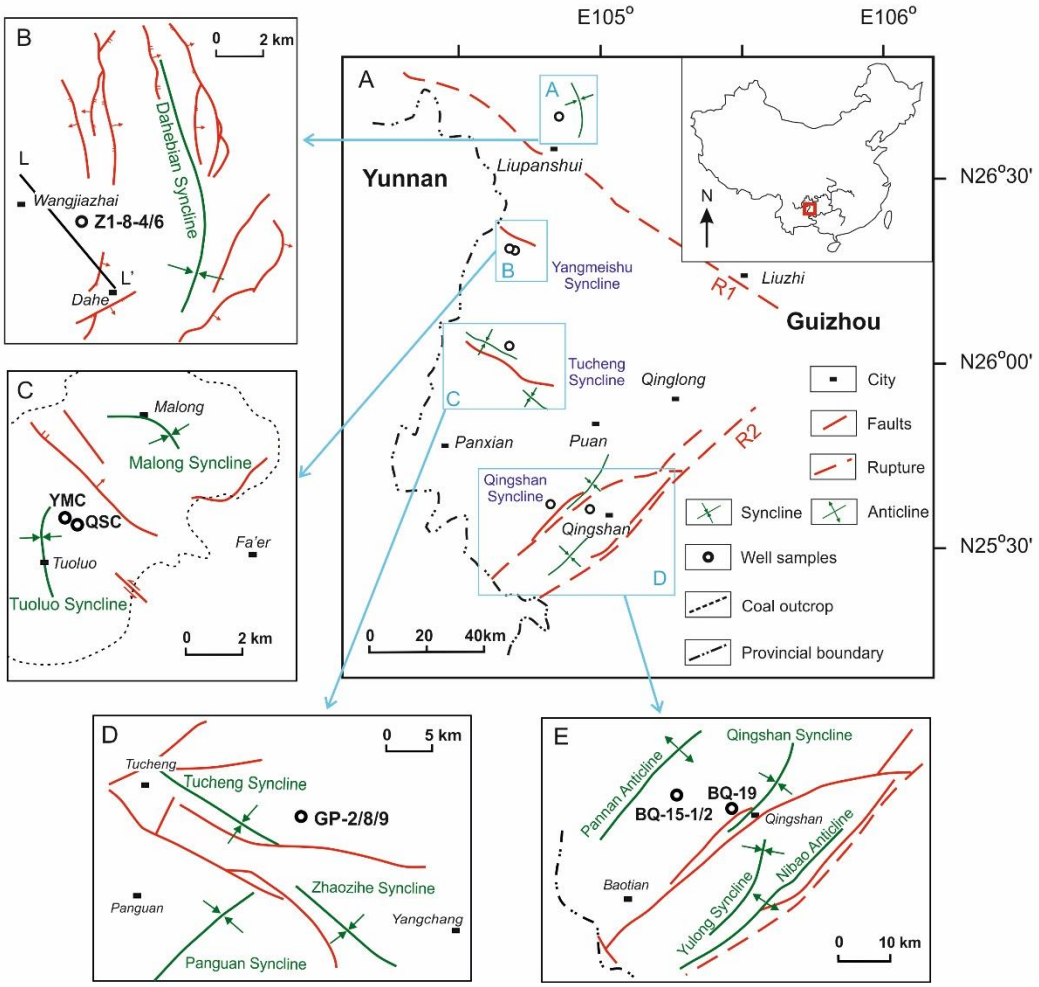

Figure 4.1. A. Location of Liupanshui Coalfield and sampling blocks; B. Dahebian block, after Bao (2019); C. Yangshumei block, after Zhou et al. (2019); D. Tucheng block, after Wu et al. (2016); E. Qingshan block, after Lei et al. (2012). R1, Shuicheng-Ziyun rupture belt; R2, Huangnihe-Panjiazhuang rupture belt, after Wu et al. (2018). LL' is a transect profile, shown in Figure 4.2.

The Liupanshui Coalfield is located on the passive southern margin of the upper Yangtze platform (Figure 4.1; Gui, 1999; Xu, 2012). The basin is dominated by a sedimentary succession from middle Silurian to Quaternary. Upper Silurian, lower Devonian, upper Jurassic and Cretaceous sediments are largely absent (Xu, 2012). The major mineable coal in the region is located in the Late Permian Longtan and Changxing formations (Figure 4.2). The Longtan Formation unconformably

overlies Late Permian Emeishan basalts (Ali et al., 2005; He et al., 2005). Following several cycles of marine transgression and regression during the Late Permian, several thick coal beds were deposited in a deltaic-lagoon sedimentary environment (Zheng, 2013). Approximately 3,500-5,000 m of marine sediments were deposited during the Early-Mid Triassic (Dou, 2012), followed by a regional regression and deposition of terrestrial sediments at the end of the Mid Triassic. Upper Triassic and lower-middle Jurassic mudstones and sandstones are present in the Shuicheng and Langdai area (northern LPC). Paleogene and Neogene lacustrine deposits are present around Panxian and Puan (Figure 4.1) (Zhang, 2017). Quaternary deposits are sparsely distributed in the coalfield.

Two regional rupture belts cut the LPC; the Shuicheng-Ziyun and Huangnihe-Panjiazhuang belts (Figure 4.1) (Zhang, 2017). They existed prior to the Triassic and have influenced the burial conditions of coals and induced the generation of minor faults within coal seams. The Shuicheng-Ziyun rupture belt in the north of LPC is approximately 250 km in length, 40 km in width, and is characterised by NW-trending folds and thrust faults (Dou, 2012). It is a deep-rooted rupture that may persist to the upper mantle (Zhang, 2017). It was formed at the end of Caledonian orogeny (Ordovician to Early Devonian) and re-activated during the Indosinian orogeny (Triassic to early Jurassic). The major thrust faults and folds were mainly developed in the main stage of Yanshanian orogeny (late Jurassic to early Cretaceous). The NE-trending Huangnihe-Panjiazhuang rupture belt in the south of LPC was formed before the Late Permian (Zhang, 2017). It developed synchronously with post-Emeishan sedimentation and affected the deposition of coal-bearing strata on both sides of the fault. Small-scale NW-trending faults widely formed in LPC during the Yanshanian orogeny (Jurassic to Cretaceous) under E-W compression (Zhang, 2017).

Lower Permian limestones in Maokou and Qixia formations and lower Triassic limestones in Yongningzhen Formation and dolomites in Guanling Formation have well-developed cave systems and act as the main aquifer layers within the LPC

(Bao, 2019; Zhang, 2017). The Emeishan basalt and Feixianguan mudstones are the main relative aquifuges. The coal-bearing strata have weak water accumulation and are sealed by the overlying Feixianguan mudstones and underlain Emeishan basalts, which limits water recharge and benefits gas preservation in coal seams (Xu, 2012; Zhang, 2017).

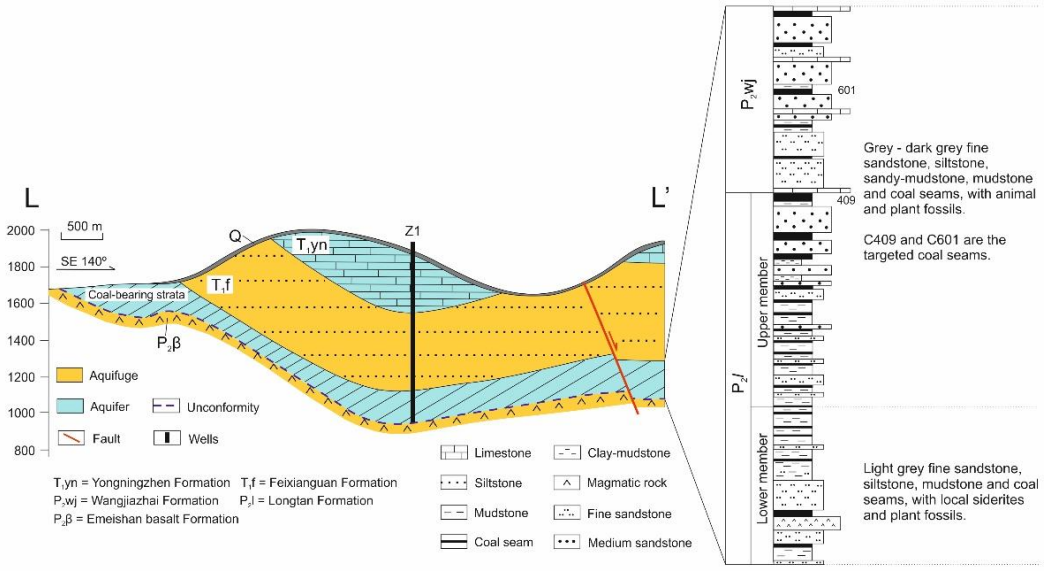

Figure 4.2. Transect profile of sediments in Dahebian block (LL', Figure 4.1B) of the Liupanshui coalfield and stratigraphic column of main coal-bearing strata, after Bao (2019). Wangjiazhai Formation from the Late Permian in Dahebian block is corresponding to Changxing Formation in the text.

The Dahebian syncline block (DA) occupies an area of about 130 km^2 (Figure 4.1B; Bao, 2019). The main coal-bearing strata are the Longtan and Changxing formations which are 206-241 m thick. There are approximately 40 coal seams with a total thickness of 35 m. The minable coal seams (16-20 layers) have a total thickness of 17-21 m. The main syncline is N-S trending. The coals tend to crop out in the western part of the block. The maturity of the coal (vitrinite reflectance, R_o) ranges from 0.7 to 0.9% in the Dahebian area and approximately 1.2% in the Wangjiazhai area (Figure 4.1B) (Bao, 2019).

The Yangmeishu syncline block (YA) has an area of about 350 km^2 (Figure 4.1C; Shan et al., 2018). The main coal-bearing strata are present in the Longtan Formation. They dip at 0-45° near the surface and 0-16° at depth (Du and Wu, 2019). The coal-bearing strata are at 344-487 m depth. There are 47-78 coal seams with a total thickness of 45 m, with a total mineable thickness of about 17.7 m. The major folds in the region are mainly NW-NNW trending short-axis synclines. Faulting is typically tensile normal type. The coals have R_o range of 1.5-2.0% (Shan et al., 2018).

The Tucheng block (TU) is an N-W trending syncline in north Panxian county (Figure 4.1D; Wu et al., 2016). The strata dip at 20-35°. Tensional normal faults are well developed in this area with a high dip of 45-80°. The main coal-bearing strata are the Longtan Formation with an average thickness of 341 m. There are approximately 50 coal layers with a total thickness of 41 m. The average mineable thickness is 11.7 m. The R_o in the coals is about 0.9-1.3% (Gui, 1999; Liu et al., 2020).

The Qingshan syncline block (QI) occupies about 1,009 km^2 in Pan county and Puan county (Figure 4.1E; Lei et al., 2012; Wen et al., 2008). NE-SW trending Qinshan syncline and Xiaganhe faults traverse the whole block. The strata in this block trend NW and SW with 3-25° dip. The main coals are in the Longtan Formation. There are 16-33 coal layers, and the total mineable thickness is up to 21.3 m. The R_o value of the coals is the highest in the region, 1.7-3.0%, with an average value of 2.1% in anthracite (Lei et al., 2012; Wen et al., 2008).

4.4 The generation of methane in Liupanshui Coalfield

Vitrinite reflectance values (R_o) of the LPC coals range from 0.8 to 3.4% (Gui, 1999), reflecting the different maximum burial depth of coals (~3000 to 5500 m) in different blocks (Dou, 2012). The burial history and thermal evolution of the LPC coal seams are poorly constrained. The temperature history is based on models

constrained by coal mineralogy and geothermal gradients constrained by practical exploration information and coal R_o values (Dou, 2012; Tang et al., 2016; Tao et al., 2010).

The thermal history models of Dou (2012) indicate that before the Late Jurassic, the LPC coals experienced two stages of burial. The first occurred in the Upper and Middle Triassic, resulting in the first stage of coal maturation. It was followed by the basin inversion in the Late Triassic. Deposition restarted in the Early Jurassic, finally exceeding the initial burial depth reached in the Middle Triassic, inducing further coal maturation. Methane was likely generated throughout the coalification process. The model of Tang et al. (2016) and Tao et al. (2010), however, does not require Late Triassic basin inversion. Thus there is considerable uncertainty in the history of methane formation.

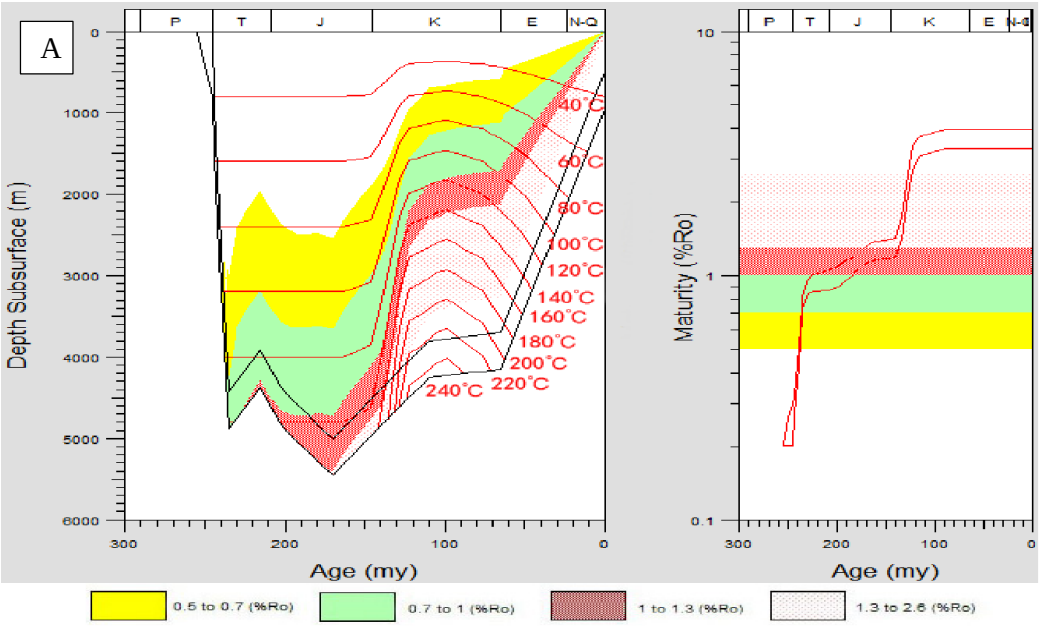

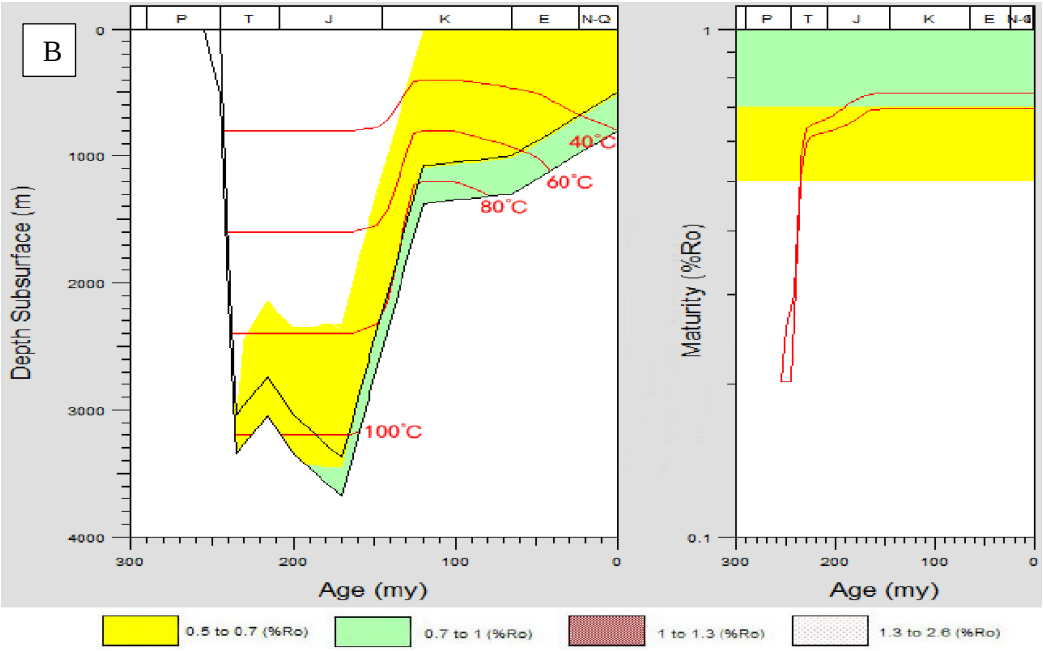

Figure 4.3. Burial history of the Permian coals in A) the eastern Qingshan syncline block and B) the southern Dahenbian syncline block of the Liupanshui coalfield. Taken from (Dou, 2012).

Magmatic activity during the Yanshanian orogenic event is argued to have enhanced the coalification process in some parts of the LPC (Dou, 2012). A 115 Ma dolerite sill is present within the lower Carbonaceous strata in the Pannan anticline (Chen, 1995; Zhang, 2017). The highest homogenization temperature (135-150°C) of fluid inclusions in vein quartz from Panxian coals cannot be reached by the maximum burial (~ 3500 m) with a normal thermal gradient (Tang et al., 2016). The presence of shallow hydrothermal fluid implies the presence of local magmatism which would have led to further coal maturation at shallow levels (Tang et al., 2016).

The Qingshan block experienced two cycles of burial-inversion and three main peaks of methane generation (Figure 4.3A; Dou, 2012). The burial in the Early and Middle Triassic to 5,000 m led to the reservoir temperature reaching ~140°C (R_o=0.8-1.0%) and the first peak of methane generation. It was followed by the removal of 500 m in the Late Triassic then burial in Early-Middle Jurassic to reservoir temperature of over 160°C (R_o=1.2-1.4%). This induced further methane

generation. Since the Late Jurassic, the basin has experienced uplift and erosion. In the Early Cretaceous, a thermal pulse heated the coal-bearing strata to about 240°C, maturing the coal seams to semi-anthracite grade (R_o >2%). Basin inversion resulted in the erosion of 3,200 m during the Cenozoic bringing the coal seams to depths of less than 1000 m.

The Dahenbian block has experienced two peaks of methane generation (Figure 4.3B; Dou, 2012). The tectonic history before the Late Jurassic is similar to Qingshan block except for a lower burial depth and less inversion. The R_o of coal after the second stage of methane generation reached only ~0.7%. The Late Jurassic thermal pulse coincided with the main phase of basin inversion (~2,300 m). Since then 500-600 m of basin inversion has occurred, and the coal seams have not experienced further coalification.

The Tucheng block has experienced a history similar to the Qingshan block (Wu et al., 2016). Three methane generation stages are predicted for this block. The coals experienced lower maximum burial depth at the end of mid-Jurassic (< 4 km) and a reduced thermal effect during Yanshanian orogeny where the maximum reservoir temperature attained 140°C, leading into R_o = 1.0-1.3%. Two basin inversions happened in the middle stage of Yanshanian orogeny and Cenozoic, the latter being dominant.

The thermal history of the Yangmeishu block is currently unknown. Based on the R_o values of the coals in this block, I assume the maximum burial depth of the coal seam and influence from the heating event are between TU and QI blocks.

4.5 Sampling and analytical procedures

Ten CBM samples were collected in April 2018 from the four blocks identified in Figure 4.1; Dahebian (2), Yangmeishu (2), Tucheng (3) and Qingshan (3). All gases are from oblique wells which extract methane from three or more coal seams. The coal seams exploited in each block are different. Although the sampling sites are in

close proximity, within each block, the oblique-well technology makes the distance of subsurface coal seams between any two wells more than 200 m. Well depths range from 740 to 1200 m (Table 4.1). The time between initial drilling and gas sampling in these wells varies from 1 to 37 months (Table 4.1).

Gas samples were collected from the same two wells in the Dahebian block in October 2018, approximately 7 months after gas extraction started. In order to differentiate the two batches of samples collected from this block, the initial samples have suffix -1 and the gases collected later are -2.

A detailed explanation of sampling processes and analysis methods are reported in Appendix I. Samples were collected and stored in Cu tubes at 1.5-2 bar using the method described in Györe et al. (2015). Approximately 50% of the gas in each tube was used for the determination of the major gas composition and stable isotopes.

Major gas composition was determined in nine samples using a Hewlett Packard 5890 gas chromatograph in SUERC. The uncertainty (1σ) of gas abundance is ±0.3%. The methane carbon isotopic composition ($\delta^{13}C_{CH4}$) was determined using a VG SIRA II dual inlet isotope ratio mass spectrometer (Dunbar et al., 2016) using established procedures in Györe et al. (2018). $\delta^{13}C_{CH4}$ values were determined relative to PDB (Craig, 1957). The hydrogen isotope composition of the methane (δD_{CH4}) was analysed using a VG Optima dual inlet isotope ratio mass spectrometer (Donnelly et al., 2001). δD_{CH4} values were determined relative to V-SMOW (Gonfiantini, 1978). Experimental uncertainties at 1σ level of $\delta^{13}C_{CH4}$ and δD_{CH4} values are ±0.3‰ and ±3‰, respectively.

The remaining gas was used for the analysis of noble gas isotopes using a MAP 215-50 mass spectrometer following the procedures described in Györe et al. (2015). Blank levels for all isotopes are negligible compared with the signal of samples, so no correction is applied. The mass spectrometer sensitivity and mass fractionation factors were determined using the HESJ standard for He (Matsuda et al., 2002), and air (Eberhardt et al., 1965; Lee et al., 2006; Mark et al., 2011; Ozima

and Podosek, 2002) for Ne, Ar, Kr and Xe. The reproducibility of the absolute concentrations is <4% in all cases, and isotopic ratios are less than 1%.

4.6 Results

4.6.1 Major gas and stable isotopic compositions

The major gas compositions are CH_4 (90.3-98.3%), N_2 (1-5.1%), C_2H_6 (0.1-4.5%), C_3H_8 (0.2-1.1%) and trace CO_2 (0.1-0.3%) (Table 4.1). The DA gases have the lowest methane (90.3-92.9%) and CO_2 contents (≤0.1%) and the highest wet gas (C_{2+}, >2%) concentrations. The QI and YA gases have higher methane (>96%) and CO_2 contents and lower wet gas concentrations. CH_4/CO_2 ratios varied from 80 to 950, and $CH_4/(C_2H_6 + C_3H_8)$ (C_1/C_{2+}) ratios also have a wide range of 16-971. After 6 months of gas extraction in the DA field, the content of CH_4 and CO_2 increases, while the content of wet gases and nitrogen declines. Consequently, there is a small increase in C_1/C_{2+} ratio (2-4) but a decrease in CH_4/CO_2 ratio (>75) (Table 4.1).

Across the region, the carbon and hydrogen isotopic compositions of the methane range from -34.9 to -42.9‰ and -140 to -206‰, respectively (Table 4.1). The stable isotopic composition of the QI and YA gases (δC_{CH4} = -34.9 to 36.6‰ and δD_{CH4}= -140 to -158‰) are evidently heavier than that of the DA and TU gases (δC_{CH4} = -39.9 to 42.9‰ and δD_{CH4}= -160 to -206‰). There is a slight depletion of the stable isotopic composition in the DA gases with time (~1.5‰ for δC_{CH4} and ~16‰ for δD_{CH4}).

Table 4.1. Major gas and stable isotope composition of coalbed methane from Liupanshui coalfield, Southern China.

Sample ID	Block	Vitrinite reflectance (R_o /%) [a]	Depth (m)	Gas extraction duration (month)	CH_4	C_2H_6	C_3H_8	CO_2	N_2	C_1/C_{2+}	CH_4/CO_2	$\delta^{13}C$	δD
BQ-19	Qingshan block (QI)	1.7-3.0	899	6	97.1	0.1	-	0.5	2.3	971	194	-35.8	-148
BQ-15-D1			1000	11	98.3	0.1	-	0.5	1.0	983	192	-35.8	-141
BQ-15-D2			874	11	96.0	0.5	-	1.2	2.3	192	80	-36.6	-140
1-4-8X-1	Dahebian block (DA)*	0.7-1.2	1200	1	90.3	3.7	0.9	-	5.1	20	>1000	-41.6	-176
1-4-8X-2				7	92.9	3.6	0.7	0.1	2.7	22	929	-42.9	-192
1-6-8X-1			1150	1	90.6	4.5	1.1	-	3.8	16	>1000	-41.1	-185
1-6-8X-2				7	92.5	3.7	0.9	0.1	2.7	20	925	-42.7	-206
YMC	Yangmeishu block (YA)	1.5-2.0	740	14	97.7	1.1	-	0.2	1.1	89	489	-34.9	-158
QSC			840		96.5	1.1	-	0.6	1.8	88	161	-35.9	-147
GP-9	Tucheng block (TU)	0.9-1.3	1033	34	95.0	2.2	0.3	0.1	2.4	38	950	-39.9	-164
GP-8			1062	37	95.1	2.4	0.3	0.3	1.9	35	317	-40.1	-160
GP-2			953	51	95.9	2.2	0.2	0.2	1.5	40	480	-41.4	-172

1σ standard deviations for major gas abundance, C_1/C_{2+}, CH_4/CO_2, $\delta^{13}C$ and δD are 0.3%, 2%, 2%, 0.3‰ and 3‰, respectively.

δC_{CH4} and δD_{CH4} are in permil and relative to PDB (Craig, 1957) and V-SMOW (Gonfiantini, 1978), respectively.

* Samples collected in April 2018 have suffix -1, and those collected in October 2018 -2.

- below the detection limit.

[a] R_o values are from other studies; QI block (Lei et al., 2012; Wen et al., 2008), DA block (Bao, 2019), YA block (Shan et al., 2018) and TU block (Liu et al., 2020).

Table 4.2. Noble gas compositions of well gases from Liupanshui coalfield, Southern China.

Sample ID	^{4}He ($\times10^{-6}$)	^{20}Ne ($\times10^{-8}$)	^{40}Ar ($\times10^{-5}$)	^{84}Kr ($\times10^{-10}$)	^{132}Xe ($\times10^{-11}$)	$^{3}He/^{4}He$ (R_A)	$^{20}Ne/^{22}Ne$	$^{21}Ne/^{22}Ne$	$^{40}Ar/^{36}Ar$	$^{38}Ar/^{36}Ar$
BQ-19	47 (2)	1.30 (5)	2.89 (10)	7.3 (3)	2.6 (1)	0.018 (1)	9.71 (5)	0.0313 (5)	530 (3)	0.187 (1)
BQ-15-D1	41 (1)	1.61 (6)	1.44 (5)	3.2 (1)	1.5 (1)	0.026 (2)	9.71 (5)	0.0308 (5)	598 (7)	0.187 (1)
BQ-15-D2	68 (2)	1.78 (7)	3.82 (14)	7.8 (3)	1.8 (1)	0.022 (2)	9.69 (5)	0.0312 (4)	497 (3)	0.185 (1)
1-4-8X-1	1048 (34)	4.32 (16)	4.09 (15)	18.8 (8)	9.2 (5)	0.006 (1)	9.75 (5)	0.0394 (6)	529 (2)	0.189 (1)
1-4-8X-2	325 (11)	1.03 (4)	2.83 (10)	13.5 (4)	7.7 (2)	0.008 (1)	9.68 (3)	0.0435 (5)	652 (4)	0.188 (1)
1-6-8X-1	1136 (37)	4.34 (16)	3.63 (13)	15.6 (6)	8.0 (4)	0.007 (1)	9.76 (5)	0.0406 (7)	568 (4)	0.188 (1)
1-6-8X-2	216 (7)	0.80 (3)	1.80 (7)	8.1 (2)	5.3 (1)	0.006 (1)	9.80 (3)	0.0419 (9)	637 (4)	0.188 (1)
YMC	67 (2)	0.68 (3)	0.58 (2)	1.7 (1)	1.3 (1)	0.006 (1)	9.77 (5)	0.0339 (7)	454 (3)	0.188 (1)
QSC	133 (4)	0.42 (2)	0.39 (1)	2.5 (1)	1.6 (1)	0.007 (1)	9.84 (5)	0.0436 (8)	647 (6)	0.187 (1)
GP-9	401 (13)	1.66 (6)	1.42 (5)	5.1 (2)	3.0 (1)	0.008 (1)	9.79 (5)	0.0383 (6)	593 (5)	0.187 (1)
GP-8	266 (9)	1.62 (6)	1.39 (5)	6.3 (3)	2.3 (1)	0.009 (1)	9.76 (5)	0.0359 (5)	500 (4)	0.187 (1)
GP-2	289 (9)	1.34 (5)	1.27 (5)	5.7 (2)	2.8 (1)	0.014 (1)	9.73 (5)	0.0381 (5)	548 (4)	0.187 (1)
Air	5.24 (5)	1645 (4)	934 (1)	6498 (57)	2339 (27)	1.000 (9)	9.80 (8)	0.0290 (3)	298.6 (3)	0.1885 (3)

1σ standard deviation is shown as the last significant figures in parentheses.

Noble gas concentrations are in unit of cm^3 STP/cm^3 with standard conditions after (Ozima and Podosek, 2002) (p =0.101 MPa, T = 0 °C).

Air composition is after Eberhardt et al. (1965);Györe et al. (2019); Lee et al. (2006); Mark et al. (2011); Ozima and Podosek (2002).

R_A is the atmospheric $^{3}He/^{4}He$ ratio of 1.34×10^{-6} (Mishima et al., 2018).

4.6.2 Noble gases

The concentration and isotopic composition of noble gases are listed in Table 4.2. ^{4}He concentrations range from 41 to 1,136 ppmv while $^{3}He/^{4}He$ ratios vary from 0.006 to 0.026 R_A, where R_A is the atmospheric ratio of 1.34×10^{-6} (Mishima et al., 2018). The variation in $^{3}He/^{4}He$ ratios shows no clear correlation with ^{4}He abundance. ^{4}He concentrations and $^{3}He/^{4}He$ ratio of gases in each block are relatively uniform. Helium concentrations generally decrease as the maturity of coal increases. For example, the QI gases from the most mature coals have the lowest ^{4}He concentration (41-68 ppmv). The ^{4}He concentration of the gases from the two DA wells does not appear to change significantly over the 6 months between sampling.

^{20}Ne concentrations range from 0.004 to 0.043 ppmv. $^{20}Ne/^{22}Ne$ and $^{21}Ne/^{22}Ne$ ratios vary from 9.68 ± 0.03 to 9.84 ± 0.05 and from 0.0308 ± 0.0005 to 0.0436 ± 0.0008, respectively. Although $^{20}Ne/^{22}Ne$ ratios overlap the air value (9.80 ± 0.08), $^{21}Ne/^{22}Ne$ ratios are distinctly higher than the air value of 0.0290 ± 0.0003 (Eberhardt et al., 1965). Both the concentration and isotopic composition of neon from the DA-2 gases is different from the DA-1 values. ^{20}Ne concentrations drop from ~0.04 to ~0.01 ppmv, while $^{21}Ne/^{22}Ne$ values increase by up to 10%.

^{40}Ar concentrations range from 4 to 41 ppmv. $^{40}Ar/^{36}Ar$ ratios range from 454 ± 3 to 652 ± 4, significantly higher than air value (298.5, Lee et al. (2006); Mark et al. (2011)), showing no trend with ^{40}Ar or ^{36}Ar concentrations. $^{38}Ar/^{36}Ar$ ratios are indistinguishable from the air. ^{84}Kr and ^{132}Xe concentrations range from 1.7-18.8 $\times 10^{-4}$ ppmv and 1.3-9.2 $\times 10^{-5}$ ppmv, respectively. Similar to ^{4}He and ^{20}Ne, after half-year gas extraction, the concentrations of ^{40}Ar, ^{84}Kr and ^{132}Xe in the DA-2 gases decline slightly. $^{40}Ar/^{36}Ar$ ratio increases. Both are consistent with lower atmospheric noble gas content.

4.7 Discussion

4.7.1 The origin of methane

The relative abundances of the major gases and the stable isotope composition of methane in each block are broadly consistent (Table 4.1). This implies that the CBM in each block has a similar origin. The stable isotopic composition of methane (δC_{CH4} and δD_{CH4}) from all fields plots within the thermogenic field and provide no indication of a significant contribution of microbial methane (Figure 4.4). C_1/C_{2+} ratios in the TU, YA and DA gases (16-89) are also within the typical range of thermogenic methane from natural gas systems that are not associated with oil (<100, Golding et al. (2013)). The QI gases have elevated C_1/C_{2+} ratios (192-971), inconsistent with the conclusion.

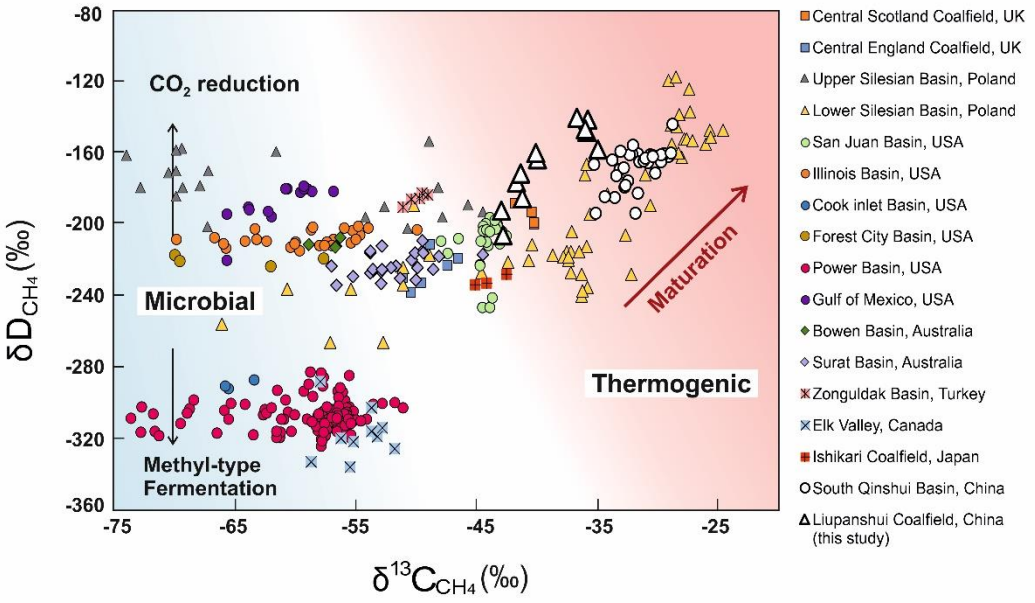

Figure 4.4. Compilation of the stable carbon and hydrogen isotope composition of coal bed methane. Field lines from Whiticar (1999). Data source: San Juan Basin, (Zhou et al., 2005); Powder Basin, (Flores et al., 2008); Central Scotland Coalfield and Central England Coalfield (Györe et al., 2018); Bowen Basin, (Kinnon et al., 2010); South Qinshui Basin, (Li et al., 2014; Zhang et al., 2018) and Chapter 3; Ishikari Coalfield, (Shimizu et al., 2007); Lower Silesian Basin, (Kotarba and Rice, 2001); Forest City Basin, (McIntosh et al., 2008); Illinois Basin, (Moore et al., 2018; Strąpoć et al., 2008); Elk Valley Coalfield, (Aravena et

al., 2003); Zonguldak Basin, (Hosgörmez, 2007); Cook Inlet, (Dawson et al., 2012); Upper Silesian Basin, (Kotarba, 2001); Surat Basin, (Baublys et al., 2015);Gulf of Mexico Basin, (McIntosh et al., 2010).

The addition of secondary microbial methane is frequently used to explain coeval variations in the C_1/C_{2+} ratio and stable isotope composition of coalbed methane (Scott et al., 1994; Tao et al., 2007). Microbial methane is enriched in $^{12}CH_4$ and C^1H_4 relative to thermogenic methane, which results in a lowering of $\delta^{13}C_{CH4}$ and δD_{CH4}. It typically has a higher C_1/C_{2+} ratio (Bernard et al., 1976), which means the addition of microbial methane tends to increase the ratio in CBM. The observed weak positive relationship between C_1/C_{2+} ratio, $\delta^{13}C_{CH4}$ and δD_{CH4} tend to rule this out as an explanation for the variation seen in the LPC gases (Figure 4.5b and c).

Preferential dissolution of $^{13}CH_4$ in groundwater has been used to explain the variation in CBM isotope compositions (Qin et al., 2006). However, experimental work that determines how $\delta^{13}C_{CH4}$ and δD_{CH4} change during methane dissolution into aqueous solutions demonstrates only a small depletion of $\delta^{13}C$ (< -0.5‰) coincides with significant enrichment of δD (<16‰) in the free methane phase (Bacsik et al., 2002). This is in the opposite sense and smaller than the observed changes in $\delta^{13}C_{CH4}$-δD_{CH4} space.

C_1/C_{2+} ratio, $\delta^{13}C_{CH4}$ and δD_{CH4} appear to increase coherently with coal maturity (R_o) (Figure 4.5a), implying that the variation of major gas components and stable isotopic values of methane across the LPC region has some relationship to the extent of coalification. Thermogenic methane released from coals becomes enriched in ^{13}C and D as coalification process progresses (Rice, 1993; Strąpoć et al., 2011). The thermal cracking of wet gas with coal rank over high volatile bituminous coals (R_o >1.2%) results in a reversal of the increasing of C_1/C_{2+} ratio (Faiz and Hendry, 2006; Rice, 1993). This may go some way to explaining the positive trend between C_1/C_{2+} ratio and coal maturity (R_o) and also the abnormally high C_1/C_{2+} ratio in QI gases (192-971). It is worth noting that the C and H isotopic

composition of methane in the QI gases overlap with that in YA gases, even though C_1/C_{2+} ratio and coal rank in QI block are evidently higher. This may reflect differences in source organic matter or the result of post-generation fractionation caused by adsorption/desorption.

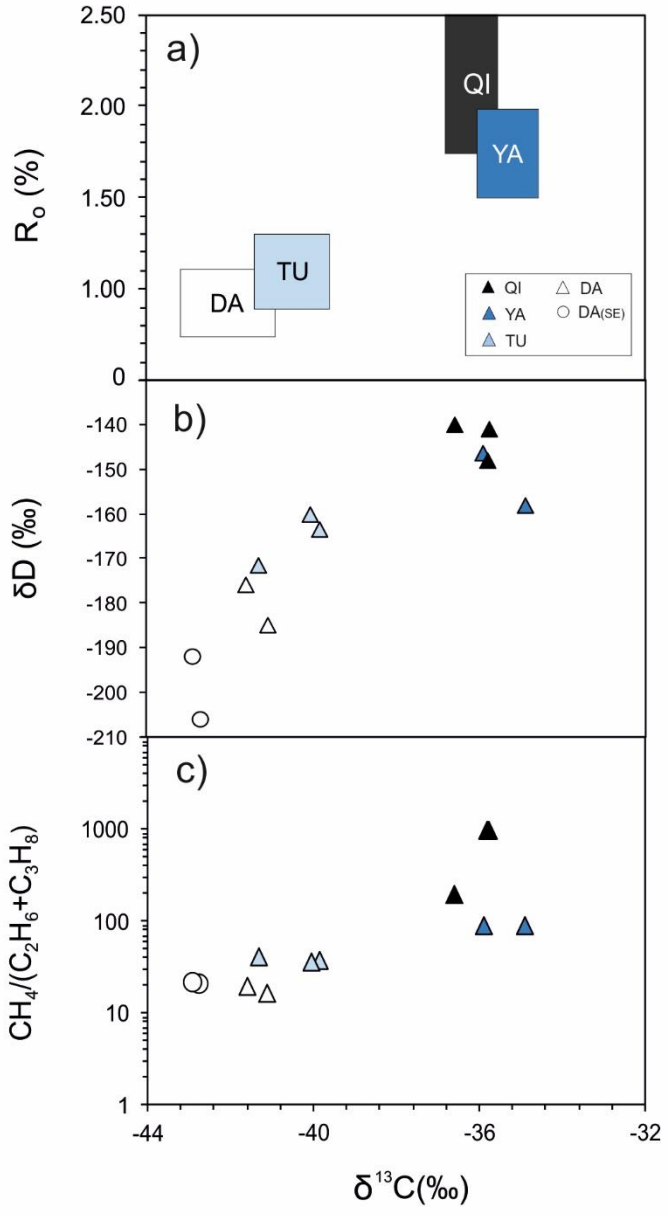

Figure 4.5. Carbon isotopes plotted against a) R_o; b) hydrogen isotopes; c) C_1/C_{2+} ratio. The colour of the legend displays the coal rank. The darkest colour represents the highest R_o. The stable isotopic composition and C_1/C_{2+} ratio indicate a thermogenic origin of methane without a discernible contribution of microbial methane. The positive relationships among the stable isotopic composition of methane, C_1/C_{2+} ratio and R_o of

coals in each block indicate that the thermal degradation process of organic matter is the main controlling factor on the stable isotopic composition of methane in the region. The depletion in the stable isotope composition of methane and the slight increase of C_1/C_{2+} ratio in the DA-2 gases might be due to the addition of desorbed methane from coals away from the wellbores (see the text).

The small increase in the proportion of the methane, and the modest depletion of $\delta^{13}C_{CH4}$ (~1.5‰) and δD_{CH4} (~16‰), in the DA gases over 6 months does not appear to require a radical reinterpretation of the source of the methane. However, it demonstrates that the major gas and isotopic compositions evolve with extraction time. The trend of the change contrasts with the experimental determination of an increase of $\delta^{13}C_{CH4}$ and the proportion of wet gas content with desorption time (Strąpoć et al., 2006). A temporary drop of $\delta^{13}C_{CH4}$ and δD_{CH4} but an increase of C_1/C_{2+} ratio at the early stage of production is explained by the readily desorption of light gases from coals (Niemann and Whiticar, 2017; Xia and Tang, 2012). With continuous gas extraction, $\delta^{13}C_{CH4}$ increases again and might exceed the initial value in the reservoir (Xia and Tang, 2012). The first sampling of DA well gases occurred after less than one month of gas extraction. Thus the gas production in these two wells was at an early stage when desorbed gas, enriched in methane with depleted $\delta^{13}C$, is likely the main source. The gases sampled in the initial phase span up to 37 months since gas extraction commenced, which may be the cause of the variation observed between the blocks. However, this possibility is low as no trend has been observed between gas extraction time and the major gas and isotopic compositions (Table 4.1). It again suggests that the variation of coal maturity is the main cause of variation of major gas and stable isotopic composition within the LPC.

The δC_{CH4} of the LPC well gases is lower than the southern Qinshui Basin (-35.2 to -28.7‰; Zhang et al. (2018); Li et al. (2014) and Chapter 3) but comparable with the northeast Qinshui Basin (-40.8 to -33.2‰; Xu et al. (2016)). They are higher than the eastern margin of Ordos Basin (δC_{CH4} = -60.0 to -33.5‰; Chen et al. (2015))

where a discernible contribution of secondary microbial methane has modified the stable isotopic composition of methane. δD_{CH4} data is only available from southern Qinshui Basin CBM. The δD_{CH4} of LPC (-206 to -140‰) is comparable with the southern Qinshui Basin (-194 to -144‰; Li et al. (2014); Zhang et al. (2018) and Chapter 3). The lower maturity of the LPC coals compared to the SQB coals likely explains the lower δC_{CH4}. Thermogenic methane is generated by thermal cracking of organic matter which then is the main source of the hydrogen of methane (Schimmelmann et al., 2006). The isotopically heavy H in the LPC methane may reflect the distinct composition of organic matter in two coalfields. The aqueous environment is critical for δD_{CH4} as the high-temperature exchange of hydrogen between methane and organic matter with formation water cannot be neglected (Schimmelmann et al., 2006). The hydrogen isotope composition of formation water in LPC is -50 to -25‰ (Wu et al., 2018). This is markedly heavier than the equivalent waters from the southern Qinshui basin (-82 to -38‰, mainly < -70‰) (Wei and Ju, 2015; Zhang et al., 2018). Thus, the exchange with isotopically heavier hydrogen from the formation water might also influence the LPC methane δD composition.

4.7.2 The origin of the light noble gases

4.7.2.1 Helium isotopes

The low $^3He/^4He$ ratios (0.006 to 0.026 R_A) of the LPC gases are consistent with a dominantly radiogenic origin for the He. The QI gases have $^3He/^4He$ (0.018 to 0.026 R_A) that are systematically higher than recorded by the gases from the other fields (0.006 to 0.014 R_A). The high $^4He/^{20}Ne$ ratios (2,554-31,784) exclude a discernible contribution of air-derived He. A plot of $^4He/^{20}Ne$ against $^3He/^4He$ (Figure 4.6) supports the contention that the variation of $^3He/^4He$ ratios is unrelated to the addition of air. Radiogenic production of ^4He occurs by U and Th decay (Morrison and Pine, 1955). The production of ^3He in crustal rocks is dominantly nucleogenic,

from the reaction $^{6}Li(n,\alpha)^{3}H(\beta^{-})^{3}He$ (Morrison and Pine, 1955). Nucleogenic production of ^{3}He, and therefore the $^{3}He/^{4}He$, is largely dependent on the concentration of Li in the source rock and the abundance of large neutron cross-section elements (B, Be, Nd, Gd, etc.). Using the range of Li (9-105 ppm, n=46) and the average concentration of the large neutron cross-section elements in the Liupanshui coals (Li, 2015; Zhuang et al., 2000), the production ratio of $^{3}He/^{4}He$ ranges from 0.008 to 0.093 R_A. This range covers the majority of the values measured in the Liupanshui CBM gases. The extremely low $^{3}He/^{4}He$ ratios in DA and YA gases (0.006-0.008 R_A) might be attributed to local variation in the concentration of Li and the large neutron cross-section elements. Alternatively, as the neutrons for nucleogenic He production are derived from particles generated by U and Th decay, heterogeneity in radioelement concentrations may have led to low $^{3}He/^{4}He$ production ratios (Martel et al., 1990).

The $^{3}He/^{4}He$ ratios of the QI gases (0.018 to 0.026 R_A) are slightly higher than the other blocks, but they are within the range produced by the Liupanshui coals and crustal radiogenic He (0.007 to 0.022 R_A; Ballentine and Burnard (2002)). There is no obvious lithological reason why the QI gases should have systematically higher $^{3}He/^{4}He$ than the other coalfields. The possibility that the QI gases contain a small contribution of mantle He cannot be ignored, not least because the thermal history of the block requires external heating from magmatic activity during Yanshanian orogeny (Dou, 2012). If the lowest measured ratio (0.006 R_A) represents the reservoir gas value, and magmatic gas has $^{3}He/^{4}He$ = 6.1 R_A (sub-continental lithospheric mantle, Gautheron and Moreira (2002)), the addition of 0.4 % mantle He is enough to explain the He isotope composition of the QI gases.

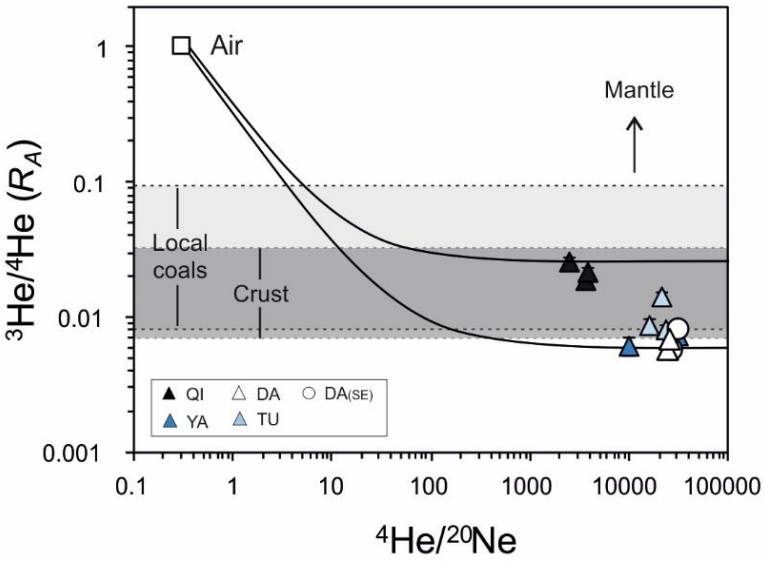

Figure 4.6. $^{3}He/^{4}He$ ratios plotted against $^{4}He/^{20}Ne$ ratios for the LPC gases. The solid black lines are mixing lines between air and the highest and lowest values defined by the data. They fall within the range defined by average crust and are predicted to have been generated in the LPC coals (0.008-0.093 R_A) based on the local range of Li concentration and average large neutron cross-section elements.

4.7.2.2 Neon and argon isotopes

The Ne isotope composition of the LPC gases (Figure 4.7A) requires a significant contribution of nucleogenic Ne in addition to air. The YA, DA and TU gas data fall in a triangle defined by air, average crust ($^{20}Ne/^{22}Ne = 0$, $^{21}Ne/^{22}Ne = 0.47$, Kennedy et al. (1990)) and one or more component with higher $^{20}Ne/^{22}Ne$ for given $^{21}Ne/^{22}Ne$. One source of the high $^{20}Ne/^{22}Ne$ gas is mantle-derived Ne ($^{20}Ne/^{22}Ne = 12.5$, $^{21}Ne/^{22}Ne = 0.06$ Ballentine et al. (2005)). In this case, the sample with the highest $^{20}Ne/^{22}Ne$ (QSC, 9.84 ± 0.05) would be a mixed gas that contains 17% mantle-derived Ne. This is inconsistent with the complete absence of mantle He in the LPC gases. The QI gases, which have slightly elevated $^{3}He/^{4}He$ and thus most likely contain mantle Ne, have the least discernible mantle-derived Ne (Figure 4.7A).

It appears that the Ne isotope data are more likely explained by the presence of crust-derived Ne that has higher $^{20}Ne/^{22}Ne$ than the average crustal value Kennedy

et al. (1990)). Neon isotopes are mainly produced in the crust by alpha-particle reactions on O (^{17,18}O (α, n) ^{20,21}Ne) and F (^{19}F (α, n) ^{22}Na (β^+) ^{22}Ne) (Wetherill, 1954). Consequently, variation in the ^{20}Ne/^{22}Ne and ^{21}Ne/^{22}Ne ratios of crustal gases is strongly dependent on the O/F ratio in the proximity (< 40 μm) of U and Th-derived α particles (Kennedy et al., 1990). Assuming an oxygen concentration of 10% based on the concentration of major oxides Li (2015) and the average F concentration of 42 ppm Li (2015)), the O/F ratio in LPC coals is ~2,400. This is three times higher than the average crustal value (752) (Kennedy et al., 1990) and would result in ^{20}Ne/^{22}Ne and ^{21}Ne/^{22}Ne production ratios of 1.1 and 11.4, respectively. This yields a mixing line with air that is more horizontal than the trend with average crust (Figure 4.7A), and undoubtedly a better fit to the data.

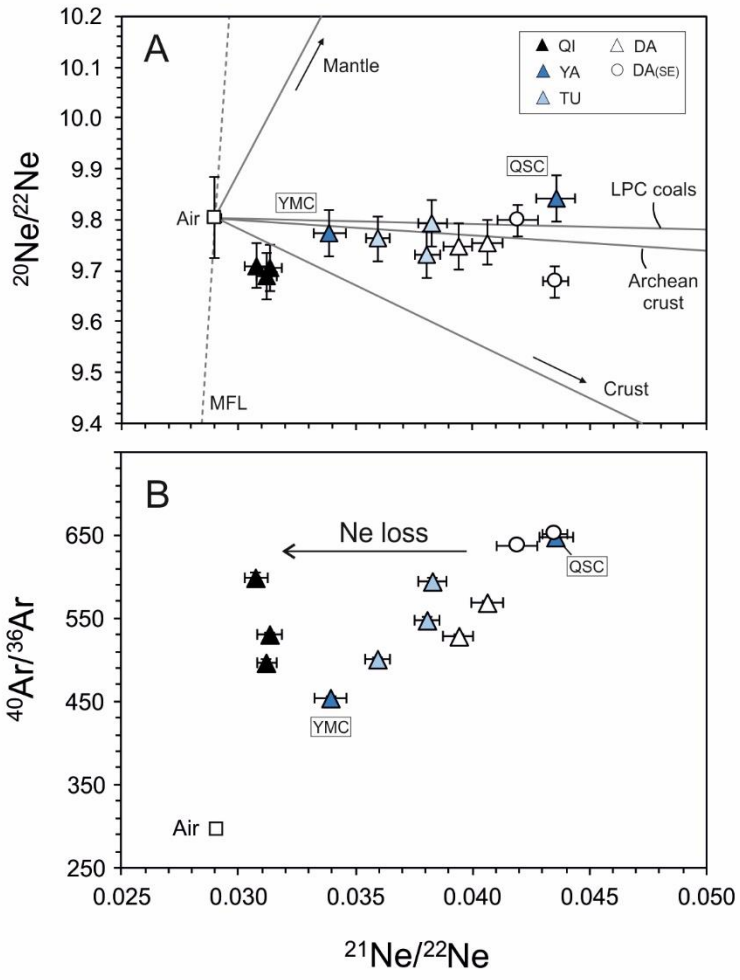

Figure 4.7. (A) ^{20}Ne/^{22}Ne vs ^{21}Ne/^{22}Ne for LPC CBM. The black square represents the air (^{20}Ne/^{22}Ne = 9.80, ^{21}Ne/^{22}Ne = 0.029). MFL (grey dotted line) is the mass fractionated line

(Kaneoka, 1980). The solid grey lines are air-mantle and air-Phanerozoic crust mixing lines ($^{20}Ne/^{22}Ne_{mantle}$ = 12.5, $^{21}Ne/^{22}Ne_{mantle}$ = 0.06, $^{20}Ne/^{22}Ne_{crust}$ = 0, $^{21}Ne/^{22}Ne_{crust}$ = 0.47; (Ballentine et al., 2005; Kennedy et al., 1990)). Mixing lines between air and average local coal ($^{20}Ne/^{22}Ne$ = 1.1, $^{21}Ne/^{22}Ne$ = 11.4), Archaean crust ($^{20}Ne/^{22}Ne$ = 0, $^{21}Ne/^{22}Ne$ = 3.3 ± 0.2; Lippmann-Pipke et al. (2011)) are also shown by grey solid lines. (B) $^{20}Ne/^{22}Ne$ vs. $^{40}Ar/^{36}Ar$ for LPC CBM.

There is increasing evidence that Archaean crust has generated Ne with a $^{20}Ne/^{22}Ne$ and $^{21}Ne/^{22}Ne$ that are higher than Phanerozoic crust because of the low fluorine abundance (Holland et al., 2013; Lippmann-Pipke et al., 2011). The LPC is located in the western part of the Yangtze block. Although the basement in the region is dominantly Proterozoic, it is likely that the region is underlain by Archean metamorphic rocks (Wang et al., 2012; Zheng et al., 2006). In addition to the diffusion of a crustal flux of Ne, the extensive network of deep faults (Zhang, 2017) may act as a conduit for the transport of deep crustal gases.

The QI gases plot slightly below the air-crust mixing line in Figure 4.7A. The long-term production of nucleogenic Ne from a crustal reservoir that is extremely O-depleted or F-enriched is unlikely and has not previously been observed. A more likely explanation is that the Ne isotope composition of the QI gases has been affected by mass fractionation, which has been observed elsewhere (e.g. (Kaneoka, 1980; Zhou et al., 2005; Zhou et al., 2012)).

As with Ne isotopes, the $^{21}Ne/^{22}Ne$-$^{40}Ar/^{36}Ar$ compositions of the YA, DA and TU gases fall on a broad linear trend that is consistent with mixing between air and one or more crustal gases that have variable concentrations of nucleogenic ^{21}Ne and ^{22}Ne, and radiogenic ^{40}Ar (Figure 4.7B). The ratio of nucleogenic ^{21}Ne ($^{21}Ne^{*}$) to radiogenic ^{40}Ar ($^{40}Ar^{*}$) in these gases is in the range of 1.1-3.0×10^{-6}. This range is higher than the crustal average production ratio of about 0.3×10^{-6} (Ballentine and Burnard, 2002), and may reflect the greater mobility of Ne than Ar in the shallow crust. These issues are discussed in more detail in section 4.7.4.

The QI gases define a mixing relationship between air and deep gas with distinctly lower $^{21}Ne/^{22}Ne$ yet similar $^{40}Ar/^{36}Ar$. The $^{21}Ne^{*}/^{40}Ar^{*}$ of the QI gases ($0.3\text{-}0.5\times10^{-6}$) is considerably lower than that of YA, DA and TU gases, albeit comparable with the average crustal value. This difference can be explained if the QI block gases have experienced a preferential loss of light noble gases. The diffusive loss of noble gases will, for instance, decrease the $^{21}Ne^{*}/^{40}Ar^{*}$ of the residual methane. In order to explain the lower $^{21}Ne/^{22}Ne$ but rather constant $^{40}Ar/^{36}Ar$ (Figure 4.7B), the Ne loss must have occurred before the addition of air-derived noble gases. As I will show in the following section, it is likely that the air-derived gases are ultimately from groundwater. The diffusive loss of Ne from high concentration gas reservoirs can result in isotopic fractionation (Bourg and Sposito, 2008; Marty, 1984). In this case, it will leave isotopically heavy Ne in the reservoir, consistent with Ne isotope composition of the QI gases which have lower $^{21}Ne/^{22}Ne$ than air (Figure 4.7A).

The DA-2 gases lie on the same mixing lines as the DA-1 samples in Figure 4.7, albeit having higher $^{40}Ar/^{36}Ar$ and $^{21}Ne/^{22}Ne$. This is consistent with a slightly lower proportion of air-derived Ne and Ar than the DA-1 gases. The DA-1 gases were collected within the first month of gas production. The air-derived noble gases may originate from drilling fluids and have declined with the continuous gas production.

4.7.3 Non-radiogenic noble gases

The concentrations of ^{20}Ne, ^{36}Ar, ^{84}Kr and ^{132}Xe in natural gases are mainly derived from air, typically entering the reservoir dissolved in the recharge groundwater (Ballentine et al., 2002). In addition, contributions were trapped within the organic sediments. Enrichments of Xe and Kr are widely observed in sediments and natural gas systems (e.g., (Barry et al., 2016; Podosek et al., 1980; Torgersen and Kennedy, 1999; Zhang et al., 2019b; Zhou et al., 2005)), and are consistently explained by the preferential sorption onto organic source rock (Torgersen and Kennedy, 1999).

In coal-derived gases, they are likely from within the coal matrix (Zhou et al., 2005), and subsequently released into groundwater or a free gas phase during the biodegradation or gas expulsion. The addition of mantle volatiles could also supply the non-radiogenic noble gases. For instance, the mantle-derived ^{20}Ne in CBM from Central Scotland coalfield accounts for up to 20% of the total ^{20}Ne (Györe et al., 2018).

It is assumed that the recharge waters are air-saturated. This has well-established noble gas concentrations and elemental ratios. Typically they are calculated following Henry's law corrected from an assumed recharge temperature at a known air pressure, determined based on elevation, and often includes a modest excess due to direct dissolution of air (Kipfer et al., 2002). Air-saturated water (ASW) in the LPC region has $^{20}Ne/^{36}Ar = 0.16$, $^{84}Kr/^{36}Ar = 0.039$, $^{132}Xe/^{36}Ar = 0.0026$ (Appendix II). The LPC CBM yields $^{20}Ne/^{36}Ar$ (0.23-0.70) that are significantly higher than the local ASW, while $^{84}Kr/^{36}Ar$ (0.010-0.025) and $^{132}Xe/^{36}Ar$ (0.0002-0.0012) in all samples except QSC ($^{84}Kr/^{36}Ar = 0.041$, $^{132}Xe/^{36}Ar = 0.0027$) are below the ASW values (Figure 4.8; Table 4.3). Most samples have $^{20}Ne/^{36}Ar$ that is higher than the air value (0.53), and $^{84}Kr/^{36}Ar$ and $^{132}Xe/^{36}Ar$ that are lower than the air values (0.021 and 0.0007, respectively). Thus the relative enrichment of Ne and depletion of Kr and Xe cannot be explained by simple mixing with air-derived noble gases (Figure 4.8).

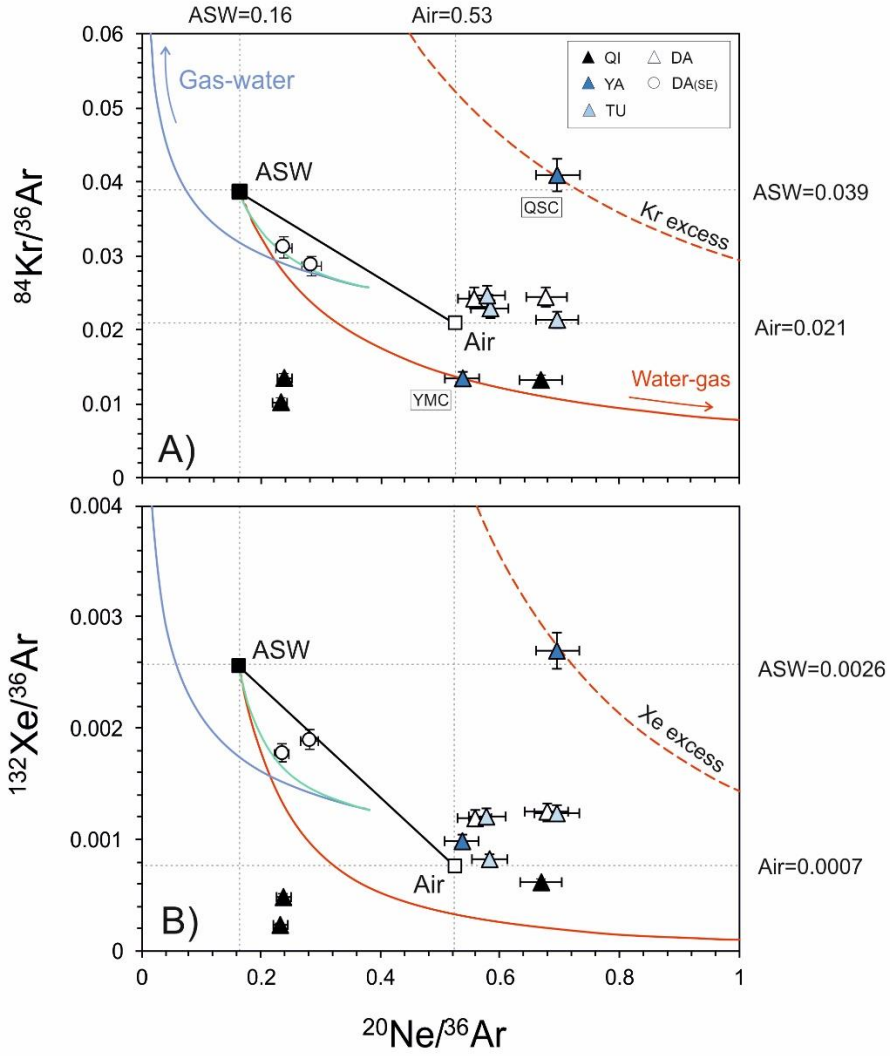

Figure 4.8. The plot of $^{20}Ne/^{36}Ar$ against A) $^{84}Kr/^{36}Ar$ and B) $^{132}Xe/^{36}Ar$ in the LPC well gases. The solid black lines reflect the mixing of ASW and modern air. The green and blue lines represent a closed system (batch) fractionation of gas exsolving from groundwater for different water/gas volume ratios in the reservoir. The blue lines represent the open system fractionation (Rayleigh) of noble gases from the water phase to the gas phase with initial ASW composition. The red lines represent the composition of gas from the second stage of a re-dissolution model (see text for details). The red dashed lines represent the composition of gas generated during re-dissolution where the starting composition includes an excess of ^{84}Kr and ^{132}Xe compared to ^{36}Ar. The arrows indicate the changing trend with continuous fractionation. Re-dissolution of exsolved gases can explain the high $^{20}Ne/^{36}Ar$ ratio in LPC gases. However, the samples (except two QI samples) are above the predicted line, indicating that enrichment of ^{84}Kr and ^{132}Xe is required. The two QI gases indicate the strong adsorption capacity of local coals to the heavy noble gases and results in the low $^{84}Kr/^{36}Ar$ and $^{132}Xe/^{36}Ar$ than the predicted values.

Table 4.3. Elemental ratio of air-derived noble gases

Sample ID	$^{20}Ne/^{36}Ar$	$^{84}Kr/^{36}Ar$	$^{123}Xe/^{36}Ar$
BQ-19	0.24 (1)	0.013 (1)	0.00048 (3)
BQ-15-D1	0.67 (4)	0.013 (1)	0.00061 (4)
BQ-15-D2	0.23 (1)	0.010 (1)	0.00024 (1)
1-4-8X-1	0.56 (3)	0.024 (1)	0.0012 (1)
1-4-8X-2	0.24 (1)	0.031 (1)	0.0018 (1)
1-6-8X-1	0.68 (4)	0.024 (1)	0.0012 (1)
1-6-8X-2	0.28 (2)	0.029 (1)	0.0019 (1)
YMC	0.54 (3)	0.014 (1)	0.0010 (1)
QSC	0.70 (4)	0.041 (2)	0.0027 (2)
GP-9	0.70 (4)	0.021 (1)	0.0012 (1)
GP-8	0.58 (3)	0.023 (1)	0.0008 (1)
GP-2	0.58 (3)	0.025 (1)	0.0012 (1)

1σ standard deviation is shown as the last significant figures in parentheses.

Elemental fractionation occurs in response to solubility-related partitioning between different reservoir fluids (e.g., (Ballentine et al., 2002; Ballentine et al., 1991; Battani et al., 2000; Gilfillan et al., 2008)). As no oil is present in this system, partitioning is likely only between free gas and water. The solubility-controlled fractionation factor in LPC reservoir can be calculated from Henry's constants of noble gas and corrected from liquid-phase activity coefficients and gas-phase fugacity coefficients (Ballentine et al., 2002; Crovetto et al., 1982; Smith and Kennedy, 1983) in groundwater at 44°C and 9.5 MPa, and salinity of 0.15 mol/L (Wu et al., 2018). The detailed calculation is shown in Appendix II. Considering that the solubility of noble gases in water increases with mass, the higher $^{20}Ne/^{36}Ar$ and lower $^{84}Kr/^{36}Ar$ and $^{132}Xe/^{36}Ar$ in LPC CBM might be due to partitioning into a degassed free gas phase from the water phase. The maximum $^{20}Ne/^{36}Ar$ ratio in the gas phase, caused by closed-system (batch) or open-system (Rayleigh) fractionation (Figure 4.8), can be calculated from the following equation:

$$\left(\frac{A}{B}\right)_{gm} = \left(\frac{A}{B}\right)_{o} \alpha \tag{4.1}$$

where $\left(\frac{A}{B}\right)_{gm}$ is the maximum elemental ratio in the gas phase, $\left(\frac{A}{B}\right)_{o}$ is the initial elemental ratio in the water phase, α the fractionation factor given for gas/water

system. This equation assumes that the relative volume of gas to water is infinitely low, i.e. V_g /V_w tends to zero (Ballentine et al., 2002). From the initial ASW $^{20}Ne/^{36}Ar$ of 0.16, the maximum fractionated $^{20}Ne/^{36}Ar$ that the gas phase can obtain is 0.38. This cannot explain the measured $^{20}Ne/^{36}Ar$ of the DA, TU and YA gases (0.56-0.70) (Figure 4.8). An increase in the amount of air-derived noble gases dissolved in recharge groundwater might raise the maximum initial $^{20}Ne/^{36}Ar$ (Battani et al., 2000; Davis and Squires, 1954; Kipfer et al., 2002; Zhou et al., 2012). The maximum air excess observed in groundwater is ~35% on Ar (Battani et al., 2000; Heaton and Vogel, 1981), corresponding to an excess Ne of ~65% assuming complete dissolution of trapped air bubbles without further fractionation (Kipfer et al., 2002). It is much higher than the assumption of 10% excess air on Ne used in this study to calculate the initial ASW $^{20}Ne/^{36}Ar$. This Ne excess would mean the starting $^{20}Ne/^{36}Ar$ = 0.28, and lead to an upper limit of $^{20}Ne/^{36}Ar$ of 0.66 from Rayleigh fractionation. This overlaps the highest $^{20}Ne/^{36}Ar$ ratio (0.70 ± 0.04) in the LPC gases. However, such a high amount of air excess is an extreme case. Heaton and Vogel (1981) suggested that the semi-arid climate in the study site might favour the existence of excess air in groundwater. The humid monsoon climate in LPC is the opposite. Thus, the likelihood that the excess air in groundwater is the reason for high $^{20}Ne/^{36}Ar$ ratios in LPC gases is low, and I discuss the other possibilities below.

Enrichments of ^{20}Ne ($^{20}Ne/^{36}Ar$ =0.21-2.94) and depletions of ^{84}Kr (^{84}Kr /^{36}Ar =0.010-0.041) have been observed in CBM from the Illinois Basin (Moore et al., 2018). They have been explained by a dual-phase (free gas + brine) migration of exogenous super-saturated hydrocarbon gas-rich brines from the underlying source rocks, during which the elevated $^{20}Ne/^{36}Ar$ ratio develops in the free gas phase based on solubility (Darrah et al., 2015; Darrah et al., 2014; Moore et al., 2018). In the Illinois Basin, thermogenic gas generated in underlying shales appears to have stripped the noble gases from the water that migrated into the coals. He and Ne were further enriched in the gas phase during the migration due to the preferential

dissolution of ^{36}Ar and ^{84}Kr back into the surrounding water, resulting in the positive trend among $^{20}Ne/^{36}Ar$, $^{4}He/CH_4$, $\delta^{13}C$ and C_1/C_{2+} ratio observed in thermogenic CBM (Moore et al., 2018). The extreme condition is that hydrocarbon gas strips out of all air-derived noble gases from the water in the shales. The subsequent dissolution of the more soluble noble gases during the migration can be modelled by a gas phase with ASW composition dissolving into a water phase initially containing no noble gases following open system Rayleigh fractionation (Gilfillan et al., 2008; Moore et al., 2018):

$$(\frac{A}{B})_g = (\frac{A}{B})_o f^{(\alpha'-1)} \quad (4.2)$$

where $(\frac{A}{B})_g$ is the current elemental ratio in the gas phase, $(\frac{A}{B})_o$ is the initial elemental ratio in the gas phase, f is the proportion of residue B in the gas, and α' is the fractionation factor from gas to water. This mechanism might have operated in the LPC. The shales underlying the late Permian coals in the LPC could supply the hydrocarbon-rich fluids (Zhang, 2017). The two-phase solubility migration (gas-water) is depicted in Figure 4.8. It could cover the high $^{20}Ne/^{36}Ar$ ratio in LPC gases. However, no systematic trend exists between $^{20}Ne/^{36}Ar$ and methane C and H isotopes composition, nor C_1/C_{2+} ratio (Table 4.1 & 4.2). In addition, the variable $^{4}He/^{36}Ar$ is inconsistent with the narrow range of $^{20}Ne/^{36}Ar$ in TU, YA and DA gases (Figure 4.9), indicating that ^{4}He-^{20}Ne-^{36}Ar system does not follow the solubility-controlled fractionation considering the close solubility of He and Ne in formation water of LPC coals (Appendix II). The loss of light noble gas (He and Ne) before the addition of air-derived noble gases would not have affected the mixing trends in ^{4}He-^{20}Ne-^{36}Ar space. Thus there is no evidence to support an externally-sourced hydrocarbon-charged brine in the LPC.

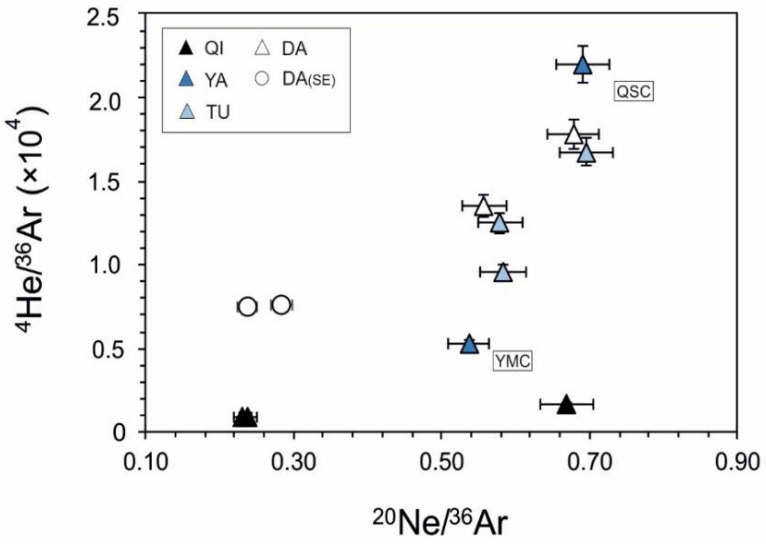

Figure 4.9. $^{20}Ne/^{36}Ar$ vs. $^{4}He/^{36}Ar$ in LPC CBM. No systematic trend exists between $^{20}Ne/^{36}Ar$ and $^{4}He/^{36}Ar$.

An enrichment of ^{20}Ne caused by the re-dissolution of gases exsolved from groundwater is also commonly observed in CO_2 systems (Gilfillan et al., 2008; Zhou et al., 2012). In these cases, injection of mantle CO_2 into a reservoir has been proposed to generate gas bubbles that strip the dissolved ASW-derived noble gas from the water. The noble gases re-equilibrate and re-dissolve into the water phase once CO_2 filling ceases. This re-dissolution process is similar to that discussed above, and follows the Rayleigh fractionation law (Eq 4.2) if the water continuously migrates relatively to the gas phase. The low CO_2 content in LPC rules out a recent injection of magmatic CO_2. However, effervescence and then re-dissolution of CBM could have occurred in response to the continuous or episodic drop in reservoir pressure and temperature during basin uplift events since the Late Jurassic (Dou, 2012). Over 170 Myr the coals in the DA block have, for instance, likely uplifted from 3,800 m to 1,000 m depth. Assuming that the reservoir pressure was equal to the hydrostatic pressure and the average methane proportion remained at 92% during basin inversion, the methane solubility in the formation water decreased from 0.0016 to 0.006 cm^3/cm^3 at reservoir conditions (Ballentine et al., 2002; Tishchenko et al., 2005). Consequently, the formation water will have

become over-saturated with respect to the dissolved methane, resulting in the generation of methane bubbles which would have stripped the dissolved noble gases from the water. Methane bubble generation will cease with the cessation of basin inversion and the gas-phase noble gases can re-dissolved into the groundwater. The effect on noble gas abundances would be similar to the two-phase solubility migration depicted by the model lines in Figure 4.8. In this case, no positive relationship between $^{20}Ne/^{36}Ar$ with $\delta^{13}C$ and C_1/C_{2+} ratio is expected because this process does not cause further coalification nor involve an external source of hydrocarbons.

While re-dissolution may be the most likely explanation for the high $^{20}Ne/^{36}Ar$ of LPC gases, this cannot explain why $^{4}He/^{36}Ar$ and $^{20}Ne/^{36}Ar$ do not follow a solubility-controlled fractionation (Figure 4.9). It indicates that 1) the process that causes the enrichment of ^{4}He and ^{20}Ne is different; or 2) some process has happened after the re-dissolution that has caused the further fractionation of He/Ne. In the latter case, the possibility that preferential loss of light noble gases suggested based on Ne-Ar isotopes causes the uncoupled $^{4}He/^{36}Ar$ and $^{20}Ne/^{36}Ar$ could be ruled out as the main gas loss is supposed to have happened before the addition of air-derived noble gases. The evident decrease of both $^{4}He/^{36}Ar$ and $^{20}Ne/^{36}Ar$ ratios in DA-2 gases compared to the DA-1 gases may go some way to identifying the source of the variation in elemental ratios. The change in $^{4}He/^{36}Ar$ and $^{20}Ne/^{36}Ar$ ratios in DA-2 gases are similar, which indicates that the elemental fractionation during gas extraction may be solubility-controlled. Thus, it cannot explain the variable $^{4}He/^{36}Ar$ but consistent $^{20}Ne/^{36}Ar$ in most samples, which suggests the different enrichment mechanism of radiogenic ^{4}He and ASW-derived ^{20}Ne in LPC.

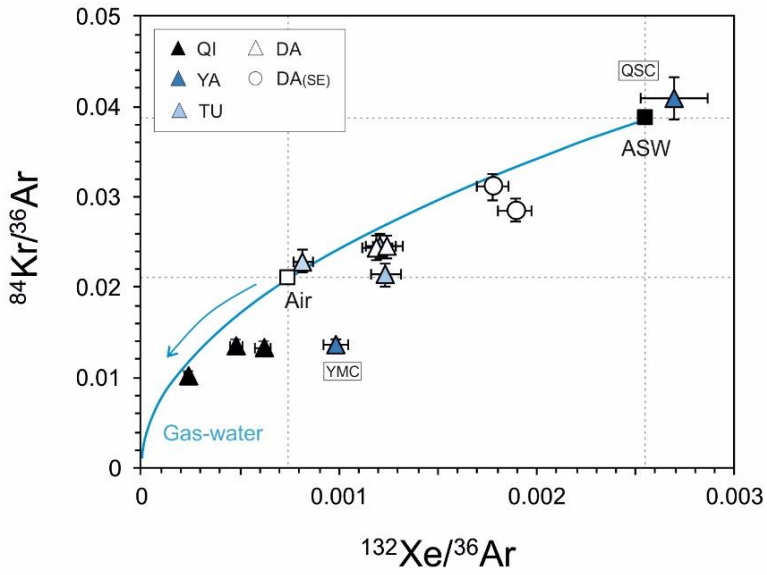

Figure 4.10. The plot of $^{84}Kr/^{36}Ar$ against $^{132}Xe/^{36}Ar$ in the LPC well gases. Samples are mostly lower than the fractionation line, indicating the excess of ^{132}Xe compared with ^{84}Kr

In ^{20}Ne-^{36}Ar-^{84}Kr space, only gas from the YMC well plots on fractionation line expected if the formation water starts with an ASW noble gas composition (Figure 4.8A). With the exception of the two QI gases, all samples plot above the water-gas fractionation lines in ^{20}Ne-^{36}Ar-^{84}Kr and ^{20}Ne-^{36}Ar-^{132}Xe space (Figure 4.8). Variable $^{84}Kr/^{36}Ar$ and $^{132}Xe/^{36}Ar$ ratios with the narrow range of $^{20}Ne/^{36}Ar$ suggest that $^{84}Kr/^{36}Ar$ and $^{132}Xe/^{36}Ar$ are not only controlled by the re-dissolution fractionation process. An excess of ^{84}Kr of up to 280%, and a 1300% excess of ^{132}Xe, over the modelled values are required to explain the range of $^{84}Kr/^{36}Ar$ and $^{132}Xe/^{36}Ar$ ratios. Most samples plot below the ASW fractionation line in ^{36}Ar-^{84}Kr-^{132}Xe space, except for one TU and QSC gases (Figure 4.10), indicating that the majority of the gases appear to contain excess ^{132}Xe relative to ^{84}Kr. A 200% excess of Xe relative to Kr is required to explain the $^{132}Xe/^{36}Ar$ values. Xe and Kr excesses are frequently recorded by CBM (McKavney, 2019; Zhou et al., 2005). The relative enrichment pattern (Xe > Kr > Ar) is consistent with the decreasing atomic radius, and is consistent with expected adsorption on organic matter or trapped in the coal matrix (Torgersen et al., 2004). They are desorbed from the coals due to the de-pressure during the gas extraction process.

The two QI gases (BQ-19 and BQ-15-D2) plot below the model lines in Figure 4.8. The three QI gases have strongly varying $^{20}Ne/^{36}Ar$. The three QI wells have similar pump durations which excludes the possibility that variable $^{20}Ne/^{36}Ar$ reflects the gas extraction history. Additionally, if the ASW-derived ^{20}Ne enrichment process occurred after gas loss, the low $^{20}Ne/^{36}Ar$ ratio in the two QI gases could not be explained by the Ne/Ar fractionation during the gas loss. The low $^{84}Kr/^{36}Ar$ and $^{132}Xe/^{36}Ar$ of the two QI block gases may reflect stronger adsorption onto local coals (Figure 4.8). This phenomenon has been observed in Southeast Qinshui Basin (section 3.8.4). This suggests a relatively low permeable coefficient for reservoir fluids and implies weak groundwater flow in the coal beds. This is consistent with the low fractionation extent during the re-dissolution process and thus the low $^{20}Ne/^{36}Ar$ in the two QI block gases. The high $^{20}Ne/^{36}Ar$ in the third QI block gas may be a result of relatively strong groundwater flow, corresponding to a higher permeability and thus effective desorption and transportation of heavy noble gases during gas extraction.

4.7.4 Accumulation of radiogenic noble gases

Without discernible addition of mantle-derived noble gases, the nucleogenic $^{21}Ne^*$ and radiogenic $^{40}Ar^*$ originates in the crust. The amount of crustal $^{21}Ne^*$ and $^{40}Ar^*$ are calculated by subtraction of air-derived component normalised to the non-radiogenic isotopes (^{20}Ne, ^{36}Ar):

$$[^{21}Ne^*] = [^{20}Ne]_m \times \{(^{21}Ne/^{20}Ne)_m - (^{21}Ne/^{20}Ne)_{air}\} \quad (4.3)$$

$$[^{40}Ar^*] = [^{36}Ar]_m \times \{(^{40}Ar/^{36}Ar)_m - (^{40}Ar/^{36}Ar)_{air}\} \quad (4.4)$$

where the subscripts m and air refer to the measured concentrations and the isotopic composition of air.

Table 4.4. Radiogenic and nucleogenic noble gas composition.

Sample ID	$^{21}Ne^{*}$ ($\times10^{-12}$)	$^{40}Ar^{*}$ ($\times10^{-6}$)	$^{4}He/^{40}Ar^{*}$	$^{21}Ne^{*}/^{40}Ar^{*}$ ($\times10^{-6}$)	$^{4}He/^{21}Ne^{*}$ ($\times10^{7}$)
BQ-19	3.5 (7)	12.6 (5)	3.7 (2)	0.27 (6)	1.4 (3)
BQ-15-D1	3.3 (9)	7.2 (3)	5.7 (3)	0.46 (12)	1.2 (3)
BQ-15-D2	4.6 (9)	15.2 (6)	4.5 (2)	0.30 (6)	1.5 (3)
1-4-8X-1	47 (3)	17.8 (7)	58 (3)	2.6 (2)	2.2 (2)
1-4-8X-2	16 (1)	15.3 (6)	21 (1)	1.0 (1)	2.1 (1)
1-6-8X-1	52 (4)	17.3 (6)	66 (3)	3.0 (2)	2.2 (2)
1-6-8X-2	11 (1)	9.6 (4)	23 (1)	1.1 (1)	2.0 (2)
YMC	3.5 (5)	2.0 (1)	34 (2)	1.8 (3)	1.9 (3)
QSC	6.1 (4)	2.1 (1)	63 (3)	2.9 (2)	2.2 (2)
GP-9	16 (1)	7.1 (3)	57 (3)	2.2 (2)	2.5 (2)
GP-8	12 (1)	5.6 (2)	48 (2)	2.1 (2)	2.3 (2)
GP-2	13 (1)	5.8 (2)	50 (2)	2.2 (2)	2.3 (2)

1σ standard deviation is shown as the last significant figures in parentheses.

Noble gas concentrations are in unit of cm^3 STP/cm^3 with standard conditions after (Ozima and Podosek, 2002) (p =0.101 MPa, T = 0 °C).

$^{21}Ne^{*}$ and $^{40}Ar^{*}$ concentrations in the LPC gases range from 3.3-52×10^{-12} and 2.0-18×10^{-6} cm^3 STP/cm^3 respectively (Table 4.4; Figure 4.11). Like ^{4}He, the $^{21}Ne^{*}$ and $^{40}Ar^{*}$ concentrations in the DA-2 gases are lower than in DA-1 gases. This might be caused by the non-static solubility-controlled partition of noble gases from water into the gas phase, and/or the dilution by progressive desorption of sorbed gases, like methane, from coals during the gas extraction (Zhou et al., 2005). The limited data restrict making firm conclusions. However, that the concentration of radiogenic and nucleogenic noble gases vary with time and gas extraction weakens the reliability to identify the source by comparing the observed concentrations with the calculated *in situ* generation rate based on the abundance of parent material (U, Th, K, etc.) in coals.

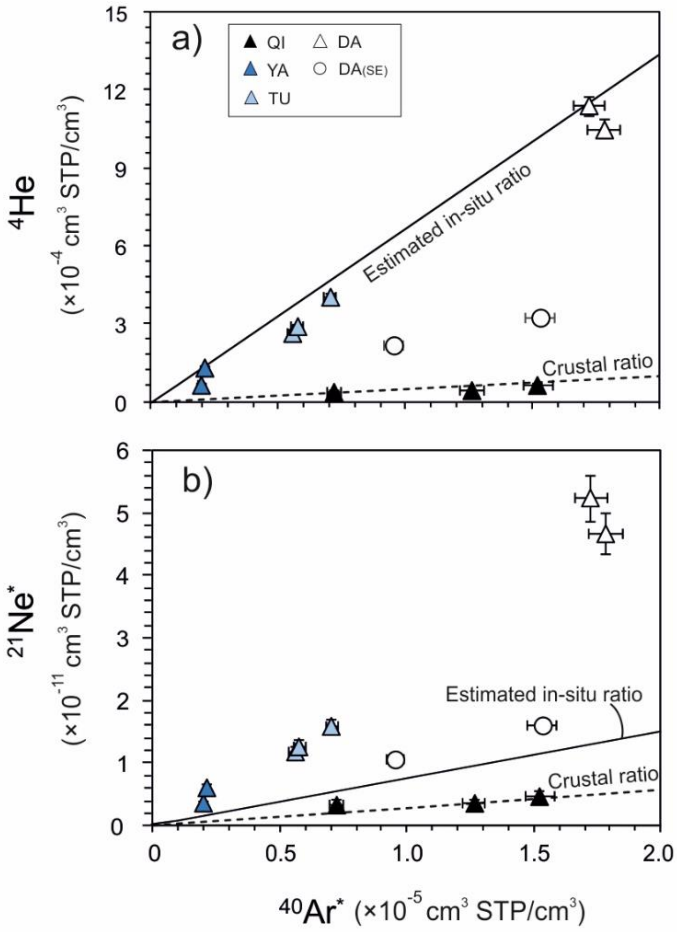

Figure 4.11. Radiogenic and nucleogenic noble gas isotope abundances in LPC gases. Solid lines indicate the calculated production ratios based on the chemical composition of the local rocks. Dash lines indicate the average crustal ratios.

As the light noble gases (He, Ne and Ar) are less prone to sorption, the elemental ratios are a better tracer of the physical processes that have acted upon the gases. $^4He/^{40}Ar^*$ and $^{21}Ne^*/^{40}Ar^*$ ratios span wide ranges, 4-66 and 0.27-3.0×10^{-6}, respectively (Table 4.4). Taking the average U (5.2 ppm), Th (4.6 ppm), K (0.3%), Mg (0.1%) and O (10%) concentration values in local coals (Li, 2015), the *in situ* production ratios of $^4He/^{40}Ar^*$ and $^{21}Ne^*/^{40}Ar^*$ are 67 and 7.5×10^{-7}, respectively. The $^4He/^{40}Ar^*$ ratios of the TU, DA and YA gases are comparable and slightly lower to the predicted *in situ* ratio but significantly higher than the average crustal value (~5, Ballentine and Burnard (2002)). The $^{21}Ne^*/^{40}Ar^*$ ratios are above the predicted value and also the average crustal value (~2.9×10^{-7}, Ballentine and Burnard (2002))

(Figure 4.11). The $^{4}He/^{40}Ar^{*}$ and $^{21}Ne^{*}/^{40}Ar^{*}$ ratios in QI gases, in contrast, are both lower than the *in situ* generation rate, albeit comparable with the average crustal values. The lower $^{4}He/^{40}Ar^{*}$ and $^{21}Ne^{*}/^{40}Ar^{*}$ ratios and constant $^{4}He/^{21}Ne^{*}$ ratio in DA-2 gases over the half-year gas pumping supports a non-static solubility-controlled fractionation as discussed before. This fractionation process might have influenced the composition of other gases. However, the high and constant air-derived $^{20}Ne/^{36}Ar$ ratios in DA, TU, YA and one QI gases rule out this possibility.

The elevated $^{21}Ne^{*}/^{40}Ar^{*}$ in most LPC coals relative to *in situ* production ratio likely reflects the addition of external $^{21}Ne^{*}$. However, $^{4}He/^{40}Ar^{*}$ ratios are not supportive of excess ^{4}He, despite the mobility of He in the shallow crust (Jähne et al., 1987; Marty, 1984). The decoupling of $^{4}He/^{40}Ar^{*}$ with $^{21}Ne^{*}/^{40}Ar^{*}$ indicates a regional gas loss during which He preferentially escapes from the coals. QI gases have much lower $^{4}He/^{40}Ar^{*}$ and $^{21}Ne^{*}/^{40}Ar^{*}$ than other blocks, which suggests the larger extent of He and Ne loss in this block, consistent with the previous conclusion from Ne-Ar isotopes (section 4.7.2.2). The gas loss might be inferred to the Cenozoic basin exhumation suggested in Dou (2012). $^{4}He/^{40}Ar^{*}$ and $^{21}Ne^{*}/^{40}Ar^{*}$ show a linear relationship and decrease coherently with the increasing maturity of coals (except QSC; Figure 4.12). The QI block has experienced the most intensive basin inversion (Dou, 2012). Thus it is reasonable to expect that the gases have lost most He. Han et al. (2010a) has proved the weak sorption of Ar in high mature coals. The adsorption capacity of coals generally increases with maturity (Moore, 2012). High-maturity coals theoretically have stronger adsorption capacity and may retain more Ar than lower rank coals. It results in similar $^{40}Ar^{*}$ concentration in QI gases compared with other gases but variable ^{4}He and consequently the lowest $^{4}He/^{40}Ar^{*}$ ratio in QI gases. Assuming the $^{4}He/^{40}Ar^{*}$ in DA gases as the initial ratio, more than 96% of the ^{4}He has lost from QI gases compared with Ar. More details about the gas loss mechanism are presented in Chapter 5.

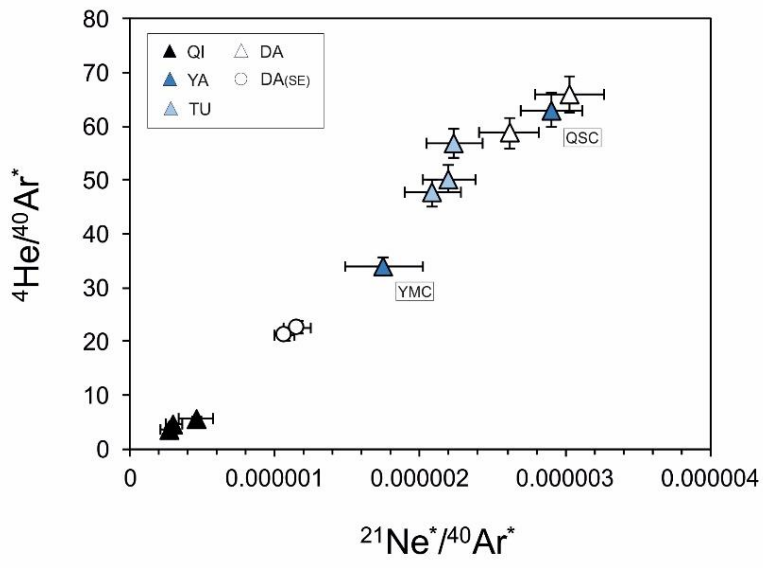

Figure 4.12. $^{4}He/^{40}Ar^{*}$ vs. $^{21}Ne^{*}/^{40}Ar^{*}$ in CBM gases from LPC. These two ratios show a linear trend and decease with the increasing maturity of the coals (except QSC).

4.8 Conclusion

The Liupanshui coalfield is a promising target for commercial CBM production in southern China. This is the first gas geochemical study of the LPC gases. The major gas, stable isotope and noble gas isotope composition of the LPC CBM has produced several important conclusions:

- The major gas and stable isotope of methane in LPC indicate a thermogenic origin without a significant contribution of microbial methane. The compositional variability between four blocks is mainly controlled by the thermal degradation of organic matter in each block.
- Noble gases reveal a mixture of air-derived gases from groundwater (ASW) with *in situ* generated gases in the reservoir, and likely the external crustal ^{4}He, $^{21}Ne^{*}$ and $^{40}Ar^{*}$. The enrichment of light Ne isotopes relative to the general air-crust mixing line implies the likely source of external Ne from Archean crust or *in situ* Ne from local (F-poor) coals.

- The lower proportion of crustal Ne but comparable $^{40}Ar/^{36}Ar$ in QI gases suggests a gas loss event during which Ne is preferentially lost compared with Ar, and subsequent addition of air-derived noble gases (e.g. ^{20}Ne, ^{36}Ar).
- A re-dissolution fractionation process is required to explain the extremely high $^{20}Ne/^{36}Ar$ ratio in the gas phase. The excess of heavy noble gases to the fractionation model is observed in most gases from LPC and explained by the desorption of initial trapped Xe and Kr in the coal matrix. Local high mature coals in QI block show strong adsorption capacity to Xe and Kr, resulting in the lower $^{84}Kr/^{36}Ar$ and $^{132}Xe/^{36}Ar$ than the modelled values in produced CBM.
- The gas loss is also supported by the various $^{4}He/^{40}Ar^{*}$ and $^{21}Ne^{*}/^{40}Ar^{*}$ in LPC CBM, which has happened during basin inversion (after the late Jurassic). In high mature coals, a mass fractionation has also observed. The extent of gas diffusion is positively correlated with the maturity of coals, which could reach 96% He discrepancy compared to Ar. It implies the increasing storage capacity of coals with maturity to more sorbed gas. The block which has experienced the most intensive Cenozoic basin exhumation has lost the most free gas (He and Ne). The link between He-Ne-Ar system and basin history demonstrates the potential of using light noble gas content in natural gases to track gas evolution caused by recent basin activities.

Chapter 5 Helium loss from coalbed methane deposits during basin inversion

5.1 Overview

In Chapters 3 and 4, I have identified, for the first time, the loss of a significant proportion of the accumulated He from coal bed methane reserves in the Southeast Qinshui Basin and the Liupanshui Coalfield. This has been inferred, in particular for the Southeast Qinshui Basin, to be a consequence of rapid and intensive basin inversion during the Cenozoic, and implies that the light noble gas composition of CBM can be used to trace the tectonic history of sedimentary basins. In this chapter, I review the extent that the light noble gas content of previously studied coal deposits supports this hypothesis. This is followed by a detailed discussion of the mechanism of gas loss from CBM deposits during basin inversion, then a review of the implications of this for the use of He isotopes as tracers and for the retention of methane by coal beds.

5.2 Helium loss from coalbed methane deposits: link to basin inversion

The loss of over 90% He from the CBM reserves of the Southeast Qinshui Basin (SQB) is identified from the low He concentration and the low $^{4}He/^{40}Ar^{*}$ ratio (Chapter 3). Helium loss has been inferred to have occurred during rapid basin inversion in the last 10 million years that is suggested by the fission-track thermochronology of detrital apatite from sediments overlying the SQB coal seams (Cao et al., 2015; Ren et al., 2005). A similar helium loss has likely occurred in Liupanshui Coalfield (LPC; Chapter 4). Evident He loss from the Qingshan block (QI) in the LPC is proposed due to the depletion of He and light Ne isotopes compared with CBM from other blocks in the region. Thermal history models based on geothermal gradients constrained by practical exploration information and

vitrinite reflectance (R_o) in coals reveals that the coalfield has experienced basin inversion since Mid-Mesozoic (Dou, 2012; Wu et al., 2016). It suggests a relatively late (majority in Cenozoic) and more intensive basin exhumation (> 3 km erosion) in the QI block compared with other blocks (major in Mid-Mesozoic, with ~2 km-thick erosion) (Dou, 2012). However, the absence of precise low-temperature thermochronological work on the LPC means that the thermal basin history remains unclear.

The main storage mechanism of gas in coal is by sorption on the coal matrix or in the micro-pores (Gray, 1987; Rice, 1993; Yee et al., 1993). Basin inversion leads to a drop of hydrostatic pressure that can induce the desorption of sorbed gases (Moore, 2012; Yee et al., 1993). Desorbed gases accumulate in coal microstructures, generating concentration and pressure gradient that results in gas escape by diffusion or viscous flow (details in section 5.3) (Han et al., 2010a; Han et al., 2010b; Hildenbrand et al., 2012; Rice, 1993). The occurrence of viscous flow is dependent on the scale of the pressure difference, indicating the extent of basin exhumation is a key factor for gas escape. The subsequent ingrowth of radiogenic and nucleogenic noble gases will mask the impact of gas loss. Thus recent He loss is easier to identify. Thus it is likely that the intensive and recent basin inversion is the reason for the discernible He loss in SQB and QI block of LPC. In order to test this hypothesis, it is worth reviewing worldwide CBM deposits.

To date, He concentrations have been measured in San Juan Basin (USA), Illinois Basin (USA), Forest City Basin (USA), northern Gulf of Mexico Basin (USA), Clackmannan coalfield in central Scotland (UK), South Yorkshire and Nottinghamshire coalfields in central England (UK), southern Bowen Basin (Australia), Qinshui Basin (China), Lower Silesia Basin (Poland) and Upper Silesia Basin (Poland). The published He concentration data is considered equal to ^4He abundances in Forest City Basin, Bowen Basin, Qinshui Basin (except this study), Gulf of Mexico Basin, Lower Silesia Basin and Upper Silesia Basin, considering the low ^3He abundance (~10^{-6}) in the coal bed methane deposits.

^{4}He concentrations have a wide range from 4×10^{-8} to 0.019 cm^3 STP/cm^3 and bear no relation to the age of coal deposition (Figure 5.1). The lowest concentration is observed in the Late Cretaceous coals in San Juan Basin, while the younger Paleocene-Eocene coals in Gulf of Mexico Basin have ^{4}He abundances that are almost two orders of magnitudes higher. The absence of a relationship between ^{4}He concentration and coal basin age can be explained by the loss of ^{4}He, and subsequent He ingrowth.

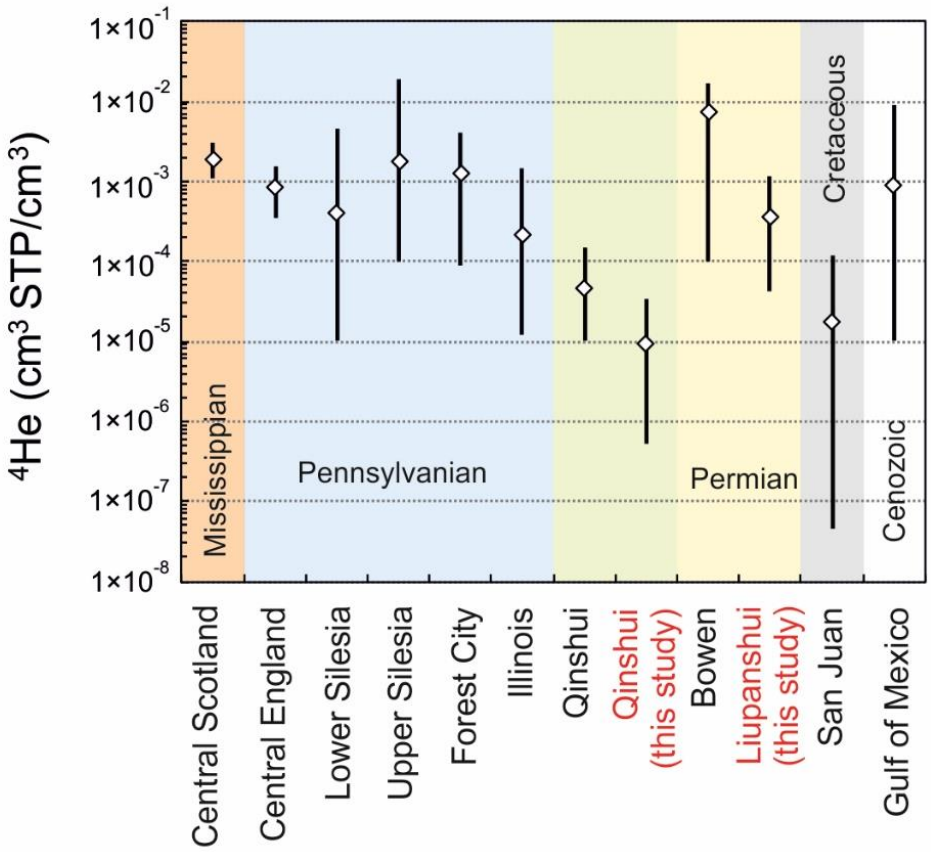

Figure 5.1. Compilation of He concentrations in CBM. The black lines represent the range of He concentrations in coals, and the diamonds represent the average value. The colour columns represent the age of coals. Qinshui Basin contains coals aged from Pennsylvanian to early Permian, shown as the overlap of the corresponding colour columns. The minimum value below the detection limit in the literature is shown as the lowest detection limit here to avoid exaggerating the various ranges. Data source: San Juan Basin, (Zhou et al., 2005); Clackmannan coalfield in central Scotland (thereafter noted as Central Scotland, Györe et al., 2018); South Yorkshire and Nottinghamshire coalfields in central England

(thereafter noted as Central England), (Györe et al., 2018); Forest City Basin, (McIntosh et al., 2008); southern Bowen Basin, (Kinnon et al., 2010); Qinshui Basin, (Xu et al., 2016; Zhang et al., 2018); Lower Silesia Basin, (Kotarba and Rice, 2001); Upper Silesia Basin, (Kotarba, 2001); Illinois Basin, (Moore et al., 2018); northern Gulf of Mexico Basin, (McIntosh et al., 2010). The published He concentration data is considered equal to ^{4}He abundance in Forest City Basin, Bowen Basin, Qinshui Basin (except this study), Gulf of Mexico Basin, Lower Silesian Basi and Upper Silesia Basin, considering generally low ^{3}He isotopic abundance ($\approx 10^{-6}$) in the continental reservoirs.

Table 5.1 reviews the age and inversion history of the coal deposits that have reported noble gas contents. A late Cenozoic basin exhumation likely has occurred in the Illinois and San Juan basins. This is broadly consistent with the lower average ^{4}He concentration in the CBM from these basins (Figure 5.1), supporting the notion that a recent basin inversion has resulted in He loss.

It is important to note that ^{4}He concentrations can change during gas extraction from coals. Zhou et al. (2005) has identified that noble gas concentrations are diluted by desorbed methane from coals and also declined with the continuous production process. The repeated sampling in Dahebian (DA) block of Liupanshui coalfield in this study shows an apparent drop of helium concentration after half-year gas extraction (section 4.7.4). Thus, in addition to the absolute ^{4}He concentration, other indicators should be used to trace He loss.

Table 5.1. A review of possible recent basin inversion in coalbed methane deposits.

Basin	Coal age	Time of most recent basin inversion	Eroded Strata	Methods	Reference
San Juan (USA)	Late Cretaceous	13-5 Ma	> 1000 m	Stratigraphic comparison	Law (1992)
Illinois (USA)	Pennsylvanian	< 50 Ma	~ 2000 m	Apatite fission-track	Zimmerman (1986)
		Late Tertiary	~ 1500 m	Clay mineral evolution	Gharrabi and Velde (1995)
Northern Gulf of Mexico Basin (USA)	Paleocene-Eocene	Mid Cretaceous and Early Eocene	hundreds of meters	Stratigraphic comparison	Galloway (2008)
Central Scotland (UK)	Mississippian	70-40 Ma*	<1000 m*	Apatite fission-track	Łuszczak et al. (2018)*
Central England (UK)	Pennsylvanian	70-40 Ma*	<1000 m*	Apatite fission-track	Łuszczak et al. (2018)*
Upper Silesia (Poland)	Pennsylvanian	260-100 Ma		Apatite fission-track	Botor (2014)
Southern Bowen (Australia)	Late Permian	100-80 Ma	~1900 m	Apatite fission-track	Raza et al. (2009)
Qinshui (China)	Pennsylvanian-Permian	26-11 Ma	~1000 m	Apatite fission-track	Ren et al. (2005)
Lipanshui (China)	Late Permian	< 60 Ma	~3000 m	Basin mod-1D	Dou, (2012); Wu et al. (2016)

* No thermochronological work has been done in these two regions. The closest work is carried in Central west Britain and present here for reference.

** No related information about basin inversion has found in Forest City Basin and Lower Silesia Basin.

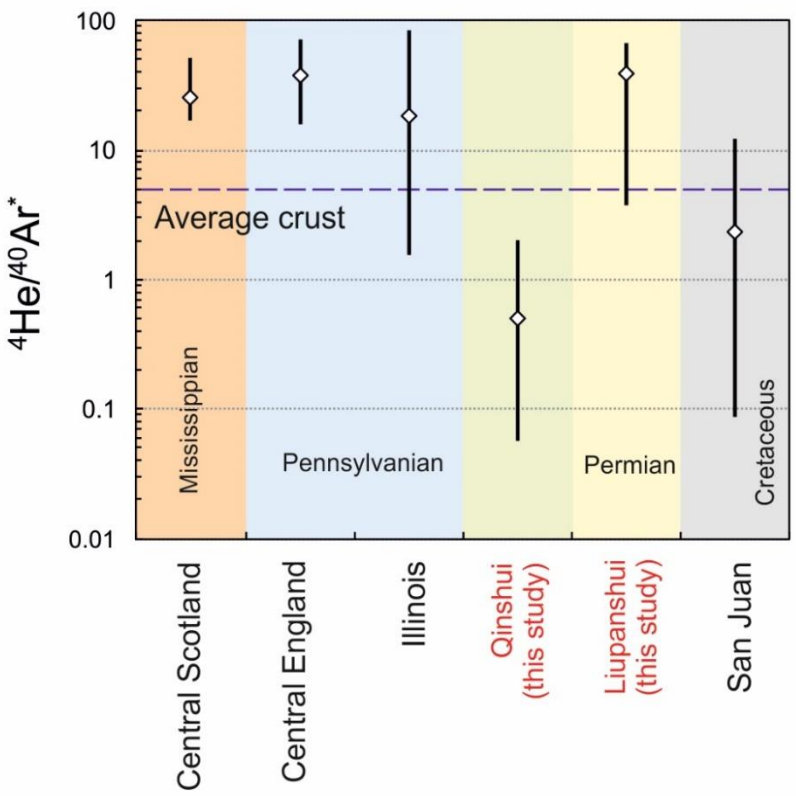

Figure 5.2. The $^4He/^{40}Ar^*$ ratio in CBM. The black lines represent the range of $^4He/^{40}Ar^*$ ratio, and the diamonds represent the average value. The blue dashed line represents the average crust value (~5; Ballentine and Burnard (2002)). The colour columns represent the age of coals. Qinshui Basin contains coals aged from Pennsylvanian to early Permian, shown as the overlap of the corresponding colour columns. CBM fields have a wide range (0.1-83.3) of $^4He/^{40}Ar^*$. The Illinois Basin, Central Scotland, Central England and Liupanshui coalfields have similar average values that are higher than the average crust, while southern Qinshui Basin and San Juan Basin coalfields have lower average values. Data sources are the same as Figure 5.1.

Normalising the ^4He content to another radiogenic noble gas isotope eliminates the influence of desorbed methane on noble gas concentration during sampling. The $^4He/^{40}Ar^*$ ratio is widely used as an indicator of gas migration in conventional and unconventional hydrocarbon systems (Byrne et al., 2020; Moore et al., 2018; Pujol et al., 2018). $^4He/^{40}Ar^*$ ratios have only been reported in coal deposits from the Illinois Basin, San Juan Basin, Central England and Central Scotland coalfields, SQB and LPC. $^4He/^{40}Ar^*$ range from 0.1 to 83.3 (Figure 5.2). This range is significantly less than that of ^4He content. Again there

is no relationship between $^{4}He/^{40}Ar^{*}$ and CBM deposit age (Figure 5.2). Natural gases generally have $^{4}He/^{40}Ar^{*}$ above the average production rate in the continental crust (~5; Ballentine and Burnard (2002)) (e.g. (Ballentine et al., 1994; Ballentine et al., 1996; Byrne et al., 2020; Györe et al., 2018)). $^{4}He/^{40}Ar^{*}$ that is lower than this value is likely a strong indication of recent He loss as He is more mobile in crustal fluids than Ar (Ballentine et al., 1994). Low $^{4}He/^{40}Ar^{*}$ are present in gases from the SQB and QI block of LPC (this study), and also the Illinois and San Juan basins (Figure 5.2) (Moore et al., 2018; Zhou et al., 2005). The low $^{4}He/^{40}Ar^{*}$ ratio of San Juan Basin gases is a consequence of solubility-controlled fractionation during the gas extraction. In this case, He is preferentially degassed from water due to its lower solubility than Ar, resulting in the low $^{4}He/^{40}Ar^{*}$ ratio in the residual gases (Zhou et al., 2005). The initial $^{4}He/^{40}Ar^{*}$ ratio of the San Juan Basin gases corrected for fractionation is about 13, close to its production ratio in the basin (Zhou et al., 2005). It is unlikely that the San Juan Basin has experienced basin inversion-driven He loss. However, the lack of precise thermochronological data for the basin also hinders making any firm conclusion. The gas in Illinois Basin is a mixture of endogenous microbial source and migrated gas that previously underwent phase partitioning (Moore et al., 2018). The fractionation process during production has not been observed. The low ^{4}He concentration and $^{4}He/^{40}Ar^{*}$ ratio in the endogenous gas might be associated with a gas loss caused by basin inversion within the last 50 Myr (Zimmerman, 1986). The absence of significant Tertiary exhumation in southern Bowen Basin, Central England and Central Scotland is consistent with the high He concentration and also $^{4}He/^{40}Ar^{*}$ ratio in CBM (Györe et al., 2018; Kinnon et al., 2010).

The limited He-Ar isotope data from CBM reservoirs appears to support the hypothesis that Tertiary inversion of coal-bearing strata has induced significant He loss that has not subsequently grown in.

5.3 Mechanism of helium loss from coal beds

Methane is mainly stored in coals by sorption to the surface of the coal matrix or within micro-pores (Ceglarska-Stefańska and Brzóska, 1998; Gray, 1987; Milewska-Duda et al.,

2000). Helium, however, is not affected by sorption, behaving as free gas in coals or dissolving in the formation water (Milewska-Duda et al., 2000; Zhou and Ballentine, 2006). Water fills the void spaces in the coal beds, sealing the gas sorbed to the coal matrix (Al-Jubori et al., 2009). The accessibility of water to nanometer-scale pores is under argument (Prinz and Littke, 2005; Thomas and McGaughey, 2009). Rapid basin inversion will cause: 1) a drop of hydrostatic pressure, inducing the desorption of sorbed gases; and 2) the generation of cleats in coals, facilitating the transport of gas (Moore, 2012).

Gases in coal systems during de-pressurisation can be transported by pressure-driven gas flow or concentration-driven diffusion. In the case of dry coals, gas flow will occur instantaneously upon the generation of a pressure gradient (Hildenbrand et al., 2012). The intrinsic permeability of a rock is supposed to be independent on temperature, pressure and the type of fluid by definition (Hildenbrand et al., 2012). Thus, this transport mechanism would not differentiate the noble gas species. However, in fact, the type of fluids and the properties of coals (e.g. swelling and shrinkage) will affect the permeability coefficient of gas flows (Massarotto, 2002). The coal swelling induced by Ar sorption may reduce the porosity and permeability, while He sorption is negligible (Bae and Bhatia, 2006; Han et al., 2010a). It implies that the transport by viscous flow in dry coals can lead to the fractionation of He and Ar. Most coal reservoirs are saturated with formation water in the cleats and macro-pores, which act as a barrier for gas migration by viscous flow (Han et al., 2010a). Gas flow through water-saturated coal occurs when the initial gas pressure difference exceeds the capillary threshold pressure of the gas–water–coal system (Han et al., 2010a; Han et al., 2010b; Hildenbrand et al., 2012). Gas-breakthrough experiments on the transport of He and Ar through a water-saturated coal plug (vitrinite reflectance, R_o = 2.3%) from Qinshui Basin suggest that He and Ar could escape by capillary-viscous flow when macro fractures (e.g. cleats) exist (Han et al., 2010a). It shows that the capillary threshold pressure for He and Ar at the same confining pressure are similar, while the effective permeability for He is slightly higher than that of Ar (Han et al., 2010a). Thus, a weak elemental fractionation of He/Ar ratios could occur when they are transported by viscous flow either in dry or wet coals. Diffusive transport becomes dominant when viscous gas flow is impeded (Hildenbrand et al., 2012; Hildenbrand et al., 2002). The same

experiment in Han et al. (2010a) indicates that, when no evident cleats exist, the transport mechanism of He and Ar in wet coals is diffusion. The diffusive capacity for He and Ar is different during the process that the escaped He could completely pass through the water-saturated coal matrix, while two-thirds of the escaped Ar should be store in the coals. Elemental fractionation definitely occurs during this process.

These observations are based on the laboratory experiments of single gases in coal plugs with a length of tens of millimetres (Han et al., 2010a; Han et al., 2010b). The evident drop of $^{4}He/^{40}Ar^{*}$ ratio in SQB and QI block of LPC suggests a significantly basin-scale elemental fractionation during the gas loss process. I have determined that the initial $^{4}He/^{40}Ar^{*}$ in SQB is 13 times lower than the *in situ* production ratio and 5 times lower than that of average crust. The $^{4}He/^{40}Ar^{*}$ in QI block is also 13 times lower than *in situ* production ratio. The strong fractionation suggests the main phase of gas loss is controlled by diffusion. The fractionation of He/Ar ratios by diffusion in the gas phase can be approximated as the ratio of the square-root of their masses (Ballentine et al., 2002), giving a fractionation factor of ~3. The gas diffusion coefficient in the water phase is also almost controlled by their masses (Jähne et al., 1987). The higher solubility of Ar in water would strengthen the diffusion of Ar in water phase, resulting in a He flux through a porous rock that is only 1.3 times higher than the Ar flux (Sathaye et al., 2016b). These factors cannot explain the extent of He/Ar fractionation in SQB and QI. The sorptive uptake of gas by coals during migration should be considered. So far, this phenomenon has only been observed in coals (Hildenbrand et al., 2012). The superimposed impact caused by different diffusion coefficients of He and Ar, and also the sorption of Ar during the migration cause the significantly low He/Ar ratio in SQB and QI block.

The drop of reservoir pressure during basin inversion will result in the desorption of methane (Moore, 2012) and the degassing of He from water to the gas phase (Smith, 1985). The capillary pressure for He at a hydrostatic pressure of 20 MPa is about 0.7 MPa (Han et al., 2010a). For coal beds in SQB, the hydrostatic pressure dropped from 40 MPa (~4 km) to 4 MPa (~420 m deep) after basin inversion based on a pressure gradient of 10 MPa/km. Assuming an initial He concentration of 1000 ppm before the gas loss, the partial pressure difference of He in the gas phase with ambient water is only 0.05 MPa, much

lower than the experiment result of 0.7 MPa (Han et al., 2010a). It indicates the difficulty of He flow in wet coals, supporting the main diffusion mechanism during the gas loss. The capillary pressure for He might decrease with declining confining pressure and more existence of cleats (Han et al., 2010a), which suggests the possibility of He escaping by gas flow at a late stage of basin inversion.

5.4 Implications of He loss from coalbed methane systems

5.4.1 Tracking input of mantle volatiles and heat to coalbed methane

The abnormally high geothermal gradient caused by the igneous intrusions and underplating may enhance the maturation of coals and induce the development of methane (Law, 1992; McElwain et al., 2005; Rahman et al., 2017; Schimmelmann et al., 2009; Su et al., 2005). Helium isotopes have proved to be an unequivocal tool for identifying the presence of mantle fluids in crustal fluids (Ozima and Podosek, 2002). The presence of mantle-derived He in natural gases is typically introduced from mantle melts that stall within the continental crust (e.g., (Ballentine and O'Nions, 1992; Ballentine et al., 1991; Gilfillan et al., 2008; Gilfillan et al., 2011; Phinney et al., 1978)). Consequently, the role of magmatism in the maturation of coals and generation of CBM can ideally be tracked using He isotopes.

Previous studies have demonstrated the presence of mantle-derived helium in natural gases from several coalfields (Figure 5.3). The $^{3}He/^{4}He$ ratios of the San Juan Basin gases are consistent with 1- 4% mantle ^{4}He assuming a depleted asthenosphere mantle $^{3}He/^{4}He$ of 8 R_A (Zhou et al., 2005), which might be sourced from Oligocene magmatism (Law, 1992). The circulation of water heated by San Juan Basin batholith has enhanced the maturation of coals in the northern part of the basin (Law, 1992; Scott et al., 1994). The contribution of mantle ^{4}He in the Illinois Basin gases reaches 10% (Moore et al., 2018), which might be associated with an intensive magmatic event in the Early Permian recorded by ultramafic intrusion dikes found in the southeastern margin of the basin (Kolata and Nelson, 1990; Schimmelmann et al., 2009). Proximity to the intrusive dikes has promoted the R_o

value, while a release of large amounts of thermogenic methane is under argument (Rahman et al., 2017; Yoksoulian et al., 2016). Central Scotland coalfield gases contain approximately 3% mantle ^{4}He, based on sub-continental lithosphere mantle (6.1 R_a) origin for the magmatic He (if Late Carboniferous-Early Permian), or 0.3% if it is derived from Tertiary Iceland plume (50 R_A) (Györe et al., 2018).

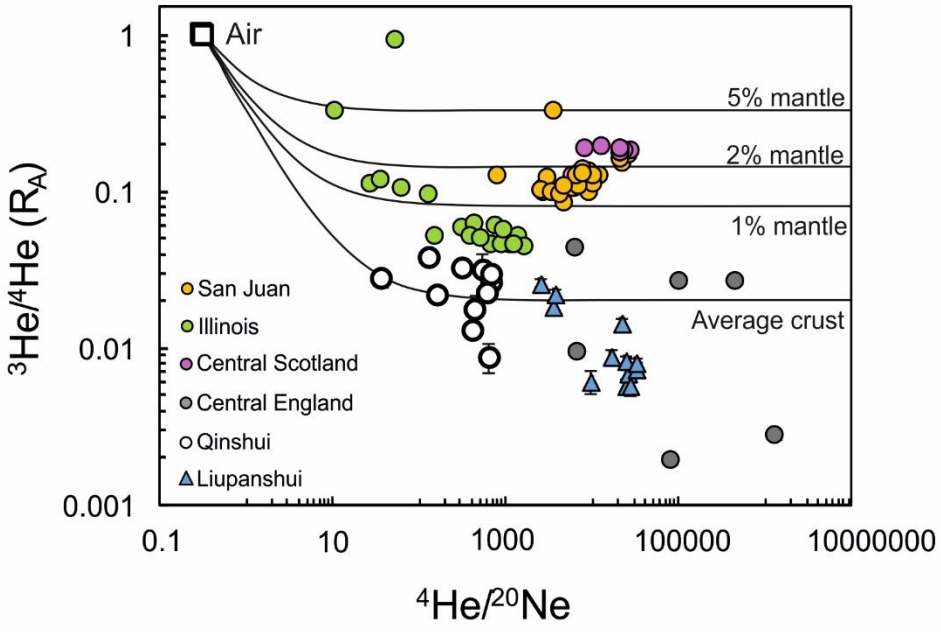

Figure 5.3. ^{3}He/^{4}He vs. ^{4}He/^{20}Ne ratios in global CBM gases. The solid black lines are mixing lines between air and the pure average crust (0.02 R_A, Ballentine and Burnard (2002)) with increasing contribution of mantle volatile. The endmember of mantle helium ratio used in the study is 6.1 R_A from sub-continental lithospheric mantle (Gautheron and Moreira, 2002). The mantle helium is present in Illinois Basin, San Juan Basin and Central Scotland coalfield. CBM gases from central England coalfields, SQB and LPC have pure crustal helium. Data sources are the same as Figure 5.1.

Neon isotopes can also be used to trace the presence of magmatic volatiles in natural gases (e.g., (Ballentine, 1997; Ballentine et al., 2005; Ballentine and O'Nions, 1992)). However, mantle-derived Ne has only been measured in the Central Scotland coalfield (Figure 5.4). This likely reflects the contribution of crustal radiogenic and atmospheric Ne, and emphasises the importance of He isotopes as a tracer. If He is lost from CBM during basin inversion, and a significant contribution of radiogenic He accumulates after the gas loss

phase, there is the potential that the thermal effect of magmatism has gone unnoticed in previous studies of CBM.

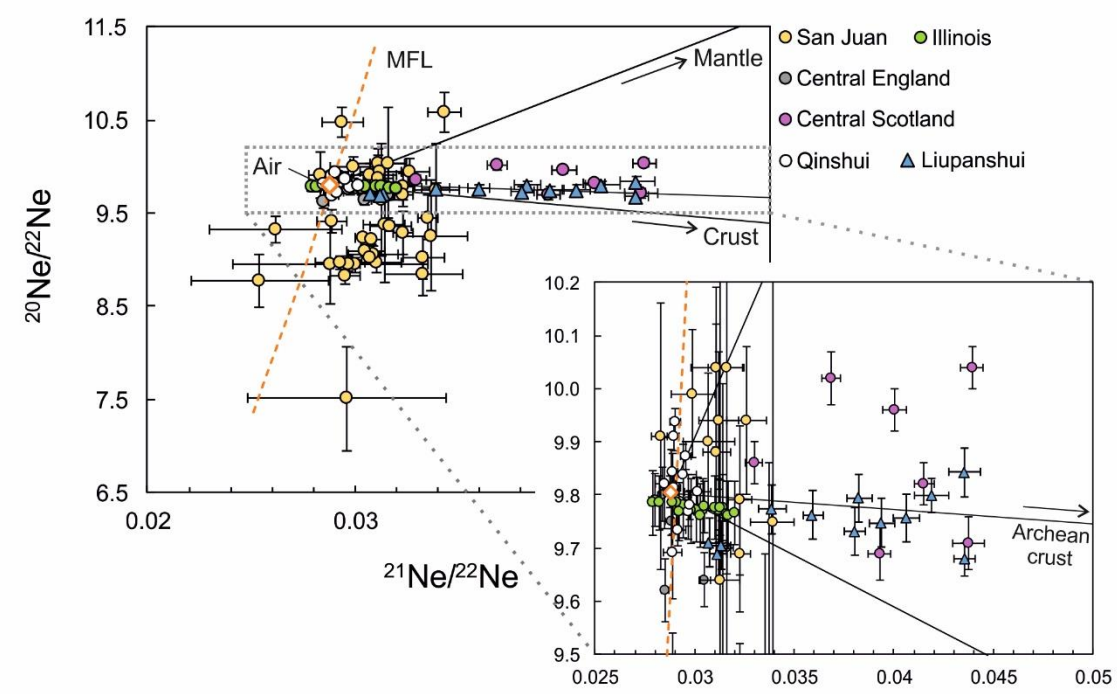

Figure 5.4. Neon isotopes in coal systems. The orange diamond represents the air ($^{20}Ne/^{22}Ne$ = 9.80, $^{21}Ne/^{22}Ne$ = 0.029). The orange dash line is the mass fractionated line (Kaneoka, 1980). Black solid lines are the mixing lines of air with mantle and average crust ($^{20}Ne/^{22}Ne_{mantle}$ = 12.5, $^{21}Ne/^{22}Ne_{mantle}$ = 0.06, $^{20}Ne/^{22}Ne_{crust}$ = 0, $^{21}Ne/^{22}Ne_{crust}$ = 0.47; (Ballentine et al., 2005; Kennedy et al., 1990)). Only Central Scotland coalfield contains evident mantle Ne component. The deviation of LPC data from crust-air mixing line is explained by the *in situ* produced high $^{21}Ne/^{22}Ne$ or addition of Archean crust ($^{20}Ne/^{22}Ne$ = 0, $^{21}Ne/^{22}Ne$ = 3.3 ± 0.2; Lippmann-Pipke et al. (2011)) (see section 4.7.2.2). Data sources are the same as Figure 5.1.

The magmatic activity that occurred during the main stage of Yanshanian Orogeny (Late Jurassic to Early Cretaceous) is argued to have enhanced the coalification in both SQB and LPC, accompanied by a peak of methane generation (e.g. Dou, 2012; Luo et al., 2017; Ren et al., 2005; Su et al., 2005; Tang et al., 2016). The maximum burial depth that the coal-bearing strata of SQB (~4 km) reached in the Late Triassic cannot account for the high coal maturity ($R_o \approx$ 2.2-4.5%) with a normal geothermal gradient of 30°C/km (Luo et al., 2017; Ren et al., 2005; Ren and Zhao, 1997). A paleo-temperature of 200-300°C is

suggested by detrital zircon fission-track data, which requires an abnormally high geothermal gradient of over 50°C/km (Ren et al., 2005). This is consistent with the results based on vitrinite reflection, homogenisation temperature of fluid/gas phase inclusions (Ren et al., 2005; Ren and Zhao, 1997). The youngest zircon fission-track ages (100-150 Ma) represent the time of a thermal pulse (Ren et al., 2005). This timing overlaps with the $^{40}Ar/^{39}Ar$ ages of the hornblendes (125-127 Ma) from syenodiorite intrusion in Linfen (western margin of the basin) and Changzhi (eastern margin of the basin) (Xu et al., 2004). It relates the heat event with the magmatic activities in Yanshanian Orogeny. Although no magmatic rocks have been observed at the study site, Ren et al. (2005) argued that deep magma intrusion is responsible for the local high R_o (3-4.5%) values of coals.

A similar argument also exists for the LPC. Magmatism during the Yanshanian Orogeny in the region is supported by the presence of a 115 Ma dolerite sill present within the lower Carbonaceous in the Pannan anticline (Chen, 1995; Zhang, 2017). Fluid inclusions in vein quartz from Panxian coals have a homogenisation temperature up to 150°C, which cannot be reached by the maximum deep burial with a normal thermal gradient (Tang et al., 2016). The presence of shallow hydrothermal fluid is supposed to be related to local magmatism which would have led to further coal maturation at shallow levels. The modelled temperature history based on coal mineralogy and the evaluation of geothermal gradient constrained by practical exploration information and R_o values requires an abnormally high geothermal gradient during Late Jurassic to Early Cretaceous, indicating the contribution of the magmatism and inducing further coalification and methane generation in Tucheng and QI blocks of the study sites (Dou, 2012; Wu et al., 2016).

The $^3He/^4He$ ratios of SQB and LPC gases are low (Figure 5.4; 0.008 to 0.035 R_A for SQB and 0.006 to 0.026 R_A for LPC), indicating a crustal radiogenic origin for the He. A maximum proportion of mantle ^4He is 0.4 - 0.5% based on the SCLM mantle end-member (6.1 R_A) and the lowest measured $^3He/^4He$ in each region (section 3.8.2 and 4.7.2.1). This is inconsistent with the previous studies which indicate that Late Jurassic-Early Cretaceous magmatism has played an important role in coalification in these two areas (Dou, 2012; Ren et al., 1999; Su et al., 2005; Tang et al., 2016). It is possible that the helium lost during basin inversion (Chapters 3 and 4) contained a significant mantle component. Subsequent

ingrowth of radiogenic helium in the coals and upward diffusion from the deep crust (Castro et al., 1998; Torgersen and Clarke, 1985) would lower $^3He/^4He$ ratios and could potentially mask the mantle signature. Here I model the timing and extent of He loss required to explain the low $^3He/^4He$ ratios in SQB and LPC.

The model assumes an initial He concentration and isotopic composition that reflects the proportion of mantle and crustal He. The main He loss event occurs instantaneously at time t (Ma) lowering the He concentration but leaving $^3He/^4He$ ratio unaffected. After that, radiogenic He grows in. The timing (t_l Ma) and the proportion of He loss (f %) are modelled. Except for the He loss process, the coal reservoir is considered to be a closed system.

Prior to He loss, the total amount of accumulated *in situ* and external (crust + mantle) ^4He is set to 1. With the constant accumulation rate of crustal radiogenic (*in situ* + external) ^4He over the burial history, the amount of radiogenic ^4He at each stage is proportional to time. The proportion of crustal ^4He before ($[^4He]_b$) and after ($[^4He]_a$) the loss event can be calculated as follows:

$$[^4He]_b = (t- t_l)/t \times (1-[^4He]_m) \quad (5.1)$$

$$[^4He]_a = t_l/t \times (1-[^4He]_m) \quad (5.2)$$

where $[^4He]_m$ is the proportion of mantle ^4He. The lowest measured $^3He/^4He$ ratio is used to represent the isotopic composition of crustal He, noted as $(^3He/^4He)_c$. The mantle $^3He/^4He$ ratio, $(^3He/^4He)_m$, is assumed to be 6.1 R_A, the best estimate of sub-continental lithosphere mantle (Gautheron and Moreira, 2002). The final $^3He/^4He$ ratio is determined from the following equation:

$$^3He/^4He = \frac{([\,^4He]_b \times (\,^3He/\,^4He)_c + [\,^4He]_m \times (\,^3He/\,^4He)_m) \times (1-f) + [\,^4He]_a \times (\,^3He/\,^4He)_c}{([\,^4He]_b + [\,^4He]_m) \times (1-f) + [\,^4He]_a} \quad (5.3)$$

To constrain the timing and extent of He loss, the model tests the effect of He loss at 10, 20 and 60 Ma. The mantle proportion in CBM ($[^4He]_m$) is mainly ranging from 1-5% (Figure 5.3), where the results from $[^4He]_m$ = 1 and 5 % are shown in this study. It is worth noting that Eq 5.3 ignores isotopic fractionation during the He loss. As discussed in section 5.4, the transport mechanism of He in coals is mainly by diffusion. Thus, it is likely that

isotopic fractionation of He isotopes has occurred. Assuming that the diffusion process follows the Rayleigh fractionation (Ballentine et al., 2002), the He ratio after the gas loss can be present as:

$$(^3He/^4He)_{after} = (^3He/^4He)_{initial} \times (1\text{-}f)^{(\alpha\text{-}1)} \quad (5.4)$$

where α is the fractionation factor. Then the Eq. 5.3 can be modified to Eq. 5.5:

$^3He/^4He =$

$$\frac{([\,^4He]_b \times (\,^3He/\,^4He)_c + [\,^4He]_m \times (\,^3He/\,^4He)_m) \times (1-f)^{\alpha} + [\,^4He]_a \times (\,^3He/\,^4He)_c}{([\,^4He]_b + [\,^4He]_m) \times (1-f) + [\,^4He]_a} \quad (5.5)$$

Jähne et al. (1987) proposed that the isotopic fractionation factor of $^3He/^4He$ during diffusion is 1.15 ± 0.03, close to the ratio of the square-root of their masses. Bourg and Sposito (2008) suggested a lower fractionation factor, less than 1.06, based on molecular dynamics simulations of noble gases in ambient water. Here, the fractionation factor of 1.15 is chosen to reach the minimum estimation of *f*.

The SQB coals were deposited in the Pennsylvanian (~300 Ma). The lowest measured $^3He/^4He$ (0.09 R_A) is used as the crustal He. The results are shown in Figure 5.5. The earlier the He loss event, and the lower the initial contribution of mantle He, the lower the amount of He loss required to achieve measured values. Using the calculated He accumulation age of the SQB gases (< 11 Myr) (section 3.8.3) as the time of gas loss, with a starting gas having 1% mantle He, requires the loss of more than 93-98% of ^4He with/without considering isotopic fractionation during gas loss. This model suggests that the measured low $^3He/^4He$ ratio in SQB can be explained by the He loss and ingrowth mechanism, but requires the loss of essentially the total He inventory.

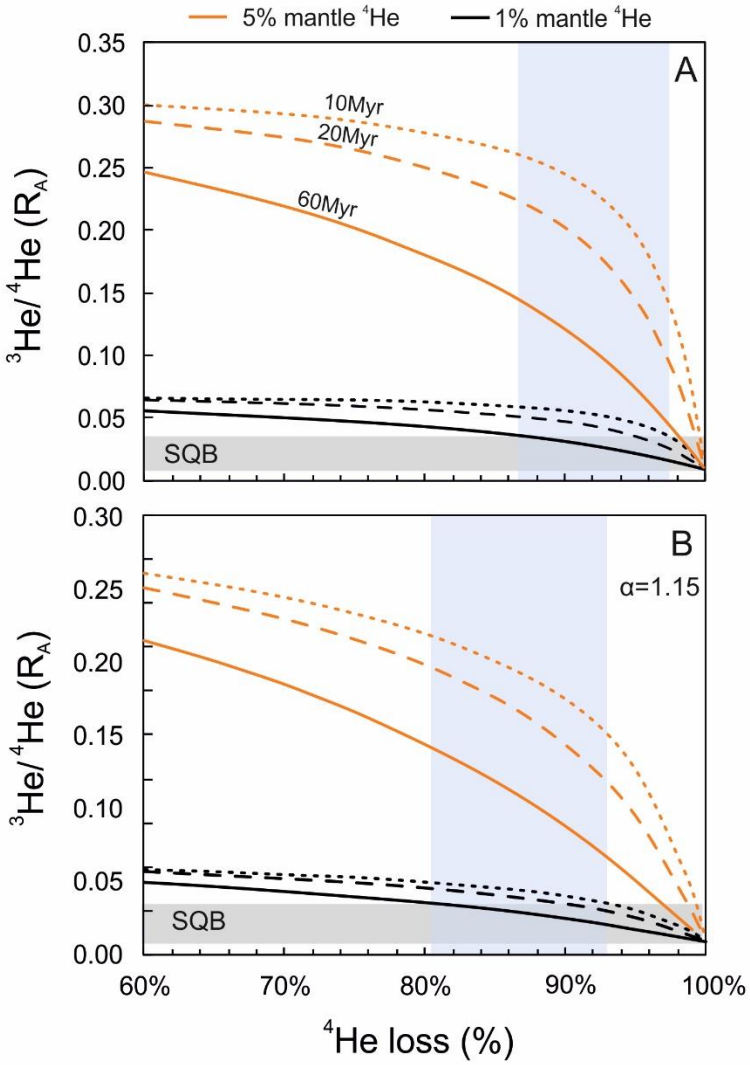

Figure 5.5. The modelled result after gas loss and refilling process in SQB without isotopic fraction (A) and with isotopic fractionation (B). The black and orange lines represent 1% and 5% mantle He, respectively. The dotted, dashed and solid lines represent the timing of gas loss at 10, 20 and 60 Ma. The blue columns represent the range of the proportion of He loss with 1% mantle He in the pre-loss CBM. The result reveals that the earlier the gas loss happens and the higher the proportion of gas loss, the lower the final $^{3}He/^{4}He$ ratio.

Achieving total He loss is a challenge. Here, I estimate the time required to cause 93-98% of He loss by upward diffusion. The roof of the coal seams that He diffuses through is an average 35 m-thick water-saturated mudstone (Su et al., 2005), and assumed to contain no He in order to estimate the maximum diffusion flux of dissolved He, which is (Sathaye et al., 2016b):

$$L = \frac{-D\phi\, dC}{\tau\, dz} \quad (5.4)$$

where L is the He diffusion flux in atoms/(cm^2·yr), and ϕ and τ are porosity and tortuosity of the mudstone, respectively, prescribed to be 1% and 100 (Ballentine et al., 2002). C is the concentration of He in the formation water at the interface of coals and mudstone in atoms/(cm^3 yr). Z is the vertical position in cm. D is the diffusion coefficient of He, which mainly changes with temperature (Jähne et al., 1987). The maximum diffusion coefficient is calculated to be 2.6×10^{-4} cm^2/s corresponding to the maximum burial depth of 4 km that the coals have experienced. For simplification, the coal seam is assumed to be a thin plate, and the internal transport of He is ignored. Then, the change of He concentration (dC') caused by diffusion is:

$$dC' = -C(t) \times \frac{D\phi}{\tau z h \varphi} \times dt \quad (5.5)$$

where h, φ is the thickness (860 cm) and porosity (5%) of the SQB coal seams, respectively (section 3.8.3). t is the time of diffusion. The time required to cause a drop of He is:

$$t = -\frac{\tau z h \varphi}{D\phi} \ln\left(\frac{C}{C_0}\right) \quad (5.6)$$

C_0 is the initial concentration of He before the gas loss. The 93-98% loss of He, i.e. C/C_0 = 0.02-0.07, gives a diffusion time to be ~0.5-0.7 Myr. It means that total loss of He could be reached by diffusion, but requires a geological-scale time even under an unrealistic maximum diffusion flux. It strengthens the possible occurrence that He escapes through the roof by advective flow in the late stage of basin exhumation. Pressure-driven gas flow is generally more efficient as its escape time is proportional to the migration length, while diffusion time increases with the square of the length (Hildenbrand et al., 2012). This is more consistent with the above assumption that the main He loss event occurs instantaneously.

The results of modelling He loss from the Permian coals (260 Ma) is similar to that from SQB (not shown). Assuming the gas loss event at 10 Ma and 1% mantle He addition, the minimum loss of 96-98% of ^{4}He is required to establish the measured ^{3}He/^{4}He ratios. The extent of basin inversion in each block in LPC is different based on thermal history models (Dou, 2012). The QI block experienced the most intense inversion, experiencing over

4,000 m of rock uplift since the Late Jurassic. The coals in the DA block uplifted from over 3,500 m to 1000 m. This lower pressure decrease would mean less He loss in DA block. Thus, if all other factors were the same (e.g. initial $^{3}He/^{4}He$ and He concentration, the timing of basin inversion, etc), the DA gases would be expected to have contained higher He concentration and higher $^{3}He/^{4}He$ ratio. However, $^{3}He/^{4}He$ ratio in DA block (0.006 – 0.008 R_A) is lower than that in QI block (0.018 – 0.026 R_A). This may reflect an earlier He loss event, consistent with the basin inversion history of Dou (2012), or a lower proportion of mantle He in the initial DA block CBM.

The minimum 93-98% He loss in SQB coals resulted from the modelling is above the estimation of 92% He loss assuming no Ar loss based on the difference of $^{4}He/^{40}Ar^{*}$ ratio with predicted *in situ* generation rate. It means that Ar likely has been lost during the basin inversion. Based on the local $^{4}He/^{40}Ar^{*}$ production rate of 13, assuming 1% mantle He addition and 93-98% He loss, the initial $^{4}He/^{40}Ar^{*}$ ratio of 1 before fractionation gives 9-74% Ar lost during the basin inversion. The same calculation for LPC gases suggests that 49-74% of Ar has been lost during the process. Ar is less strongly adsorbed onto the coals compared with methane, but more strongly than He (Han et al., 2010a; Han et al., 2010b). These estimations lower the upper limit of methane loss during the basin inversion.

5.4.2 Methane storage

Based on the assumption that the pore space in the coals is full of free methane I have determined that approximately 40% of the methane would escape during the inversion of the SQB coals from 4 km to 400 m (section 3.8.3). This was based on a model which considers both adsorption/desorption and diffusion during methane loss introduced by Xia and Tang (2012). This value is higher than the lowest estimation of loss Ar in SQB (9%), contradictive with the stronger sorption of methane to Ar. However, this prediction (40% methane loss) is based on an assumption that the pore space in the coals is full of free methane. For water-saturated cleats and fractures in the coals, the proportion of free methane in the reservoir would be significantly lower. In this case, methane loss in SQB is much less than 40%. Over 98% of the methane in coals is adsorbed and absorbed (Flores,

1998; Gray, 1987). The model reveals that the adsorbed gas amount only drops from 786 mol/m^3 to 749 mol/m^3 following the Langmuir equation (Xia and Tang, 2012), indicating only about 5% of methane was desorbed during the basin inversion. Methane transportation in wetted SQB coals has been proved only by diffusion with/without cleats in a laboratory situation (Han et al., 2010b). Less than 2% of methane could pass through the wet coal plug during the process. This laboratory result is consistent with the modelling result (9% Ar loss). This could explain that SQB is still one of the most productive CBM regions in China, even though a recent gas loss happened and caused significant He loss.

According to well records, gas production in the LPC is generally lower than the SQB. This may be due to an initially lower methane content, a function of the less mature coals in the LPC. This might also mean the weaker adsorption capacity of coals to methane in LPC during basin inversion, resulting in greater desorbed methane. It is consistent with the higher estimation of 49% of Ar loss than that in the SQB. Wells in the QI block are less productive compared with DA block. However, the QI block has more mature coals, which are supposed to have higher methane content. Based on the burial history, the inversion extent of QI block (from over 5,000 m to 800 m) is stronger than DA block (3,500 m to 1000 m) (Dou, 2012) and may cause more methane loss from the QI block.

This study hints that CBM fields which have experienced a recent and intensive basin inversion still could contain commercial gas resource as long as the maturity of coals is high enough to adsorb methane.

5.5 Conclusion

A review of He-Ne-Ar system in coal deposits other than SQB and LPC suggest that its high potential to trace the recent gas loss in CBM fields. The gas escaping mechanism from SQB and QI block coalbeds is mainly by diffusion. Viscous gas flows highly likely has also occurred at the late stage of basin inversion. The strong fractionation between He and Ar is the consequence of different diffusion coefficients and also the sorptive uptake of Ar during the migration in coals. The modelled He loss suggests that over 93% and 96% of He has been lost for SQB and LPC, respectively, during the basin exhumation assuming 1% SCLM-mantle input and gas loss at 10 Ma. It explains the low He isotopic ratio in the

CBM from SQB and LPC although these two regions were thought to be heated during a magmatic activity in Yanshanian movement. A proportion of Ar (> 9% for SQB and > 49% for LPC) is suggested to have been lost with He under the same modelling parameters. Due to the strong adsorption of methane in coals, it supports the upper limit for methane loss during basin inversion.

Chapter 6 Summary and future work

6.1 Summary

Coalbed methane (CBM) is an important energy source in many countries. It is comparatively cheap to extract, and it lowers fugitive methane escape during mining operations. The overall aim of this PhD is to develop an understanding of the origin of CBM in China, the role of magmatic heating on methane generation and to determine the extent to which geologically recent basin inversion has affected gas composition. In this study, Southeast Qinshui Basin (SQB, northern China) and Liupanshui Coalfield (LPC, southern China) are chosen as the study sites for the former is the most developed CBM filed in China and the latter has a high potential for commercial CBM production.

The origin of methane

The major gas composition, $\delta^{13}C_{CH4}$ and δD_{CH4} of CBM from SQB and LPC indicate a thermogenic origin for the methane with no significant contribution from microbial production. The stable isotope composition of the methane from the SQB is slightly fractionated compared to the predicted values based on the maturity of the coals (based on vitrinite reflectance) due to the desorption from coal matrix and diffusion during the gas extraction process. The variance of stable isotopes among different blocks in LPC is the result of different degrees of thermal degradation of organic matter in each block. The small increase in the proportion of the methane (< 3%) and the modest decline of $\delta^{13}C_{CH4}$ (~1.5‰) and δD_{CH4} (~16‰) after 6 months of production from Dahenbian (DA) block of LPC are also probably the result of desorption. The modest changes in C and H isotope composition are not enough to account for much of the basin-wide variation and to require different origin for the gas.

The influence of recent basin inversion on gas storage

The He-Ne-Ar isotope composition of SQB gases is consistent with contributions from both air-saturated water and radiogenic/nucleogenic gases (^{4}He, $^{21}Ne^{*}$ and $^{40}Ar^{*}$) (section 3.8.2). The radiogenic $^{4}He/^{40}Ar^{*}$ ratio is significantly lower than the composition that should be produced in the SQB coals and by local continental crust. This coincides with

low ^{4}He concentrations relative to coals of a similar age. Modelling shows that radiogenic ^{4}He and $^{40}Ar^{*}$ and ASW-derived noble gases (^{20}Ne, ^{36}Ar) previously mixed in the water phase and subsequently degassed from water following open system Rayleigh fractionation during commercial gas extraction. Extremely low $^{4}He/^{40}Ar^{*}$ ratios existed prior to gas extraction. I infer that the He trapped by the coal over 100s Myr was lost during the rapid exhumation of the basin at 30-10 Ma.

The noble gases in LPC CBM are also a mixture of air-derived gases from groundwater with crustal radiogenic/nucleogenic noble gases produced from both *in situ* decay in the coal and externally (sections 4.7.2 and 4.7.4). The nucleogenic Ne in the LPC methane does not fit a typical crustal signature. It is more likely derived from the Archean crust basement or from local (F-poor) coals, rather than the addition of mantle Ne. The loss of He from the LPC gases is predicted because $^{4}He/^{40}Ar^{*}$ ratios are mostly lower than *in situ* production ratio. Gases from the QI block have experienced the most severe light noble gas loss; $^{4}He/^{40}Ar^{*}$ and $^{21}Ne^{*}/^{40}Ar^{*}$ ratios are lower than other blocks. This observation is consistent with the most intensive and recent basin inversion history in QI block compared with the other three blocks.

This study also provides insight into noble gas transport in coal seams during a basin-scale inversion. He, Ne and Ar mainly escape from coalbeds by diffusion. Viscous He gas flow likely occurs during the late stage of basin exhumation for efficient total He loss. The different diffusion coefficients for He and Ar transport in coals and the sorptive uptake of Ar during the migration in coals is required to explain the strong fractionation between He and Ar during the gas loss.

The role of magmatic heating

In a model of He loss, assuming 1% of SCLM mantle ^{4}He addition and gas loss at 10 Ma, I show that over 93% of the He in the SQB and 96% in the LPC coals has been lost in response to basin inversion. The significant He loss from CBM during exhumation events, and subsequent ingrowth of radiogenic He, explains the absence of mantle He in SQB and LPC in which the methane generation is widely believed to have been influenced by Yanshanian magmatic activities (Late Jurrasic to Early Cretaceous). This phenomenon

hinders using He isotopes to trace the role of magmatic heating on coal maturation. The modelling also implies that a significant proportion of Ar (> 9% in SQB and > 49% in LPC) was lost with He. Despite this, economic methane reserves are retained in the SQB and LPC coal beds due to the strong sorption capacity of high mature coals for methane.

These two cases indicate that high mature coals which have experienced a recent and intensive basin inversion still could preserve a large methane resource. They also demonstrate the potential of He-Ne-Ar isotope composition of CBM to track recent gas loss event due to basin inversion. A review of He-Ne-Ar isotopes in coal deposits worldwide likely supports this conclusion; CBM from basins that have experienced Cenozoic inversion tend to have lower He contents (section 5.2). However, more study on the CBM fields which has experienced Cenozoic inversion is needed for the currently limited available data. The conclusion, once verified, could be reversely used as a tracer for the existence and extent of recent basin inversion.

The fractionation process during production

The stable isotope composition of the methane from the SQB and LPC shows slight fractionation due to the desorption of gases from the coal matrix and diffusion during the gas extraction process.

Open system Rayleigh fractionation during gas extraction can explain the ASW-derived $^{20}Ne/^{36}Ar$ ratios in SQB CBM, while a re-dissolution fractionation process (similar to that proposed for CO_2 gas reservoirs (Gilfillan et al., 2008)) before gas extraction is required to explain the extremely high $^{20}Ne/^{36}Ar$ ratio of the LPC gases. $^{84}Kr/^{36}Ar$ and $^{132}Xe/^{36}Ar$ ratios in the LPC gases are mostly higher than predicted values based on re-dissolution modelling, indicating the addition of initial trapped Xe and Kr in/on the coal matrix. In contrast, the Xe and Kr contents of the SQB gases, and the local QI block of the LPC, are low. The depletion of Xe and Kr without significant enrichment of Ne is, for the first time, observed in natural gas systems. It is best explained by the strong adsorption capacity of high maturity coals to Kr and Xe, resulting in the depleted Kr and Xe in produced gas. If the assumption is true, the link between $^{132}Xe/^{36}Ar$, $\delta^{13}C_{CH4}$ and gas production rate, and

the strong retention of heavy noble gases in SQB and QI block might suggest the application of Kr and Xe in the indication of methane storage

6.2 Future work

The influence of Cenozoic basin exhumation on gas storage

The review of He-Ne-Ar system and thermal histories in worldwide CBM fields demonstrates the limited available data (section 5.2). It results in the difficulty to reach a general conclusion that recent basin inversion would induce a significant gas loss. More researches on light noble gases and basin history in other CBM fields that have experienced a recent basin inversion are required. In addition, the understanding of the role of coal maturity on the reaction to gas loss is restrained in medium-high mature coals. A more comprehensive comparison of gas reserve in all different mature coal basins would benefit a more accurate evaluation of the influence of basin inversion on gas storage.

Coal basin thermal histories, role in controlling CBM reserves.

As pointed out in Chapter 4, the thermal history of the LPC basin is poorly constrained, mainly from the model based on vitrinite reflectance and field information (Dou, 2012). Precise low-temperature thermochronological work, such as fission-track and (U-Th)/He dating of apatite and zircon from sandstones or inter-bedded volcanic rocks, are the most suitable techniques for determining the thermal history of sedimentary basins (e.g. Ren et al., 2005). This is essential for quantification of the timing and amount of basin exhumation and consequently its impact on gas retention.

Evolution of stable and noble gas isotopes in CBM gases during commercial gas extraction

Open system solubility-controlled fractionation of dissolved gases during gas extraction has been identified in SQB gases (Chapter 3) and in the San Juan Basin (Zhou et al., 2005). The repeat gas samples from the DA block of LPC after 6 months of gas production might suggest the same fractionation process occurred. A firm conclusion is not possible due to the limited available data. However, the data suggest that the open system solubility-controlled fractionation process is common during CBM extraction. The formation water

plays an important role in gas sealing within coal seams (Moore, 2012). It enhances the likelihood that the dissolution of radiogenic noble gases (^{4}He, $^{21}Ne^{*}$ and $^{40}Ar^{*}$) in formation water and subsequent solubility-controlled degassing of both radiogenic and ASW-derived noble gases (^{20}Ne, ^{36}Ar, ^{84}Kr and ^{132}Xe). If this hypothesis is correct, identification of the influence of this process on noble gas and stable isotopic composition in produced CBM will be required in future studies. Continuous monitoring of the composition of CBM will be required to test this hypothesis. It also would allow the initial intrinsic gases characteristics to be determined before extraction, an estimation of the age of the groundwater associated with CBM.

Identifying the role of groundwater in the preservation of CBM

This study has identified the solubility-controlled fractionation processes in both fields. Further quantification of interacted water-gas volume ratio could be carried based on existing air saturated water-derived noble gas data. This would help to constrain the role of groundwater on CBM preservation and its relation with practical production. It might also support insight into gas escaping by estimating the primitive gas reserve based on water/gas volume ratio and initial water volume in the reservoir (Barry et al., 2016).

Kr and Xe storage in high mature coals

It would be an interesting research direction to detect the Kr and Xe content in coal cores from SQB and QI block where the coal rank is semi-anthracite or anthracite. This is a direct test to the hypothesis that most of Kr and Xr is still adsorbed to the coals even under the depressuring condition. If it is correct, it will hint at the potential large storage of heavy noble gases in extreme-high mature coals. A comparison of the adsorption capacity of these coals to methane, carbon dioxide, Kr and Xe would also provide new insight into carbon capture and storage.

Appendices

Appendix I Sampling and Analytical techniques

Collection methods and analysis procedures of samples from Southeast Qinshui Basin (SQB) and Liupanshui Coalfield (LPC) are similar, dominantly following that used by Györe (2015).

AI.1 Sampling technique

All samples were taken directly from the producing wellheads and stored in internally polished ~6 mm (internal diameter) refrigeration-grade copper tubes (Figure A1.1). The ~70 mm copper tubes can provide about 10 cm^3 (STP) gas for analysis. The pressure of extracted gas in the production wellheads ranged from 0.1 to 3 MPa. A stainless steel step-down regulator (high-pressure input up to 20 MPa, low-pressure output up to 0.2 MPa) was added between the sampling port and the copper tube. The regulator replaced the port of the pressure monitor and was connected to the wellheads. The other end of the regulator was connected to the copper tube via a flexible high-pressure Buna-N hose (~100 cm) and Jubilee clamps. Another hose (~20 cm) was connected to the outflow end of the copper tube as an exhaust to ensure no backflow from the air to the tube. The sampling device was flushed by well gas for 2 min to expel air, and the flow pressure through the tube was adjusted to about 0.15 MPa by the regulator. The copper tube was then sealed from the downstream to the upstream by closing the pinch-off clamps to reach cold welding. All samples were shipped back to the UK for analysis with the clamps and aluminium rack intact.

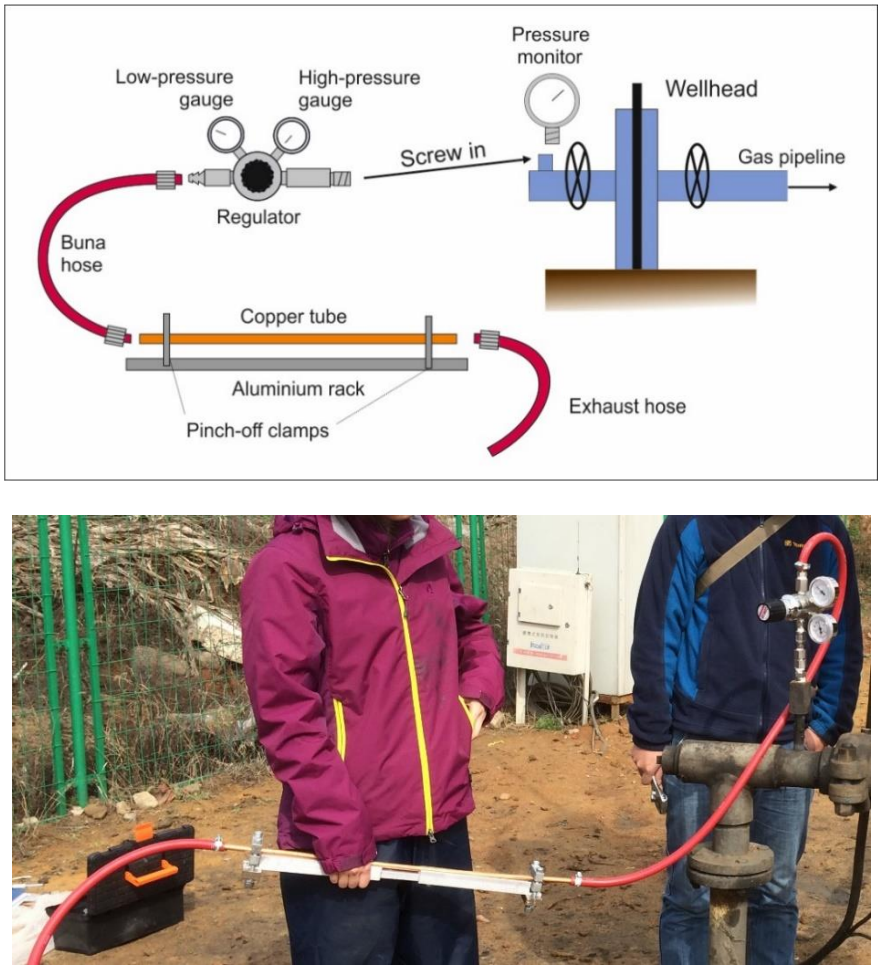

Figure AI.1. Diagram of the sampling set-up (top) and fieldwork photo (bottom). The regulator is connected to the wellhead. The copper tube held by an aluminium rack is attached to the regulator via the flexible high-pressure Buna-N hose. Another hose is connected to the outflow end of the copper tube to avoid the backflow mixing of air.

AI.2 Analytical techniques

All analyses were conducted at the Scottish Universities Environmental Research Centre (SUERC). Aluminium racks were unscrewed in order to separate the copper tubes into two halves using another pinch-off clamp.

Major gas composition

The first half of each copper tube was connected to a steel-glass vacuum line ($p<0.1$ mbar) by Swagelok 3/8" tube fittings (Figure AI.2). The clamp was released, and the tube was open to a gas extraction zone (P1 in Figure AI.2) for 5 min to reach equilibrium. Then the

valve in P1 closest to the tube was closed. About 5 cm^3 gas at a pressure of ~1.5 bar was expanded to P1 (~ 2.5 cm^3), resulting in the pressure in P1 close to atmospheric pressure. An aliquot (~ 20 μL) of gas was extracted manually using a 100 μL Hamilton gas-tight syringe through a rubber membrane (R1in Figure AI.2) and injected into a Hewlett Packard 5890 gas chromatograph (GC) for major gas composition analysis.

The GC is equipped with a single filament thermal conductivity detector (TCD), a 2.13 m long and 1.0 mm inner diameter Restek 100/120 packed column and operated with helium carrier gas. Helium is kept at 20 kPa with a flow rate of 45 mL/min. During the analysis, the temperature of the column was kept at 30°C for 3 min, and then increased by 15°C/min until reaching 150 °C. It stayed at maximum temperature for 5 min. The gas components are eluted at a specific time for a given set of carrier gas flow rate and column temperature conditions and detected by the TCD. This GC system separates methane, carbon dioxide, ethane, propane and butane from each other and all from a single peak of nitrogen and oxygen. The TCD output is in voltage and proportional to the difference in thermal conductivity of the component gas compared to the helium carrier gas. The alkane calibration was carried out by gases with known compositions supplied by CALGAZ Ltd. Certain amounts of gas were transferred into a pre-evacuated glass bottle for daily usage. Different aliquots of calibration gas (10-100 μL) were injected into GC to determine linearity (e.g. butane in Figure AI.3). The reproducibility of each gas component is generally 0.3% (1σ).

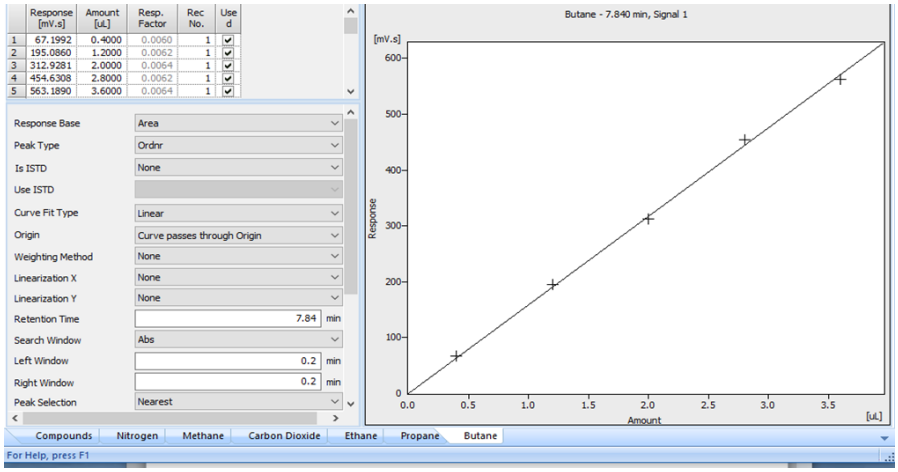

Figure AI.3. TCD response versus the injected amount of butane.

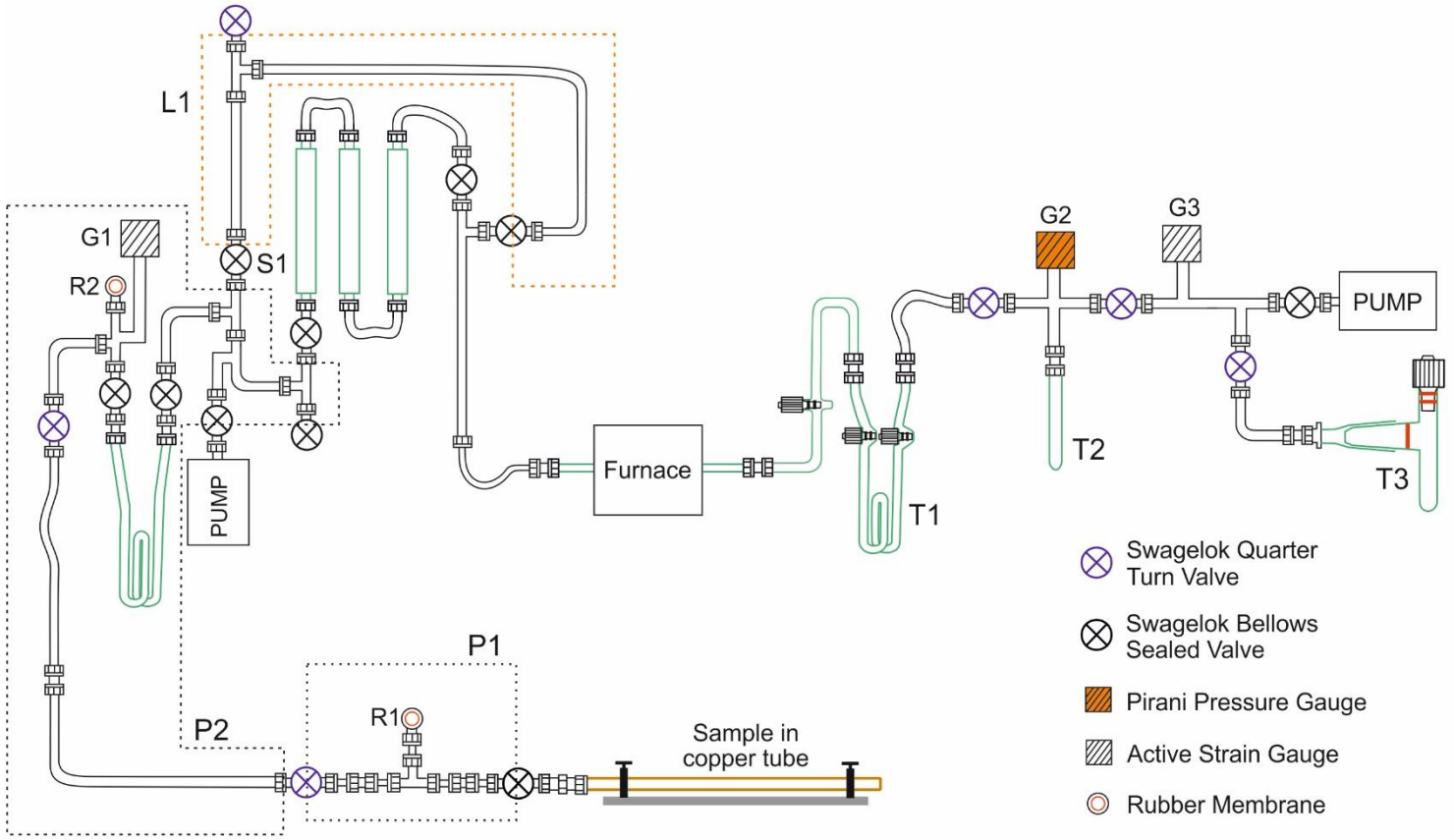

Figure AI.2. Gas extraction and methane combustion line in SUERC. P1 zone is where gas was extracted for GC analysis. Black line: stainless steel piping; Green line: glass. Red line: Rubber sealing.

Carbon and hydrogen stable isotopes of methane

After the bulk gas composition determination, the remaining gas in P1 was expanded further into P2 zone (Figure AI.2). The wet gases (C_{2+}), water and carbon dioxide were trapped in an isopentane slush (~ -160 °C) that a loop filled with isopentane and immersed in liquid nitrogen. Pure oxygen (> 99.99%), of the amount well over stoichiometrically needed, was added through a rubber membrane at R2 to the system via a needle connected to an oxygen SKC Flexfoil bag until the pressure in the system equilibrated with the atmosphere. The valve S1 was then open slowly, and the mixed gas was driven by the pressure gradient and flowed through L1 line and a platinum-granule furnace equipped with a CuO catalyst, kept at the temperature of 900 °C. Methane was combusted into CO_2 and H_2O which then were captured by a removable glass sample tube (T1; Figure AI.2) cooled by liquid nitrogen (-196 °C). The process was considered ended when the reading in pressure gauge G1 was close to 0 mbar. The glass track between the furnace and the cold finger was heated by a heating gun at the end of combustion to avoid water precipitation and adsorption due to the sharp drop of temperature. After combustion, the cold finger was isolated from the furnace. Non-condensable gases were pumped out, and then the liquid nitrogen was replaced by a slush trap (mixed dry ice with acetone, ~ -78 °C), allowing retention of H_2O but vaporisation of CO_2. The separated CO_2 was collected in an adjacent cold finger (T2) cooled by liquid nitrogen and then isolated from the finger holding H_2O (T1). Then CO_2 was released into a calibrated volume, allowing a quantitative check on the chemical reaction by pressure gauge G2. . The CO_2 gas, in the end, was stored by a removable glass sample tube (T3) dipped in liquid nitrogen.

The carbon isotopic composition of combusted CO_2 was determined using a VG SIRA II dual inlet isotope ratio mass spectrometer. The measured results are expressed in delta values relative to a standard based on the equation AI.1:

$$\delta = \left(\frac{R_{sample}}{R_{standard}} - 1\right) * 1000\ (‰) \qquad \text{(AI.1)}$$

R_{sample} and $R_{standard}$ are isotope ratios of samples and standard, respectively. $\delta^{13}C_{CO2}$ is reported relative to the V-PDB international standard (Craig, 1957). The calibration gas

produced from standard reference materials NBS19 and IAEA-CO-1 have daily measured (Dunbar et al., 2016), and showed a replicate uncertainty (1σ) of 0.3 ‰.

The cold finger retaining condensed water was connected to a hydrogen-reducing glass vacuum system attached to a VG Optima dual inlet isotope ratio mass spectrometer (Donnelly et al., 2001). The water was heated to vapour and captured in a small cold finger cooled by liquid nitrogen. This process was repeated three times for full vaporisation of water. Then, the cold finger was isolated from the sample finger, and exposed to a chromium catalyst at 800 °C for reduction of water into H_2. The small cold finger was heated three times to avoid isotopic fractionation. The produced quantity of H_2 was monitored by a pressure transducer. A suitable amount of H_2 was adjusted by a strain-compression device to enter the mass spectrometer. The mass spectrometer then analysed the hydrogen isotope composition of H_2. δD values were expressed relative to V-SMOW (Gonfiantini, 1978) based on Eq AI.1. The system is daily calibrated from in-house reference gas. Before running samples, a calibration water sample, Arctic ice sheet (SUERC standard) which has δD = -150.5‰, was measured to rule out the memory effect in the mass spectrometer. The experimental uncertainty of δD determination is 3 ‰ (1σ).

Noble gases

The gas in the other half of the copper tubes was used to analyse the isotopic composition of noble gases following Györe (2015) using a steel ultra-high vacuum preparation system and a dual collector magnetic sector MAP 215-50 mass spectrometer in a static state (Figure AI.4 and AI.5). The commission and test of the system were carried out and demonstrated in Györe (2015). Here, I give a brief description of the analysis procedures.

The copper tube was attached to the gas-purifying system by Swagelok 3/8” tube fittings. The volume of each section in this system was determined with an uncertainty of 0.5% (1σ). The air in the connection zone was first pumped by a Pfeiffer Vacuum HiPace 80 dual-stage turbo-molecular pump. The pressure was monitored by a Pfeiffer Vacuum PKR 251 Compact Full Range pressure gauge. Once the pressure was below 1×10^{-6} mbar, sample gas was open to V0 zone in the system (Figure AI.4). Then the sample in V0 zone

was isolated from the copper tube and expanded into a known-volume zone of V1 and Pipette No.1. An aliquot of the was taken into a zone where the pressure is monitored by an MKS 615-A Baratron capacitance manometer by a pipette (~1 cm^3), allowing the calculation of the initial pressure of the stored gas in V1. A suitable amount of gas was then expanded into a VG Scienta ST22 titanium sublimation pump to remove the non-noble-gas components (e.g. H_2O, N_2, CO_2) and thermally crack the hydrocarbon molecules (e.g. CH_4, C_2H_6) at 900 °C. Until the pressure monitored by Baratron manometer dropped to be stabilised, the purified gas was then exposed to a SAES GP50 ZrAl getter at 250°C and a ~500 cm^3 reservoir where the gas was finally stored for 20 mins. Different gas aliquots were subsequently taken from the reservoir for noble gas analyses.

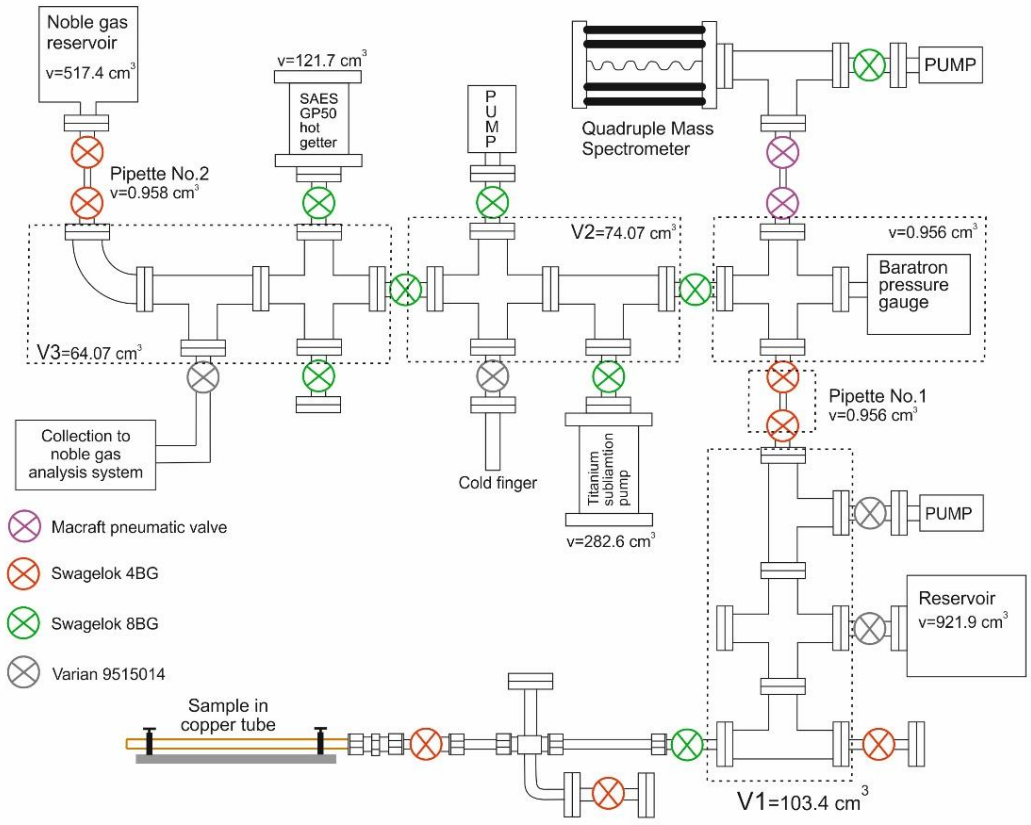

Figure AI.4. Simplified illustration of the gas-purifying system for noble gases in SUERC. Black lines represent stainless steel. Crossed circles represent valves. Redrawn after Györe (2015).

The procedure to analyse each noble gas is different. An aliquot of gas was taken to the mass spectrometer for a semi-quantitative analysis that allowed designing quantitative analysis. For helium, gas was taken from the reservoir and retained in the system exposed to three SAES GP50 ZrAl getters at 250°C and charcoal cooled by liquid nitrogen (capturing Ar, Kr and Xe) for 20 min, and then expanded into the mass spectrometer. For neon analysis, the removal of Ar, Kr and Xe followed the above procedure as for the He analysis. Then the gas was expanded to a Janis cryogenic pump equipped with activated charcoal. Ne was trapped at -243°C for 15 min. Helium was then pumped out by a Pfeiffer Vacuum HiPace 80 dual-stage turbo-molecular pump for 10 sec. Neon was released then by increasing the finger temperature to -173 °C for 10 min for analysis. For argon, to remove the potential non-noble gas components, the gas was exposed only to the three getters for 10 min and then to the liquid nitrogen cooled charcoal for 10 min. He and Ne were removed by pumping. Gas stored in the cooled charcoal was desorbed by heating to room temperature for 10 min and expanded to the mass spectrometer. The purification of Kr and Xe aliquots were the same as for Ar before releasing them from the charcoal. The liquid nitrogen was then replaced with a dry ice-acetone slush trap (-78 °C) for 10 min, allowing desorption of part of captured gas, containing ~100% of Ar, ~15% of Kr and ~5% of Xe, for the first analysis of Kr and Xe. Then the charcoal was isolated from the pumped system for 5 min. After this, the charcoal was open and heated by boiled water to release remained gases for the second run. The sum of Kr and Xe amount in two analyses was used for concentration calculation.

During the analysis of He and Ne, charcoal cooled by liquid nitrogen in the mass spectrometer was used to capture Ar, Kr, Xe and active gases. A cold GP50 getter was open to the mass spectrometer to reduce the hydrogen level. For SQB samples, ^{4}He, all Ar isotopes were measured with a 10^{11} Ω resistance Faraday amplifier, and ^{3}He, all Ne isotopes, ^{84}Kr and ^{132}Xe were measured with a Burle Channeltron electron multiplier operated in pulse counting mode at 2.5 kV. For LPC samples, ^{40}Ar and ^{36}Ar were measured with the Faraday detector, while ^{36}Ar and ^{38}Ar were measured in the multiplier for more precise ^{38}Ar/^{36}Ar ratio determinations.

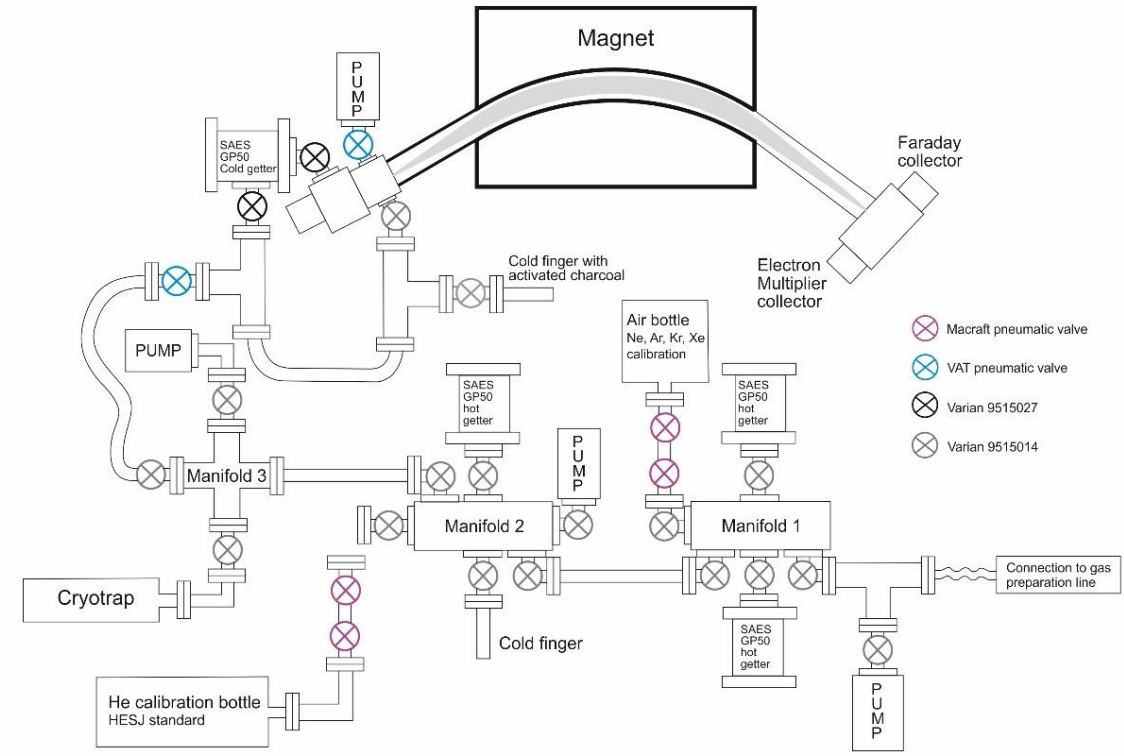

Figure AI.5. Illustrative picture of noble gas purification-separation line in SUERC. Black lines represent stainless steel. Crossed circles represent valves. Redrawn after Györe (2015).

Blank levels for all isotopes were checked weekly by running the same analysis procedure as for sample gas and were negligible compared with the signal of samples. The mass spectrometer (resolution power = ~600) could separate the HD^+ peak from the $^3He^+$ peak. However, the interferences from $^{40}Ar^{2+}$, $^1H^{19}F^+$, $^1H_2{}^{18}O^+$ at ^{20}Ne, $^{20}NeH^+$, $^{63}Cu^{3+}$ at ^{21}Ne, and $CO_2{}^{2+}$ at ^{22}Ne and hydrocarbons occurring at all masses cannot be resolved. The contributions of $^1H^{19}F^+$, $^1H_2{}^{18}O^+$ to total ^{20}Ne and $^{63}Cu^{3+}$ to total ^{21}Ne were quantified to be less than 0.05% and 0.01% (Györe, 2015), respectively. Correction of interference from $^{40}Ar^{2+}$ at ^{20}Ne and $CO_2{}^{2+}$ at ^{22}Ne was achieved by monitoring $40^+/40^{2+}$, $44^+/44^{2+}$ ratios and hydrogen concentration in the dynamic blank and 40^+, 44^+ and $H_2{}^+$ during the Ne analysis assuming linearity from dynamic (pumping) to the sample pressure level. The contribution of $^{20}NeH^+$ to $^{21}Ne^+$ is negligible. By repeated analysis of standards, HESJ international standard (20.63 R_A) for helium (Matsuda et al., 2002), air for neon (Eberhardt et al., 1965;

Györe et al., 2019), argon (Lee et al., 2006; Mark et al., 2011), krypton and xenon (Ozima and Podosek, 2002), the mass fractionation, the reproducibility of the analysing procedures, and mass spectrometer sensitivity were determined (Györe, 2015). The reproducibilities of the analyses of standard gases for He, Ne, Ar, Kr and Xe are listed in Table AI.1. The absolute amounts were calibrated prior from a pyroxene standard CRONUS-P for He (Blard et al., 2015), a quartz standard CREU-1 for Ne (Vermeesch et al., 2015) and a biotite standard GA1550 for Ar (McDougall and Wellman, 2011). Ne and Ar are both checked for elemental fractionation.

Table AI.1. Reproducibility (1σ) of standard gases for He, Ne, Ar, Kr and Xe during analysis.

	SQB samples	LPC samples
^{3}He	1.61%	1.33%
^{4}He	0.37%	0.54%
$^{3}He/^{4}He$	0.80%	0.57%
^{20}Ne	0.65%	0.64%
$^{20}Ne/^{22}Ne$	0.38%	0.33%
$^{21}Ne/^{22}Ne$	1.07%	0.47%
^{40}Ar	0.35%	0.40%
$^{40}Ar/^{36}Ar$	0.30%	0.26%
$^{38}Ar/^{36}Ar$	1.66%	0.23%
^{84}Kr	1.83%	1.34%
^{132}Xe	1.34%	2.52%

Appendix II Noble gas composition in air-saturated water and their solubility-controlled fractionation factor in gas-liquid system

In Chapter 3 and 4, I have used the predicted elemental ratios of noble gas in air-saturated water (ASW) and the solubility-controlled fractionation factors of noble gases from liquid to gas phase. This appendix introduces the calculation procedures of these values in detail.

AII.1 Noble gas composition in ASW

The computation of noble gas composition in ASW is mainly following (Kipfer et al., 2002). In the non-ideal gas and liquid phase, the noble gas solubility is calculated from:

$$\Phi_i p_i = \gamma_i H_i x_i \quad \text{(AII.1)}$$

where p_i is the partial pressure of gas i. x_i is the mole fraction of i in liquid. H is Henry's constant. Φ_i and γ_i are the gas phase fugacity coefficient and liquid phase activity coefficient, respectively, and both equal to ~1 in the surface water. x_i of sole gas in pure water at 101 kPa (1 atm) follows the smoothing equation (Gevantman, 2000):

$$\ln(x_i) = A + B/(T/100) + C \times \ln(T/100) \quad \text{(AII.2)}$$

where T is the temperature in kelvin. A, B and C are the equation constants from Gevantman (2000) (Table AII.1).

Table AII.1. Equation constants of AII.2.

	A	B	C
He	-41.46	42.60	14.01
Ne	-52.86	61.05	18.92
Ar	-57.67	74.76	20.14
Kr	-66.99	91.02	24.22
Xe	-74.74	105.2	27.47

The Henry's constant for each noble gas in pure water at 1 atm then is calculated following Eq AII.1. Henry's constant is a function of temperature (Crovetto et al., 1982). At the same temperature, the solubility of noble gases in ASW is proportional to their partial pressure

in the air. The partial pressure of noble gas (p_i) needs correction from water vapour content (p_w). The partial pressure of noble gas i in the atmosphere is described as:

$$p_i = z_i (p_t - p_w) \qquad \text{(AII.3)}$$

where z_i is the mole fraction of noble gas in dry air (Table AII.2; Ozima and Podosek (2002)). p_t is the total atmospheric pressure.

Table AII.2. The mole fraction of noble gas isotopes in dry air.

	Mole fraction (dry air)
^{20}Ne	1.64×10^{-5}
^{36}Ar	3.12×10^{-5}
^{84}Kr	6.50×10^{-7}
^{132}Xe	2.34×10^{-8}

In addition, the atmospheric pressure drops as altitude increases following a barometric altitude formula (Kipfer et al., 2002):

$$p_l = p_t^{sl} \times \exp(-h/h_t) \qquad \text{(AII.4)}$$

where p_l and h are the local pressure and altitude. p_t^{sl} is the local and sea level pressure. h_t is the typical local scale height (8000-8300 m, (Kipfer et al., 2002)), chosen as 8300 m here.

Excess air which cannot be explained by atmospheric equilibrium is ubiquitous in groundwater (Aeschbach-Hertig et al., 1999, 2000; Heaton and Vogel, 1981; Kipfer et al., 2002; Peeters et al., 2003; Stute et al., 1995). The relative excess abundance of noble gases is almost atmospheric (Heaton and Vogel, 1981). However, in groundwater from some locations, noble gas excess is enriched in heavy noble gases more than the light noble gases, which is recognised as a further fractionation after dissolution by 1) molecular diffusion of gas at the water/air interface (Stute et al., 1995); or 2) re-equilibration of gas between groundwater and trapped air bubbles (Aeschbach-Hertig et al., 2000). Here, I assume that

excess gas has the same composition as that of the atmosphere without further fractionation and a common 10% excess for Ne in both cases (Gilfillan et al., 2008).

In SQB, the noble gas concentrations in ASW are calculated assuming a recharge temperature of 10°C and the local average elevation of 750 m. In LPC, they are corrected for a recharge temperature at 15°C and the average elevation of 1500 m. The calculated results are shown in Table AII.3.

Table AII.3. Concentrations and elemental ratios of noble gases in ASW.

	^{20}Ne ($\times10^{-7}$)	^{36}Ar ($\times10^{-6}$)	^{84}Kr ($\times10^{-8}$)	^{132}Xe ($\times10^{-9}$)	$^{20}Ne/^{36}Ar$	$^{84}Kr/^{36}Ar$	$^{132}Xe/^{36}Ar$
SQB	1.9	1.2	4.8	3.3	0.154	0.040	0.0027
LPC	1.6	1.0	3.8	2.5	0.163	0.039	0.0026

AII.2 Solubility-controlled fractionation factor of noble gases from liquid to gas phase

The calculation in this section is following Ballentine et al. (2002). The solubility-controlled fractionation factor (α) of noble gases is defined as:

$$\alpha = \frac{H_A \frac{\Phi_A}{\gamma_A}}{H_B \frac{\Phi_B}{\gamma_B}} \quad \text{(AII.5)}$$

where *A*, *B* stand for two different noble gas elements. The Henry's constants (in GPa) for noble gases in water at different temperatures can be calculated based on the fitting experimental results from Crovetto et al. (1982) and Smith (1985):

$$\ln(H_i) = \sum_{i=0}^{n} \left(D_i / (0.001T)^i\right) \quad \text{(AII.6)}$$

$$\ln(F_{He}) = \sum_{i=0}^{n} \left(D_i / (0.001T)^i\right) \quad \text{(AII.7)}$$

$$F_{He} = (X_{He}/X_{Ar})_{liquid}/(X_{He}/X_{Ar})_{gas} \quad \text{(AII.8)}$$

where X is the mole fraction. D is the coefficients for the equations AII.6 and AII.7 (Table AII.4; Crovetto et al., 1982; Smith, 1985).

Table AII.4. Coefficients for the fitting equations AII.6 and AII.7.

	D_o	D_1	D_2	D_3
He	-0.00953	0.107722	0.001969	-0.04383
Ne	-7.259	6.95	-1.3826	0.0538
Ar	-9.52	8.83	-1.8959	0.0698
Kr	-6.292	5.612	-0.8881	-0.0458
Xe	-3.902	2.439	0.3863	-0.221

The fugacity coefficient (Φ) is a function of temperature and real molar volume (V_m):

$$\Phi(p,T) = \exp\left(B(T)/V_m + \left(C(T) + B(T)^2/2\ V_m^2\right)\right) \quad \text{(AII.9)}$$

$$pV_m/RT = 1 + B(T)/V_m + C(T)/\ V_m^2 \quad \text{(AII.10)}$$

where p is the hydrostatic pressure, R is the gas constant. $B(T)$ and $C(T)$ are the second and third virial coefficients from Dymond and Smith (1980). Eq AII.10 is solved by using Newton's method. The results converge at 10-14 iterations. Taking the average depth of 410 m in SQB and 970 m in LPC, the hydrostatic pressures and temperatures in the reservoirs are 40 atm and 27 °C (SQB), 95 atm and 44 °C (LPC), respectively, calculated with an assumed geothermal gradient of 0.03 K/m. The calculated B, C and final Φ are listed in Table AII.5.

Table AII.5. Noble gas viral and fugacity coefficients.

	B	C	Φ
SQB			
He	11.73	65.75	1.019
Ne	11.47	237.1	1.019
Ar	-15.06	1135	0.977
Kr	-51.11	3158	0.923
Xe	-127.3	5985	0.802
LPC			
He	11.63	63.49	1.043
Ne	11.75	234.8	1.044

Ar	-12.40	1302	0.964
Kr	-45.11	2916	0.864
Xe	-114.74	5510	0.748

The liquid phase activity coefficient (γ_i) is a function of the salinity (s) and the empirical Setchenow coefficient (k_i) (Ballentine et al., 2002; Smith and Kennedy, 1983):

$$\gamma_i = exp\ (s \times k_i) \quad \text{(AII.11)}$$

$$ki = G_1 + G_2/(0.01T) + G_3\, ln(0.01T) \quad \text{(AII.12)}$$

where Gi are the constants obtained by fitting experimental results from Smith and Kennedy (1983). The calculated Setchenow and liquid phase activity coefficients are displayed in Table AII.6.

Table AII.6. Noble gas Setchenow and liquid phase activity coefficients.

	He	*Ne*	*Ar*	*Kr*	*Xe*
SQB s=0.04 mol/L					
k	0.24	0.27	0.33	0.35	0.37
γ	1.01	1.01	1.01	1.01	1.01
LPC s=0.15 mol/L					
k	0.24	0.24	0.31	0.32	0.34
γ	1.04	1.04	1.05	1.05	1.05

α is then calculated following Eq AII.5 and listed in Table AII.7.

Table AII.7. The solubility-controlled fractionation factors of noble gases from liquid to gas phase.

	$^{4}He/^{36}Ar$	$^{20}Ne/^{36}Ar$	$^{84}Kr/^{36}Ar$	$^{132}Xe\ /^{36}Ar$
SQB	3.27	2.85	0.59	0.41
LPC	2.55	2.33	0.66	0.50

References

Aeschbach-Hertig, W., Peeters, F., Beyerle, U., Kipfer, R., 1999. Interpretation of dissolved atmospheric noble gases in natural waters. Water Resour. Res., 35(9): 2779-2792.

Aeschbach-Hertig, W., Peeters, F., Beyerle, U., Kipfer, R., 2000. Palaeotemperature reconstruction from noble gases in groundwater taking into account equilibration with entrapped air. Nature, 405(6790): 1040-1044.

Al-Jubori, A., Johnston, S., Boyer, C., Lambert, S.W., Bustos, O.A., Pashin, J.C., Wray, A., 2009. Coalbed methane: clean energy for the world. Oilfield Review, 21(2): 4-13.

Allègre, C.J., Moreira, M., Staudacher, T., 1995. $^{4}He/^{3}He$ dispersion and mantle convection. Geophys. Res. Lett., 22(17): 2325-2328.

Ali, J.R., Thompson, G.M., Zhou, M.-F., Song, X., 2005. Emeishan large igneous province, SW China. Lithos, 79(3): 475-489.

American Association of Petroleum Geologists, E.M.D., 2015. Unconventional Energy Resources: 2015 Review. Natural Resources Research, 24(4): 443-508.

Aravena, R., Harrison, S.M., Barker, J.F., Abercrombie, H., Rudolph, D., 2003. Origin of methane in the Elk Valley coalfield, southeastern British Columbia, Canada. Chem. Geol., 195(1–4): 219-227.

Bacon, M., 1995. Coalbed methane: development and techniques used on the Airth No. 1 well in Scotland, International conference on planning for profit: coalbed methane in the UK and Europe

Bacsik, Z., Lopes, J.N.C., Gomes, M.F.C., Jancsó, G., Mink, J., Pádua, A.A.H., 2002. Solubility isotope effects in aqueous solutions of methane. J. Chem. Phys., 116(24): 10816-10824.

Bae, J.-S., Bhatia, S.K., 2006. High-Pressure Adsorption of Methane and Carbon Dioxide on Coal. Energy Fuels, 20(6): 2599-2607.

Ballentine, C.J., 1997. Resolving the mantle He/Ne and crustal $^{21}Ne/^{22}Ne$ in well gases. Earth Planet. Sci. Lett., 152(1): 233-249.

Ballentine, C.J., Burgess, R., Marty, B., 2002. Tracing Fluid Origin, Transport and Interaction in the Crust. In: Porcelli, D., Ballentine, C.J., Wieler, R. (Eds.), Rev. Mineral. Geochem., pp. 539-614.

Ballentine, C.J., Burnard, P.G., 2002. Production, Release and Transport of Noble Gases in the Continental Crust. In: Porcelli, D., Ballentine, C.J., Wieler, R. (Eds.), Rev. Mineral. Geochem., pp. 481-538.

Ballentine, C.J., Marty, B., Sherwood Lollar, B., Cassidy, M., 2005. Neon isotopes constrain convection and volatile origin in the Earth's mantle. Nature, 433(7021): 33-38.

Ballentine, C.J., Mazurek, M., Gautschi, A., 1994. Thermal constraints on crustal rare gas release and migration: Evidence from Alpine fluid inclusions. Geochim. Cosmochim. Acta, 58(20): 4333-4348.

Ballentine, C.J., O'Nions, R.K., 1992. The nature of mantle neon contributions to Vienna Basin hydrocarbon reservoirs. Earth Planet. Sci. Lett., 113(4): 553-567.

Ballentine, C.J., O'Nions, R.K., Coleman, M.L., 1996. A Magnus opus: Helium, neon, and argon isotopes in a North Sea oilfield. Geochim. Cosmochim. Acta, 60(5): 831-849.

Ballentine, C.J., O'Nions, R.K., Oxburgh, E.R., Horvath, F., Deak, J., 1991. Rare gas constraints on hydrocarbon accumulation, crustal degassing and groundwater flow in the Pannonian Basin. Earth Planet. Sci. Lett., 105(1): 229-246.

Ballentine, C.J., Schoell, M., Coleman, D., Cain, B.A., 2001. 300-Myr-old magmatic CO2 in natural gas reservoirs of the west Texas Permian basin. Nature, 409(6818): 327-331.

Bao, Q., 2019. Coalbed Methane System and Its Geological Controls in Dahebian Syncline, Guizhou, China. Master Thesis, China University of Mining and Technology, 89 pp.

Barry, P.H., Kulongoski, J.T., Landon, M.K., Tyne, R.L., Gillespie, J.M., Stephens, M.J., Hillegonds, D.J., Byrne, D.J., Ballentine, C.J., 2018. Tracing enhanced oil recovery signatures in casing gases from the Lost Hills oil field using noble gases. Earth Planet. Sci. Lett., 496: 57-67.

Barry, P.H., Lawson, M., Meurer, W.P., Danabalan, D., Byrne, D.J., Mabry, J.C., Ballentine, C.J., 2017. Determining fluid migration and isolation times in multiphase crustal domains using noble gases. Geology, 45(9): 775-778.

Barry, P.H., Lawson, M., Meurer, W.P., Warr, O., Mabry, J.C., Byrne, D.J., Ballentine, C.J., 2016. Noble gases solubility models of hydrocarbon charge mechanism in the Sleipner Vest gas field. Geochim. Cosmochim. Acta, 194: 291-309.

Battani, A., Sarda, P., Prinzhofer, A., 2000. Basin scale natural gas source, migration and trapping traced by noble gases and major elements: the Pakistan Indus basin. Earth Planet. Sci. Lett., 181(1): 229-249.

Baublys, K.A., Hamilton, S.K., Golding, S.D., Vink, S., Esterle, J., 2015. Microbial controls on the origin and evolution of coal seam gases and production waters of the Walloon Subgroup; Surat Basin, Australia. Int. J. Coal Geol., 147-148: 85-104.

Bernard, B.B., Brooks, J.M., Sackett, W.M., 1976. Natural gas seepage in the Gulf of Mexico. Earth Planet. Sci. Lett., 31(1): 48-54.

Bigeleisen, J., Wolfsberg, M., 1957. Theoretical and Experimental Aspects of Isotope Effects in Chemical Kinetics. In: Prigogine, I., Debye, P. (Eds.), Adv. Chem. Phys., pp. 15-76.

Blard, P.H., Balco, G., Burnard, P.G., Farley, K.A., Fenton, C.R., Friedrich, R., Jull, A.J.T., Niedermann, S., Pik, R., Schaefer, J.M., Scott, E.M., Shuster, D.L., Stuart, F.M., Stute, M., Tibari, B., Winckler, G., Zimmermann, L., 2015. An inter-laboratory comparison of cosmogenic ^{3}He and radiogenic ^{4}He in the CRONUS-P pyroxene standard. Quaternary Geochronology, 26: 11-19.

Blaut, M., 1994. Metabolism of methanogens. Antonie Leeuwenhoek, 66(1): 187-208.

Board, N.E., 2018. Canada's Energy Future 2018: Energy Supply and Demand Projections to 2040.

Botor, D., 2014. Timing of coalification of the upper carboniferous sediments in the upper silesia coal basin on the basis of by apatite fission track and helium dating. Gospodarka Surowcami Mineralnymi / Mineral Resources Management, 30(1): 85-103.

Bourg, I.C., Sposito, G., 2008. Isotopic fractionation of noble gases by diffusion in liquid water: Molecular dynamics simulations and hydrologic applications. Geochim. Cosmochim. Acta, 72(9): 2237-2247.

Brown, H., 1949. Rare gases and formation of the Earth's atmosphere. In: Kuiper, G.P. (Ed.), Atmospheres of the Earth and Planets. University of Chicago Press, pp. 258-266

Burruss, R.C., Laughrey, C.D., 2010. Carbon and hydrogen isotopic reversals in deep basin gas: Evidence for limits to the stability of hydrocarbons. Org. Geochem., 41(12): 1285-1296.

Bustin, R.M., Clarkson, C.R., 1998. Geological controls on coalbed methane reservoir capacity and gas content. Int. J. Coal Geol., 38(1): 3-26.

Butler, W.A., Jeffery, P.M., Reynolds, J.H., Wasserburg, G.J., 1963. Isotopic variations in terrestrial xenon. J. Geophys. Res., 68(10): 3283-3291.

Byrne, D.J., Barry, P.H., Lawson, M., Ballentine, C.J., 2017. Noble gases in conventional and unconventional petroleum systems. Geological Society, London, Special Publications, 468.

Byrne, D.J., Barry, P.H., Lawson, M., Ballentine, C.J., 2018. Determining gas expulsion vs retention during hydrocarbon generation in the Eagle Ford Shale using noble gases. Geochim. Cosmochim. Acta, 241: 240-254.

Byrne, D.J., Barry, P.H., Lawson, M., Ballentine, C.J., 2020. The use of noble gas isotopes to constrain subsurface fluid flow and hydrocarbon migration in the East Texas Basin. Geochim. Cosmochim. Acta, 268: 186-208.

Cai, Y., Liu, D., Yao, Y., Li, J., Qiu, Y., 2011. Geological controls on prediction of coalbed methane of No. 3 coal seam in Southern Qinshui Basin, North China. Int. J. Coal Geol., 88(2–3): 101-112.

Cao, X., Li, S., Xu, L., Guo, L., Liu, L., Zhao, S., Liu, X., Dai, L., 2015. Mesozoic–Cenozoic evolution and mechanism of tectonic geomorphology in the central North China Block: Constraint from apatite fission track thermochronology. Journal of Asian Earth Sciences, 114: 41-53.

Castro, M.C., Jambon, A., Marsily, G., Schlosser, P., 1998. Noble gases as natural tracers of water circulation in the Paris Basin: 1. Measurements and discussion of their origin and mechanisms of vertical transport in the basin. Water Resour. Res., 34(10): 2443-2466.

Ceglarska-Stefańska, G., Brzóska, K., 1998. The effect of coal metamorphism on methane desorption. Fuel, 77(6): 645-648.

Chen, B., Stuart, F.M., Xu, S., Györe, D., Liu, C., 2019a. Evolution of coal-bed methane in Southeast Qinshui Basin, China: Insights from stable and noble gas isotopes. Chem. Geol., 529: 119298.

Chen, S., Tang, D., Tao, S., Yang, Y., Chen, L., 2019b. Current status and key factors for coalbed methane development with multibranched horizontal wells in the southern Qinshui basin of China. Energy Science & Engineering, 7(5): 1572-1587.

Chen, X., 1995. Distribution and origin of Longtan Formation Coals in Guizhou Province. Coal Geology & Exploration, 23(2): 21-24.

Chen, Y., Tang, D., Xu, H., Li, Y., Meng, Y., 2015. Structural controls on coalbed methane accumulation and high production models in the eastern margin of Ordos Basin, China. Journal of Natural Gas Science and Engineering, 23: 524-537.

Chen, Z., Song, Y., Qin, S., 2007. Geochemical characteristics of CBM reservoirs in southern Qinshui Basin. Natural Gas Geoscience, 18: 561-564.

Clayton, C., 1991. Carbon isotope fractionation during natural gas generation from kerogen. Marine and Petroleum Geology, 8(2): 232-240.

Clayton, J.L., 1998. Geochemistry of coalbed gas - A review. Int. J. Coal Geol., 35(1): 159-173.

Conrad, R., 2005. Quantification of methanogenic pathways using stable carbon isotopic signatures: a review and a proposal. Org. Geochem., 36(5): 739-752.

Craig, H., 1957. Isotopic standards for carbon and oxygen and correction factors for mass-spectrometric analysis of carbon dioxide. Geochim. Cosmochim. Acta, 12(1): 133-149.

Craig, H., 1978. A mantle helium component in Circum-Pacific volcanic gases: Hakone, the Marianas and Mt. Lassen. Terrestrial Rare Gases.

Craig, H., Lupton, J.E., 1976. Primordial neon, helium, and hydrogen in oceanic basalts. Earth Planet. Sci. Lett., 31(3): 369-385.

Criss, R.E., 1999. Principles of stable isotope distribution. Oxford University Press New York

Crovetto, R., Fernández-Prini, R., Japas, M.L., 1982. Solubilities of inert gases and methane in H_2O and in D_2O in the temperature range of 300 to 600 K. The Journal of Chemical Physics, 76(2): 1077-1086.

Darrah, T.H., Jackson, R.B., Vengosh, A., Warner, N.R., Whyte, C.J., Walsh, T.B., Kondash, A.J., Poreda, R.J., 2015. The evolution of Devonian hydrocarbon gases in shallow aquifers of the northern Appalachian Basin: Insights from integrating noble gas and hydrocarbon geochemistry. Geochim. Cosmochim. Acta, 170: 321-355.

Darrah, T.H., Vengosh, A., Jackson, R.B., Warner, N.R., Poreda, R.J., 2014. Noble gases identify the mechanisms of fugitive gas contamination in drinking-water wells overlying the Marcellus and Barnett Shales. Proceedings of the National Academy of Sciences, 111(39): 14076-14081.

Davis, J.B., Squires, R.M., 1954. Detection of Microbially Produced Gaseous Hydrocarbons Other than Methane. Science, 119(3090): 381.

Dawson, K.S., Strąpoć, D., Huizinga, B., Lidstrom, U., Ashby, M., Macalady, J.L., 2012. Quantitative Fluorescence *In Situ* Hybridization Analysis of Microbial Consortia from a Biogenic Gas Field in Alaska's Cook Inlet Basin. Appl. Environ. Microbiol., 78(10): 3599-3605.

Di, G., Yong, Q., Tong-sheng, Y., 2009. CBM geology and exploring-developing stratagem in Guizhou Province, China. Procedia Earth and Planetary Science, 1(1): 882-887.

Donnelly, T., Waldron, S., Tait, A., Dougans, J., Bearhop, S., 2001. Hydrogen isotope analysis of natural abundance and deuterium-enriched waters by reduction over chromium on-line to a dynamic dual inlet isotope-ratio mass spectrometer. Rapid Commun. Mass Spectrom., 15(15): 1297-1303.

Dou, X., 2012. Tectonic Evolution and Its Control on Coalbed Methane Reservoiring in Western Guizhou, Doctoral Thesis, China University of Mining and Technology, 152 pp.

Du, Z., Wu, Y., 2019. CBM Geological Condition and Exploitation Potential Assessment in Yangmeishu Syncline, Liupanshui City. Coal Geology of China, 31(7): 27-31.

Dudley, B., 2019. BP Statistical Review of World Energy, BP Statistical Review, London, UK.

Dunbar, E., Cook, G.T., Naysmith, P., Tripney, B.G., Xu, S., 2016. AMS ^{14}C Dating at the Scottish Universities Environmental Research Centre (SUERC) Radiocarbon Dating Laboratory. Radiocarbon, 58(1): 9-23.

Dymond, J.H., Smith, E.B., 1980. The virial coefficients of pure gases and mixtures: a critical compilation. Oxford: Clarendon Press

Eberhardt, P., Eugster, O., Marti, K., 1965. Notizen: A Redetermination of the Isotopic Composition of Atmospheric Neon, Zeitschrift für Naturforschung A, pp. 623.

EIA, 2010. International Energy Outlook, U.S. Energy Information Administration

EIA, 2018. U.S. Crude Oil and Natural Gas Proved Reserves, Year-end 2017, U.S. Energy Information Administration.

EIA, 2019. Annual Energy Outlook 2019, US Energy Information Administration, Washington, DC.

Elliot, T., Ballentine, C.J., O'Nions, R.K., Ricchiuto, T., 1993. Carbon, helium, neon and argon isotopes in a Po basin (northern Italy) natural gas field. Chem. Geol., 106(3): 429-440.

Faiz, M., Hendry, P., 2006. Significance of microbial activity in Australian coal bed methane reservoirs — a review. Bulletin of Canadian Petroleum Geology, 54(3): 261-272.

Flores, R.M., 1998. Coalbed methane: From hazard to resource. Int. J. Coal Geol., 35(1–4): 3-26.

Flores, R.M., Rice, C.A., Stricker, G.D., Warden, A., Ellis, M.S., 2008. Methanogenic pathways of coal-bed gas in the Powder River Basin, United States: The geologic factor. Int. J. Coal Geol., 76(1–2): 52-75.

FYP, 2006. The Eleventh Five-year Plan of CBM Development and Utilization, China's National Energy Administration, Beijing.

FYP, 2011. The Twelfth Five-year Plan of CBM Development and Utilization, China's National Energy Administration, Beijing.

FYP, 2016. The Thirteenth Five-year Plan of CBM Development and Utilization, China's National Energy Administration, Beijing.

Galloway, W.E., 2008. Chapter 15 Depositional Evolution of the Gulf of Mexico Sedimentary Basin. In: Miall, A.D. (Ed.), Sedimentary Basins of the World. Elsevier, pp. 505-549.

Games, L.M., HayesRobert, J.M., Gunsalus, P., 1978. Methane-producing bacteria: natural fractionations of the stable carbon isotopes. Geochim. Cosmochim. Acta, 42(8): 1295-1297.

Gautheron, C., Moreira, M., 2002. Helium signature of the subcontinental lithospheric mantle. Earth Planet. Sci. Lett., 199(1): 39-47.

Geny, F., 2010. Can Unconventional Gas be a Game Changer in European Gas Markets? Oxford Institute for Energy Studies

Gevantman, L., 2000. Solubility of selected gases in water. Nitric oxide (NO), 308(3.348): 10-4.

Gharrabi, M., Velde, B., 1995. Clay mineral evolution in the Illinois Basin and its causes. Clay Miner., 30(4): 353-364.

Gilfillan, S.M.V., Ballentine, C.J., Holland, G., Blagburn, D., Lollar, B.S., Stevens, S., Schoell, M., Cassidy, M., 2008. The noble gas geochemistry of natural CO_2 gas reservoirs from the Colorado Plateau and Rocky Mountain provinces, USA. Geochim. Cosmochim. Acta, 72(4): 1174-1198.

Gilfillan, S.M.V., Lollar, B.S., Holland, G., Blagburn, D., Stevens, S., Schoell, M., Cassidy, M., Ding, Z., Zhou, Z., Lacrampe-Couloume, G., Ballentine, C.J., 2009. Solubility trapping in formation water as dominant CO_2 sink in natural gas fields. Nature, 458(7238): 614-618.

Gilfillan, S.M.V., Wilkinson, M., Haszeldine, R.S., Shipton, Z.K., Nelson, S.T., Poreda, R.J., 2011. He and Ne as tracers of natural CO2 migration up a fault from a deep reservoir. International Journal of Greenhouse Gas Control, 5(6): 1507-1516.

Golding, S.D., Boreham, C.J., Esterle, J.S., 2013. Stable isotope geochemistry of coal bed and shale gas and related production waters: A review. Int. J. Coal Geol., 120: 24-40.

Gonfiantini, R., 1978. Standards for stable isotope measurements in natural compounds. Nature, 271: 534.

Gray, I., 1987. Reservoir Engineering in Coal Seams: Part 1-The Physical Process of Gas Storage and Movement in Coal Seams. SPE-12514-PA, 2(01): 28-34.

Green, M.S., Flanegan, K.C., Gilcrease, P.C., 2008. Characterization of a methanogenic consortium enriched from a coalbed methane well in the Powder River Basin, U.S.A. Int. J. Coal Geol., 76(1–2): 34-45.

Gui, B., 1999. Geological characteristics and enrichment controlling factors of coalbed methane in Liupan Shui region. Acta Petrolei Sinica, 20(3): 31-37.

Gunter, W.D., Gentzis, T., Rottenfusser, B.A., Richardson, R.J.H., 1997. Deep coalbed methane in Alberta, Canada: A fuel resource with the potential of zero greenhouse gas emissions. Energy Conversion and Management, 38, Supplement: S217-S222.

Györe, D., 2015. Noble gases as tracers of injected CO_2 in the Cranfield enhanced oil recovery field. Doctoral Thesis, University of Glasgow.

Györe, D., Gilfillan, S.M.V., Stuart, F.M., 2017. Tracking the interaction between injected CO_2 and reservoir fluids using noble gas isotopes in an analogue of large-scale carbon capture and storage. Appl. Geochem., 78: 116-128.

Györe, D., McKavney, R., Gilfillan, S.M.V., Stuart, F.M., 2018. Fingerprinting coal-derived gases from the UK. Chem. Geol., 480: 75-85.

Györe, D., Stuart, F.M., Gilfillan, S.M.V., Waldron, S., 2015. Tracing injected CO_2 in the Cranfield enhanced oil recovery field (MS, USA) using He, Ne and Ar isotopes. International Journal of Greenhouse Gas Control, 42: 554-561.

Györe, D., Tait, A., Hamilton, D., Stuart, F.M., 2019. The formation of NeH^+ in static vacuum mass spectrometers and re-determination of $^{21}Ne/^{20}Ne$ of air. Geochim. Cosmochim. Acta, 263: 1-12.

Han, F., Busch, A., Krooss, B.M., Liu, Z., van Wageningen, N., Yang, J., 2010a. Experimental Study on Fluid Transport Processes in the Cleat and Matrix Systems of Coal. Energy Fuels, 24(12): 6653-6661.

Han, F., Busch, A., van Wageningen, N., Yang, J., Liu, Z., Krooss, B.M., 2010b. Experimental study of gas and water transport processes in the inter-cleat (matrix) system of coal: Anthracite from Qinshui Basin, China. Int. J. Coal Geol., 81(2): 128-138.

Harris, S.H., Smith, R.L., Barker, C.E., 2008. Microbial and chemical factors influencing methane production in laboratory incubations of low-rank subsurface coals. Int. J. Coal Geol., 76(1–2): 46-51.

He, B., Xu, Y., Wang, Y., Xiao, L., 2005. Nature of the Dongwu movement and its temporal and spatial evolution. Earth science, 30(1): 89-96.

Heaton, T.H.E., Vogel, J.C., 1981. "Excess air" in groundwater. Journal of Hydrology, 50: 201-216.

Hildenbrand, A., Ghanizadeh, A., Krooss, B.M., 2012. Transport properties of unconventional gas systems. Marine and Petroleum Geology, 31(1): 90-99.

Hildenbrand, A., Schlömer, S., Krooss, B.M., 2002. Gas breakthrough experiments on fine-grained sedimentary rocks. Geofluids, 2(1): 3-23.

Hiyagon, H., Ozima, M., Marty, B., Zashu, S., Sakai, H., 1992. Noble gases in submarine glasses from mid-oceanic ridges and Loihi seamount: Constraints on the early history of the Earth. Geochim. Cosmochim. Acta, 56(3): 1301-1316.

Holland, G., Lollar, B.S., Li, L., Lacrampe-Couloume, G., Slater, G.F., Ballentine, C.J., 2013. Deep fracture fluids isolated in the crust since the Precambrian era. Nature, 497(7449): 357-360.

Hosgörmez, H., 2007. Origin and secondary alteration of coalbed and adjacent rock gases in the Zonguldak Basin, western Black Sea Turkey. Geochem. J., 41(3): 201-211.

Hoşgörmez, H., Namık Yalçın, M., Cramer, B., Gerling, P., Faber, E., Schaefer, R.G., Mann, U., 2002. Isotopic and molecular composition of coal-bed gas in the Amasra region (Zonguldak basin—western Black Sea). Org. Geochem., 33(12): 1429-1439.

Hu, G., Li, J., Ma, C., Li, Z., Zhang, M., Zhou, Q., 2007. Characteristics and Implications of the Carbon Isotope Fractionation of Desorbed Coalbed Methane in Qinshui Coalbed Methane Field, China. Earth Science Frontiers, 14(6): 267-272.

Hu, G., Liu, S., Li, J., Zhang, L., Li, Z., 2001. Origin of coal-bed gases in Jincheng area of Qinshui Basin. Oil and Gas Geology, 22: 319-321.

Hunt, J.M., 1979. Petroleum Geochemistry and Geology. W. H. Freeman and Co.

Jähne, B., Heinz, G., Dietrich, W., 1987. Measurement of the diffusion coefficients of sparingly soluble gases in water. Journal of Geophysical Research: Oceans, 92(C10): 10767-10776.

Jeris, J.S., McCarty, P.L., 1965. The Biochemistry of Methane Fermentation Using C14 Tracers. Journal (Water Pollution Control Federation), 37(2): 178-192.

Jones, W.J., Leigh, J.A., Mayer, F., Woese, C.R., Wolfe, R.S., 1983. Methanococcus jannaschii sp. nov., an extremely thermophilic methanogen from a submarine hydrothermal vent. Arch. Microbiol., 136(4): 254-261.

Jüntgen, H., Karweil, J., 1966. Gasbildung und gasspeicherung in steinkohlenflozen. Part I and II: Erdol and Kohle, Erdgas, Petrochemie, 19: 251-258, 339-344.

Jüntgen, H., Klein, J., 1975. Entstehung von erdgas gus kohligen sedimenten: Erdol and Kohle. Erdgas, Petrochemie, Erganzungsband, 1: 52-69.

Kaneoka, I., 1980. Rare gas isotopes and mass fractionation: An indicator of gas transport into or from a magma. Earth Planet. Sci. Lett., 48(2): 284-292.

Karacan, C.Ö., Ruiz, F.A., Cotè, M., Phipps, S., 2011. Coal mine methane: A review of capture and utilization practices with benefits to mining safety and to greenhouse gas reduction. Int. J. Coal Geol., 86(2): 121-156.

Kennedy, B.M., Hiyagon, H., Reynolds, J.H., 1990. Crustal neon: a striking uniformity. Earth Planet. Sci. Lett., 98(3): 277-286.

Kinnon, E.C.P., Golding, S.D., Boreham, C.J., Baublys, K.A., Esterle, J.S., 2010. Stable isotope and water quality analysis of coal bed methane production waters and gases from the Bowen Basin, Australia. Int. J. Coal Geol., 82(3–4): 219-231.

Kipfer, R., Aeschbach-Hertig, W., Peeters, F., Stute, M., 2002. Noble Gases in Lakes and Ground Waters. In: Porcelli, D., Ballentine, C.J., Wieler, R. (Eds.), Rev. Mineral. Geochem., pp. 615-700.

Kolata, D.R., Nelson, W.J., 1990. Tectonic History of the Illinois Basin. In: Leighton, M.W., Kolata, D.R., Oltz, D.F., Eidel, J.J. (Eds.), Interior Cratonic Basins American Association of Petroleum Geologists.

Kotarba, M.J., 2001. Composition and origin of coalbed gases in the Upper Silesian and Lublin basins, Poland. Org. Geochem., 32(1): 163-180.

Kotarba, M.J., Rice, D.D., 2001. Composition and origin of coalbed gases in the Lower Silesian basin, southwest Poland. Appl. Geochem., 16(7–8): 895-910.

Lau, H.C., Li, H., Huang, S., 2017. Challenges and Opportunities of Coalbed Methane Development in China. Energy Fuels, 31(5): 4588-4602.

Law, B.E., 1992. Thermal maturity patterns of Cretaceous and Tertiary rocks, San Juan Basin, Colorado and New Mexico. GSA Bulletin, 104(2): 192-207.

Laxminarayana, C., Crosdale, P.J., 1999. Role of coal type and rank on methane sorption characteristics of Bowen Basin, Australia coals. Int. J. Coal Geol., 40(4): 309-325.

Lee, J.-Y., Marti, K., Severinghaus, J.P., Kawamura, K., Yoo, H.-S., Lee, J.B., Kim, J.S., 2006. A redetermination of the isotopic abundances of atmospheric Ar. Geochim. Cosmochim. Acta, 70(17): 4507-4512.

Lei, B., Qin, Y., Gao, D., Fu, X., Wang, G.G.X., Zou, M., Shen, J., 2012. Vertical Diversity of Coalbed Methane Content and its Geological Controls in the Qingshan Syncline, Western Guizhou Province, China. Energy Exploration & Exploitation, 30(1): 43-57.

Levine, J.R., 1993. Coalification: The Evolution of Coal as Source Rock and Reservoir Rock for Oil and Gas. In: Law, B.E., Rice, D.D. (Editors), Hydrocarbons from Coal. American Association of Petroleum Geologists, pp. 39-77.

Li, B., 2015. Mineralogy and Geochemistry of Longtan Formation Coals of Late Permian in the Western Guizhou Province, Southwest China, Doctoral Thesis, China University of Geosciences, 115 pp.

Li, J., Bai, P., Mao, H., Han, W., Wang, X., Zhang, J., 2014. Analysis of geochemistry characteristics and its origin of CBM in Zhengzhuang and Hudi blocks. Journal of China Coal Society, 39(9): 1802-1811.

Lippmann-Pipke, J., Sherwood Lollar, B., Niedermann, S., Stroncik, N.A., Naumann, R., van Heerden, E., Onstott, T.C., 2011. Neon identifies two billion year old fluid component in Kaapvaal Craton. Chem. Geol., 283(3): 287-296.

Liu, C., Zhu, J., Che, C., Yang, H., Fan, M., 2009. Methodologies and results of the latest assessment of coalbed methane resources in China. Natural gas industry, 29(11): 130-132.

Liu, J., Nechaev, V.P., Dai, S., Song, H., Nechaeva, E.V., Jiang, Y., Graham, I.T., French, D., Yang, P., Hower, J.C., 2020. Evidence for multiple sources for inorganic components in the Tucheng coal deposit, western Guizhou, China and the lack of critical-elements. Int. J. Coal Geol., 223: 103468.

Liu, S.-Q., Sang, S.-X., Liu, H.-H., Zhu, Q.-P., 2015. Growth characteristics and genetic types of pores and fractures in a high-rank coal reservoir of the southern Qinshui basin. Ore Geology Reviews, 64: 140-151.

Luke, H., Brueckner, M., Emmanouil, N., 2018. Unconventional gas development in Australia: A critical review of its social license. The Extractive Industries and Society, 5(4): 648-662.

Luo, D., Dai, Y., 2009. Economic evaluation of coalbed methane production in China. Energy Policy, 37(10): 3883-3889.

Luo, X., Gong, S., Sun, F.J., Wang, Z.H., Qi, J.S., 2017. Effect of volcanic activity on hydrocarbon generation: Examples in Songliao, Qinshui, and Bohai Bay Basins in China. Journal of Natural Gas Science and Engineering, 38: 218-234.

Łuszczak, K., Persano, C., Stuart, F.M., 2018. Early Cenozoic Denudation of Central West Britain in Response to Transient and Permanent Uplift Above a Mantle Plume. Tectonics, 37(3): 914-934.

Lv, Y., Tang, D., Xu, H., Luo, H., 2012. Production characteristics and the key factors in high-rank coalbed methane fields: A case study on the Fanzhuang Block, Southern Qinshui Basin, China. Int. J. Coal Geol., 96–97: 93-108.

Lyu, Z., Shao, N., Akinyemi, T., Whitman, W.B., 2018. Methanogenesis. Curr. Biol., 28(13): R727-R732.

Ma, X., Song, Y., Liu, S., Jiang, L., Hong, F., 2016. Experimental study on history of methane adsorption capacity of Carboniferous-Permian coal in Ordos Basin, China. Fuel, 184: 10-17.

Mark, D.F., Stuart, F.M., de Podesta, M., 2011. New high-precision measurements of the isotopic composition of atmospheric argon. Geochim. Cosmochim. Acta, 75(23): 7494-7501.

Martel, D.J., O'Nions, R.K., Hilton, D.R., Oxburgh, E.R., 1990. The role of element distribution in production and release of radiogenic helium: the Carnmenellis Granite, southwest England. Chem. Geol., 88(3): 207-221.

Marty, B., 1984. On the noble gas, isotopic fractionation in naturally occurring gases. Geochem. J., 18(3): 157-162.

Massarotto, P., 2002. 4-D coal permeability under true triaxial stress and constant volume conditions. PhD Thesis, University of Queensland, 140 pp.

Mastalerz, M., 2014. Chapter 7 - Coal Bed Methane: Reserves, Production and Future Outlook. In: Letcher, T.M. (Ed.), Future Energy (Second Edition). Elsevier, Boston, pp. 145-158.

Matsuda, J., Matsumoto, T., Sumino, H., Nagao, K., Yamamoto, J., Miura, Y., Kaneoka, I., Takahata, N., Sano, Y., 2002. The 3He/4He ratio of the new internal He Standard of Japan (HESJ). Geochem. J., 36(2): 191-195.

McDougall, I., Wellman, P., 2011. Calibration of GA1550 biotite standard for K/Ar and $^{40}Ar/^{39}Ar$ dating. Chem. Geol., 280(1): 19-25.

McElwain, J.C., Wade-Murphy, J., Hesselbo, S.P., 2005. Changes in carbon dioxide during an oceanic anoxic event linked to intrusion into Gondwana coals. Nature, 435(7041): 479-482.

McGlade, C., Speirs, J., Sorrell, S., 2013. Unconventional gas – A review of regional and global resource estimates. Energy, 55: 571-584.

McIntosh, J., Martini, A., Petsch, S., Huang, R., Nüsslein, K., 2008. Biogeochemistry of the Forest City Basin coalbed methane play. Int. J. Coal Geol., 76(1): 111-118.

McIntosh, J.C., Warwick, P.D., Martini, A.M., Osborn, S.G., 2010. Coupled hydrology and biogeochemistry of Paleocene–Eocene coal beds, northern Gulf of Mexico. GSA Bulletin, 122(7-8): 1248-1264.

McKavney, R., 2019. Geochemical characteristics of unconventional gas resources in the UK and the applications for gas tracing. Doctoral Thesis, University of Edinburgh, 267 pp.

Milewska-Duda, J., Duda, J., Nodzeñski, A., Lakatos, J., 2000. Absorption and Adsorption of Methane and Carbon Dioxide in Hard Coal and Active Carbon. Langmuir, 16(12): 5458-5466.

Mishima, K., Sumino, H., Yamada, T., Ieki, S., Nagakura, N., Otono, H., Oide, H., 2018. Accurate Determination of the Absolute $^{3}He/^{4}He$ Ratio of a Synthesized Helium Standard Gas (Helium Standard of Japan, HESJ): Toward Revision of the Atmospheric $^{3}He/^{4}He$ Ratio. Geochemistry, Geophysics, Geosystems, 19(10): 3995-4005.

Moore, M.T., Vinson, D.S., Whyte, C.J., Eymold, W.K., Walsh, T.B., Darrah, T.H., 2018. Differentiating between biogenic and thermogenic sources of natural gas in coalbed methane reservoirs from the Illinois Basin using noble gas and hydrocarbon geochemistry. Geological Society, London, Special Publications, 468.

Moore, T.A., 2012. Coalbed methane: A review. Int. J. Coal Geol., 101: 36-81.

Morrison, P., Pine, J., 1955. Radiogenic origin of the helium isotopes in rock. Ann. N. Y. Acad. Sci., 62(3): 71-92.

Niedermann, S., Bach, W., Erzinger, J., 1997. Noble gas evidence for a lower mantle component in MORBs from the southern East Pacific Rise: Decoupling of helium and neon isotope systematics. Geochim. Cosmochim. Acta, 61(13): 2697-2715.

Niemann, M., Whiticar, J.M., 2017. Stable Isotope Systematics of Coalbed Gas during Desorption and Production. Geosciences, 7(2).

Ning, J., 2017. China Statistical Yearbook 2017, National Bureau of Statistics of China.

Ozima, M., Podosek, F.A., 2002. Noble gas geochemistry. Cambridge University Press, Cambridge

Park, S.Y., Liang, Y., 2016. Biogenic methane production from coal: A review on recent research and development on microbially enhanced coalbed methane (MECBM). Fuel, 166: 258-267.

Peeters, F., Beyerle, U., Aeschbach-Hertig, W., Holocher, J., Brennwald, M.S., Kipfer, R., 2003. Improving noble gas based paleoclimate reconstruction and groundwater dating using $^{20}Ne/^{22}Ne$ ratios. Geochim. Cosmochim. Acta, 67(4): 587-600.

Phinney, D., Tennyson, J., Frick, U., 1978. Xenon in CO_2 well gas revisited. Journal of Geophysical Research: Solid Earth, 83(B5): 2313-2319.

Podosek, F.A., Honda, M., Ozima, M., 1980. Sedimentary noble gases. Geochim. Cosmochim. Acta, 44(11): 1875-1884.

Porcelli, D., Ballentine, C.J., 2002. Models for Distribution of Terrestrial Noble Gases and Evolution of the Atmosphere. Rev. Mineral. Geochem., 47(1): 411-480.

Prinz, D., Littke, R., 2005. Development of the micro- and ultramicroporous structure of coals with rank as deduced from the accessibility to water. Fuel, 84(12): 1645-1652.

Prinzhofer, A., Pernaton, É., 1997. Isotopically light methane in natural gas: bacterial imprint or diffusive fractionation? Chem. Geol., 142(3): 193-200.

Prinzhofer, A.A., Huc, A.Y., 1995. Genetic and post-genetic molecular and isotopic fractionations in natural gases. Chem. Geol., 126(3): 281-290.

Profiles, C.M.M.C., 2015. Chapter 6: Canada U.S. Environmental Protection Agency.

Pujol, M., Van den Boorn, S., Bourdon, B., Brennwald, M., Kipfer, R., 2018. Physical processes occurring in tight gas reservoirs from Western Canadian Sedimentary Basin: Noble gas signature. Chem. Geol., 480: 128-138.

Qin, S., Tang, X., Song, Y., Wang, H., 2006. Distribution and fractionation mechanism of stable carbon isotope of coalbed methane. Science in China Series D: Earth Sciences, 49(12): 1252-1258.

Qin, Y., Ye, J., 2015. A review on development of CBM industry in China, AAPG Asia Pacific Region, Geoscience Technology Workshop, Opportunities and Advancements in Coal Bed Methane in the Asia Pacific, Brisbane, Queensland, Australia, Feb

Rahman, M.W., Rimmer, S.M., Rowe, H.D., Huggett, W.W., 2017. Carbon isotope analysis of whole-coal and vitrinite from intruded coals from the Illinois Basin: No isotopic evidence for thermogenic methane generation. Chem. Geol., 453: 1-11.

Raza, A., Hill, K.C., Korsch, R.J., 2009. Mid-Cretaceous uplift and denudation of the Bowen and Surat Basins, eastern Australia: relationship to Tasman Sea rifting from apatite fission-track and vitrinite-reflectance data. Australian Journal of Earth Sciences, 56(3): 501-531.

Ren, P., Xu, H., Tang, D., Li, Y., Sun, C., Tao, S., Li, S., Xin, F., Cao, L., 2018. The identification of coal texture in different rank coal reservoirs by using geophysical logging data in northwest Guizhou, China: Investigation by principal component analysis. Fuel, 230: 258-265.

Ren, Z., Xiao, H., Liu, L., Zhang, S., Qin, Y., Wei, C., 2005. The evidence of fission-track data for the study of tectonic thermal history in Qinshui Basin. Chin. Sci. Bull., 50: 104-110.

Ren, Z., Zhao, C., Chen, G., 1999. Tectonic thermal events of late Mesozoic in Qinshui Basin. Oil and Gas Geology, 20(1): 46-48.

Ren, Z., Zhao, Z., 1997. Late Mesozoic Comparative Research on the Geothermal Field of the Ordos Basin and Qinshui Basin. Acta Sedimentologica Sinica, 15(2): 134-137.

Rice, D.D., 1993. Composition and origins of coalbed gas. In: Law, B.E., Rice, D.D. (Editors), Hydrocarbons from Coal American Association of Petroleum Geologists, pp. 159-184.

Rice, D.D., Claypool, G.E., 1981. Generation, accumulation, and resource potential of biogenic gas. AAPG Bulletin, 65(1): 5-25.

Rogers, H., 2011. Shale gas—the unfolding story. Oxford Review of Economic Policy, 27(1): 117-143.

Sathaye, K.J., Larson, T.E., Hesse, M.A., 2016a. Noble gas fractionation during subsurface gas migration. Earth Planet. Sci. Lett., 450: 1-9.

Sathaye, K.J., Smye, A.J., Jordan, J.S., Hesse, M.A., 2016b. Noble gases preserve history of retentive continental crust in the Bravo Dome natural CO_2 field, New Mexico. Earth Planet. Sci. Lett., 443: 32-40.

Schimmelmann, A., Lewan, M.D., Wintsch, R.P., 1999. D/H isotope ratios of kerogen, bitumen, oil, and water in hydrous pyrolysis of source rocks containing kerogen types I, II, IIS, and III. Geochim. Cosmochim. Acta, 63(22): 3751-3766.

Schimmelmann, A., Mastalerz, M., Gao, L., Sauer, P.E., Topalov, K., 2009. Dike intrusions into bituminous coal, Illinois Basin: H, C, N, O isotopic responses to rapid and brief heating. Geochim. Cosmochim. Acta, 73(20): 6264-6281.

Schimmelmann, A., Sessions, A.L., Mastalerz, M., 2006. Hydrogen Isotopic (D/H) Composition of Organic Matter During Diagenesis and Thermal Maturation. Annu. Rev. Earth Planet. Sci., 34(1): 501-533.

Schoell, M., 1980. The hydrogen and carbon isotopic composition of methane from natural gases of various origins. Geochim. Cosmochim. Acta, 44(5): 649-661.

Schoell, M., 1988. Multiple origins of methane in the Earth. Chem. Geol., 71(1): 1-10.

Schopf, J.M., 1956. A definition of coal. Econ. Geol., 51(6): 521-527.

Scott, A.R., 2002. Hydrogeologic factors affecting gas content distribution in coal beds. Int. J. Coal Geol., 50(1–4): 363-387.

Scott, A.R., Kaiser, W.R., Ayers, W.B., 1994. Thermogenic and secondary biogenic gases, San Juan Basin, Colorado and New Mexico; implications for coalbed gas producibility. AAPG Bulletin, 78(8): 1186-1209.

Sessions, A.L., Sylva, S.P., Summons, R.E., Hayes, J.M., 2004. Isotopic exchange of carbon-bound hydrogen over geologic timescales 11Associate editor: J. Horita. Geochim. Cosmochim. Acta, 68(7): 1545-1559.

Shan, Y., Bi, C., Chi, H., 2018. Geologcial characteristics of coalbed methane and optimization for favorable productive intervals of Yangmeishu syncline in Liupanshui area. Natural Gas Geoscience, 29(1): 122-129.

Sherwood Lollar, B., Ballentine, C.J., Onions, R.K., 1997. The fate of mantle-derived carbon in a continental sedimentary basin: Integration of CHe relationships and stable isotope signatures. Geochim. Cosmochim. Acta, 61(11): 2295-2307.

Shimizu, S., Akiyama, M., Naganuma, T., Fujioka, M., Nako, M., Ishijima, Y., 2007. Molecular characterization of microbial communities in deep coal seam groundwater of northern Japan. Geobiol., 5(4): 423-433.

Smith, J.W., Rigby, D., Gould, K.W., Hart, G., Hargraves, A.J., 1985. An isotopic study of hydrocarbon generation processes. Org. Geochem., 8(5): 341-347.

Smith, S., 1985. Noble gas solubility in water at high temperature. EOS, 66: 397.

Smith, S.P., Kennedy, B.M., 1983. The solubility of noble gases in water and in NaCl brine. Geochim. Cosmochim. Acta, 47(3): 503-515.

Song, Y., Liu, S., Zhang, Q., Tao, M., Zhao, M., Hong, F., 2012. Coalbed methane genesis, occurrence and accumulation in China. Petroleum Science, 9(3): 269-280.

Song, Y., Ma, X., Liu, S., Jiang, L., Hong, F., Qin, Y., 2018. Accumulation conditions and key technologies for exploration and development of Qinshui coalbed methane field. Petroleum Research, 3(4): 320-335.

Soot, P.M., 1988. Non-conventional fuel tax credit. Geology and coal-bed methane resources of the northern San Juan Basin, Colorado and New Mexico, 24. Rocky Mountain Association of Geologists, Geological Survey, Lakewood, CO (United States), 362 pp

Staudacher, T., 1987. Upper mantle origin for Harding County well gases. Nature, 325(6105): 605-607.

Strąpoć, D., Mastalerz, M., Dawson, K., Macalady, J., Callaghan, A.V., Wawrik, B., Turich, C., Ashby, M., 2011. Biogeochemistry of Microbial Coal-Bed Methane. Annu. Rev. Earth Planet. Sci., 39(1): 617-656.

Strąpoć, D., Mastalerz, M., Eble, C., Schimmelmann, A., 2007. Characterization of the origin of coalbed gases in southeastern Illinois Basin by compound-specific carbon and hydrogen stable isotope ratios. Org. Geochem., 38(2): 267-287.

Strąpoć, D., Mastalerz, M., Schimmelmann, A., Drobniak, A., Hedges, S., 2008. Variability of geochemical properties in a microbially dominated coalbed gas system from the eastern margin of the Illinois Basin, USA. Int. J. Coal Geol., 76(1): 98-110.

Strąpoć, D., Schimmelmann, A., Mastalerz, M., 2006. Carbon isotopic fractionation of CH_4 and CO2 during canister desorption of coal. Org. Geochem., 37(2): 152-164.

Stuart, F.M., Lass-Evans, S., Godfrey Fitton, J., Ellam, R.M., 2003. High $^{3}He/^{4}He$ ratios in picritic basalts from Baffin Island and the role of a mixed reservoir in mantle plumes. Nature, 424(6944): 57-59.

Stute, M., Clark, J.F., Schlosser, P., Broecker, W.S., Bonani, G., 1995. A 30,000 yr Continental Paleotemperature Record Derived from Noble Gases Dissolved in Groundwater from the San Juan Basin, New Mexico. Quaternary Research, 43(2): 209-220.

Su, X., Lin, X., Liu, S., Zhao, M., Song, Y., 2005. Geology of coalbed methane reservoirs in the Southeast Qinshui Basin of China. Int. J. Coal Geol., 62(4): 197-210.

Tang, S., Tang, D., Xu, H., Tao, S., Li, S., Geng, Y., 2016. Geological mechanisms of the accumulation of coalbed methane induced by hydrothermal fluids in the western Guizhou and eastern Yunnan regions. Journal of Natural Gas Science and Engineering, 33: 644-656.

Tao, M., Shi, B., Li, J., Wang, W., Li, X., Gao, B., 2007. Secondary biological coalbed gas in the Xinji area, Anhui province, China: Evidence from the geochemical features and secondary changes. Int. J. Coal Geol., 71(2–3): 358-370.

Tao, S., Tang, D., Qin, Y., Xu, H., Li, S., Cai, J., 2010. Analysis on thermal history of coal strata of typical mining areas in western Guizhou and eastern Yunnan Coal Geology & Exploration, 38(6): 17-21.

Teichmüller, M., 1989. The genesis of coal from the viewpoint of coal petrology. Int. J. Coal Geol., 12(1): 1-87.

Thomas, J.A., McGaughey, A.J.H., 2009. Water Flow in Carbon Nanotubes: Transition to Subcontinuum Transport. Phys. Rev. Lett., 102(18): 184502.

Tishchenko, P., Hensen, C., Wallmann, K., Wong, C.S., 2005. Calculation of the stability and solubility of methane hydrate in seawater. Chem. Geol., 219(1): 37-52.

Torgersen, T., 1980. Controls on pore-fluid concentration of ^{4}He and ^{222}Rn and the calculation of 4He/222Rn ages. J. Geochem. Explor., 13(1): 57-75.

Torgersen, T., Clarke, W.B., 1985. Helium accumulation in groundwater, I: An evaluation of sources and the continental flux of crustal ^{4}He in the Great Artesian Basin, Australia. Geochim. Cosmochim. Acta, 49(5): 1211-1218.

Torgersen, T., Ivey, G.N., 1985. Helium accumulation in groundwater. II: A model for the accumulation of the crustal ^{4}He degassing flux. Geochim. Cosmochim. Acta, 49(11): 2445-2452.

Torgersen, T., Kennedy, B.M., 1999. Air-Xe enrichments in Elk Hills oil field gases: role of water in migration and storage. Earth Planet. Sci. Lett., 167(3–4): 239-253.

Torgersen, T., Kennedy, B.M., Hiyagon, H., Chiou, K.Y., Reynolds, J.H., Clarke, W.B., 1989. Argon accumulation and the crustal degassing flux of ^{40}Ar in the Great Artesian Basin, Australia. Earth Planet. Sci. Lett., 92(1): 43-56.

Torgersen, T., Kennedy, B.M., van Soest, M.C., 2004. Diffusive separation of noble gases and noble gas abundance patterns in sedimentary rocks. Earth Planet. Sci. Lett., 226(3): 477-489.

Trull, T., Nadeau, S., Pineau, F., Polve´, M., Javoy, M., 1993. C-He systematics in hotspot xenoliths: Implications for mantle carbon contents and carbon recycling. Earth Planet. Sci. Lett., 118(1): 43-64.

Vanwonterghem, I., Evans, P.N., Parks, D.H., Jensen, P.D., Woodcroft, B.J., Hugenholtz, P., Tyson, G.W., 2016. Methylotrophic methanogenesis discovered in the archaeal phylum Verstraetearchaeota. Nature Microbiology, 1(12): 16170.

Vermeesch, P., Balco, G., Blard, P.-H., Dunai, T.J., Kober, F., Niedermann, S., Shuster, D.L., Strasky, S., Stuart, F.M., Wieler, R., Zimmermann, L., 2015. Interlaboratory comparison of cosmogenic ^{21}Ne in quartz. Quaternary Geochronology, 26: 20-28.

Vinson, D.S., Blair, N.E., Martini, A.M., Larter, S., Orem, W.H., McIntosh, J.C., 2017. Microbial methane from in situ biodegradation of coal and shale: A review and reevaluation of hydrogen and carbon isotope signatures. Chem. Geol., 453: 128-145.

Wang, B., Sun, F., Tang, D., Zhao, Y., Song, Z., Tao, Y., 2015a. Hydrological control rule on coalbed methane enrichment and high yield in FZ Block of Qinshui Basin. Fuel, 140: 568-577.

Wang, D.T., Gruen, D.S., Lollar, B.S., Hinrichs, K.-U., Stewart, L.C., Holden, J.F., Hristov, A.N., Pohlman, J.W., Morrill, P.L., Könneke, M., Delwiche, K.B., Reeves, E.P., Sutcliffe, C.N., Ritter, D.J., Seewald, J.S., McIntosh, J.C., Hemond, H.F., Kubo, M.D., Cardace, D., Hoehler, T.M., Ono, S., 2015b. Nonequilibrium clumped isotope signals in microbial methane. Science, 348(6233): 428.

Wang, H., Fu, X., Zhang, X., Niu, Q., Ge, Y., Tian, J., Cheng, X., Chen, N., Hou, X., Du, H., 2018. Source, Age, and Evolution of Coal Measures Water in Central-South Qinshui Basin, China. Energy Fuels, 32(7): 7358-7373.

Wang, L.-J., Yu, J.-H., Griffin, W.L., O'Reilly, S.Y., 2012. Early crustal evolution in the western Yangtze Block: Evidence from U–Pb and Lu–Hf isotopes on detrital zircons from sedimentary rocks. Precambrian Res., 222-223: 368-385.

Wang, Q., 2013. The Output Mechanism and Control Factors of the Coal Powder in Panzhuang Area, Qinshui Basin. Doctoral Thesis, China Univerisity of Mining & Technology (Beijing), 127 pp.

Wang, Y., Zhang, Q., Zhu, W., Wang, L., Xie, G., Ge, R., Liu, C., Zou, X., 2014. Meso-Cenozoic Structural Deformation and Tectonic Stress Fields in the South Margin of Qinshui Basin. Geological Journal of China Universities, 20(2): 249-259.

Wang, Z., Tang, S., Sun, P., Zheng, G., 2013. Feasibility study of multi-layer drainage for No. 3 and 9 Coal Seams in Shouyang Block, Qinshui Basin. Coal Geology of China, 25(11): 21-26.

Wei, M., Ju, Y., 2015. Chemical characteristics and origin of produced waters from coalbed gas field in the southern of Qinshui Basin. Journal of China Coal Society, 40(3): 629-635.

Wen, H., Jun, L., Huazhou, H., 2008. A Study on Coal Seam Reservoir Characteristics and CBM Exploitation Condition in Baotian-Qingshan Region, Guizhou Coal Geology of China, 20(2): 20-23.

Wen, T., Castro, M.C., Ellis, B.R., Hall, C.M., Lohmann, K.C., 2015. Assessing compositional variability and migration of natural gas in the Antrim Shale in the Michigan Basin using noble gas geochemistry. Chem. Geol., 417: 356-370.

Wen, T., Castro, M.C., Nicot, J.-P., Hall, C.M., Larson, T., Mickler, P., Darvari, R., 2016. Methane Sources and Migration Mechanisms in Shallow Groundwaters in Parker and Hood Counties, Texas—A Heavy Noble Gas Analysis. Environ. Sci. Technol., 50(21): 12012-12021.

Wetherill, G.W., 1954. Variations in the Isotopic Abundances of Neon and Argon Extracted from Radioactive Minerals. Physical Review, 96(3): 679-683.

Whiticar, M.J., 1996. Stable isotope geochemistry of coals, humic kerogens and related natural gases. Int. J. Coal Geol., 32(1): 191-215.

Whiticar, M.J., 1999. Carbon and hydrogen isotope systematics of bacterial formation and oxidation of methane. Chem. Geol., 161(1–3): 291-314.

Whiticar, M.J., Faber, E., Schoell, M., 1986. Biogenic methane formation in marine and freshwater environments: CO_2 reduction vs. acetate fermentation—Isotope evidence. Geochim. Cosmochim. Acta, 50(5): 693-709.

Wilkins, R.W.T., George, S.C., 2002. Coal as a source rock for oil: a review. Int. J. Coal Geol., 50(1): 317-361.

Winfrey, M.R., Zeikus, J.G., 1977. Effect of sulfate on carbon and electron flow during microbial methanogenesis in freshwater sediments. Appl. Environ. Microbiol., 33(2): 275.

Wu, C., Lin, X., Yang, Z., Jin, J., Zhang, Z., 2016. Features and causes of coal measures fluid pressure in Tucheng Syncline Songhe Block of western Guizhou. Coal Science and Technology, 44(10): 88-94.

Wu, C., Yang, Z., Qin, Y., Chen, J., Zhang, Z., Li, Y., 2018. Characteristics of Hydrogen and Oxygen Isotopes in Produced Water and Productivity Response of Coalbed Methane Wells in Western Guizhou. Energy Fuels, 32(11): 11203-11211.

Xia, X., Tang, Y., 2012. Isotope fractionation of methane during natural gas flow with coupled diffusion and adsorption/desorption. Geochim. Cosmochim. Acta, 77: 489-503.

Xu, H., 2012. Geological Theory and Technology for Coalbed Methane Development with Thin and Medium Coal Seam Zones in Guizhou, Doctoral Thesis, China University of Mining and Technology, 171 pp.

Xu, S., Nakai, S.i., Wakita, H., Wang, X., 1995. Mantle-derived noble gases in natural gases from Songliao Basin, China. Geochim. Cosmochim. Acta, 59(22): 4675-4683.

Xu, W., Wang, D., Wang, Q., Pei, F., Lin, J., 2004. $^{40}Ar/^{39}Ar$ dating of hornblende and biotite in Mesozoic intrusive complex from the North China Block: Constraints on the time of lithospheric thining. Geochimica, 33(3): 221-231.

Xu, Z., 2017. Study on Isotopic Geochemistry and Origins of Coalbed Methane in the Northern Qinshui Basin. Doctoral Thesis, China Univerisity of Mining & Technology (Beijing), 132 pp.

Xu, Z., Liu, Q., Zheng, Q., Cheng, H., Wu, Y., 2016. Isotopic composition and content of coalbed methane production gases and waters in karstic collapse column area, Qinshui Coalfield, China. J. Geochem. Explor., 165: 94-101.

Yatsevich, I., Honda, M., 1997. Production of nucleogenic neon in the Earth from natural radioactive decay. Journal of Geophysical Research: Solid Earth, 102(B5): 10291-10298.

Yee, D., Seidle, J.P., Hanson, W.B., 1993. Gas Sorption on Coal and Measurement of Gas Content. In: Law, B.E., Rice, D.D. (Editors), Hydrocarbons from Coal American Association of Petroleum Geologists, pp. 203-218.

Yin, S., Ding, W., Hu, Q., Liu, J., Mei, Y., Liu, Z., 2016. Hydrocarbon source rock characteristics and favorable hydrocarbon-generating area evaluation of Carboniferous-Permian coal measures strata in Qinshui basin, Shanxi, China. Journal of Chengdu University of Technology (Science & Technology Edition), 43(2): 163-176.

Yoksoulian, L.E., Rimmer, S.M., Rowe, H.D., 2016. Anatomy of an intruded coal, II: effect of contact metamorphism on organic $\delta^{13}C$ and implications for the release of thermogenic methane, Springfield (No. 5) Coal, Illinois Basin. Int. J. Coal Geol., 158: 129-136.

Zartman, R., Wasserburg, G., Reynolds, J., 1961. Helium, argon, and carbon in some natural gases. J. Geophys. Res., 66(1): 277-306.

Zazzeri, G., Lowry, D., Fisher, R.E., France, J.L., Lanoisellé, M., Kelly, B.F.J., Necki, J.M., Iverach, C.P., Ginty, E., Zimnoch, M., Jasek, A., Nisbet, E.G., 2016. Carbon isotopic signature of coal-derived methane emissions to the atmosphere: from coalification to alteration. Atmos. Chem. Phys., 16(21): 13669-13680.

Zeikus, J.G., Winfrey, M.R., 1976. Temperature limitation of methanogenesis in aquatic sediments. Appl. Environ. Microbiol., 31(1): 99.

Zeng, Y., Fan, B., Liu, H., Wang, C., 1999. An analysis to the history of thermal evolution hydrocarbon- generating and the heat source about main seam of Shanxi formation in southeastern Shanxi Province. Scientia Geologica Sinica, 34(1): 90-98.

Zhang, C., 2017. Resource Characteristics and Optimization of Coalbed Methane in Liu Panshui Coalfield, Master Thesis, China University of Mining and Technology, 120 pp.

Zhang, J., Liu, D., Cai, Y., Yao, Y., Ge, X., 2018. Carbon isotopic characteristics of CH_4 and its significance to the gas performance of coal reservoirs in the Zhengzhuang area, Southern Qinshui Basin, North China. Journal of Natural Gas Science and Engineering, 58: 135-151.

Zhang, J., Tao, M., 2000. Geological significances of coal bed methane carbon isotope in coal bed methane exploration. Acta Sedimentologica Sinica, 18(4): 611-614.

Zhang, J.Y., Zheng, C.G., Ren, D.Y., Chou, C.L., Liu, J., Zeng, R.S., Wang, Z.P., Zhao, F.H., Ge, Y.T., 2004. Distribution of potentially hazardous trace elements in coals from Shanxi province, China. Fuel, 83(1): 129-135.

Zhang, S., Tang, S., Li, Z., Guo, Q., Pan, Z., 2015. Stable isotope characteristics of CBM co-produced water and implications for CBM development: The example of the Shizhuangnan block in the southern Qinshui Basin, China. Journal of Natural Gas Science and Engineering, 27, Part 3: 1400-1411.

Zhang, S., Zhang, X., Li, G., Liu, X., Zhang, P., 2019a. Distribution characteristics and geochemistry mechanisms of carbon isotope of coalbed methane in central-southern Qinshui basin, China. Fuel, 244: 1-12.

Zhang, W., Li, Y., Zhao, F., Han, W., Li, Y., Wang, Y., Holland, G., Zhou, Z., 2019b. Using noble gases to trace groundwater evolution and assess helium accumulation in Weihe Basin, central China. Geochim. Cosmochim. Acta, 251: 229-246.

Zhao, F., 1997. Study on the mechanism of distributions and occurrences of hazardous minor and trace elements in coal and leaching experiments of coal combustion residues. Doctoral Thesis, China University of Mining & Technology, 157 pp.

Zhao, L., Ward, C.R., French, D., Graham, I.T., Dai, S., Yang, C., Xie, P., Zhang, S., 2018. Origin of a kaolinite-NH_4-illite-pyrophyllite-chlorite assemblage in a marine-influenced anthracite and associated strata from the Jincheng Coalfield, Qinshui Basin, Northern China. Int. J. Coal Geol., 185: 61-78.

Zhao, X., Yang, Y., Sun, F., Wang, B., Zuo, Y., Li, M., Shen, J., Mu, F., 2016. Enrichment mechanism and exploration and development technologies of high coal rank coalbed methane in south Qinshui Basin, Shanxi Province. Petroleum Exploration and Development, 43(2): 332-339.

Zheng, J., 2013. Sedimentary Environment and Coal Accumulation Pattern of Late Permian Low Sulfur Coal in Guizhou. Coal Geology of China, 25(6).

Zheng, J., Griffin, W.L., O'Reilly, S.Y., Zhang, M., Pearson, N., Pan, Y., 2006. Widespread Archean basement beneath the Yangtze craton. Geology, 34(6): 417-420.

Zhou, P., Liang, L., Bai, L., Zeng, J., 2019. Study on the structural complexity of Yangmeishu syncline based on the fractal theory. Natural Gas Technology and Economy, 13(2): 25-27.

Zhou, Z., Ballentine, C.J., 2006. ^{4}He dating of groundwater associated with hydrocarbon reservoirs. Chem. Geol., 226(3–4): 309-327.

Zhou, Z., Ballentine, C.J., Kipfer, R., Schoell, M., Thibodeaux, S., 2005. Noble gas tracing of groundwater/coalbed methane interaction in the San Juan Basin, USA. Geochim. Cosmochim. Acta, 69(23): 5413-5428.

Zhou, Z., Ballentine, C.J., Schoell, M., Stevens, S.H., 2012. Identifying and quantifying natural CO2 sequestration processes over geological timescales: The Jackson Dome CO2 Deposit, USA. Geochim. Cosmochim. Acta, 86: 257-275.

Zhuang, X., Querol, X., Zeng, R., Xu, W., Alastuey, A., Lopez-Soler, A., Plana, F., 2000. Mineralogy and geochemistry of coal from the Liupanshui mining district, Guizhou, south China. Int. J. Coal Geol., 45(1): 21-37.

Zimmerman, R., 1986. Fission-track dating of samples of the Illinois drill hole core. US Geological Survey Bulletin, 1622: 100-108.

Zinder, S.H., 1993. Physiological Ecology of Methanogens. In: Ferry, J.G. (Ed.), Methanogenesis: Ecology, Physiology, Biochemistry & Genetics. Springer US, Boston, MA, pp. 128-206.